

PRESSURE DROP AND HEAT TRANSFER IN INVERTED FILM BOILING HYDROGEN

By

JAMES PASCH

A DISSERTATION PRESENTED TO THE GRADUATE SCHOOL
OF THE UNIVERSITY OF FLORIDA IN PARTIAL FULFILLMENT
OF THE REQUIREMENTS FOR THE DEGREE OF
DOCTOR OF PHILOSOPHY

UNIVERSITY OF FLORIDA

2006

Copyright 2006

by

James Pasch

The effort put forth over the last four and a half years to complete this Ph.D. is dedicated to my children, Nicholas and Connor. This is one component in my continuing efforts to be a good father and role model for them. Life is much more interesting and rewarding when you remain challenged.

ACKNOWLEDGMENTS

I would like to thank Dr. Samim Anghaie for agreeing to work with me on this effort that started four and half years ago. I understand that working with a long-distance student is difficult – all the more reason I appreciate his patient support to achieve this goal. I thank my wife, Melynda, who supported my efforts by giving me time to study. I express my gratitude for having a great and supportive family; John and Alice Pasch, brother Jack, and sisters Alison and Lorelei. I also express my gratitude to Robert Hendricks for giving freely of his memories of these experiments in which he was centrally involved. His efforts, then and now, provide the engineering community with unique information.

TABLE OF CONTENTS

	<u>page</u>
ACKNOWLEDGMENTS	4
LIST OF TABLES	7
LIST OF FIGURES	8
ABSTRACT	16
Chapter	
1 INTRODUCTION AND STATE OF THE ART	18
Introduction.....	18
Motivation	18
Objectives	19
Pressure Drop.....	20
Heat Transfer	23
2 MODELLING APPROACHES FOR TWO-PHASE FLOW	38
Angular Simplifications.....	38
Basic Models	38
Flow Regime Analysis.....	40
3 TEST DATA DESCRIPTION AND EVALUATION AND MODEL DEVELOPMENT...44	
Description of Experiments	44
Experimental Setup	44
Experimental Conditions	45
Heat Leaks	46
Instrumentation.....	46
Data Validation.....	49
Comparison with Similar Data	49
End Effects	51
Hydrogen States: Parahydrogen and Orthohydrogen	55
Model Development	58
Nature of Data	60
Magnitude of Radiation Heating	63
Conservation Equations.....	64
Entrance Lengths	66
Boundary Conditions.....	68
Closure Conditions	70
Vapor superheat.....	70
Liquid energy flow	71

Wall friction	74
Model Implementation	75
4 ANALYSIS AND VALIDATION OF MOMENTUM MODEL RESULTS	90
Data Referencing	90
Data Refinement	90
Omitted Data	90
Problematic Data	90
Data Representation.....	93
Problematic Runs.....	93
Vapor Superheat	95
Model Results	96
Validation of Model Results	97
Range of Validity.....	98
5 EVALUATION AND CORRELATION OF DATA AND CORRELATION ASSESSMENT	106
Data Correlation.....	106
Low Pressure Slip Correlation.....	111
Low Pressure Slip Correlation Assessment.....	113
High Pressure Slip Correlation	115
High Pressure Slip Correlation Assessment	115
Accuracy of the Slip Correlations.....	116
Validation of the Slip Correlations	118
Observations	119
6 HEAT TRANSFER ANALYSIS	168
Data Omission	168
The Nature of IFB Heat Transfer.....	168
The General HTC Profile	169
An Interpretation of Controlling Effects in IFB Heat Transfer	170
Assessment of Various Models	172
7 CONCLUSIONS AND RECOMMENDATIONS	180
General Conclusions.....	180
Pressure Drop Conclusions and Recommendations	181
Heat Transfer Conclusions and Recommendations.....	182
Recommendations for Future Efforts	182
LIST OF REFERENCES	184
BIOGRAPHICAL SKETCH	190

LIST OF TABLES

<u>Table</u>	<u>page</u>
3-1. Table of experimental conditions.	77
3-2. Comparison of Core et al. and Hendricks et al. heat transfer coefficients	78
3-3. Comparison of heat transfer coefficients for Wright and Walters data and TN 765.....	79
3-4. Summary of test conditions for major hydrogen heat transfer studies	79
3-5. Result of parametric sensitivity study of end axial heat conduction.	79
3-6. Tube wall axial heat transfer analysis.....	79
4-1. List of tube numbers, dimensions, and runs executed with the tubes.	99
4-2. Statistical analysis of pressure data	100
5-1. Accuracies of some common slip correlations.	121
5-2. Comparison of pressure drop prediction accuracies.	122
6-1. Comparison of predictive accuracy of various IFB models.	176

LIST OF FIGURES

<u>Figure</u>	<u>page</u>
2-1. Various flow regimes for IFB.....	43
2-2. Flow regime map generated by Takenaka for IFB (1989).	43
3-1. TN 765 experimental setup.....	80
3-2. TN 3095 experimental setup.....	81
3-3. 1961 data test section.....	82
3-4. TN 3095 test section.....	83
3-5. TN 3095 instrumentation.....	84
3-6. Nodal distribution and heat generation distribution used to model end effects	85
3-7. Radial metal temperature profiles as a function of metal thermal conductivity.....	85
3-8. Radial metal temperature profiles as a function of metal thickness.	86
3-9. Effect of specified parameters on tube end wall axial heat transfer.....	86
3-10. Difference in wall to liquid temperature for all data considered.....	87
3-11. Wall to liquid hydrogen temperature differences for four runs.....	87
3-12. Theoretical liquid core temperature profile at the exit of the heated test section.....	88
3-13. Flow diagram for momentum and energy analysis of data.	89
4-1. Sample of 1961 data wall temperatures.....	101
4-2. Tube 3 exhibits a consistent reduction in wall temperature at 34 cm.....	101
4-3. Comparison of runs 7 and 8 pressure profiles	102
4-4. Run 14 energy and momentum balances.....	102
4-5. Results of modifying the coefficient in Burmeister's equation.....	103
4-6. Culled data momentum and energy balance results from model.....	103
4-7. Calculated void fraction from model for the culled data set.	104
4-8. Velocity slip ratio vs quality from model for the culled data set.	104

4-9. Void fraction vs. equilibrium quality for three runs of Ottosen’s experiments.....	105
5-1. Vapor velocity vs. superficial velocity.....	122
5-2. Comparison of model slip and slip predicted from correlations.....	123
5-3. Predicted versus measured pressure gradients for all data used in correlating slip.....	123
5-4. Model and prediction results for run 1.....	124
5-5. Model and prediction results for run 2.....	125
5-6. Model and prediction results for run 3.....	126
5-7. Model and prediction results for run 4.....	127
5-8. Model and prediction results for run 5.....	128
5-9. Model and prediction results for run 6.....	129
5-10. Model and prediction results for run 7.....	130
5-11. Model and prediction results for run 9.....	131
5-12. Model and prediction results for run 10.....	132
5-13. Model and prediction results for run 11.....	133
5-14. Model and prediction results for run 12.....	134
5-15. Model and prediction results for run 13.....	135
5-16. Model and prediction results for run 15.....	136
5-17. Model and prediction results for run 16.....	137
5-18. Model and prediction results for run 17.....	138
5-19. Model and prediction results for run 18.....	139
5-20. Model and prediction results for run 19.....	140
5-21. Model and prediction results for run 20.....	141
5-22. Model and prediction results for run 21.....	142
5-23. Model and prediction results for run 33.....	143
5-24. Model and prediction results for run 34.....	144

5-25. Model and prediction results for run 35.	145
5-26. Model and prediction results for run 37.	146
5-27. Model and prediction results for run 38.	147
5-28. Model and prediction results for run 39.	148
5-29. Model and prediction results for run 40.	149
5-30. Model and prediction results for run 41.	150
5-31. Model and prediction results for run 42.	151
5-32. Model and prediction results for run 43.	152
5-33. Model and prediction results for run 45.	153
5-34. Model and prediction results for run 46.	154
5-35. Model and prediction results for run 47.	155
5-36. Model and prediction results for run 48.	156
5-37. Model and prediction results for run 49.	157
5-38. Model and prediction results for run 50.	158
5-39. Model and prediction results for run 51.	159
5-40. Model and prediction results for run 23.	160
5-41. Model and prediction results for run 24.	161
5-42. Model and prediction results for run 25.	162
5-43. Model and prediction results for run 27.	163
5-44. Model and prediction results for run 32.	164
5-45. Model and prediction results for run 36.	165
5-46. Model and prediction results for run 44.	166
5-47. Model and prediction results for run 8.	167
6-1. Variation of the HTC as a function of quality in IFB flow.	176
6-2. Variation of HTC versus equilibrium quality in the IAFB flow regime.	177

6-3. Variation of HTC versus mass quality for runs 39-42.....	177
6-4. Variation of HTC versus mass quality for runs 44-47.....	178
6-5. Variation of Dittus-Boelter vapor properties with pressure and temperature.	178
6-6. Comparison of predicted HTC using the TN 3095 correlation with the experimental	179
6-7. Comparison of predicted HTC using the modified equilibrium bulk Dittus-Boelter.....	179

NOMENCLATURE

A	area
AIAFB	agitated inverted annular film boiling
A_s	surface area
b	y-intercept of line
Bo	boiling number
C	conversion constants for ortho-para conversion
CHF	critical heat flux
Co	Colburn number
C_0	drift flux model distribution parameter
c_p	specific heat at constant pressure
c_v	specific heat at constant density
D	diameter
DFB	dispersed film boiling
f	friction factor
F	Chen's enhancement factor
f_1	low pressure slip correlating parameter
f_2	high pressure slip correlating parameter
Fr	Froude number
G	mass flux
G_0	reference mass flux
Gr	Grasshof number

g	gravity
h	mass-specific enthalpy
h, or HTC	heat transfer coefficient
IAFB	inverted annular film boiling
IFB	inverted film boiling
ISFB	inverted slug film boiling
j	superficial velocity
k	thermal conductivity
K	conversion factor for ortho-para conversion
L	length
LOCA	loss of coolant accident
m	slope of line
n	number density
Nu	Nusselt number
p	pressure
Pr	Prandtl number
q''	heat flux
q ₀ ''	reference heat flux
\dot{Q}	heat flow rate
r	radial direction, radial distance
Re	Reynolds number
s	velocity slip
S	Chen's suppression factor

t	time
T	temperature
u	velocity
w	mass flow rate
x	mass quality
x_{eq}	equilibrium quality
z	elevation

Greek symbols

α	void fraction
β	volumetric quality
ΔT	temperature differential
χ	Lockheed-Martinelli parameter
ϕ	friction multiplier
μ	viscosity
ρ	density
σ	surface tension, Stefan-Boltzmann constant
τ	shear stress
υ	specific volume

Subscripts

av	average
b	bulk

c	cross section
calc	calculated
CL	centerline
crit	critical condition
exp	experimental
f	film conditions
h	hydraulic
i	inlet, interface
int	y-intercept
l	liquid phase
lo	all fluid flowing as liquid
m	mean conditions
mac	macroscopic, in Chen's correlation
mic	microscopic, in Chen's correlation
o	orthoxygen
p	parahydrogen
rad	radiation
s	saturated conditions
slope	slope
tt	turbulent-turbulent liquid-vapor phases
TP	two-phase
v	vapor phase
w	wall

Abstract of Dissertation Presented to the Graduate School
of the University of Florida in Partial Fulfillment of the
Requirements for the Degree of Doctor of Philosophy

PRESSURE DROP AND HEAT TRANSFER IN INVERTED FILM BOILING HYDROGEN

By

James Pasch

December 2006

Chair: Samim Anghaie

Major: Nuclear Engineering Sciences

Two-phase boiling hydrogen pressure drop and heat transfer is studied in the context of high velocity upflow in a constant, high heat flux, steady state, internal pipe flow environment. These data were generated by NASA in the early and mid 1960s in support of the manned space flight programs. Measurements taken were local pressure, temperature, and voltage drop. System measurements included mass flow rate, and test section inlet and discharge pressure and temperature.

This effort establishes the nature of the flow as inverted film boiling, which has been studied to some degree. In this structure, the wall temperatures are too hot to allow liquid to remain at the surface. Therefore, a vapor film is established at the wall throughout the flow. The approach of this analysis is to reverse-engineer the data to determine mass quality, void fraction, and velocity slip. This is accomplished by applying a one-dimensional, five-equation model, with pressure gradient being the one combined equation for the liquid and vapor phases. Other major assumptions are that all of the vapor is at the mean film temperature, and the liquid core experiences no sensible heating.

The resulting velocity slips are correlated for high and low pressure conditions, with the cutoff established at 600 kPa. Good agreement is achieved between the pressures predicted

using the slip correlations and the measured pressures. Results are in general significantly better than those from the homogeneous equilibrium model.

Various established heat transfer coefficient models are also applied to these data. It is shown that pre-critical heat flux models fail absolutely to predict the heat transfer coefficient. It is further shown that film boiling models that focus on buoyancy fail as well. While all forced convection film boiling models are within a reasonable range of the data, recommendations for appropriate models are made.

The range of pipe inlet conditions are 188 kPa to 1265 kPa, mass fluxes from 327 kg/m²-s to 3444 kg/m²-s, and heat fluxes from 294 kW/m² to 2093 kW/m². Two heated test section lengths are 30.5 cm. and 61.0 cm. long, and five different diameters range from 0.48 cm. to 1.29 cm.

CHAPTER 1 INTRODUCTION AND STATE OF THE ART

Introduction

This dissertation investigates the state of understanding of and prediction capabilities for boiling hydrogen, and the needs for improving the current condition. It presents an engineering-based approach to improve on the prediction capabilities for pressure drop and heat transfer.

Motivation

Accurate predictions of pressure drop in and heat transfer from a pipe to hydrogen during forced convective two-phase flow benefit engineers throughout the life of a product. During the design phase, good pressure drop and heat transfer models will help the engineer reduce the uncertainty in the design parameters. During the product test and development phase, good models will help the engineer to correctly interpret test data, therefore allowing him to determine where modifications are necessary. During the use of the product, problems inevitably arise that require the engineer to search for the root cause. This investigation requires a good understanding of how the product will react under off-nominal operating conditions. Accurate, mechanistic models allow the engineer to perform this investigation with confidence that the thermal-hydraulics – related results of the investigation are valid.

The rocket industry uses liquid hydrogen as a fuel. Heat transfer to two-phase flowing hydrogen routinely occurs during three phases of rocket operation; fuel tanking, rocket engine conditioning, and possibly during rocket firing. Nuclear Thermal Propulsion (NTP) systems are powered by high temperature nuclear reactors that are used to heat up hydrogen propellant to temperatures in excess of 3,000 K. Hydrogen is the only viable propellant for the NTP systems because of its low molecular weight that generates the highest specific impulse (I_{sp}) at the maximum operating temperatures of these reactors. Hydrogen is pumped at cryogenic

temperatures and relatively high pressures to cool the rocket nozzle before entering the reactor core. Heat removal in the rocket nozzle and reactor core areas transform subcooled liquid hydrogen to superheated hydrogen gas. The evolution of hydrogen flow in the system involves two-phase flow and heat transfer under subcooled, saturated, and superheated thermodynamic conditions. In addition to the rockets, a nascent industry that may require modeling of this sort is the hydrogen-fueled car industry.

Objectives

This research effort includes a number of objectives. First, it is necessary to conduct a literature search to determine the best battery of two-phase hydrogen tests to analyze. Using the data from this test series, the next objective is to evaluate the quality of these data. The primary objective is to improve the accuracy of predicted pressure drop of and heat transfer to two-phase hydrogen in a forced convection, highly heated, internal pipe flow environment.

Mechanistically-based models are preferred, but correlations that provide improvements to pressure drop and heat transfer predictions are considered acceptable. Since very high wall to bulk temperature ratios can reasonably be expected with liquid hydrogen flowing in a heated pipe, the effect of radial temperature variation will necessarily be included. This goal will include the generation of void fraction, quality, and slip information that must be evaluated against data. It is an objective to develop a predictive model for one or more of these parameters so the pressure drop can be predicted. An important criterion of success is to reproduce the pressure drop data with minimal error using the predictive model.

Additionally, it is an objective to either improve on the accuracy of current heat transfer models, or at least review the current understanding of this subject and recommend models to use for two-phase hydrogen.

Pressure Drop

Pressure change for a vaporizing fluid is comprised of three contributing effects: momentum decrease due to increasing fluid velocity as it vaporizes, friction between the fluid and the wall, and pressure change due to a change in height of the fluid. From Collier (1981), these three terms for a homogeneous flow are

$$\left(\frac{dp}{dz} \right)_a = -G \frac{d\bar{u}}{dz} \quad (1.1)$$

$$\left(\frac{dp}{dz} \right)_F = -\frac{2 f_{TP} \rho \bar{u}^2}{D} \quad (1.2)$$

$$\left(\frac{dp}{dz} \right)_z = -\rho g \quad (1.3)$$

In these equations, p is pressure, a refers to acceleration, F refers to friction, z refers to elevation, G is mass flux, u is velocity, f_{TP} is the two-phase friction factor, ρ is density, D is tube diameter, and g is gravity. The frictional term is often determined by calculating what the frictional loss would be if the entire flow were liquid, then applying a two-phase frictional multiplier. This method was developed by Lockhart, Martinelli, Nelson, and others at the University of California in the 1940's (Martinelli et al., 1944, 1946; Martinelli and Nelson, 1948; Lockhart and Martinelli, 1949). The form of their equation is

$$\left(\frac{dp}{dz} \right)_F = \left(\frac{dp}{dz} \right)_{F_{lo}} \phi_{lo}^2 \quad (1.4)$$

The two-phase frictional multiplier, ϕ_{lo}^2 , is modeled as a function of flow quality and system pressure. Determining this multiplier is the goal of much research, particularly since the research of Martinelli and coworkers was limited to atmospheric pressure.

The frictional multiplier can take four different forms. Two of them develop from using only the liquid or vapor mass that is present in the flow and are represented by a single letter subscript “l” or “v” to indicate liquid or vapor. The other two develop from using the entire flow as either liquid or vapor, and have a two-letter subscript “lo” or “vo” to signify that the entire flow is liquid or vapor. Traditionally, liquid conditions are used in evaporating systems, and vapor conditions are used for condensing systems. Relations can be developed between these various frictional multipliers.

A correlating parameter developed by Martinelli and his coworkers is X_{tt} , which they determined to have the following form

$$X_{tt} = \left(\frac{1-x}{x} \right)^9 \left(\frac{\mu_l}{\mu_v} \right)^{.1} \left(\frac{\rho_v}{\rho_l} \right)^{.5} \quad (1.5)$$

In this equation, x is quality and μ is viscosity. The subscripts l and v refer to liquid and vapor phases, respectively. This parameter, in various similar forms, has been used to evaluate the frictional multipliers. The exact forms of the frictional multiplier models depend on the nature of the flow of the liquid and vapor phases – turbulent or laminar. Thus, there are four combinations of turbulent/laminar flows.

The currently preferred model for predicting the frictional multiplier was developed by Chisholm (1973). His model uses a property index, composed of the property terms in equation (1.5) above without the quality term. Mass flux is also a factor in his model.

$$\phi_{lo}^2 = 1 + \left(\frac{\rho_l}{\rho_v} - 1 \right) \left(Bx(1-x) + x^2 \right) \quad (1.6)$$

B is a function of the saturated liquid and vapor densities and the flow regime combination of the two phases (i.e., turbulent-turbulent, turbulent-laminar, laminar-turbulent, or laminar-laminar), and x is quality.

Hendricks et al. (1961) derived a version of X_{tt} for the peculiar case of inverted annular flow. The primary difference in the derivation is the position of the phases in the flow.

Martinelli et al. (1944) assumed that liquid was adjacent to the wall and vapor was at the tube core, or that the flow is homogeneous. For convective hydrogen, the flow is usually better described as separated and the phase adjacent to the wall is vapor, not liquid. However, Hendricks et al. (1961) determined that the correlating parameter, presented in equation (1.5), was the same in both cases.

Papadimitriou and Skorek (1991) processed data from two of Hendricks' tests with their one-dimensional thermohydraulic model THESEUS. They observed that the pressure drop due to viscous shear forces is about 100 times smaller than that caused by momentum change. The Chisholm (1973) method was used to model the two-phase friction multiplier.

John Rogers at Los Alamos Laboratories contributed significantly to the understanding of parahydrogen flow friction characteristics in the 1960's (1963, 1968). His efforts included extending Martinelli's friction multiplier quantification work beyond one atmosphere. His results were based upon theoretically determining the values of vapor void fraction and its derivative with respect to pressure at one atmosphere and at the critical point pressure with quality as a parameter, then interpolating the curves of void fraction verses pressure between these boundaries for the specified qualities. The empirical equation he developed for turbulent-turbulent flow as a result of his work is

$$\phi_t^2 = \left(\frac{1}{1-x} \right)^{1.8} \left\{ 1 + \frac{x^{.8187} \left[0.1324(p_{crit} - p) + 0.03966(p_{crit} - p)^3 \right]}{p^E} \right\} \quad (1.7)$$

where

$$E = 1.896x - 2.646x^2 + 1.695x^3 \quad (1.8)$$

In this equation, the subscript crit refers to the critical condition. Note that pressure is in atmospheres, x is quality, and the correlation gives the multiplier for the pressure drop for the liquid only in the tube, not for all the flow considered as liquid. Comparison of predicted versus experimental pressure drop with one set of parahydrogen data at various pressures indicated good agreement, with the error generally smaller at lower system pressures.

More recent work on separated two-phase flow pressure drop and heat transfer with vapor core was performed by Fu and Klausner (1997). In their work, conservation of mass, momentum, and energy laws are applied with closure relationships for vapor-liquid interface friction, liquid film turbulent viscosity, turbulent Prandtl number, and liquid droplet entrainment rate. Their results compared with 12 data sets of upflow and downflow were good. Although this theory assumes a liquid film and vapor core, the general procedure may prove useful with inverted annular flow after making the appropriate modifications to the various correlations.

Heat Transfer

John Chen published a correlation in 1966 that was based on the superposition of heat transfer caused by forced convective flow and by bubble generation. These terms are referenced with subscripts mac and mic for macroscopic and microscopic effects.

$$h = h_{mic} + h_{mac} \quad (1.9)$$

where

$$h_{mac} = h_l F(\chi_{tt}) \quad (1.10)$$

$$h_{mic} = 0.00122 \left[\frac{k_l^{0.79} c_{pl}^{0.45} \rho_l^{0.49}}{\sigma^{0.5} \mu_l^{0.29} h_{lv}^{0.24} \rho_v^{0.24}} \right] [T_w - T_s(P_l)]^{0.24} [P_s(T_w) - P_l]^{0.75} S(F, Re_l) \quad (1.11)$$

h_l is the heat transfer coefficient associated with single phase liquid flowing alone in the pipe. In this equation, k is thermal conductivity, c_p is specific heat, σ is the surface tension, h_{lv} is the heat

of vaporization, T is the temperature, S is a boiling suppression terms, F is an enhancement term, and Re is the Reynolds number. The subscripts w and s refer to wall and saturation conditions.

$$h_l = 0.023 \text{Re}_l^{0.8} \text{Pr}_l^{0.4} \left(\frac{k_l}{D} \right) \quad (1.12)$$

$$\text{Re}_l = \frac{G(1-x)D}{\mu_l} \quad (1.13)$$

In the above equation, Pr is the Prandtl number. The model incorporated heat transfer data from water, methane, pentane, and cyclohexane in the form of two factors, F and S, that were applied to the two different heat transfer components. His model proved to be very successful.

Modifications to the original model have been proposed. Collier provided curve fits for the factors F and S as a function of χ_{tt} .

Shah (1984) developed a correlation for saturated flow boiling for both vertical and horizontal tubes as a function of the Colburn, boiling, and Froude numbers, represented as Co, Bo, and Fr.

$$h = h_l f(\text{Co}, \text{Bo}, \text{Fr}_{le}) \quad (1.14)$$

where

$$\text{Co} = \left(\frac{1-x}{x} \right)^{0.8} \left(\frac{\rho_v}{\rho_l} \right)^{0.5} \quad (1.15)$$

$$\text{Bo} = \frac{q''}{Gh_{lv}} \quad (1.16)$$

$$\text{Fr}_{le} = \frac{G^2}{\rho_l^2 gD} \quad (1.17)$$

In the above equations, q'' is the heat flux.

Schrock and Grossman (1959) reviewed vertical, upward flowing boiling heat transfer data for water with the following result;

$$h = h_l C_1 \left[Bo + C_2 \left(\frac{1}{\chi_{tt}} \right)^{0.66} \right] \quad (1.18)$$

where C_1 and C_2 are constants with values of 7390 and 0.00015, respectively.

Gungor and Winterton (1986, 1987) developed the following for vertical, convective flow boiling;

$$h_{mac} = h_l \left[1 + 3000 Bo^{0.86} + \left(\frac{x}{1-x} \right)^{0.75} \left(\frac{\rho_l}{\rho_v} \right)^{0.41} \right] \quad (1.19)$$

Bjorge, Hall, and Rohsenow (1982) developed a correlation for vertical, internal, upward forced flow boiling for qualities above 0.05. Note that this correlation is a superposition of heat fluxes as opposed to Chen's superposition of heat transfer coefficients.

$$h = \frac{q_{tot}''}{T_w - T_s} \quad (1.20)$$

$$q_{tot}'' = q_{fc}'' + q_{fdb}'' \left[1 - \left(\frac{(T_w - T_s)_i}{T_w - T_s} \right)^3 \right] \quad (1.21)$$

$$q_{fc}'' = F_B Pr_l \left(\frac{k_l}{D} \right) (T_w - T_s) \frac{Re_l^{0.9}}{C_2} \quad (1.22)$$

$$F_B = 0.15 \left(\frac{1}{\chi_{tt}} + \frac{2}{\chi_{tt}^{0.32}} \right) \quad (1.23)$$

$$C_2 = f(Pr_l, Re_l) \quad (1.24)$$

$$q_{fdb}'' = B_M \mu_l h_{lv} \left[\frac{g(\rho_l - \rho_v)}{\sigma} \right]^{1/2} \left[\frac{k_l^{1/2} \rho_l^{17/8} c_{pl}^{19/8} \rho_v^{1/8} (T_w - T_s)^3}{\mu_l h_{lv}^{7/8} (\rho_l - \rho_v)^{9/8} \sigma^{5/8} T_s^{1/8}} \right] \quad (1.25)$$

$$(T_w - T_s)_i = \frac{8\sigma T_s h_{fc}}{k_l h_{lv}} (\nu_v - \nu_l) \quad (1.26)$$

In the above equation, ν is the specific volume.

Kandlikar (1990) developed the correlation below for vertical and horizontal flow boiling heat transfer in tubes;

$$h_{mac} = h_l \left[C_1 Co^{C_2} (25Fr_{le})^{C_5} + C_3 Bo^{C_4} F_K \right] \quad (1.27)$$

where the constants C_1 through C_5 can each take on two different values depending on the Colburn number. The value of the constant F_K depends upon the fluid being modeled.

Hendricks et al. (1961) performed experiments with hydrogen flowing inside a highly heated tube. Nusselt numbers were determined from measurements. The deviation from these measurements that the calculated Nusselt numbers generate approaches 80% at large values of Martinelli parameters, and roughly 40% at low values. As a result, the researchers found it necessary to curve fit the Nusselt number ratio as a function of the Martinelli parameter. This technique significantly improved the predictive accuracy, with most experimental Nusselt numbers lying within $\pm 15\%$ of the curve fit.

The model for the Nusselt number, Nu , that Hendricks et al. published for their forced convective heat transfer for flowing hydrogen was as follows:

$$Nu_{exp,f} = \frac{Nu_{calc,f}}{0.611 + 1.93\chi_{tt,f}} \quad (1.28)$$

where

$$Nu_{calc,f} = 0.023 Re^{0.8} Pr_f^{0.4} \quad (1.29)$$

and

$$\text{Re} = \frac{\rho_{f,m} u_{av} D}{\mu_f} \quad (1.30)$$

$$\rho_{f,m} = \frac{1}{\frac{x}{\rho_f} + \frac{1-x}{\rho_l}} \quad (1.31)$$

The result of this method can be seen in Figure 1-1.

Hendricks et al. (1966) developed a similar equation to correlate the combined subcritical data from TN 3095 (1966) and TN 765 with somewhat worse results due to data scatter. It is critical to note that this correlation excludes those data for which the thermodynamic equilibrium quality indicates subcooled flow. This excludes possibly up to one-third of the 612 points in the data set! The authors remarked that this equation should describe subcritical convective film-boiling data up to pressures near the critical pressure when non-equilibrium characteristics are small. The correlation based on the remaining data is

$$\frac{Nu_{\text{exp},f}}{Nu_{\text{calc},fm}} = \frac{1}{0.7 + 2.4X_{t,x}} + 0.15 \quad (1.32)$$

In this equation, subscript f refers to properties evaluated at the average of wall and bulk temperatures. Subscript fm refers to mean film conditions, e.g., using the density defined above with subscript f,m.

These authors also developed a correlation based on a pseudo quality with similar results in accuracy. This correlation included some of the subcooled data, but far from all of it. Their assessment of this correlation was that it covered the liquid-hydrogen data for convective film boiling from a slightly subcooled state through two-phase and well into the superheat region.

It should be noted that all models presented above perform very poorly on the data addressed in this dissertation. The exceptions, of course, are the models from TN 765 and TN

3095. Chen's (1966) model performed the best of all the others, while those of Shah (1984), Schrock and Grossman (1959), and Gungor and Winterton (1986, 1987) predict convection coefficients that are hundreds of times too high. This is due in large part to the form of the Reynolds number used by Hendricks et al.

Heat transfer coefficient models have been developed that focus specifically on the flow structure of the data in this dissertation – inverted film boiling (IFB). In general, the forms fall into two categories: those that attempt to capture the heat transfer mechanics of a highly convective flow, and those that focus on the effects of buoyancy. The convective models generally expand on the basic Dittus-Boelter model, while the buoyancy models usually take the form of the Bromley model (1950), which was developed for laminar film boiling, and is analogous to film condensation theory. These low velocity models are generally used to model Loss Of Coolant Accidents (LOCA's) in the nuclear industry.

Bromley's model (1950) is an extension of theory developed by Nusselt (1916) for laminar film condensation on a horizontal tube. His heat transfer coefficient model for laminar film boiling from a horizontal tube is

$$h = 0.62 \left[\frac{g(\rho_f - \rho_g)\rho_g k_g^3 h'_{fg}}{D\mu_g \Delta T} \right]^{1/4} \quad (1.33)$$

where h'_{fg} is the effective latent heat of vaporization accounting for vapor superheat. Numerous film boiling models expand on this basic form.

Bromley et al. (1953) extended his own model to include forced convection. For low velocity flows, he determined the following:

$$h_{co} = 0.62 \left[\frac{g(\rho_f - \rho_g)\rho_g k_g^3 h'_{fg}}{D\mu_g \Delta T} \right]^{1/4} \quad (1.34)$$

where the subscript ‘co’ refers to convection only – excluding radiation heat transfer. ΔT refers to the temperature delta between the wall and the centerline. For higher velocity flows, he proposed the following;

$$h_{co} = 2.7 \left[\frac{uk_g \rho_g h'_{fg}}{D\Delta T} \right]^{1/2} \quad (1.35)$$

Here, the enthalpy of vaporization is defined as

$$h'_{fg} = h_{fg} \left[1 + \frac{0.4\Delta TC_p}{h_{fg}} \right]^2 \quad (1.36)$$

Berenson (1961) modified the Bromley model by incorporating the hydrodynamic instabilities predicted by Taylor instability theory. He published the following result;

$$h = 0.425 \left[\frac{g(\rho_f - \rho_g)\rho_g k_g^3 h'_{fg}}{\mu_g \Delta T_s \left[\frac{\sigma}{g}(\rho_f - \rho_g) \right]^{1/2}} \right]^{1/4} \quad (1.37)$$

The vapor properties are evaluated at the mean film temperature, liquid properties at saturation temperature, and 0.425 is used as a coefficient instead of the 0.62 in equation 1.34 above to account for enthalpy of vaporization to superheated conditions.

The analogy to liquid film condensation has been extended to the assumption of turbulent flow in the vapor film. Wallis and Collier (1968) presented conclusions from this theory and offered

$$\frac{h(z)z}{k_g} = 0.056 \text{Re}_g^{0.2} [\text{Pr} Gr^*]^{1/3} \quad (1.38)$$

where the modified Grasshoff number is defined as

$$Gr^* = \frac{z^3 g \rho_g (\rho_f - \rho_g)}{\mu_g^2} \quad (1.39)$$

An obvious characteristic of the heat transfer coefficient models presented thus far is their inclusion of buoyancy effects. The models that focus on highly convective flows ignore buoyancy effects. In these models, heat transfer is quantified within the framework of the traditional Dittus-Boelter forced convection concept.

Dougall and Rohsenow (1963) developed the following model for dispersed flow and inverted annular film boiling (IAFB) of Freon 113:

$$h = 0.023 \frac{k_{v,s}}{D_h} \text{Re}_{TP}^{0.8} \text{Pr}_{v,s}^{0.4} \quad (1.40)$$

where

$$\text{Re}_{TP} = \rho_{v,s} D_h \frac{\left[\frac{wx}{\rho_{v,s}} + \frac{w(1-x)}{\rho_l} \right]}{A} \quad (1.41)$$

The velocity term applied here is the throughput velocity. This effort focused on low quality mass flows. In this equation, w is the mass flow rate, and the subscript s refers to saturation.

A subsequent research program that focused on higher mass qualities was completed by Laverty and Rohsenow (1964, 1967). Their IFB nitrogen studies included visual analysis of the flow structure. Through theory, they determined that a significant amount of superheat was present in the vapor. As a result, they determined that it is impossible to obtain a simple expression for the overall heat transfer coefficient, although they did present a model for their data, presented below. Instead, they presented arguments based on the Dittus-Boelter model to set the upper bound and approximate value of the heat transfer coefficient. Their published model is as follows:

$$h = 0.023 \left(\frac{\rho_v v_b D}{\mu_v} \right)^{0.8} \text{Pr}_v^{0.4} \frac{k_v}{D} \quad (1.42)$$

In this equation, the subscript b refers to bulk conditions.

Forslund and Rohsenow (1968) also used nitrogen to improve the analysis of Lavery and Rohsenow (1964). Improvements focused on droplet breakup due to vapor acceleration, modified drag coefficients on accelerating droplets, and a Leidenfrost heat transfer from the wall to the droplets at lower qualities. Test conditions covered the quality range from saturation at the inlet to 35% to 315% at the exit. They focused on estimating the magnitude of departure from thermal equilibrium and droplet size. They concluded that vapor superheating was significant – up to 50% in vapor quality. The heat transfer model they proposed, presented below, attempted to modify the Reynolds number to reflect conditions in the vapor:

$$h = 0.019 \left(\frac{GD}{\mu_v} \right)^{0.8} \text{Pr}_v^{0.4} \left[x + (1-x) \frac{\rho_v v_v}{\rho_l v_l} \right]^{0.8} \frac{k_v}{D} \quad (1.43)$$

Kays (1980) presented an analysis for heat transfer between parallel plates. This model has been used by Hammouda (1996, 1997) in his modeling of IFB nitrogen. The Kays model is below. Note that the length dimension is the film thickness, δ .

$$h = \left[\frac{5.071}{\text{Pr}_v^{0.0439}} + 0.0028 \text{Pr}_v^{0.645} \text{Re}_v \right] \frac{k_v}{\delta} \quad (1.44)$$

Bailey (1972) presented a buoyancy-based heat transfer model as follows:

$$h = \left[\frac{2k_v^3 g \rho_v (\rho_l - \rho_v) h_{fg}}{D v_v (T_w - T_s)} \right]^{0.25} \quad (1.45)$$

Takenaka at Kobe University in Japan is associated with a number of IFB studies from the late 1980's and early 1990's. In general, his working fluids are R-113 and nitrogen flowing upward inside a vertical heated tube. Heat fluxes and mass velocities are generally an order of magnitude or more smaller than those addressed in this dissertation. His work is unique in that it

is the only research found in the literature search that produced a flow regime map for IFB. Takenaka et al. (1989, 1990) found that heat transfer coefficients, as a function of equilibrium quality, did not vary with heat flux or inlet subcooling, but segregated consistently with mass flux. As a result, their IFB flow regime map uses mass flux and equilibrium quality as coordinates. As equilibrium quality increased, higher mass fluxes produced higher heat transfer coefficients at the same quality. They found that the Nusselt Number predicted using the Dougall-Rohsenow (1963) model were reasonably close to their data. Takenaka also worked with Fujii (Fujii et al. (2005)) to investigate pressure drop in IFB. Because the mass velocities are very low, the pressure drops measured in the nitrogen flow are in general much smaller than those exhibited in the data of this dissertation. They found that the pressure drop characteristics correspond well with the heat transfer characteristic map.

Hammouda et al. (1996, 1997) investigated the effects of mass flux, inlet subcooling, and system pressure on the heat transfer coefficient using R-12, R-22, and R134a as the working fluids. The characteristic shape of the heat transfer coefficient as a function of equilibrium quality is consistent with those in Takenaka's experiments. The effect of mass flux is the same, but varying the inlet subcooling measurably segregated Hammouda's data while Takenaka noted no such influence. Different results are also noted in the effect of heat flux on the heat transfer coefficient. While Hammouda's data show that higher heat flux increases the heat transfer coefficient, Takenaka's data shows very little, if any, effect. Hammouda also observed that higher system pressure increases the heat transfer coefficient – a parametric effect that Takenaka never investigated.

Ishii has been involved with a number of experiments that focused on the flow regime characteristics and transition criteria of post-critical heat flux (IFB) flows. Ishii and De Jarlais

(1986) investigated the basic hydrodynamics of this flow regime. The mechanisms that disintegrate the liquid core were investigated, as well as the formation and entrainment of droplets in the vapor annulus. The experimental portion of this work involved adiabatic two-phase flow, resulting in a flow regime transition criterion based on the Weber number. Ishii and De Jarlais (1987) presented experimental data for an idealized IFB flow generated by injecting a liquid inside a vapor annulus in up-flow using Freon 113. Fluid heating was incorporated into the test setup. Visual observations revealed the nature of the flow structure to include smooth IAFB, agitated inverted annular film boiling (AIAFB), followed by inverted slug film boiling (ISFB) and dispersed film boiling (DFB). Obot and Ishii (1988) extended this work with the same fluids and test setup. More extensive results of flow regime transition are presented. Ishii and Denten (1990) continued this work to investigate the effects of bubbles present before post-critical heat flux is attained on the IFB flow regimes and their transitions. Three regimes were observed; rough wavy, agitated, and dispersed ligament-droplet. They found that the flow pattern in IFB depends upon the nature of the pre-CHF flow. A general flow regime transition criterion between the agitated and dispersed droplet regimes is given based on conditions at dryout. This correlation includes void fraction at this point as an important parameter. Babelli et al. (1994) used the same experimental apparatus to continue the research. He concluded that the most significant flow regime is the agitated regime, since the large interfacial surface generated in this regime probably correlates with high momentum and heat transfer. A correlation for the axial extent of this flow regime was proposed, again dependent upon the void fraction at the point that CHF occurs. It should be noted that all of the work performed by Ishii and his associates was performed for the purpose of better understanding nuclear reactor LOCA. As such, the flow velocities are quite low compared with the data in this dissertation.

Per Ottosen (1980) published the first known results from the use of γ -ray absorption to measure void fraction in low Reynolds number IFB nitrogen. He observed the transition from IAFB to DFB at void fractions between 80-90%. These void fractions were typically attained by the point at which equilibrium quality was 20%. Given that superheat will be present, this equilibrium quality probably relates to a lower actual quality. Since his work was in support of understanding LOCA's and reflooding, his fluid velocities were low. Also, the work was executed at a constant temperature condition instead of a constant heat flux condition, as is more often the case. Nonetheless, trends in heat transfer coefficients as a function of mass flux are evident.

Experiments using hydrogen as the working fluid are rare. This is primarily because of the dangerous nature of the fluid. Hendricks (personal communication, 2005) relates that, in the series of experiments during 1961 and 1966, the building in which they worked was evacuated of people, and emergency personnel were notified of each experiment. It is determined through the literature search that the only published hydrogen experiments performed in the United States that present heat transfer data occurred in support of the manned space missions in the 1960's. Published results from hydrogen experiments in the Soviet Union and Europe, though they likely occurred, have not been found.

Core et al. (1959) performed experiments with hydrogen similar to those in TN 3095, but with much fewer measuring points of pressure and temperature. Twenty-seven heat transfer tests with liquid hydrogen were completed in the series. Since only test section inlet and exit conditions were measured, the heat transfer coefficients calculated from these measured data are overall average coefficients for the entire tube. The authors did not present a theoretical correlation for the heat transfer coefficient. Their primary goal was to evaluate the utility of

hydrogen as a regenerative rocket nozzle coolant. Nonetheless, the data from this study may be considered as complementary to the data of TN 3095, and therefore useful.

Wright and Walters (1959) found that stable film boiling of hydrogen could occur for wall to bulk temperature differences as low as about 22 K to 28 K. Also, peak heat transfer coefficients were about 10% of the magnitudes of those in nucleate boiling. Their film boiling heat transfer coefficients were almost constant over the range of wall to bulk temperature differences of 22 K to 167 K.

Papadimitriou (1991) presented results of a simulated rocket engine two-phase hydrogen chilldown process using a modified form of Dougall and Rohsenow model in the computer program THESEUS. The modification is a temperature correction,

$$\left[\frac{T_v}{T_w} \right]^{0.5} \quad (1.46)$$

applied as a multiplier on the model for the heat transfer coefficient. It was stated that this better accounts for the real film conditions at high wall temperatures.

Many of the above forced convection models are based on the classic Dittus-Boelter model. Variations on this standard model are implemented by using properties and flow conditions calculated in specified ways. For example, the properties used in the Reynolds number could represent bulk calculated values for the two phases, the vapor saturated condition, or superheated vapor conditions. Below is the standard model for later reference:

$$h = C \left(\frac{\rho v D}{\mu} \right)^m \left(\frac{\mu C_p}{k} \right)^n \left(\frac{k}{D} \right) \quad (1.47)$$

In this model, the coefficient and exponents can be adjusted to fit the data. Common values are 0.023 for the coefficient and 0.8 and 0.4 for the exponents m and n. Unless stated otherwise, these are the values used in this research effort.

The literature search has found a number of experiments that are peripherally related to the data in the NASA data. However, the data addressed in this dissertation are rare or even unique in several ways. First, the working fluid is hydrogen. As stated above, there are only three other published reports of experiments with hydrogen in a convective, IFB condition. None of these three experiments operated at the high mass flux levels of the NASA data. Finally, and most importantly, the extent of measured parameters makes these data extremely valuable. These measurements provide the means to theoretically analyze the pressure drop and heat transfer characteristics of hydrogen, and to validate any proposed model or correlation.

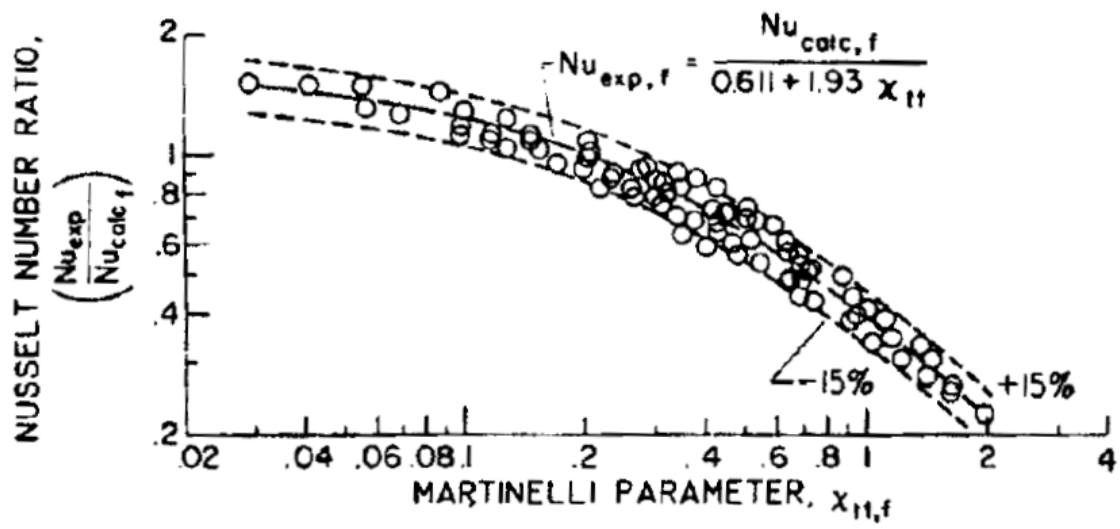


Figure 1-1. Ratio of experimental to calculated Nusselt number for the 1961 data.

CHAPTER 2 MODELLING APPROACHES FOR TWO-PHASE FLOW

Angular Simplifications

Two-phase fluid flowing in a pipe can have characteristics that vary in the axial, radial, and azimuthal directions. Axial dependencies of properties and flow structure can result from entrance effects, wall friction, turbulence, and heat addition. This dependency is typically not ignored, since it is changes in conditions in the axial direction that interest engineers typically.

Radial dependencies can result from these same sources. Since it is a great simplification to ignore this dependency, this is commonly done. Corrections can be applied to models that explicitly ignore the radial dependency. For example, the effect of a radial temperature gradient on fluid properties can be accounted for by multiplying the Dittus-Boelter Nusselt number by a ratio of wall-to-centerline temperatures, usually raised to an exponent. Another example is the drift flux model, the purpose of which is to account for radial variations in fluid density and velocity. These two examples speak to the dual importance of neglecting radial dependencies in the formal conservation equations while simultaneously including radial effects through semi-empirical adjustments.

Finally, azimuthal dependencies are usually important only in horizontal flow, where gravity strongly segregates the liquid and vapor phases due to the large difference in densities. In vertical flow with uniform heating, this dimension is typically confidently neglected.

Basic Models

There are four basic approaches that can be used to model the thermal hydraulics of two-phase flow. Each method explicitly defines the number of independent conservation equations used. The number of closure relations that link the corresponding conservation equations increases as the number of conservation equations increase, so that the number of conservation

equations minus the number of closure relations will always equal three. While complexity increases as the number of conservation equations increase, the variety of information obtained about the flow also increases. This does not necessarily mean that predictions for pressure drop and heat transfer will be better for a six-equation model compared with a three-equation model. It simply means that more predicted information will be generated. The reliability of these predictions will depend directly on the validity of the closure relations and assumptions used to develop the overall modeling approach.

The most sophisticated model is called the two-fluid model, in which there are separate mass, momentum, and energy equations for each of the phases. Closure relations must link the corresponding equations for each phase; mass, momentum, and energy transfer rate terms are defined at the phasic boundaries. The mass transfer term is relatively simple and is directly related to the change in quality. The momentum and energy transfer terms are more complicated at they depend on the momentum and energy associated with the newly vaporized fluid. They also depend upon the interfacial shear and heat transfer rates – two terms for which data are difficult to obtain. These terms are usually developed in terms of theory and assumptions, or a combination of theory and experimental findings.

In addition to the interfacial closure relations, there must also be relations for momentum and energy transfer at the fluid-wall boundary. These conditions are usually determined with more confidence because the experimental data that have been generated to understand these conditions are more complete. Research in single-phase flow, which has been extensively and reliably performed, often applies. For instance, the wall friction is a term that is of fundamental importance to engineers, and therefore has been studied since the beginning of the science of fluid mechanics. Heat transfer also is of fundamental importance. To simplify the analysis of

data from an experiment, the wall-to-fluid heat transfer boundary is usually established as one of two conditions – constant heat flux or constant wall temperature. With either, the wall heat transfer boundary condition is well defined.

The next simpler model includes five equations. In this, the developer can choose which conservation equation to simplify, but usually selects either momentum or energy. In two-phase flows, it is commonly accepted that the pressures of both phases are the same. Therefore, the momentum equations for the two phases are usually reduced to one. This is accomplished by equating the interfacial momentum transfer terms, since they must be the same. That is, the momentum that one phase loses at the interfacial boundary is gained by the other. This approach has the great advantage of eliminating the interfacial shear stress term. Alternatively, the developer may choose to equate the energy transfer terms in a similar fashion. This eliminates the need to determine the rate of sensible heating of the liquid phase.

A further simplification is made by reducing the number of independent conservation equations to four. In this case, there is sometimes a specific piece of information required, such as velocity slip.

The simplest approach is the three-equation model, also called the homogeneous equilibrium model (HEM). In this, equations of mass, momentum, and energy conservation use properties that represent the mass-weighted values of the vapor and liquid phases. There is no information regarding the separate velocities of the phases. Equilibrium quality is used, which neglects liquid subcooling or superheating, and vapor superheating. In spite of its simplicity, the HEM is often cited as a standard against which the results of other models are compared.

Flow Regime Analysis

When the more complicated models are used, it is frequently necessary to determine the structure of the two phases relative to each other. The various structures in two-phase flow have

been distilled down to a few flow regimes. A heated two-phase flow progresses through these flow regimes as it increases in quality. The specific set of flow regimes may be different for different conditions. For example, flow through a horizontal pipe can experience separated flow with the heavier species at the bottom of the pipe, and the lighter species at the top – a flow structure not developed in vertical tubes. Flow through vertical tubes can also progress through a different set of flow regimes, depending upon the amount of applied heat. Low heat loads will result in pre- Critical Heat Flux (CHF) conditions. The vapor phase is generated at the wall and migrates to the center of the tube. Liquid is always on the surface of the tube wall until dryout occurs at high qualities. After this, the liquid is dispersed as droplets in a continuous vapor matrix. High heat loads can produce post-CHF conditions, or IFB, at very low qualities. In this situation, the wall is too hot for liquid to remain. Vapor stays along the wall of the tube throughout the increase of quality. The progression of flow regimes in IFB are IAFB, AIAFB, and DFB. These flow regimes are presented in figure 2-1. If the mass flux is low, then ISFB can occur after IAFB. Note that this figure, taken from Takenaka (1989), does not include the ‘B’ for boiling in the regime nomenclature that this dissertation includes. IAFB is characterized by a relatively smooth interface between the vapor and liquid. The liquid flows through an annulus of vapor. The interfacial area is easy to determine assuming the void fraction is known. AIAFB is characterized by a rough interface. The liquid core is still whole, or in separate, parallel liquid filaments, but is rough such that determining its surface area is no longer a straight forward calculation using void fraction. The area for heat and momentum transfer likely increases relative to IAFB even though the amount of liquid is decreasing. Finally, in DFB, the liquid core completely breaks up into drops and is carried along in the continuous vapor matrix. This flow structure is very similar to pre-CHF dispersed flow.

Because the physics of the flow is strongly dependent on the flow regime, it is common to base closure conditions and other modeling decisions on the local flow regime. Of course, this requires that the various transitions between regimes be predictable. As pointed out in chapter one, Ishii has put in significant effort to develop predictive models. His more recent work is with heated Freon 113 in relatively low velocity conditions. Observations are that the void fraction at the point of dryout has a significant impact on the flow regime transition correlation. The correlation is as follows (Babelli et al. 1994):

$$\frac{L}{D} = 595 \sqrt{\frac{\mu_f j_J}{\sigma}} \left(1 - \frac{\alpha_J}{0.854}\right)^{2.25} \quad (2.1)$$

In this relation, L is the length at which the flow regime transitions from IAFB to DFB, D is diameter, μ_f is the fluid viscosity, j_J is the volumetric flux, σ is the surface tension, and α_J is the void fraction.

Takenaka (1989, 1990) generated a flow regime map for IFB, as shown in Figure 2-2 where coordinates are equilibrium quality and total mass flux. Note that inlet velocity is used on the ordinate instead of mass flux, but his final map actually used mass flux. For his test conditions, this map predicted the IFB regimes he viewed.

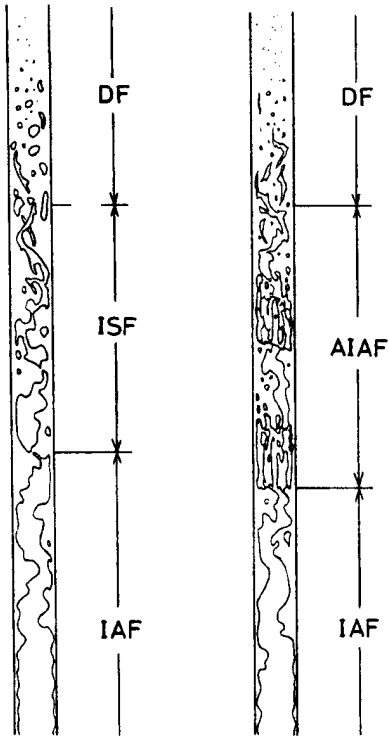


Figure 2-1. Various flow regimes for IFB (Takenaka, 1989). The ISFB regime on the left is associated with low mass flow rates.

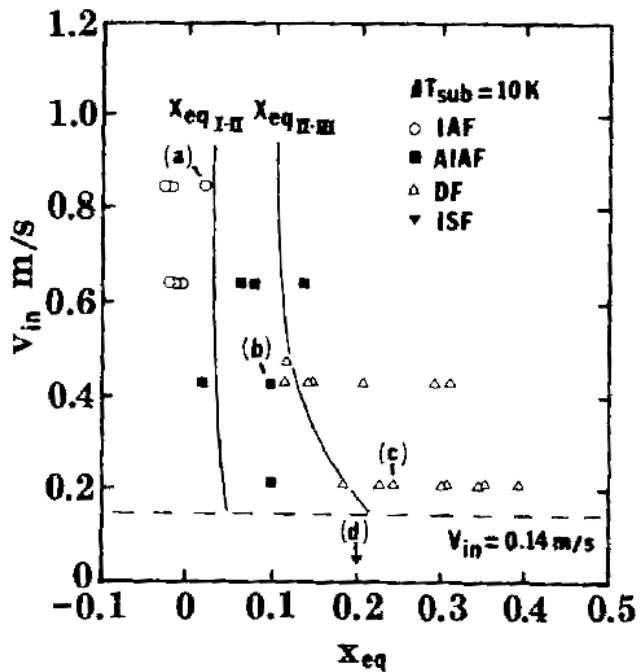


Figure 2-2. Flow regime map generated by Takenaka for IFB (1989). Flow regimes are IAFB in region (a), AIAFB in region (b), DFB in region (c), and ISFB in region (d)

CHAPTER 3
TEST DATA DESCRIPTION AND EVALUATION AND MODEL DEVELOPMENT

Description of Experiments

As referred to earlier, the data used to validate the model were generated at NASA – Glenn Research Center (formerly Lewis Research Center) and published in two separate technical notes, NASA TN 765 and NASA TN 3095, in 1961 and 1966, respectively. These data will be referred to collectively as the NASA data to distinguish it from other hydrogen experiments, or as the 1961 and 1966 data when the data from the individual reports are discussed. The experiments were performed in support of rocket engine modeling for the US manned space program.

Experimental Setup

The experimental setup for the 1961 experiments is presented in figure 3-1. Hydrogen was stored in a large tank and pressurized by gaseous hydrogen to force it through the system. Piping from the tank to the test section and the test section were enclosed in a vacuum environment to eliminate convection heat transfer to the piping and working fluid. The vacuum container was a stainless steel cylinder 38.1 cm in diameter. Heat was generated inside the tube metal by applying a voltage across its length. The power supply for heat generation was external to the vacuumed environment. Therefore, the leads for the voltage supply, along with instrumentation leads, were passed through the wall of the vacuum chamber. The voltage was applied to the heated test section through copper flanges brazed to the tube. It was found that unevenly brazed joints distributed the power unequally circumferentially in the tube. Therefore, multiple connections to the buss bar were made and the brazed joint was X-ray inspected. After passing through the heated test section, the hydrogen was completely vaporized and then exhausted through the roof of the facility into the atmosphere. All system flow conditions were remotely

controlled. The system pressure and flow rate were set by valves upstream and downstream of the test section.

The setup of the 1966 experiments is similar to that of the 1961 setup. Figure 3-2 presents the configuration. More useful information is given in the 1966 report that will be repeated here. It is pointed out that the liquid hydrogen storage tank is enclosed in a vacuum to mitigate heating. This in turn is contained within a liquid nitrogen radiation shield to mitigate conversion of parahydrogen to orthohydrogen. Finally, this is contained within a foam insulated container. The liquid hydrogen was forced through the flow system using gaseous normal hydrogen as a pressurant. Just upstream and downstream of the test section were mixing chambers of high turbulence in which the fluid bulk pressure and temperature were measured. Mixing the fluid in the mixing chambers and having an entrance length to the test section were found to be important since there could be some thermal stratification of the liquid as it is transferred from the storage tank to the test section, with warmer liquid adjacent to the wall and colder liquid in the center of flow.

Five different tube diameters were used in the NASA experiments, ranging from 0.48 cm to 1.29 cm inside diameter, and all were vertical with hydrogen flowing upwards. The heated test section length in the 1961 and 1966 experiments are 30.5 cm and 61.0 cm long, respectively. Straight, unheated approach lengths were included in all test sections; approximately 12.7 cm for the 1961 tests, and 30.5 cm for the 1966 tests. Approach sections and test sections were contained within the vacuum environment. Figure 3-3 and 3-4 present the test sections for the 1961 and 1966 data, respectively.

Experimental Conditions

Heat fluxes and mass flow velocities are very high, and tube diameters are similar to those used in regeneratively cooled rocket engine nozzles and other rocket engine piping. The

experimental conditions of these data reflect the nature of hydrogen flowing in a rocket engine. Table 3-1 presents a summary of test conditions.

Heat was generated within the test sections by applying a voltage across the length of the section. Care was taken to ensure a uniform weld of the copper flange around the tube so that current would flow uniformly down the tube. As Hendricks (personal communication, 2006) stated the problem,

The most damaging effect [on uniform heat generation] was the braze joint between the tube and the copper flange. Erratic joints distributed power unequally into the tube and the current paths in turn did not heat the tubes properly.

Heat Leaks

Paths for undesired heat transfer into or out of the system that have not already been addressed were either analyzed or otherwise considered by the authors of the 1961 data and determined to be insignificant.

Instrumentation

All test sections were instrumented for local static pressure, tube outside wall temperatures, and local voltage drops. Accuracy was of paramount importance (Hendricks, personal communication, 2006). When initial results of tube wall temperatures ran counter to anything previously experienced or expected, double and triple instrumentation redundancy was implemented to determine the source of the “error”. Data published in the reports represent those deemed most accurate of the redundant measurements. Figure 3-5 illustrates some specifics of thermocouple and pressure tap installations. The 1961 report gives no information about instrumentation measurement accuracies. The 1966 report gives information on this subject, and in general, the accuracies of instrumentation and measurements in the 1961 data are consistent (Hendricks, personal communication, 2006).

All test sections had 12 thermocouples along the outer surface of the heated lengths, plus inlet and exit temperatures in the mixing chambers. Thermocouples were either copper-constantan, which were silver soldered, or Chromel-Alumel, which were welded in place. Connections to the tube outer wall were made with great care to avoid affecting the test conditions or measurements. Leads from the thermocouples were 30 gage wire. Circumferential thermocouple placements were intended to determine the circumferential uniformity of power distribution in the tube and as checks for accuracy. The cold junction was atmospheric boiling nitrogen in the 1961 data, while the 1966 data used either liquid nitrogen or ice.

Thermocouple accuracy was determined by the recording system accuracy, standard calibration, lead wire and junction temperature gradients. The mixing chamber fluid temperature measurements were estimated to have less than 1% probable error. Multiple thermometers in the mixing chambers agreed to within ± 1.1 K at the inlet and ± 5.6 K. No percent accuracy is given for the tube surface thermocouple measurements. Tube surface temperatures were checked by comparing multiple thermocouple readings attached by different techniques. The readings usually agreed to within ± 5.6 K.

The 1961 data had five static pressure taps spaced along the length of the test section and one at each of the inlet and exit mixing chambers. These pressure measurements were not differential relative to a datum. The other four tubes from the 1966 experiments had three static pressure taps spaced along the test section, and one at each of the inlet and exit mixing chambers. These pressure measurements were differential relative to the pressure reading just upstream of the test section inlet. No pressure taps on any of the five test sections were located at the same axial location as a wall thermocouple. To complete the pressure data set, smooth curves were hand-fitted through the measurements. From these curves, pressure values were interpolated at

the locations corresponding to the 12 thermocouple measurements. Commercial transducers with a maximum of 1% full-scale nonlinearity were used. Readings from these transducers were confined to half of the full scale. Therefore, errors from the pressure readings were estimated to be 2%. Unfortunately, the range of the transducers is not given, and efforts to discover this information have been unsuccessful. The differences in local static pressure measurements were found to agree with differential pressure measurements to within 20%. This was reported to correspond to an absolute static pressure measurement uncertainty of 1%.

Mass flow rates were measured both upstream and downstream of the test section. A venturi was placed upstream of the test section and a sharp-edged flow orifice was placed downstream of the heat exchanger. A second venturi, primarily used for flow control, was also used for mass flow measurements. Measurements from these were compared for accuracy, and all agreed to within 3%.

Local values of voltage drops were measured by eight voltage taps along the length of the heated test section to assist in determining local power generation. Two sets of voltmeters and ammeters that had independent shunts or taps were used. These incremental measurements of power input were summed and compared with the overall power input measured by voltage and ammeter taps at the bottom and top of the test section. Agreement between these two methods was good (Hendricks, personal communication, 2006). Accuracies for these measurements are stated to be $\pm 1\%$.

The values of the eight voltmeter measurements were not included in either publication. However, as will be explained later, these measured local voltage drops appear to have been used to determine local heat transfer coefficients, and in this sense, the local voltage drops are included.

Data Validation

The literature search has revealed five major experimental efforts investigating the heat transfer characteristics of convective internal pipe flow boiling hydrogen. Two of these are the 1961 and 1966 NASA reports that are the focus of this dissertation. The other three were also performed during the early stages of the U.S. manned space program. These studies were scrutinized for possible use to validate the NASA data set.

Comparison with Similar Data

Core et al. (1959) performed experiments with hydrogen similar to those in the 1966 data, but with much fewer measuring points of pressure and temperature. Twenty-seven heat transfer tests with liquid hydrogen flowing through an electrically heated stainless steel test section, 6.35 cm long and 0.213 cm inside diameter, were completed in the series. Each test comprised a number of different steady state conditions, isolating the effect of changing inlet pressure, mass flux, or heat flux. As a result, there are a total of 164 steady state conditions, with two points of heat transfer coefficient measurements each, in the set. Only the inlet pressure was measured, so a pressure loss analysis cannot be compared with data. The authors did not present a theoretical correlation for the heat transfer coefficient. Their primary goal was to evaluate the utility of hydrogen as a regenerative rocket nozzle coolant. This source stands out as the only one that presents wall superheats that are likely to represent transition boiling conditions. While most experimental results indicate that transition boiling occurs between wall superheats of 5 K and 20 K, the data in this experiment show some superheats between these values. Therefore, these data may represent results from transition boiling. Table 3-2 presents comparisons of heat transfer coefficients averaged from the two points of measurement on the test section, compared with runs with similar conditions from the NASA data set. The Core et al. data set includes calculated equilibrium qualities based on pressure and enthalpy. Negative equilibrium qualities were set to

zero. Therefore, inlet subcooling is not known. The two calculated heat transfer coefficients for each run in the Core et al. data are averaged and compared with the average heat transfer coefficient for runs with similar conditions over the same equilibrium quality range in the NASA data set. Sets of compared runs are separated by bold lines in the table. The first runs listed in each comparison is from the Core et al. set, while the second listed run is from the NASA data set. The RMS difference between these comparisons is 46.2%.

Wright and Walters (1959) experimented with liquid and vapor hydrogen flowing in a 15.2 cm long and 0.635 cm inside diameter heated tube. Most of their 35 steady state liquid hydrogen experiments were pre-CHF, with 11 runs showing wall-to-bulk temperature differences consistent with IFB. In fact, their data show a marked gap in wall-to-bulk temperature differences between 2.8 K and 22.2 K. Temperature differences between these values were not obtained. This gap is consistent with a transition in flow regime from pre-CHF and CHF conditions to IFB. They concluded that stable film boiling could occur for wall to bulk temperature differences as low as about 22 K. Test section pressure measurements were not obtained. There are three runs from their data set with conditions similar to several runs in the 1961 data. Table 3-3 presents the test conditions and average heat transfer coefficient over the tube length. Note that the average heat transfer coefficient listed for the 1961 data represent an average of points two through six. This omits the first point that is affected by inlet conditions and concludes at approximately 15 cm into the test section. The heat transfer coefficients from the two different test series agree well.

Lewis et al. (1962) experimented with boiling hydrogen and nitrogen flowing upward in a type 304 stainless steel, electrically heated vertical tube 41.0 cm long and 1.41 cm inside diameter. Critical heat fluxes corresponding to transition to IFB were determined over a range of

flow rates, heat fluxes, and qualities. They noted that the maximum CHF increased with increasing mass flux and decreased as the point of transition occurred farther into the tube. These findings are consistent with the interpretation of runs 22, 26, 29, and 30 from the NASA data in figure 3-11 that will be discussed later. The mass flow rates in these experiments were so low that no measurable pressure drops were observed. Wall superheats were similar to those observed in the NASA data, with a maximum wall superheat of 500 K. Since mass fluxes and heat fluxes are an order of magnitude lower than in the NASA data set, there are no test conditions that are similar enough to warrant a comparison.

Table 3-4 summarizes the test conditions of the three forced convection heated tube flow boiling hydrogen experiments discussed above and the NASA data. From the data in these three experiments and other hydrogen experiments in geometries other than internal tube flow, it can be said that transition boiling occurs between 5 K and 20 K. Review of tables 3-2 and 3-3 show that the data from the NASA experiments are reasonably consistent with results from other, similar works. From this comparison, it is determined that the NASA data are, in general, valid.

End Effects

From the 1961 data, it is obvious that axial heat conduction occurs in the tube wall. Using the finite difference heat transfer theory presented by Incropera and DeWitt (2002), a Fortran program was generated to model the end axial heat conduction effects for the purpose of determining the data that are affected and should therefore be omitted from the analysis. It was assumed that curvature effects on axial conduction were negligible. Therefore, a two dimensional infinite plate with axial and radial heat conduction was used to approximate the tube geometry. The middle of the length of the plate corresponds to the beginning of the heated test section. Left of this position is the unheated approach section, while right of this point is the section in which heat is generated by electrical current.

To ensure that the imposed boundary conditions did not affect the solution, lengths of 50 wall thicknesses were generated on either side of the midpoint, for a total length-to-thickness ratio of 100. It was found that the number of radial nodal points were not crucial to generating acceptable results, so a minimum number of five nodal points were selected in the y direction, with nodes one and five at the tube inner and outer walls, respectively. For the length-to-thickness ratio of 100, this required 401 nodal points in the x direction. Figure 3-6 presents the nodal structure and applied power distribution. Note that the distribution in the x direction is too close to discriminate separate nodes, and the power generation is typical.

The applicable energy equation is

$$\frac{\partial^2 T}{\partial x^2} + \frac{\partial^2 T}{\partial y^2} + \frac{q'''}{k} = 0 \quad (3.1)$$

In this geometry, x is the axis parallel with the flow, and y is the radial direction. Also, q''' is the heat generation rate per unit volume. The variation in thermal conductivity as a function of temperature will have only a very small impact on the results provided a representative temperature is used to select the constant thermal conductivity. The thermal conductivity can therefore be assumed constant in the analysis.

The four boundary conditions applied to this problem are:

1. $T(x \rightarrow -\infty, y) = 25 \text{ K}$ (a representative liquid hydrogen temperature in approach section)
2. $\partial T / \partial x (x \rightarrow +\infty, y) = 0$ (adiabatic boundary far into heated test section)
3. $-k \partial T / \partial y = h(T_w - T_b)$ at $(x, y=0)$ (conduction = convection at wall/liquid interface)
4. $\partial T / \partial y = 0$ at $(x, y=Y)$ (adiabatic surface at tube outer wall)

In the heated section, boundary condition three assumes that the axial heat transfer is much less than the radial heat conduction at the wall-liquid interface. To use this boundary condition, an estimate of heat transfer coefficient that supports the purpose of the particular scenario at hand is used.

For each problem, the following four parameters must be specified; wall thickness, wall thermal conductivity, heat generation rate, and fluid-to-wall heat transfer coefficient. The heat transfer coefficients used in this analysis come from those values listed in the 1961 data set at the first point, which is 1.4 mm above the heated section inlet. The algorithm was iterated until the maximum difference in temperature in adjacent iterations was less than $1.0\text{E-}6$ K.

The computer model was validated through five observations. First, the boundary conditions at the left and right hand sides of the tube are satisfied, as is the boundary condition corresponding to the outside of the tube wall. Second, it is logical that the point of largest temperature slope should occur at the point that heat generation starts. Every scenario has satisfied this requirement. Third, the effect of varying the parameters listed above affect the results in a reasonable way. For example, increasing metal thermal conductivity causes the effect of heat conduction to be felt deeper into both sides of the point of heat generation. Fourth, magnitude of predicted inner and outer wall temperatures are reasonably close to those published in the 1966 report (1961 report did not publish outer wall temperatures). Two runs, seven and 11, were selected at random for comparison purposes. For run seven, the inner and outer wall temperatures are 231 K and 269 K, respectively, while the model calculated 207 K and 238 K. Run 11 inner and outer wall temperatures are 461 K and 482 K, with model predictions of 412 K and 431 K. Finally, the difference in tube inner and outer wall temperatures in the heated portion reasonably agree with published data. Again, using runs seven and 11, the published differences are 38 K and 19 K, while the model results are 31 K and 19 K. These differences are deemed to be well within the uncertainty in the four parameters and errors associated with the model assumptions for the intended purposes of this analysis.

Figures 3-7 and 3-8 present inner and outer wall temperatures for the scenarios in which thermal conductivity and wall thickness are parameters. The two dimensional effects are noticeable in the right hand portion of the tube.

To evaluate the effect of each parameter listed above on the tube end wall temperatures, high and low values of each parameter were run, with all other parameters set to nominal values. The length from the heated section inlet to the point at which 95% of the final temperature is achieved was determined for each run and compared. Large differences in lengths by which 95% of the final temperature is achieved indicate a significant parametric effect on tube end axial heat transfer. Figure 3-9 presents the results of the computer model. Since the difference in outer and inner wall temperatures is small, only the outer wall temperatures are presented for each scenario for clarity. Table 3-5 shows the distances in thicknesses from the heat section inlet at which 95% of the final temperatures are achieved. This analysis suggests that the effect of end axial heat conduction in the tube metal increases with increasing thickness and thermal conductivity, and decreasing heat transfer coefficient. It is approximately independent of heat flux. For a given test section, wall thickness and thermal conductivity are determined. The remaining variable that changes the end effect for a given test section is the heat transfer coefficient.

To determine the maximum distance into the heated test section that experimental results might be affected, the worst-case heat transfer coefficient of $1000 \text{ W/m}^2\text{-K}$ was used for all test sections. This is half the lowest heat transfer coefficient in the entire data set, and should represent a worst-case scenario in the unheated section where liquid hydrogen is flowing next to the tube wall. That is, liquid hydrogen will have a significantly higher heat transfer coefficient than will vapor hydrogen. Table 3-6 presents the model results and suggests that all test section

data more than 0.8 cm from the heated test section boundaries are adequately unaffected to be used in the analysis. As a result of this analysis, all 12 points in the 1966 report will be used since the end points in these runs are far more than 1 cm from the ends. However, points 1 and 12 in the 1961 data are theoretically affected, and the data of wall temperatures strongly supports this conclusion. Therefore, these 40 points will be excluded from the heat transfer and pressure drop analyses, leaving 572 points for consideration. All other data in the 1961 report are predicted to be adequately unaffected and will be used.

Hydrogen States: Parahydrogen and Orthohydrogen

Hydrogen is naturally found as a molecule composed of two atoms of hydrogen, joined by a covalent bond. The proton at the nucleus of each atom has a spin associated with it giving rise to four possible combinations of spin pairs between the two protons of a hydrogen molecule, H₂. Three of these combinations of nuclear spins are symmetric, resulting in orthohydrogen (ortho), while the fourth combination is antisymmetric, resulting in parahydrogen (para). This two-state nature of hydrogen is significant for several reasons. The heat of formation released during the transition from ortho to para, coupled with the unstable nature of ortho at low temperatures, can cause significant boil-off of stored hydrogen if ortho constitutes a large fraction of the liquid. Ortho conversion to para is an exothermic process, with the emission of 703 kJ/kg of heat at 20 K, which is significantly more than the latent heat of vaporization of 443 kJ/kg. Secondly, the thermal properties of specific heats and thermal conductivities of the two forms are known to be significantly different at cryogenic conditions, causing the need to consider the issue of the ortho-para makeup of the test fluid throughout the test section.

The relative equilibrium abundance of each form varies with temperature. At room temperature, the ratio is 3 parts ortho to 1 part para, reflecting the number of spin combinations available to each form. This state of hydrogen is called normal hydrogen. The ratio changes to a

larger proportion of para as the fluid is refrigerated. At 20.4 K, the ratio is 0.002 parts ortho to 0.998 parts para, at equilibrium. Note that time is needed to allow for equilibration, which can be hastened in the presence of a catalyst.

There are four processes in which one form of hydrogen can transition into the other; collisional, spontaneous, adsorption, and radiative. The collisional process can be further segregated to homogeneous and heterogeneous processes. Through the homogeneous collisional transition, an ortho molecule acts as a paramagnetic medium through which spin exchange occurs either with another ortho molecule or a para molecule (Iverson, 2003). The heterogeneous collisional transition requires a catalyst, such as a tank or pipe wall, that is propitious to the transition of one form to another. This method involves the interaction between the magnetic field generated by a magnetic material and the magnetic field associated with the nuclear spin of the H₂ nucleus. The interaction causes a reversal of spin in one of the nuclei, which effectively changes the form from one to the other. In both of these collisional processes, the transition from ortho to para is exothermic in the form of increased kinetic energy of the participating molecules. Natterer et al. (1997) describe a method of catalyzing the transition of ortho to para by flowing hydrogen through a tube that is charged with charcoal. Without a catalyst, the conversion from ortho to para liquid hydrogen has a time constant on the order of 180 hours (Scott, 1959). Milenko et al. (1997) measured natural ortho-para conversion rates within a wide region of hydrogen fluid states, including five different liquid temperature states. Their findings indicate a conversion time constant near 12 hours.

The spontaneous transition of ortho to para produces a photon, and is therefore also an exothermic process. Ehrlich (1991) sites theoretical results showing that the time constant for an isolated ortho molecule to transition is on the order of 10¹¹ years.

Chemical adsorption of the hydrogen on the metal can lead to conversion of hydrogen. Ptushinskiĭ (2004) addressed the physics of this process. The adsorption process is composed of physisorption and chemisorption, which denote different levels of interaction between the hydrogen molecule and the metallic surface. These two levels are separated by a repulsive barrier of variable magnitude. As of yet, no theory for the time constant of transition between the para and ortho states for this process have been found.

The fourth method considered here requires radiation bombardment of the hydrogen. In this process, H₂ molecules dissociate due to the bombardment. The subsequent hydrogen atoms can recombine with each other generating, on average, the equilibrium ratio of para and ortho forms associated with the system temperature (Kasai, 2003). Since the hydrogen storage tank used in the NASA tests was surrounded by a radiation shield, this process is not expected to contribute significantly to the production of ortho.

Iverson (2003) presents a method to quantify the dynamic equilibrium density of para and ortho in a mixture of liquid hydrogen with collisions and irradiation present. He uses the following set of equations to quantify the concentration of ortho and para, considering homogeneous and catalyzed transitions:

$$\frac{dn_o}{dt} = K_{po}n_p n_o - K_{op}n_o^2 + C_{po}n_p - C_{op}n_o, \quad (3.2)$$

$$\frac{dn_p}{dt} = K_{op}n_p n_o - K_{po}n_p^2 + C_{po}n_p - C_{op}n_o, \quad (3.3)$$

subject to the conservation equation,

$$n_o(t) + n_p(t) = N_{H_2} \quad (3.4)$$

In the above equations, n_o, n_p, and N_{H₂} are the densities of ortho, para, and all H₂ molecules, respectively. K_{po} and K_{op} are conversion factors for homogeneous conversions from para to

ortho, and from ortho to para, respectively. C_{po} and C_{op} are conversion constants for catalyzed conversions in a similar sense. Both the homogeneous and catalyzed conversion constants are strong functions of system temperature and pressure. Milenko et al. (1997) provides information about the values of the constants.

Hendricks et al. (1961) analytically quantified the various means of transition from para to ortho and visa versa and chose to neglect the effects based on the results. For the analyses in the NASA reports, 100% para was assumed. It is stated, though, that neglecting the presence of ortho may introduce error into some of the heat balance calculations. An accurate quantification of the ortho-para makeup was extremely important in the NASA analyses (Hendricks, personal communication, 2006). While the parahydrogen flowed through the heated test section, there was also concern about the transition from para to ortho as the fluid was heated.

To test for this possibility, one test section was gold plated and then used. This experiment is based on the fact that any heterogeneously catalyzed transitions from para to ortho that occur with a stainless steel test section should be eliminated by the gold plating. Since the transition from para to ortho is endothermic, a stainless steel tube should show lower wall temperatures than the gold-plated tube under the same test conditions. However, the opposite effect was observed, which was attributed to experimental error. Their assessment was that the residence time of the hydrogen molecules in the test section was not long enough to generate significant ortho concentration from the para population as it was heated and flowed in the tube to warrant adjusting the properties from the assumed 100% para makeup. 100% parahydrogen is assumed in the current analysis.

Model Development

Inverted annular film boiling of hydrogen is modeled in this analysis as a separated flow of vapor and liquid. The liquid flows as a homogeneous core through an annulus of homogeneous

vapor. In this geometry, the vapor interfaces with both the wall and the liquid core, while the liquid interfaces only with the inner boundary of the vapor annulus. All of the heat from the wall is assumed to be absorbed by the vapor through convection. Radiation of energy to the vapor or directly to the liquid is assumed, and has been shown, to be negligible. Additionally, momentum loss through friction at the wall is largely a function of vapor conditions. This approach is consistent with the experimental observations of Kawaji and Banerjee (1983, 1987). In their IFB quench front experiments with water flowing upward in a highly heated quartz tube, bubbles were seldom observed in the liquid core. They concluded that nearly all the vapor generated at the liquid-vapor interface flowed upward in the vapor film. They also found no evidence that the liquid column rewetted the tube wall.

Local static pressures, tube wall temperatures, and voltage drops were recorded. This is enough information for only a three equation model, also known as a homogeneous equation model (HEM), with mixture mass, momentum, and energy conservation equations. An extensive literature search has not uncovered data-based models for vapor superheat or vapor slip in the flow structure of this analysis. It is likely that these profiles will be unique relative to pre-CHF flows, so that information on vapor superheat and slip from pre-CHF will not apply.

It was desired to obtain void fractions from the hydrogen data. To obtain useful void fraction data, it was determined that a no-slip condition was not acceptable, since the slip ratio directly affects the void fraction. In addition, a reasonable value for vapor velocity was desired to allow for a reasonable estimate of frictional losses. Also, since void fraction and slip are related to density, it was determined that the vapor superheat needed to be quantified. Without information regarding superheat, vapor velocity slip, or applicable information regarding void

fraction profiles, theory and assumptions must be applied if more information is to be obtained from these hydrogen data than what a HEM can provide.

The desired information can be obtained with a one-dimensional, five-equation model, with separate vapor and liquid mass and energy flows, but with one momentum equation. This assumes that the local pressure is the same for both fluids, which is commonly accepted. Completing this model requires closure conditions for two of the following three quantities; vapor mass-specific energy flow, vapor slip, and liquid mass-specific energy flow. Since wall temperatures are part of the data set, it was determined that a closure condition for the vapor energy flow, through quantifying vapor superheat, could be reasonably determined. Neither the liquid heating nor the vapor slip is well understood. It was determined to model the liquid energy state. It was determined that modeling the interfacial momentum effects was not necessary for the objectives of this analysis. Including such effects would lead to a two fluid model.

Nature of Data

Consideration of figure 3-10 of tube inner wall temperatures minus liquid hydrogen temperatures leads to the expectation that the vast majority of data is IFB. The vast majority of data show very large temperature differences between the inner wall and the liquid hydrogen temperature. These large temperature differences can only be sustained in an IFB flow structure. The four runs presented in figure 3-11 exhibit at least one point with relatively low temperature difference. It is likely that these points correspond to pre-CHF conditions, or possibly transition boiling.

The trend of the temperature differences for these runs in figure 3-11 supports this explanation. For example, run 30 has an extremely high mass flux of $3406 \text{ kg/m}^2\text{-sec}$ and a very low heat flux of 310 kW/m^2 . These operating conditions are most likely to delay the onset of

CHF and the transition to IFB, and this is what is indicated by the data. It is not until approximately 40 cm into the heated section that the temperature difference increases greatly. Run 29 has a lower mass flux of $2669 \text{ kg/m}^2\text{-sec}$ and approximately the same heat flux and would thus theoretically depart from nucleate boiling at a lower elevation than run 30. This is indeed what the data show, with run 30 temperature difference increasing significantly starting after the 16 cm point. Run 22 has a similar mass flux as run 30 at $3444 \text{ kg/m}^2\text{-sec}$, but a much higher heat flux of 1128 kW/m^2 . One would expect this run also to transition to IFB at a lower elevation than run 30. While the temperature differences for run 22 at low elevations is higher than run 30's, it appears that the IFB structure is not stable until after the 24 cm point – earlier than the run 30 transition. Since runs 22, 26, 29, and 30 show that pre-CHF conditions exist at least at some points, and the model generated to analyze these data assumes IFB conditions, these four runs will be excluded from the analysis.

There are other experimental findings that support this conclusion to omit them. Previous research with hydrogen indicates the magnitude of wall to bulk superheat that hydrogen will allow before departing from nucleate boiling. Walters (1960) reported a maximum wall superheat from his single-tube forced hydrogen flow heat transfer experiments of about 2.8K. Sherley (1963) experimented with free-convection hydrogen heated by a small flat heating surface and reported wall superheats as high as 6.1K. Class et al. (1959) experimented with free-convection hydrogen on various surface conditions, heating surface orientations, and pressures. For a very thin layer of silicone grease applied to the test section, wall superheats of about 16.7K were reported. Graham et al. (1965) presented test results from parahydrogen pool boiling that showed wall superheats of up to 5.6K at a system pressure of 290 kPa before departure from nucleate boiling. Kozlov and Nozdrin (1992) measured heat fluxes and wall superheats at DNB

during pool boiling of hydrogen for steel, aluminum alloy, and copper at low pressures. They found that wall superheats at DNB varied significantly between the three metals, as did the wall superheats during return to nucleate boiling from film boiling when they reduced the heat flux. At one atmosphere on steel, the wall superheat was on the order of 16 K. All of these studies support the previously stated assumption that the vast majority of data from TN 3095 represent post critical heat flux conditions.

Carey (1992) states that the variables affecting critical heat flux are tube diameter, system pressure, and mass flux. The fourth controlling variable depends on whether the bulk flow is subcooled or saturated. For saturated flow, Carey sites the critical quality, while for subcooled flow it is the difference between saturation and bulk temperatures. Collier (1981) also lists length to diameter ratio as an important parameter.

Chun et al. (2000) developed a new theoretical model for predicting CHF for low quality flows of water and refrigerants in round tubes. Chun states that there is general agreement that for highly subcooled flow, the liquid sublayer dryout approach performs well, while for low subcooling the bubble crowding model performs better. No one model works well in all conditions, though. Chun attempts to improve this situation by proposing that the controlling factor in CHF is the evaporation of the superheated liquid layer along the tube wall.

Recent research into this issue has been performed by Celata et al. (1994, 1996, 1998, 2001) in Italy. While most of his research is focused on highly subcooled CHF of water, the general concepts will probably prove relevant to liquid hydrogen. While Carey (1992) lists three postulated mechanisms for CHF at low quality – dryout under a growing bubble, vapor crowding, and dryout under a vapor slug – Celata states that the liquid sublayer dryout theory predicts the CHF under a wide range of subcooled conditions.

Magnitude of Radiation Heating

Heat is transported from the tube inner wall to the hydrogen primarily through convection. However, the large temperature differences experienced in the test series raises the concern that radiative heat transfer from the wall to the vapor and/or liquid hydrogen may be significant. While the exact analysis of radiation heating is complex, a simplified analysis of the worst-case scenario will reveal that radiative heating is at least three orders of magnitude less than convective heating.

Sparrow (1964) presented a thorough theoretical analysis of the effect of radiation heating from a tube wall to a vapor/liquid flow in film boiling. His work generated a quantitative criterion by which the relative significance of surface-to-liquid radiation can be determined. A more recent paper by Liao et al. (2005), which presents an excerpt of his Ph.D. work, addressed this complicated problem by modeling the liquid core flow as a long inner tube at the center of a long outer tube. The equation for radiation heating he applied to this geometry is

$$q_{rad}'' = \frac{\sigma(T_w^4 - T_f^4)}{\frac{1}{\varepsilon_f} + \frac{1 - \varepsilon_w}{\varepsilon_w} \frac{r_f}{r_w}} \quad (3.5)$$

The emissivities, ε , that will lead to the largest radiative heating are 1 for both hydrogen and wall. In this equation, r is radius, and σ is Stefan-Boltzmann constant. The radiative heat flux then reduces to

$$q_{rad}'' = \sigma(T_w^4 - T_f^4) \quad (3.6)$$

The highest wall temperature from the data is 560 K, and the fluid temperature is roughly 25 K. Using these values to represent the upper limit of radiative heating, the magnitude is 5.6 kW/m². The lowest heat flux in the data set is 294 kW/m², several orders of magnitude larger. Additionally, this lowest heat flux does not correspond to the highest wall temperature of 560 K

used in this analysis, but instead has a much lower wall temperature of 178 K. In summary, there is no run in this data set that has a radiative heating contribution of more than 2% of the total applied heat flux, and in fact is certainly much less than 2%. The impact of ignoring radiative heating of hydrogen is therefore justified.

Conservation Equations

Most of the experimental runs have subcooled liquid entering the heated test section. The amount of subcooling is appreciable, up to 7 K in some runs, and cannot be ignored in the energy balance. The velocities attained in some of the experiments required that the stagnation enthalpies of the two fluids be used in the energy balance instead of the static enthalpies. Thus, the momentum and energy equations are coupled and must be solved simultaneously.

A one-dimensional model of this system was developed to calculate mass, momentum, and energy balances. It is assumed that the pressure is constant across the flow cross-section, and while separate velocities of the two phases are determined, the bulk velocity for each phase is used. Additionally, bulk thermodynamic properties are assumed.

The conservation of mass equation is simply

$$w = w_l + w_v \quad (3.7)$$

The liquid momentum equation is

$$\frac{d(\rho_l u_l A_{c,l} u_l)}{dz} dz = -\frac{d(PA_{c,l})}{dz} dz + \tau_i 2\pi r_i dz - g\rho_l A_{c,l} dz \quad (3.8)$$

where τ_i and r_i are the vapor – liquid interface shear stress and radial location, and A_c is the flow area. The corresponding equation for the vapor phase is

$$\frac{d(\rho_v u_v A_{c,v} u_v)}{dz} dz = -\frac{d(PA_{c,v})}{dz} dz - \tau_i 2\pi r_i dz - \tau_w \pi D dz - g\rho_g A_{c,v} dz \quad (3.9)$$

The velocity and area terms in these momentum equations can be replaced by use of the following relations:

$$u_v = \frac{Gx}{\rho_v \alpha} \quad (3.10)$$

$$u_l = \frac{G(1-x)}{\rho_l(1-\alpha)} \quad (3.11)$$

$$A_{c,v} = \alpha A_c \quad (3.12)$$

$$A_{c,l} = (1-\alpha)A_c \quad (3.13)$$

In these equations, α is the vapor void fraction.

During the expansion of the derivatives, the vapor density was allowed to vary as a function of z . Doing so facilitates investigating the effect of vapor superheating and its axial variation on the pressure profile. The liquid density axial variation was also allowed to vary. Also during the expansion, certain derivatives were replaced with equivalent expansions that used terms more amenable to the analysis.

In a one-dimensional analysis such as this, these separate momentum equations are combined by equating the interfacial interactions of the two phases. The result is seen in equation (3.14):

$$\begin{aligned} -\frac{dP}{dz} = & \frac{G^2 \left\{ \frac{\partial x}{\partial z} \left[\frac{-2(1-x)}{\rho_l(1-\alpha)} + \frac{2x}{\rho_v \alpha} + \frac{\partial \alpha}{\partial x} \left(\frac{(1-x)^2}{\rho_l(1-\alpha)^2} - \frac{x^2}{\rho_v \alpha^2} \right) \right] - \frac{x^2}{\rho_v^2 \alpha} \left(\frac{\partial \rho_v}{\partial T} \right)_p \frac{\partial T_v}{\partial z} \right\}}{1 - G^2 \left[\frac{x^2}{\rho_v^2 \alpha} \left(\frac{\partial \rho_v}{\partial P} \right)_T + \frac{(1-x)^2}{\rho_l^2 (1-\alpha)} \left(\frac{\partial \rho_l}{\partial P} \right)_T \right]} + \\ & - \frac{(1-x)^2}{(1-\alpha)\rho_l^2} \left(\frac{\partial \rho_l}{\partial T} \right)_p \frac{\partial T_l}{\partial z} + \tau_w \frac{4}{D} + g[\rho_l(1-\alpha) + \rho_v \alpha] \end{aligned} \quad (3.14)$$

This equation is similar to that commonly presented in two-phase flow textbooks, but with Jacobian expansions useful for this analysis. The following relation for the wall shear stress was used:

$$\tau_w = \frac{f_l G^2}{2\rho_l} \phi_l^2 \quad (3.15)$$

As previously stated, the velocities attained in some experiments were high enough that they should be included in the energy balance. Radiation heating of the liquid is ignored based on the previous analysis of liquid heating by radiation. As a result, conservation of energy is modeled as follows:

$$\dot{Q} = wx \left[h_v + \frac{1}{2} \left(\frac{Gx}{\rho_v \alpha} \right)^2 \right] + w(1-x) \left[h_l + \frac{1}{2} \left(\frac{G(1-x)}{\rho_l(1-\alpha)} \right)^2 \right] \quad (3.16)$$

where h is the enthalpy.

In the application of this equation, the total energy flow rate of the flow is determined to be the total energy of the flow at the first point of measurements, point 1, plus the cumulative energy added through heating:

$$\dot{Q} = w \left[h + \frac{1}{2} u^2 \right]_1 + q_w'' A_s \quad (3.17)$$

A_s is the cumulative tube inner surface area up to a particular point of calculation.

Entrance Lengths

There are three types of entrance lengths considered here; hydrodynamic, thermal in the fluid, and thermal in the tube metal. Although all test sections included straight entrance approach sections approximately 12.5 cm and 30.5 cm long in the 1961 and 1966 data, respectively, to develop the velocity and thermal profiles, this concern is obviated by the nearly instantaneous and violent change in flow structure from single-phase liquid to IFB. Stated

another way, the history of the flow up to the start of heating is not important. Instead of modeling liquid velocity and temperature profiles across the radius of the tube and their effects on heat transfer and pressure drop, these processes are controlled by the conditions in the vapor, the inception of which occurs at the heated section inlet, and in which the radial dimension is constantly increasing.

The developing hydrodynamic and thermal profiles in the vapor from the test section inlet onwards must still be considered. Hsu and Westwater (1960) used law-of-the-wall theory to determine that the vapor in the annulus transitions from laminar to turbulent at a $Re = 100$. Some rather arbitrary assumptions were employed in their theoretical analysis. Somewhat marginally applicable computations from Rohsenow et al. (1956) for condensation on a vertical plate were used to justify this transition Reynolds number. Regardless, this transition Reynolds number appears to be commonly quoted and used to determine transition from laminar to turbulent flow of the vapor in IFB. Note that for typical values of vapor density and viscosity, and for typical velocities at the test section entrance, the vapor annulus dimension that produces a Re of 100 is 0.001 cm – an extremely small thickness. This film thickness is achieved at a void fraction for the smallest tubes in the NASA data set, which will give the largest required void fraction, of 0.008. From this, it is reasonable to assume that the vapor is always turbulent. Additionally, it is hard to conceive of the vapor flowing in a laminar fashion after its violent generation at the heated test section entrance.

As previously discussed, in the tube metal at the boundary between the heated test section and the entrance piping, there will be a significant axial gradient in metal temperature. This will lead to axial heat conduction, which in turn will affect the local heat flux and temperature. Instead of the approximately constant heat flux established within the tube far from the

boundaries of the heated test section, the local heat flux can be significantly reduced. Measured wall temperatures from the 0.795 cm diameter tube support this conclusion. It is important to note that, while there is axial heat transfer in the metal, at any particular station near the inlet, all of the energy that is calculated to be transmitted to the flow up to that point will indeed be transmitted to the flow. Thus, the calculated total energy input to the flow up to a given point will not be in error. At the test section exit, this is not the case. Heat flows up and out of the test section at the exit. Thus, the flow will not receive all of the heat input until some point after the heated section exit.

Boundary Conditions

The first point at which enough information is given to determine the thermodynamic state of the flow is the first point listed in the tables of measurements for each run. For the 1961 and 1966 reports, this point is at 0.14 cm and 6.35 cm up from the test section inlet, respectively. If the flow at this point is subcooled, then the published quality is zero, and the published temperature and pressure is used to determine the thermodynamic state. If a positive quality is listed, then the published pressure and quality is used.

Quality and void fraction are determined from the momentum and energy balances. The balances calculate changes in static pressure and total energy. Therefore, the quality and void fraction of the first point in each run must be determined in a method other than using these balances. It was determined to initialize the quality and void to zero at the inlet. It was assumed that quality and void increased monotonically at each successive point.

Implementing this boundary condition required knowledge of the thermodynamic state of the fluid at the test section inlet. This information is not given directly. However, the energy state of the fluid at the inlet can be found by subtracting the energy added from the inlet to the first measured point from the energy of the flow at the first point. Assuming the energy

associated with the local velocity to be negligible relative to the enthalpy of the flow, this energy level per unit mass is used as the bulk enthalpy of the flow. The pressure at the inlet is determined using the same technique the authors used to determine the pressure profile – fit a smooth curve through the measured points. The cubic least squares fit of the pressure profiles, as previously described, were used to extrapolate backwards to calculate the test section inlet pressure. Thus, pressure and bulk enthalpy are determined for the inlet. From this, the thermodynamic and kinetic state of the liquid and vapor is determined. The inlet was then defined to be point one for each run, and the number of points used in the analysis of each run increased from 12 to 13.

The momentum equation requires positive qualities. However, as stated previously, many runs had subcooled inlet conditions, and in fact remained subcooled from an equilibrium sense for a number of points. Therefore, a method to establish a positive quality was necessary. The literature search produced no model for true quality.

Hammouda (1996) presented a notional graph of the variation of true mass quality as a function of length in IFB. Collier (1994) presents a similar graph on page 295. Hammouda's graph is not based on measurements, but instead from his interpretation of conditions based on his observations of IFB. The slope of mass quality in IFB is positive at negative equilibrium qualities. Near where equilibrium quality equals zero, the slope of mass quality with length increases. At some low value of quality, mass and equilibrium qualities are equal, after which equilibrium quality is greater. At an equilibrium quality of one, the mass quality is less than one due to vapor superheating. This model encompasses the following three concepts in IFB: the subcooled liquid experiences some sensible heating; vapor is present and accumulates while the

bulk flow is subcooled; due to vapor superheating, the flow will not be entirely vaporized when the equilibrium quality equals one.

Closure Conditions

To complete the set of equations, the level of bulk vapor superheat, the amount of liquid sensible heating, and the nature of the wall friction must be determined.

Vapor superheat

To quantify vapor superheat, several concepts were tried, including theory presented by Burmeister (1993). He presents a theoretical derivation for the mixing cup temperature.

Following are the applicable energy equation and boundary conditions used:

$$\rho C_p u \frac{\partial T}{\partial z} = -\frac{1}{r} \frac{\partial(rq_r)}{\partial r} \quad (3.18)$$

subject to

$$\frac{\partial T(r = r_0, z)}{\partial r} = -\frac{q_w}{k} \quad (3.19)$$

$$\frac{\partial T(r = 0, z)}{\partial r} = 0 \quad (3.20)$$

Following are the assumptions used in his development.

1. constant wall heat flux
2. circular duct
3. flow velocity and temperature profiles are fully developed
4. $u/U_{\text{avg}} \approx 1$
5. Pr is constant and ≈ 1
6. $Pr_t = 1.0$
7. Law of the wall applies, with sublayer, buffer, and core zones
8. $u/U_{\text{CL}} = (y/r_0)^{1/7}$, and radial temperature profile has the same form

The results of his analysis give a mixing cup temperature of the following form:

$$T_m = \frac{5}{6}(T_{\text{CL}} - T_w) + T_w \quad (3.21)$$

The centerline temperature in this equation is the liquid temperature.

It seemed logical that the temperature profile in the vapor could be modeled as a turbulent flow. Most of the assumptions listed above are well satisfied by these NASA data, and arguments can be made for the remaining assumptions. Use of this model with the $5/6^{\text{th}}$ coefficient caused numerous energy balance errors, primarily in the 1961 data set. Various coefficient values were tried between the theoretical $5/6^{\text{th}}$ and the commonly-used $1/2$. Energy balance errors were minimized with the smallest coefficient of $1/2$. Therefore, it was determined to proceed with this value. This coefficient value is consistent with the analyses of Takenaka (1989) in his IFB studies. Nijhawan et al. (1980) performed experiments in which they measured vapor superheats in post-CHF flowing water. They observed significant superheating of the vapor. Interestingly, their data strongly support the use in this effort of $1/2$ for the vapor superheat coefficient.

Liquid energy flow

To complete the theory for a five-equation model, an assumption must be made regarding the energy state of the liquid. Theory regarding heat transfer to the liquid flow can be found in six-equation models, also called two-fluid models. Hedayatpour et al. (1993), in their two-fluid model of a vertical line cooling with liquid nitrogen, used theory for water droplet heating in superheated steam from Lee and Ryley (1968). The Nusselt number is modeled as

$$Nu = 2 + 0.74 Re^{0.5} Pr^{0.33} \quad (3.22)$$

where the Reynolds number is evaluated at droplet conditions, and the Prandtl number is evaluated at film conditions. This model was used in a flow geometry identical to that used in this dissertation – liquid core flowing homogeneously inside an annulus of vapor.

Hammouda (1997) observed that the heat transfer coefficients for the wall-to-vapor and the vapor-to-liquid can both be modeled as functions of Reynolds number to a power and Prandtl number to a different power. With some assumptions, he concluded that the ratio of vapor-to-interface and wall-to-vapor heat fluxes were controlled as follows:

$$\frac{q''_{v-i}}{q''_{w-v}} \approx \frac{T_v - T_{sat}}{T_w - T_v} \quad (3.23)$$

He gave no experimental justification for this model except that he noted predictions from his two-fluid model provide better prediction accuracy than other IAFB prediction methods he assessed.

The assumption used in this dissertation is that the liquid experiences no sensible heating. It remains at its inlet temperature throughout the heated tube unless the local pressure drops to the saturation pressure for the liquid temperature. From this point onward, the liquid temperature assumes the saturation temperature at the local pressure.

Rationale for this assumption comes from the fact that vapor is definitely present during IFB, even for subcooled flows. Therefore, the liquid certainly does not absorb and evenly distribute 100% of the energy from the tube wall. That is, the fluid does not increase in temperature to saturation before it starts to generate vapor. This observation easily extends into the saturated condition in which it is logical to assume that a saturated liquid also does not absorb 100% of and evenly distribute the energy input from the wall. The true nature of the liquid heating almost certainly lies between the extremes of no sensible heating and thermodynamic equilibrium.

Using some assumptions, the exact theoretical time-dependent liquid temperature profile as it flows through the core of the tube can be solved. The liquid core is modeled as an infinitely long rod of constant radius R having a uniform initial temperature T_1 and instantaneously

subjected to a uniform temperature bath at temperature T_{sat} . It is assumed that the bath temperature is the saturation temperature of the fluid at the local pressure. That is, any liquid that rises above the saturation temperature evaporates and leaves the liquid core and does not heat the remaining liquid. Only liquid that is at the saturation temperature or lower remains to conduct heat from the liquid/vapor interface inwards. This model also assumes that the liquid is at a uniform temperature across its radius at the time heat is applied (the test section inlet), that liquid radial velocity gradients are unimportant to heat transfer, and properties are constant. That is, heat transfer in the liquid can be modeled by conduction alone.

The mathematical model that captures the physics of this problem is

$$\frac{\partial T}{\partial t} = \frac{k}{\rho C} \frac{1}{r} \frac{\partial}{\partial r} \left(r \frac{\partial T}{\partial r} \right) \quad (3.24)$$

subject to the following boundary conditions:

$$T(R, t) = T_s \quad (3.25)$$

$$\frac{\partial T(0, t)}{\partial t} = 0 \quad (3.26)$$

and the initial condition:

$$T(r, 0) = T_l \quad (3.27)$$

The time-dependent solution of this problem is (Arpaci, 1966)

$$T(r, t) = T_s + 2(T_l - T_s) \sum_{n=1}^{\infty} \frac{e^{-(\lambda_n)^2 kt / \rho C} J_0(\lambda_n r)}{(\lambda_n R) J_1(\lambda_n R)} \quad (3.28)$$

where $\lambda_n R$ are the characteristic roots of the Bessel function of the first kind of order zero. The solution of interest from this model is the average temperature rise for a typical differential liquid volume that passes through the heated test section. Following are the values that will be used for each term:

- $R = 2\text{E-}3 \text{ m}$
- $k = 0.1 \text{ W / m-K}$
- $\rho = 60 \text{ kg / m}^3$
- $C = 2\text{E}4 \text{ J / kg-K}$
- $T_s = 28 \text{ K}$
- $T_1 = 25 \text{ K}$

These values correspond to a liquid subcooling of 3 K, which is a typical value. Also, a typical differential fluid volume residence time in the test section of $1/30^{\text{th}}$ of a second will be used.

Figure 3-13 presents the results that strongly support the assumption to ignore sensible heating of the liquid. This is the assumption that will be applied in the model.

Wall friction

The frictional losses are modeled with a Blasius-type relation for the friction factor and a two-phase friction multiplier developed by Rogers (1968) at Los Alamos National Lab. His model was developed for friction modeled as only the liquid component of the two-phase flow flowing alone. Thus, the friction factor is

$$f = 0.079 \text{Re}_l^{-0.25} \quad (3.29)$$

Rogers' model was developed specifically for two-phase internal flow hydrogen. Although his model is largely theoretical with some data validation, it is applicable to the entire two-phase hydrogen pressure range, and is presented in closed form as follows:

$$\phi_f^2 = \left(\frac{1-x}{x}\right)^{1.8} \left\{ 1 + \frac{x^{0.8187} \left[0.1324(12.759 - P) + 0.03966(12.759 - P)^3 \right]}{P^E} \right\} \quad (3.30)$$

where pressure is in atmospheres, and E is

$$E = 1.896x - 2.646x^2 + 1.695x^3 \quad (3.31)$$

Model Implementation

During the implementation of this theory, two observations directed the final form of the algorithm. First, implementing the theory requires an iterative scheme with discretized quality and void fractions. Each combination of quality and void fraction will result in errors in predicted pressure drop and energy flow relative to measurement. Acceptable levels of error must be defined, which results in a quality-void fraction pair domain of solutions from which a final pair must be selected. Second, it was found that there are some points for which this model will not simultaneously satisfy both momentum and energy conservation. This is due mostly to the inaccuracies of the model, and probably to a lesser extent due to inaccuracies in experimental measurements. For most points, momentum and energy conservation are satisfied with negligible errors associated with the necessity of discretization.

It is for these two reasons that ‘smart’ iteration techniques failed. Several other methods of finding the correct quality-void fraction solution were implemented that relied on reducing the error in energy and momentum by determining the correct direction to change each value. However, these iteration methods were found to be inadequate due to the nature of the equations in the problem and due to the fact that, in some cases, the solution of least error is greater than the error limits for most other points.

Performing a ‘dumb’ progression of quality/void fraction pairs, while not conservative of CPU time, was found adequate. Figure 3-14 presents the flow chart of the algorithm. Note that the thermodynamic state of the vapor and liquid are known since liquid temperature, vapor temperature (through the superheat equation), and local pressure are known.

The error limits placed on calculated momentum and energy changes are 2% of measurement. All quality-void fraction pairs that agreed with the measured pressure loss to within 2% were saved for processing in the energy balance. This preliminary solution set was

then input to the energy balance. The solution domain is constrained by noting the contribution of velocity to the total energy flow. It is significantly less than that of enthalpy even for the high velocity flows. Therefore, the energy balance is a very weak function of void fraction and a very strong function of quality. Thus, the quality range is always reduced to one or a few discretized values, but with a range of void fractions that satisfy the momentum equation within the error limits.

It is logical to use the liquid and vapor velocities to discriminate between the remaining solutions. Various methods were tried. One method required the vapor velocity to be greater than the liquid velocity at all points, but this did not work best for runs near the critical pressure. A slip of less than one appears to satisfy these runs best. Another constraint that led to problems for high pressure runs was to require the vapor velocity to increase monotonically up the tube. It was finally determined to select the minimum vapor velocity from the set of solutions that satisfied the energy balance within the specified error limit. This constraint eliminated extremely high vapor velocities, some well over the sonic velocity, while giving reasonable results for high pressure runs.

To address points for which momentum and energy conservation can not simultaneously be satisfied, it was determined to equally increase the accepted momentum and energy errors until a solution was obtained for both. Note that increasing the acceptable range of errors on momentum consistently decreases the calculated errors in energy balance, so this method identified the lowest level of error for both quantities while giving preference to neither.

Table 3-1. Table of experimental conditions for the NASA data set.

set	run	G	Pin	q"	dp	Subcool T	D, inner	Wall thickness	Material
		kg/m2-s	kPa	kW/m2	kPa	K	cm	cm	
1	1.1146	327	759	1193	27	-0.1	1.288	0.025	Inconel X
2	2.1152	643	969	948	22	-3.1	1.288	0.025	Inconel X
3	3.1143	329	743	735	15	-0.1	1.288	0.025	Inconel X
4	4.1151	488	1023	768	13	-2.6	1.288	0.025	Inconel X
5	5.1115	662	1045	752	12	-3.8	1.288	0.025	Inconel X
6	6.1142	630	733	719	20	-1.3	1.288	0.025	Inconel X
7	1.1246	873	1075	1324	45	-4.1	1.113	0.081	Inconel
8	2.1247	536	1103	1308	76	-2.7	1.113	0.081	Inconel
9	3.1248	895	889	1242	41	-3.3	1.113	0.081	Inconel
10	4.1251	531	868	817	20	-2.4	1.113	0.081	Inconel
11	1.542	1237	616	1357	211	-2.9	0.851	0.051	304 Stainless steel
12	2.541	1119	861	1324	86	-4.8	0.851	0.051	304 Stainless steel
13	3.539	892	984	703	32	-6.6	0.851	0.051	304 Stainless steel
14	4.538	906	982	425	12	-7.2	0.851	0.051	304 Stainless steel
15	5.2	1553	1251	1766	102	-3.8	0.851	0.051	304 Stainless steel
16	6.201	1286	1112	1733	113	-2.7	0.851	0.051	304 Stainless steel
17	7.54	1178	759	2093	250	-2.6	0.851	0.051	304 Stainless steel
18	8.203	1129	1221	1733	93	-3.3	0.851	0.051	304 Stainless steel
19	9.204	1121	812	1635	148	-0.2	0.851	0.051	304 Stainless steel
20	10.535	945	685	1798	201	-1	0.851	0.051	304 Stainless steel
21	11.536	932	746	2076	223	-0.9	0.851	0.051	304 Stainless steel
22	1.568	3444	1265	1128	274	-6.6	0.478	0.079	Inconel
23	2.577	1965	1141	1112	232	-4.9	0.478	0.079	Inconel
24	3.559	2466	1059	1112	272	-6.2	0.478	0.079	Inconel
25	4.558	2446	1072	981	272	-6.2	0.478	0.079	Inconel
26	5.562	3186	856	670	160	-6.2	0.478	0.079	Inconel
27	6.56	2383	823	654	201	-4.3	0.478	0.079	Inconel
28	7.561	2735	817	670	146	-5.3	0.478	0.079	Inconel
29	8.564	2669	594	294	104	-3.8	0.478	0.079	Inconel
30	9.565	3406	613	310	124	-4.6	0.478	0.079	Inconel
31	10.563	2165	561	294	109	-2.7	0.478	0.079	Inconel
32	1.1802	1617	310	376	117	0	0.795	0.079	Inconel
33	2.1803	1242	279	376	68	0	0.795	0.079	Inconel
34	3.1804	849	228	376	51	0	0.795	0.079	Inconel
35	4.1805	575	188	376	38	0	0.795	0.079	Inconel
36	5.1806	1653	359	621	79	-0.8	0.795	0.079	Inconel
37	6.1807	1123	311	637	87	0	0.795	0.079	Inconel
38	7.1808	804	259	637	71	0	0.795	0.079	Inconel
39	8.2001	1553	399	981	107	-2.4	0.795	0.079	Inconel
40	9.2002	1242	359	981	103	-1.6	0.795	0.079	Inconel
41	10.2	858	303	997	114	-0.2	0.795	0.079	Inconel
42	10.2	721	257	997	101	0	0.795	0.079	Inconel
43	12.22	1379	448	1144	132	-1.3	0.795	0.079	Inconel
44	13.201	1626	457	1357	136	-3.2	0.795	0.079	Inconel
45	14.201	1206	399	1373	141	-2.1	0.795	0.079	Inconel
46	15.201	849	339	1373	146	-0.7	0.795	0.079	Inconel
47	16.201	712	286	1373	126	0	0.795	0.079	Inconel
48	17.22	1297	490	1520	149	-2	0.795	0.079	Inconel
49	18.22	922	408	1520	153	-0.8	0.795	0.079	Inconel
50	19.22	621	335	1520	132	0	0.795	0.079	Inconel
51	20.201	1516	498	1651	165	-3.2	0.795	0.079	Inconel

Table 3-2. Comparison of Core et al. (1959) heat transfer coefficients with Hendricks et al. (1961, 1966)

Source	run	G kg/(m ² -sec)	q" kW/m ²	P _{in} kPa	average h kW/(m ² -K)	difference %
Core et al.	1.3	520	474	221	3.49	
Hendricks et al.	35	575	376	188	3.10	12
Core et al.	4.4	562	343	400	2.87	
Hendricks et al.	35	575	376	188	3.05	-6
Core et al.	5.3	494	327	441	2.07	
Hendricks et al.	35	575	376	188	3.10	-33
Core et al.	8.3	520	311	662	2.33	
Hendricks et al.	35	575	376	188	3.10	-25
Core et al.	1.6	494	1553	262	5.17	
Hendricks et al.	50	621	1520	335	4.15	25
Core et al.	5.7	666	1717	386	5.51	
Hendricks et al.	50	621	1520	335	3.95	40
Core et al.	4.8	559	948	427	3.68	
Hendricks et al.	42	721	997	257	3.80	-3
Core et al.	4.9	556	1063	434	3.94	
Hendricks et al.	42	721	997	257	3.80	4
Core et al.	6.3	995	605	503	5.18	
Hendricks et al.	37	1123	637	311	3.70	40
Core et al.	6.4	991	1030	510	4.80	
Hendricks et al.	41	858	997	303	3.85	25
Core et al.	10.2	1025	932	641	6.46	
Hendricks et al.	41	858	997	303	3.70	75
Core et al.	8.4	520	899	676	4.47	
Hendricks et al.	2	643	948	969	2.70	66
Core et al.	9.3	527	1095	655	3.77	
Hendricks et al.	4	488	768	1023	2.70	40
Core et al.	9.4	527	1177	662	3.25	
Hendricks et al.	4	488	768	1023	2.50	30
Core et al.	19.3	443	703	1041	2.60	
Hendricks et al.	4	488	768	1023	3.10	-16
Core et al.	21.4	491	670	1089	4.76	
Hendricks et al.	4	488	768	1023	3.00	59
Core et al.	10.3	1012	1864	662	5.60	
Hendricks et al.	20	945	1798	685	3.85	45
Core et al.	11.2	919	1635	690	5.28	
Hendricks et al.	20	945	1798	685	4.00	32
Core et al.	12.4	954	687	655	5.51	
Hendricks et al.	13	892	703	984	2.90	90
Core et al.	14.4	749	670	862	3.26	
Hendricks et al.	13	892	703	984	2.90	12
Core et al.	16.4	967	589	1014	5.46	
Hendricks et al.	13	892	703	984	2.90	88
Core et al.	12.5	954	1210	662	5.09	
Hendricks et al.	7	873	1324	1075	4.15	23
Core et al.	20.1	874	1651	1027	4.59	
Hendricks et al.	7	873	1324	1075	4.60	0
Core et al.	12.5	954	1210	662	5.09	
Hendricks et al.	9	895	1242	889	3.30	54
Core et al.	12.6	954	1537	676	5.28	
Hendricks et al.	49	922	1520	335	4.55	16
Core et al.	13.3	322	883	703	3.37	
Hendricks et al.	3	329	735	743	2.10	61
Core et al.	15.4	377	834	952	3.85	
Hendricks et al.	3	329	735	743	2.15	79
Core et al.	13.4	456	1030	696	3.80	
Hendricks et al.	1	327	1193	759	2.50	52
Core et al.	13.5	351	1308	703	4.50	
Hendricks et al.	1	327	1193	759	2.45	84
Core et al.	14.4	749	670	862	3.26	
Hendricks et al.	6	630	719	733	2.50	30
Core et al.	19.4	446	1194	1020	3.39	
Hendricks et al.	8	536	1308	1103	4.15	-18

Table 3-3. Comparison of average heat transfer coefficients for similar runs in the Wright and Walters (1959) data set and TN 765.

Source	run	G		Pin	average h	difference
		kg/(m ² -sec)	kW/m ²			
Wright & Walters (1959)	15	908	260	250	3.83	
Hendricks et al. (1961)	34	849	376	228	3.08	24.3
Wright & Walters (1959)	23	522	385	167	3.11	
Hendricks et al. (1961)	35	575	376	188	3.00	3.7
Wright & Walters (1959)	35	427	390	179	2.47	
Hendricks et al. (1961)	35	575	376	188	3.00	-17.7

Table 3-4. Summary of test conditions for major forced convection internal tube flow boiling hydrogen experiments

Source	Mass flux, [kg/m ² -sec]		Heat flux, [kW/m ²]		System pressure, [kPa]	
	min	max	min	max	min	max
Core et al. (1959)	322	1027	16	9812	193	1469
Lewis et al. (1962)	4	23	11	126	207	510
Wright & Walters (1959)	410	1172	10	390	138	276
Hendricks et al. (1961)	575	1653	376	1651	188	498
Hendricks et al. (1966)	327	3444	294	2093	594	1265

Table 3-5. Result of parametric sensitivity study of end axial heat conduction.

set #	parameter				
	thermal cond. W/m-K	heat xfer coeff. kW/m ² -K	wall thickness 1E-4m	heat flux MW/m ²	95% length thicknesses
5	15	2	5	1	9
10	45	2	5	1	15
15	15	1	5	1	12.8
20	15	4	5	1	6
25	15	2	2	1	13.8
30	15	2	8	1	7
35	15	2	5	0.3	8.3
40	15	2	5	2	8.5

Table 3-6. Distance into tube wall from start of heating at which tube metal temperatures are reduced by at least 5% from the nominal level.

Runs	Inner Diameter [cm]	Thickness [cm]	D/T ratio	Material	Thermal Cond. [W/m ² -K]	Heat Flux [MW/m ²]	Heat xfer Coeff. [kW/m-K]	95% distance [cm]
1-6	1.288	0.025	51.5	Inconel X	13	1	1	0.41
7-10	1.113	0.081	13.7	Inconel	13	1	1	0.73
11-21	0.851	0.051	16.7	304 SS	20	1	1	0.71
22-31	0.478	0.079	6.1	Inconel	13	1	1	0.69
32-51	0.795	0.079	10.1	Inconel	13	1	1	0.71

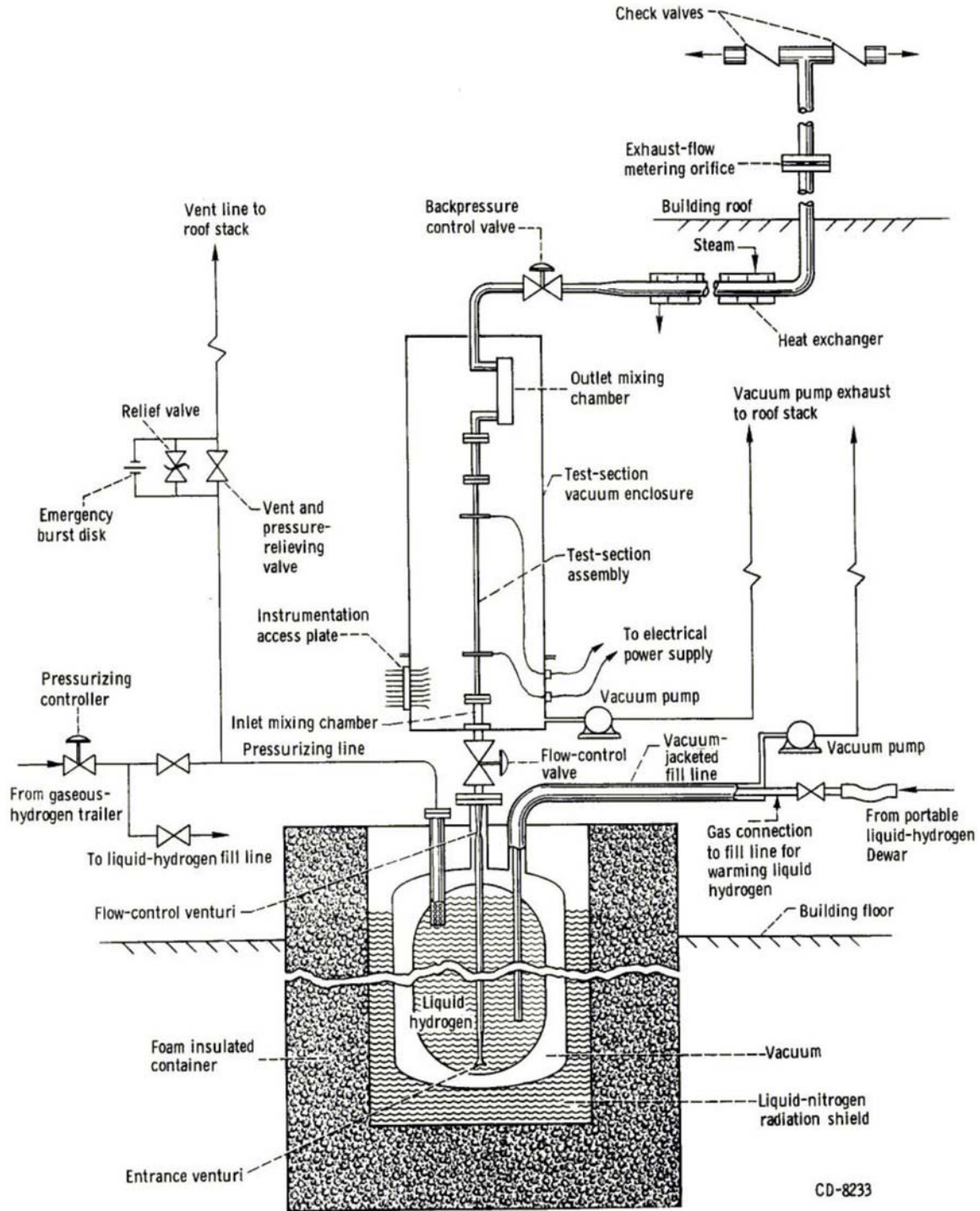


Figure 3-2. NASA TN-3095 experimental setup.

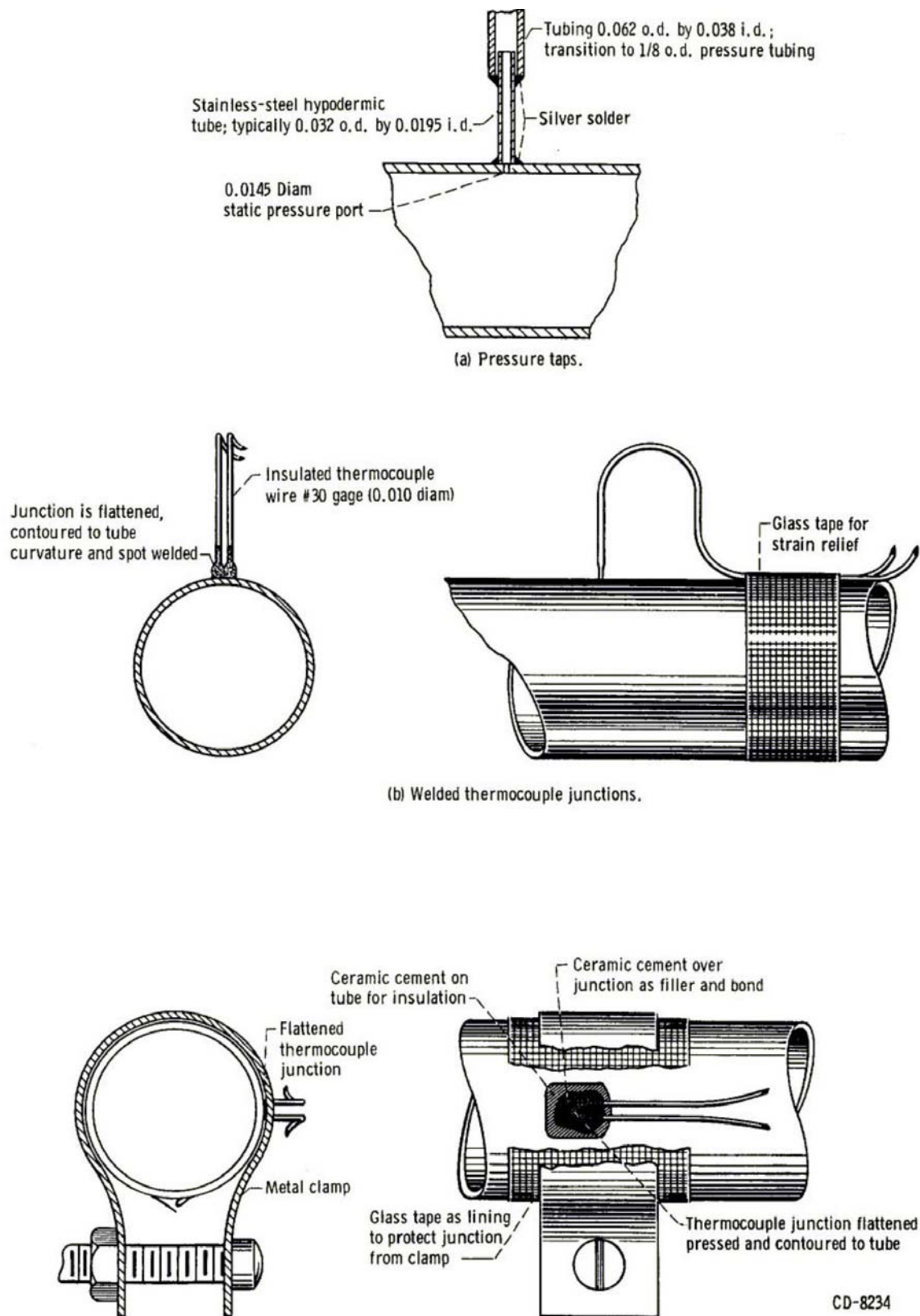


Figure 3-5. TN 3095 instrumentation.

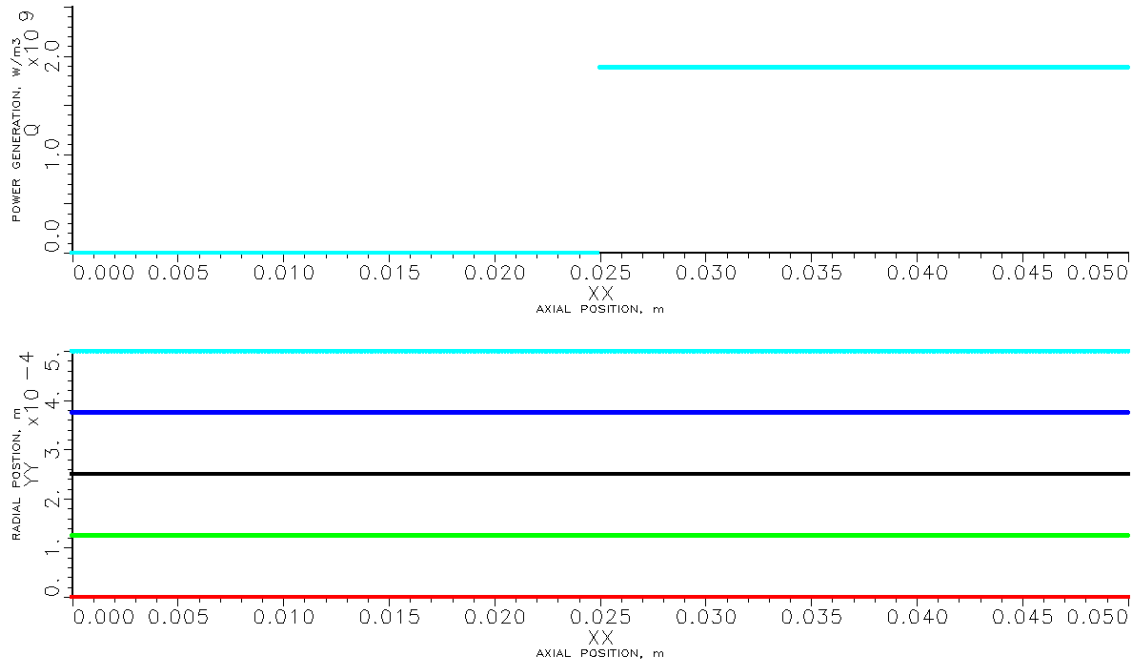


Figure 3-6. Nodal distribution and heat generation distribution used to model end effects at tube inlet.

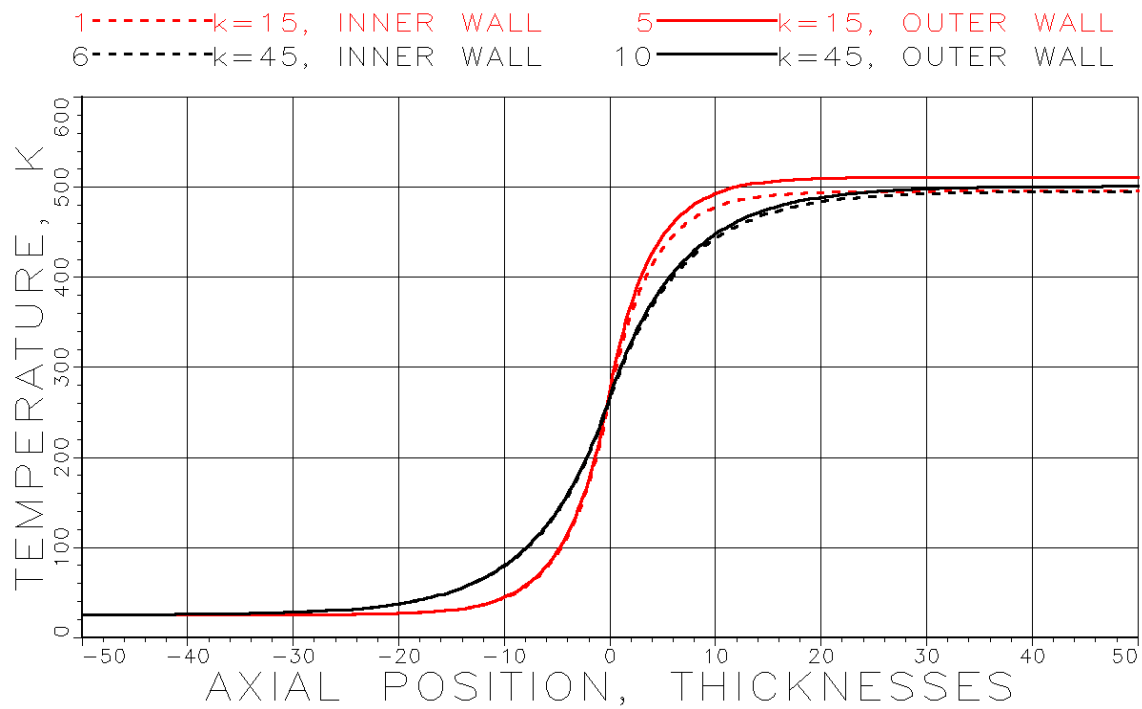


Figure 3-7. Radial metal temperature profiles as a function of metal thermal conductivity.

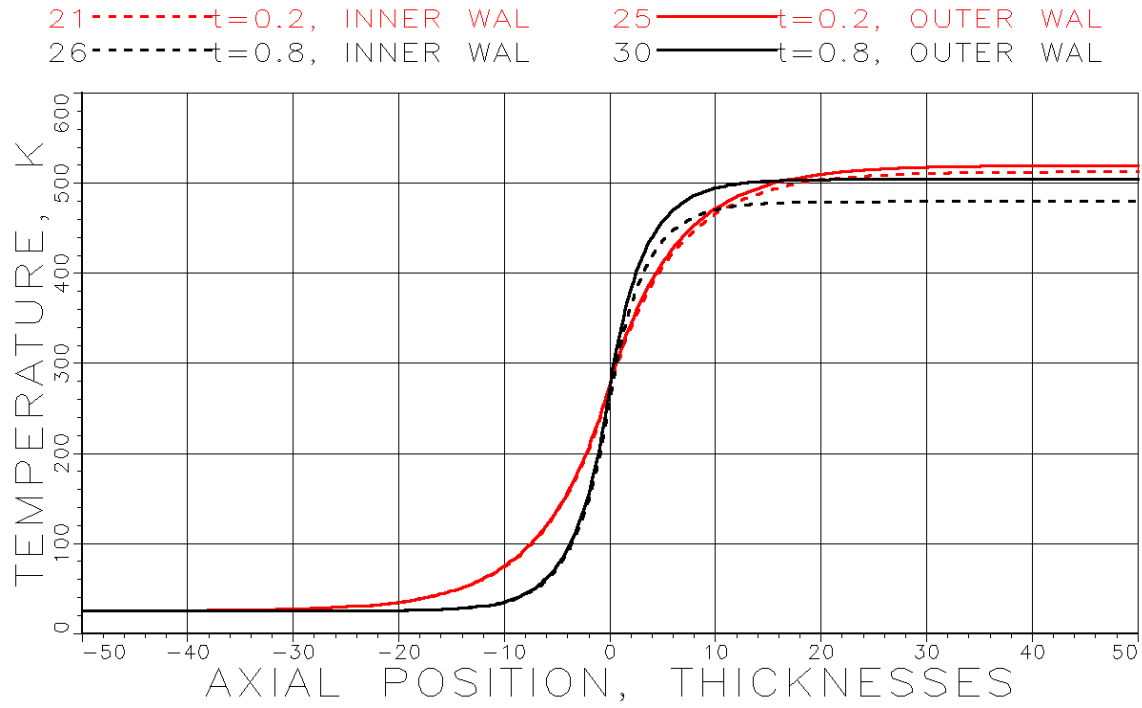


Figure 3-8. Radial metal temperature profiles as a function of metal thickness.

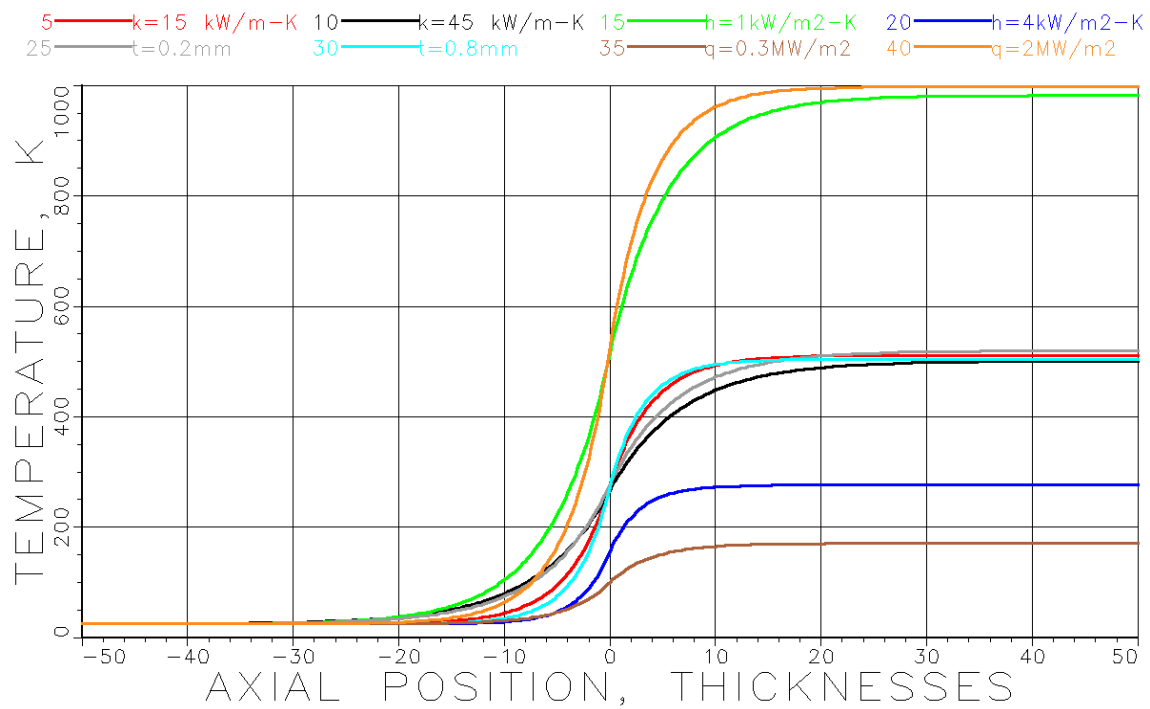


Figure 3-9. Effect of specified parameters on tube end wall axial heat transfer.

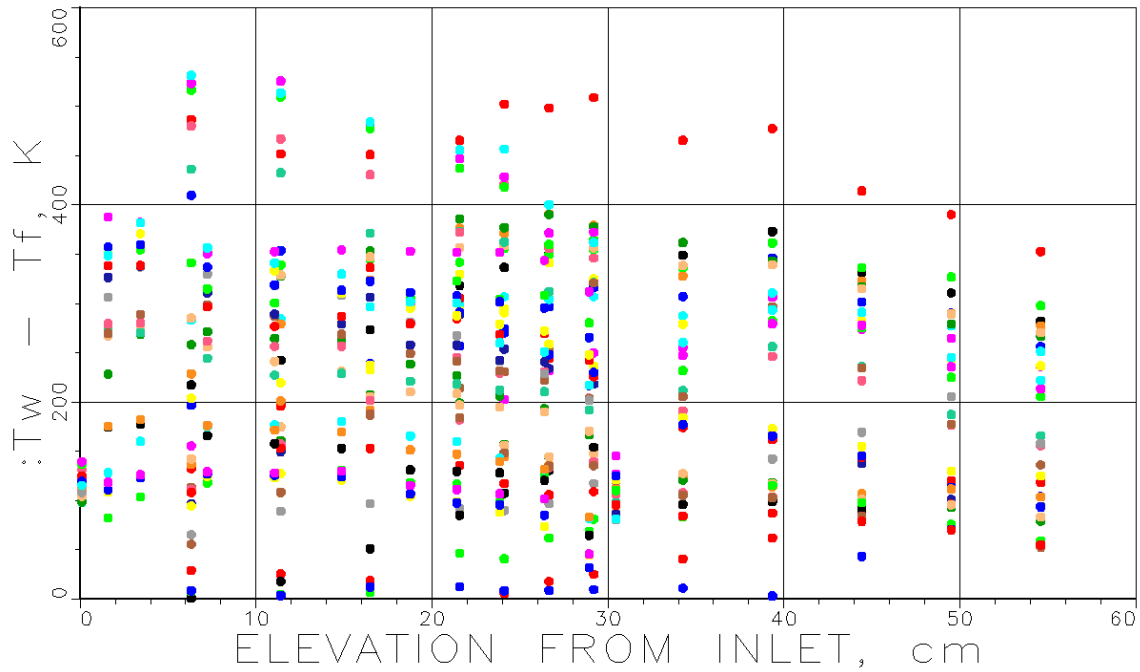


Figure 3-10. Difference in wall to liquid temperature for all data considered.

22 — $G=3444, q=1128$ 26 — $G=3186, q=670$ 29 — $G=2669, q=294$ 30 — $G=3406, q=310$

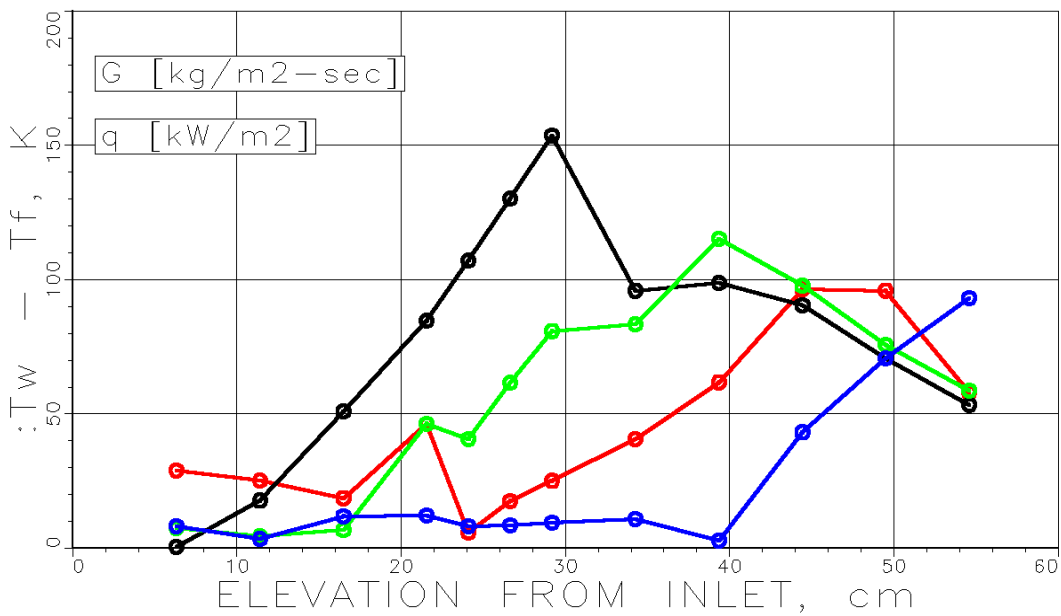


Figure 3-11. Wall to liquid hydrogen temperature differences for four runs that show at least one very low difference. These small differences are associated with pre-CHF conditions.

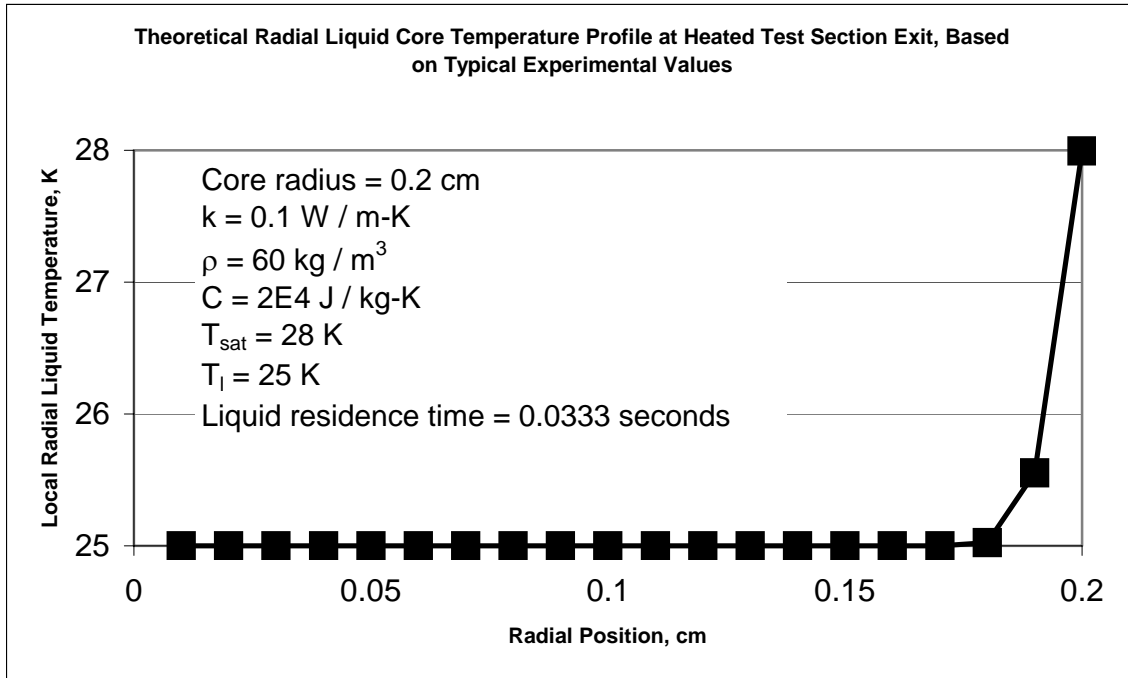


Figure 3-12. Theoretical liquid core temperature profile at the exit of the heated test section, to support the assumption to ignore sensible heating of the liquid.

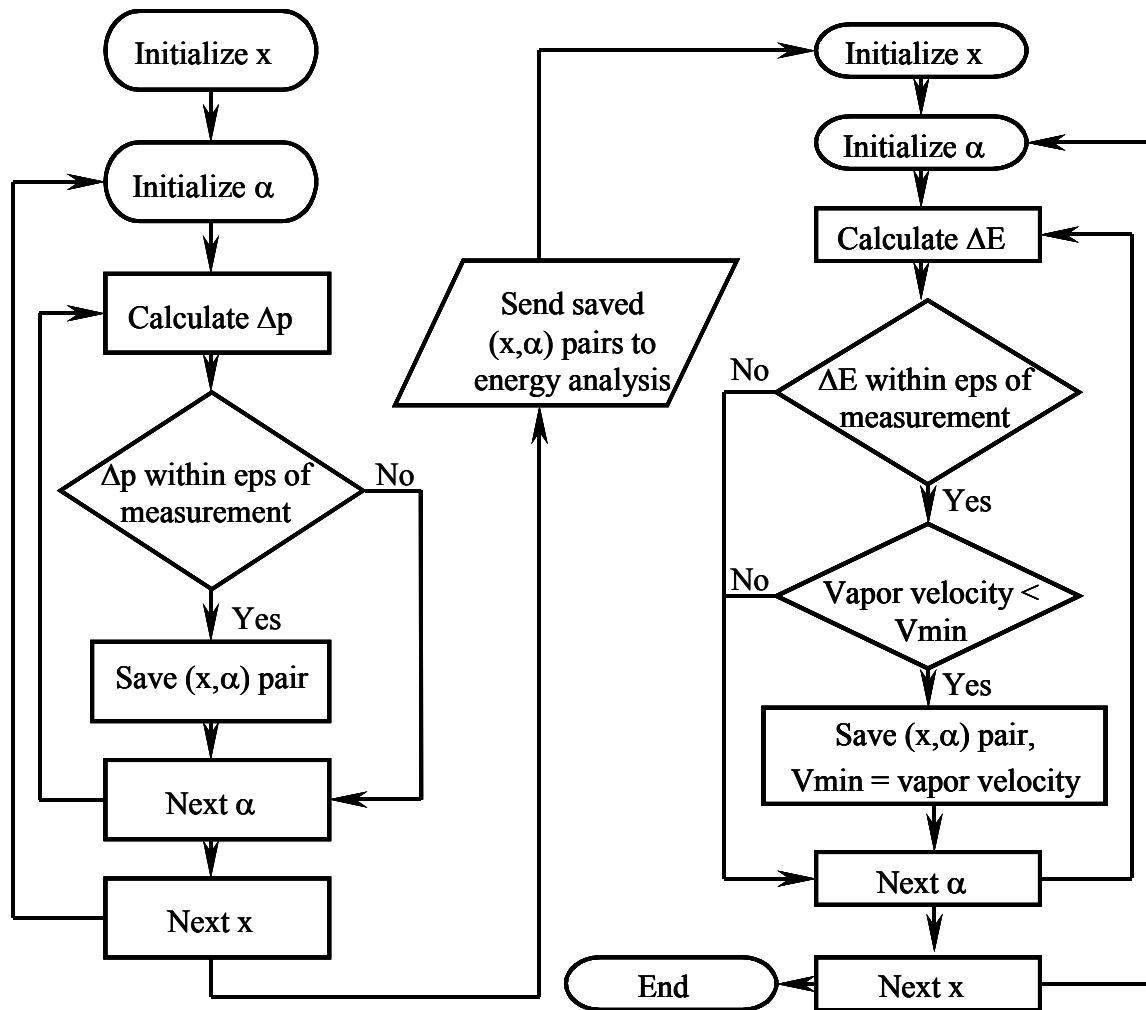


Figure 3-13. Flow diagram for momentum and energy analysis of data.

CHAPTER 4 ANALYSIS AND VALIDATION OF MOMENTUM MODEL RESULTS

Data Referencing

The NASA data set comprises 51 steady state runs in which there are 13 data points each. The first point is at the heated test section inlet. For runs 1 - 31, the 13th point is 6.3 cm before the heated test section exit. For runs 32 - 51, the 13th point is at the heated test section exit. The runs fall naturally into five groups based on inner diameter. Table 4-1 lists the tube dimensions, the run numbers associated with each tube, and a reference number that will be used for convenience in later analyses.

Data Refinement

It was determined through various means that the data set needed to be refined. Following is a description of the approach to this process.

Omitted Data

The points that are affected by inlet and end conditions, and any calculations that include these affected points, should be excluded from analyses. For runs 1-31, point 1 at the test section inlet falls into this category. Only results between point 2 at 6 cm and point 13 at 55 cm will be considered. For runs 32-51, points 1, 2, and 13 at the inlet, 0.1 cm, and at the test section exit will be excluded. Only results between point 3 at 1.6 cm and point 12 at 29 cm will be considered.

Problematic Data

Validity of some data is questioned. The basis for questioning these points lies in apparent discontinuities between adjacent values. Figure 4-1 presents several examples. Run 42 point 8 at 19 cm shows a rise in wall temperature of 40 – 50 K relative to adjacent wall temperatures. This magnitude of temperature rise and fall over a 7 cm length, and the fact that the event is

exceptional in these data, begs an explanation. A similar effect is evident in run 32 at 27 cm. It may be that a unique flow structure occurs for a short length in these runs. The computer model is robust enough to accommodate many, but not all, of these changes and solve for the momentum and energy balances within the specified limits.

For some points in which the wall temperature increases drastically from the previous point, the model cannot satisfy the energy balance. This is because of the assumption that all of the vapor at a point is at the calculated vapor temperature, which is a function of the wall temperature. If there is a large increase in wall temperature, then the increase in mean vapor enthalpy may require a larger energy addition than the energy added through heating from the previous point, even with zero change in quality. To satisfy these points, the quality would have to be reduced, which is assumed to not be possible in the model. This is why these points of high increase in wall temperature are consistently associated with negative energy addition errors – the measured added energy can not attain the increase in vapor energy.

Tube three exhibits a consistent decrease in wall temperature at the 34 cm location. Figure 4-2 presents the wall temperatures for all 11 runs on tube three. This is interpreted as a bias in the measurement. Therefore, in making calculations using the wall temperature, these erroneous experimental values have been replaced by a linear interpolation between adjacent points. The only other wall temperature point that was deemed obviously out-of-family was run 42, at the 19 cm elevation. This point also was replaced by a linear interpolation between adjacent points. While other points in the data set showed erratic trending, it was usually uncertain which points should be modified. A common characteristic is for adjacent points to trend oppositely, e.g., one low and the next high. Which point was biased was usually not determined. Therefore, no modifications were made.

Also evident in figure 4-1 are the end effects in which heat is conducted axially within the tube metal at the inlet and exit of the test section, as discussed in chapter 3. The steep gradient in wall temperatures for most runs between points 2 and 3 at 0.14 cm and 1.5 cm at the inlet and points 12 and 13 at 29 cm and 30.5 cm prove the end effect. What is of particular interest are the several runs, 32 and 36 in figure 4-1, in which the inlet and exit temperatures are actually higher than their adjacent measured temperatures inward from the ends. This indicates that there is an end effect other than axial heat conduction influencing measured wall temperatures. This can be explained by considering that the collars brazed onto the test section ends to apply a voltage will not distribute the current absolutely evenly across the tube metal radius. The current flow will distribute itself across the thickness of the metal over a finite distance, and will be concentrated near the brazed collar at the ends. Therefore, the current density will be higher at the tube outer wall where the collar is brazed and will therefore generate more heat towards the outer part of the wall, where the thermocouple is attached.

The inlet and exit wall temperatures are lower than their adjacent wall temperatures for the runs that have high wall temperatures, as runs 40, 42, 47, and 50 indicate, in spite of the concentration of current near these end thermocouples. Comparing these trends with the rising wall temperatures at the ends observed in runs 32 and 36 exemplify the relative impact of the independent effects of axial heat conduction and current concentration. For runs with low wall temperatures, the temperature rise due to current concentration is greater than the temperature decrease due to axial heat conduction, with the net effect that the measured wall temperature rises. The opposite net effect is evident in the high wall temperature runs. That is, axial heat conduction has a greater effect on measured temperature than does current concentration.

Data Representation

The pressure data exhibited uneven trending, to varying degrees, in all runs. This unevenness can present problems for a modeling algorithm using the pressure data to solve for other flow conditions. Therefore, a smooth regression line was generated for each run to represent the axial pressure profile. It was found that a third order least squares fit modeled all runs very well, with correlation coefficients very near unity for most runs. Table (4-2) presents these correlation coefficients, standard deviations, and normalized (to pressure drop across length of tube) standard deviation.

In discussing the model results, momentum and energy balances are discussed in terms of normalized values for each point. For example, the ‘fractional pressure drop error’ between two points refers to the difference in the calculated pressure drop between the previous point and the current point and the measured difference, divided by the measured difference. In the same way, the ‘fractional energy add error’ refers to the difference in the calculated energy addition between the previous point and the current point and the measured addition, divided by the measured addition.

Problematic Runs

While run eight momentum and energy balances are satisfied, its void fraction is clearly impossible. This is because, while the overall pressure drop of 76 kPa in run eight is not high, the pressure gradient in the lower portion of the tube is extremely high, as shown in figure 4-3, comparing runs seven and eight. These runs have similar system pressures and heat fluxes, while their mass fluxes are $873 \text{ kg/m}^2\text{-s}$ in run seven and $536 \text{ kg/m}^2\text{-s}$ in run eight. For most elevation intervals, there is a low and high void fraction solution for the associated pressure drop. The pressure drop between the inlet and the 6.35 cm elevation in run eight does not allow for a high void fraction solution given the energy addition and vapor temperature, leaving only the

low void fraction solution as an option. This is the only run in the data set in which this problem arises. It is noteworthy that this run has always been unique and presented difficulties regardless of the various modeling methods attempted. As will be shown in the results, run eight pressure profile is significantly different from the predicted pressure profiles from this dissertation model and the homogeneous equilibrium model, which happen to trend very closely with each other. As a result of the obviously erroneous void profile, run eight will be excluded from further analysis.

Figure 4-4 shows that the fractional pressure drop and energy addition errors for run 14 are numerous and relatively large. The algorithm cannot achieve such a low pressure drop for most points given the vapor temperature and energy addition. Run 13 is very similar to 14 in mass flow and system pressure, but with a heat flux of 703 kW/m² versus 425 kW/m² for run 14. The lower heat flux in run 14 will certainly cause lower pressure loss, but the overall pressure drop – 12 kPa versus 32 kPa - is a little more than 1/3rd that of run 13, which seems to be a great reduction given the relatively modest decrease in heat flux. The high system pressure of about 75% of the critical pressure should also mitigate the difference in pressure loss between the two runs, since the difference in liquid and vapor density is not too great, and should thus be less sensitive to the pressure loss associated with vaporization. Finally, the profile of the pressure appears to have two inflection points, which, though possible, indicates a very complicated flow structure. This reverse s-shape appears in other problem runs.

It is interesting to note that run 14 is the only run that is subcooled from an equilibrium standpoint throughout the length of the heated test section. While the model appears to handle other subcooled conditions adequately, the highly subcooled nature of run 14 may present a special problem. As a result, run 14 will be excluded from the correlation process.

Tube 4 runs, 22-31, have by far the highest mass fluxes in the database. This is likely the reason that four of these runs (22, 26, 29, and 30) exhibit low wall temperatures in the lower portions of the test section. As discussed in chapter 3 and shown in figure 3-11, these runs are associated with pre-CHF conditions and therefore will be excluded from consideration. Two other runs, 28 and 31, produce poor energy balances. Thus, four runs (23, 24, 25, and 27) remain for further consideration. As will be discussed later, these remaining four runs will be excluded from the correlation process since the nature of their test conditions and resulting slips are removed from the general body of data.

Three other runs (32, 36, 44) will also be excluded later, based on their high velocity slip profiles that are inconsistent with all other slip profiles. This will be addressed later. While there are occasional momentum and energy balance errors in other runs, it has been determined that useful information can be obtained from them. Therefore, all other runs will be considered further. Thus, after excluding pre-IFB runs (22, 26, 29, and 30), bad momentum and energy balance runs (14, 28, and 31), and run eight with a bad void profile, there remains a total of 43 runs for further consideration.

It is determined from the above discussion that these runs that cannot be satisfactorily processed by the model should be excluded from the analysis of results. This should not be interpreted as a condemnation of the data from these runs, but rather an observation that the model is not capable of resolving the data, and results using those data will be misleading.

Vapor Superheat

The effect of vapor superheat on the energy balance was investigated by modifying the coefficient to the parenthesized term in Burmeister's (1993) model, presented in equation 3-21. Figure 4-5 presents the results using run 39, in which the term 'C' in the legend refers to this coefficient. Coefficient values of $5/6^{\text{th}}$ (Burmeister's theoretical result), $2/3^{\text{rd}}$, and $1/2$ (resulting in

the commonly used mean film temperature) were tried. Increasing the vapor superheat in general improves the overall energy balance. The decision to model the vapor superheat as the mean temperature of the wall and saturation temperature was based upon this analysis. As discussed in chapter 3, using the mean film temperature is consistent with the experimental findings of Nijhawan et al. (1980).

Model Results

As figure 4-6 shows, the processing of data from these runs does not generate perfect results. Momentum balance within 10% of measurement is achieved in all but 10 instances, and to within 5% of measurement for all but 20 points. Energy balance is achieved within 10% of measurement in all but 11 cases, and to within 5% of measurement for all but 44 cases. The great majority of incremental pressure drops and energy additions for each run are well modeled. Momentum and energy balances that fall outside the targeted 2% variance from measurement are typically caused by steep changes in wall temperatures. The reason this causes problems lies in the assumption that all of the vapor is at the mean temperature. If the wall temperature increases markedly, then so too does the mean vapor enthalpy. The measured energy input to the flow is less than the energy increase determined from the local pressure and mean vapor temperature. The algorithm selects the energy solution closest to measurement from the quality/void fraction domain generated by the momentum balance, but the energy balance error is still larger than the targeted accuracy in these few cases. In these cases, the calculated quality does not change from one point to the next.

Figure 4-7 presents the resulting void profiles from the model for the 43 runs. In general, the void profiles rise steeply but smoothly. Where discontinuities occur, in general there are steep increases in wall temperatures. In this figure, the four lowest void profiles correspond to

runs 23-25, and 27, all on tube 4. These are by far the highest remaining mass flux runs in the culled data set.

Figure 4-8 presents the resulting velocity slip ratios from the model for the culled data set. The trend of the slip profiles are in general smooth. The high mass flux runs 32, 36, and 44 on tube 5 produce the highest slip ratios. The trends, while generally smooth for all runs, are somewhat diverse.

Validation of Model Results

Figure 4-7 shows that an extremely steep void fraction build-up occurs in IFB, and departs markedly from the relatively shallow build-up predicted by models such as that resulting from the Lockhart-Martinelli parameter. These results are consistent with findings of Per Ottosen (1980) in which void profiles in IFB conditions were measured using γ -ray scattering. Ottosen published the first known results from the use of γ -ray absorption to measure void fraction in low velocity IFB nitrogen. Figure 4-9 presents results from three of his many runs. It is apparent that void fractions versus equilibrium quality (he made no attempt to quantify true mass quality) rise very steeply. He observed the transition from IAFB to DF at void fractions between 80-90%. All of his experiments were at approximately constant wall temperature conditions. Additionally, all his data represent much lower mass fluxes than these hydrogen data. Perhaps most importantly, the mass velocities were at least an order of magnitude lower than those in these hydrogen data.

While a fine quantitative comparison is not made here due to the differences in experimental conditions, a qualitative comparison is reasonable. It is apparent that extremely rapid void fraction build-up is a characteristic of IFB.

Rohsenow and coworkers (Dougall and Rohsenow, 1963; Lavery and Rohsenow, 1967; Forslund and Rohsenow, 1969) used nitrogen in their studies of IFB. In their work, they determined the actual mass quality. They observed that the transition from IAF to DF occurred at a mass quality of about 10%. Combining this observation with Ottosen's of the void fraction at transition, it can be concluded that void fractions of 80 – 90% at a mass quality of 10% are typical. These experimental observations agree well with the results of this model.

Range of Validity

To avoid the momentum and energy balances of the high mass flux runs on tube 4, the range of validity of this model has been reduced in terms of mass flux only. A total of eight runs have been excluded from further analysis due to the inability of this model to reproduce the pressure drop and energy balances. Forty-three runs remain. The remaining data for which the balances are acceptable have the following range: pressures from 180 kPa to the critical pressure, mass fluxes from 300 kg/m²-s to 2500 kg/m²-s, and heat fluxes from about 370 kW/m² to about 2100 kW/m².

Table 4-1. List of tube numbers, dimensions, and runs executed with the tubes.

Tube ref #	Inner diameter	Length	Run numbers
	cm	cm	
1	1.288	60.96	1-6
2	1.113	60.96	7-10
3	0.851	60.96	11-21
4	0.478	60.96	22-31
5	0.795	30.48	32-51

Table 4-2. Statistical analysis of pressure data show goodness of fit through R^2 , and relative unevenness of data through normalized (by pressure drop across test section length) standard deviation. Results are from least squares fit of third order.

set	σ Pa	Norm σ $\sigma / \Delta P$	R^2 -
1	248	9.05E-03	0.999
2	226	1.03E-02	0.999
3	229	1.57E-02	0.998
4	221	1.64E-02	0.998
5	232	1.90E-02	0.997
6	235	1.20E-02	0.999
7	328	7.28E-03	1
8	1945	2.57E-02	0.995
9	2202	5.39E-02	0.981
10	2481	1.23E-01	0.92
11	229	1.09E-03	1
12	358	4.17E-03	1
13	195	6.15E-03	1
14	219	1.79E-02	0.998
15	232	2.28E-03	1
16	324	2.87E-03	1
17	279	1.11E-03	1
18	236	2.53E-03	1
19	288	1.95E-03	1
20	302	1.50E-03	1
21	301	1.35E-03	1
22	1288	4.71E-03	1
23	408	1.76E-03	1
24	2390	8.79E-03	0.999
25	1697	6.24E-03	1
26	681	4.26E-03	1
27	1907	9.48E-03	0.999
28	2280	1.56E-02	0.998
29	820	7.86E-03	1
30	942	7.61E-03	1
31	301	2.76E-03	1
32	527	9.00E-03	1
33	681	1.00E-02	0.999
34	490	9.63E-03	0.999
35	466	1.21E-02	0.999
36	838	1.06E-02	0.999
37	888	1.02E-02	0.999
38	642	9.07E-03	1
39	1082	1.01E-02	0.999
40	755	7.31E-03	1
41	1050	9.19E-03	0.999
42	740	7.32E-03	1
43	867	6.55E-03	1
44	1343	9.90E-03	0.999
45	1381	9.78E-03	0.999
46	1894	1.30E-02	0.999
47	1084	8.61E-03	1
48	745	4.99E-03	1
49	712	4.65E-03	1
50	440	3.34E-03	1
51	2010	1.22E-02	0.999

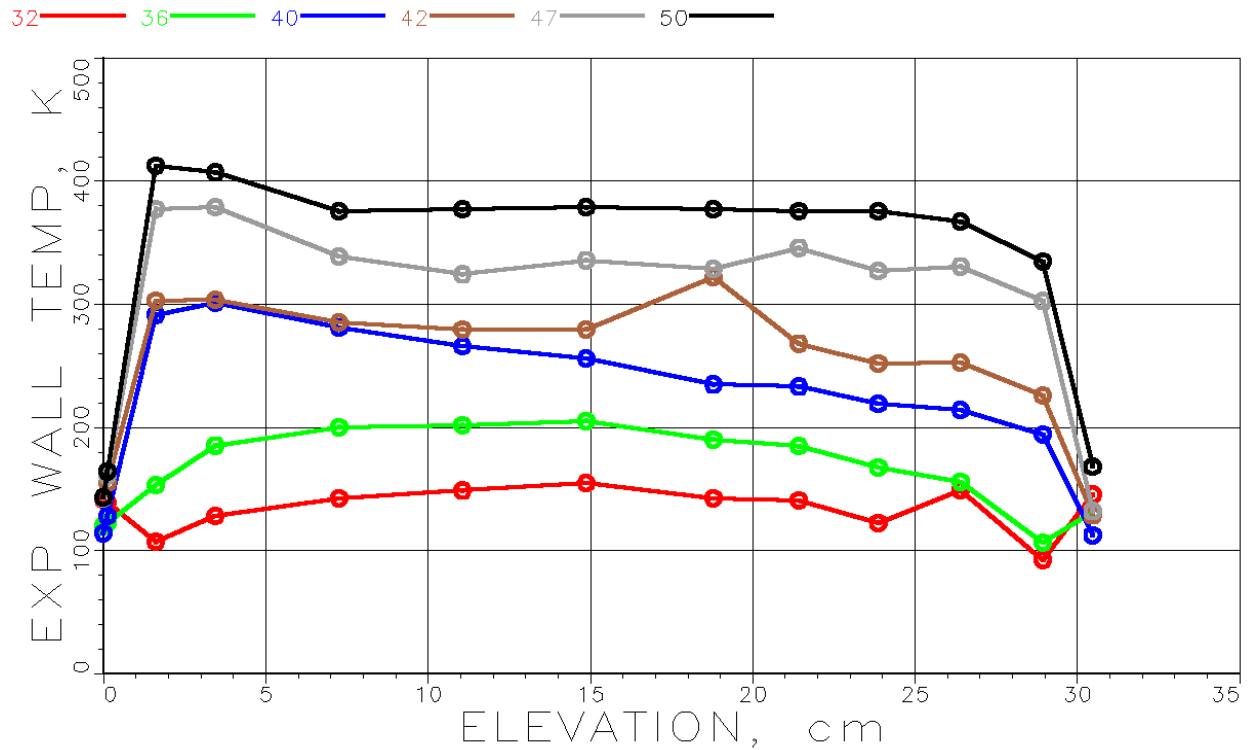


Figure 4-1. Sample of 1961 data wall temperatures. Evident are tube end effects, several apparent discontinuities, and the variation in trending between tests.

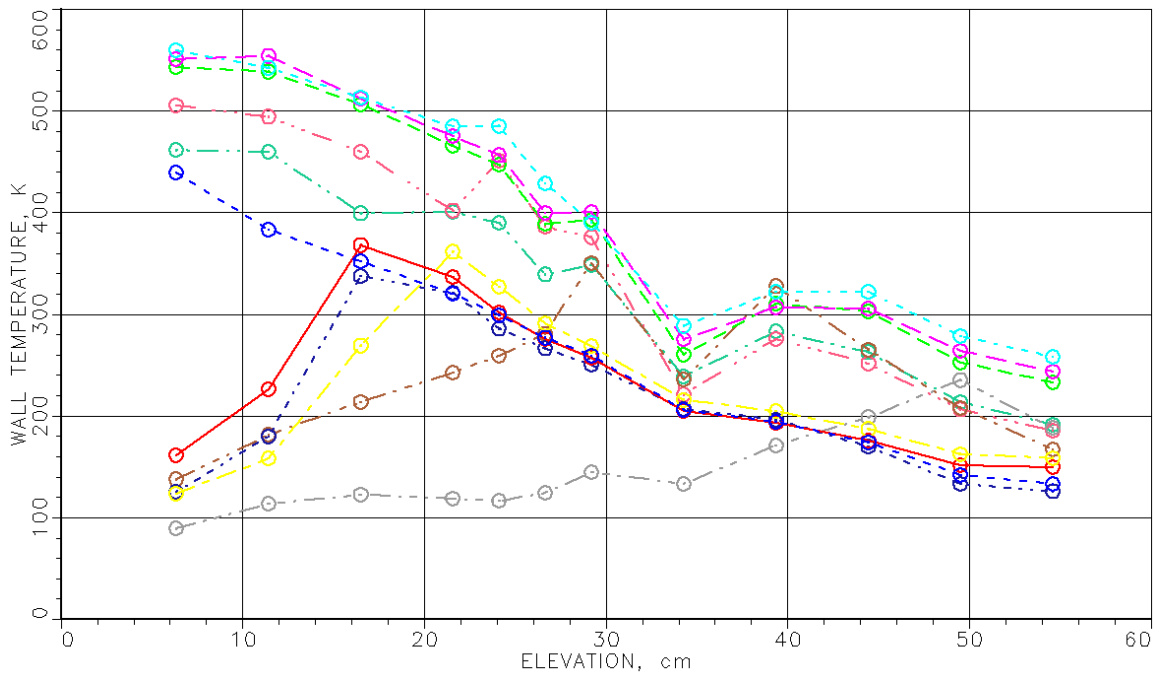


Figure 4-2. Tube 3 exhibits a consistent reduction in wall temperature at 34 cm. This is likely biased data.

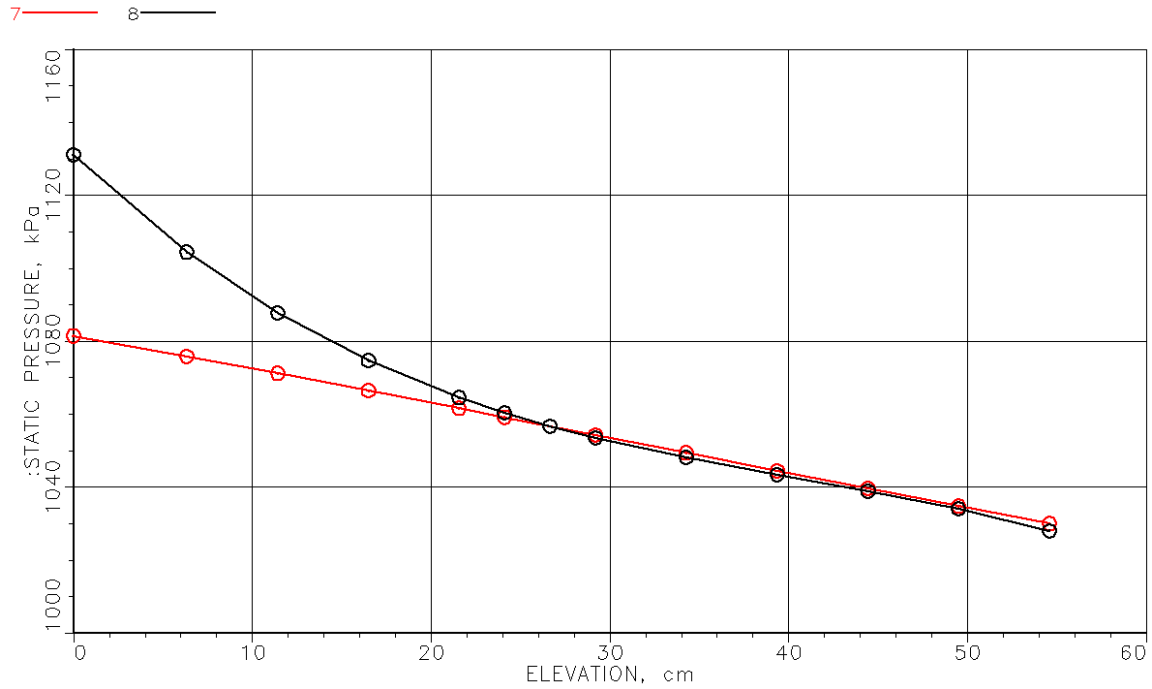


Figure 4-3. While Runs 7 and 8 have fairly similar operating conditions, run 8 pressure gradient in the lower portion of the tube is the steepest in the data set. This causes the model to have difficulty in resolving the quality and slip conditions.

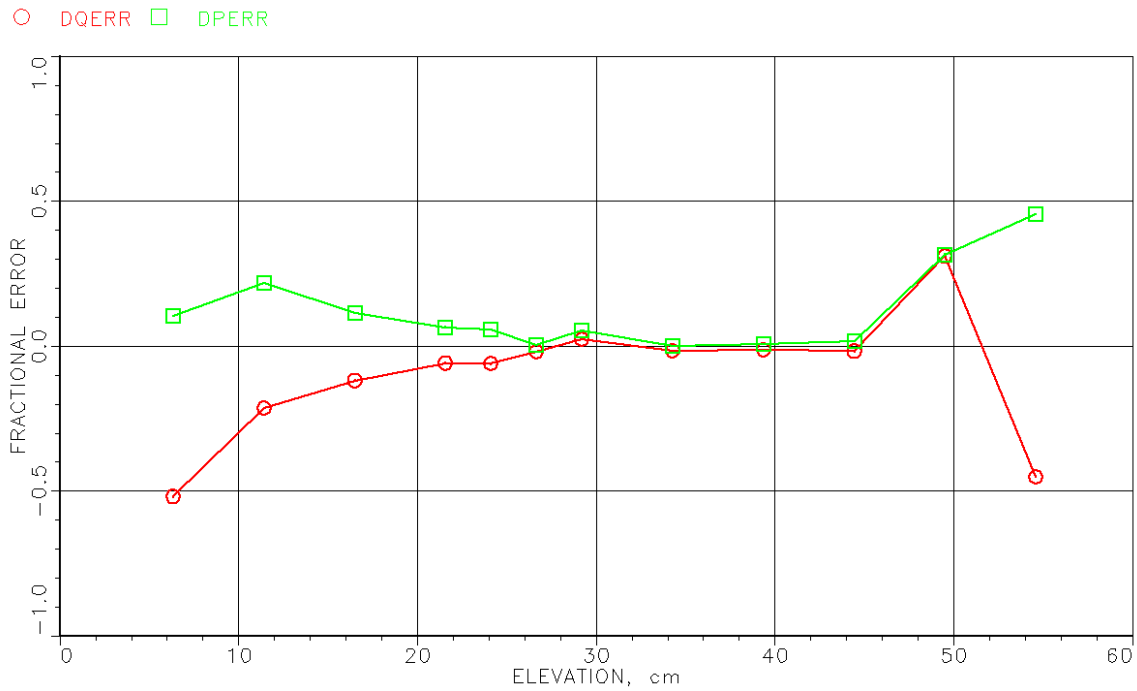


Figure 4-4. Run 14 energy and momentum balances are not well matched by the model.

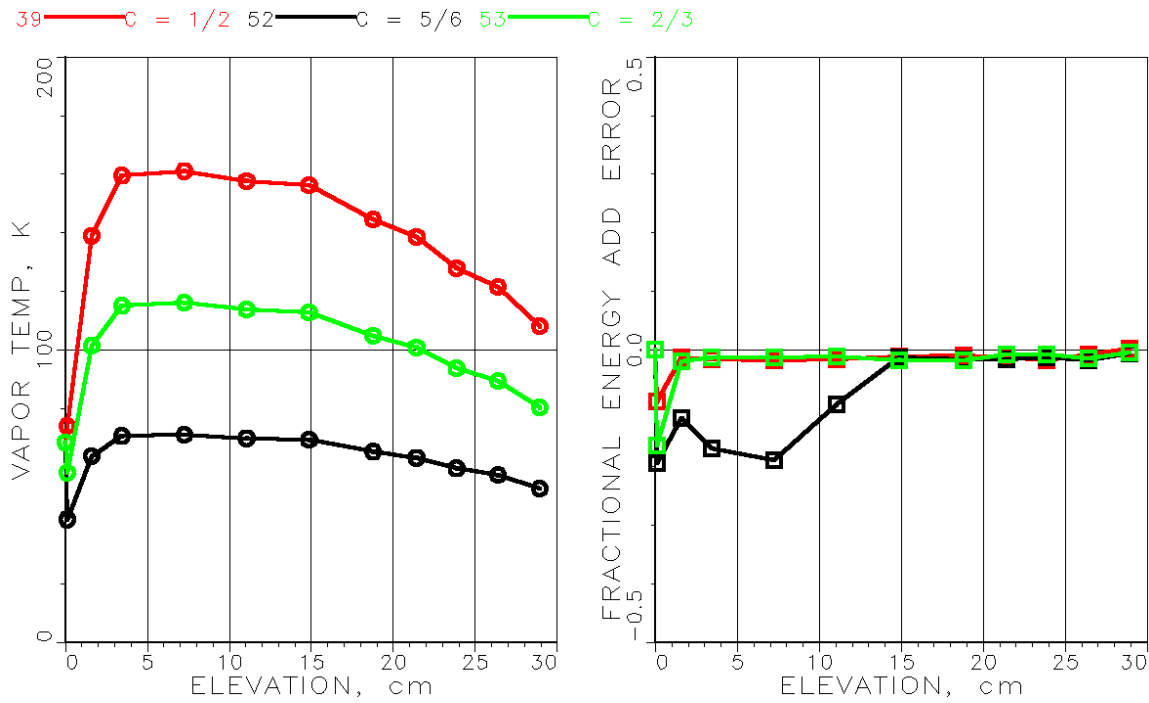


Figure 4-5. Results of modifying the coefficient in Burmeister's equation (Eq 3-21) for the effective film temperature. Increasing vapor temperature improves the energy balance for most high mass flux runs.

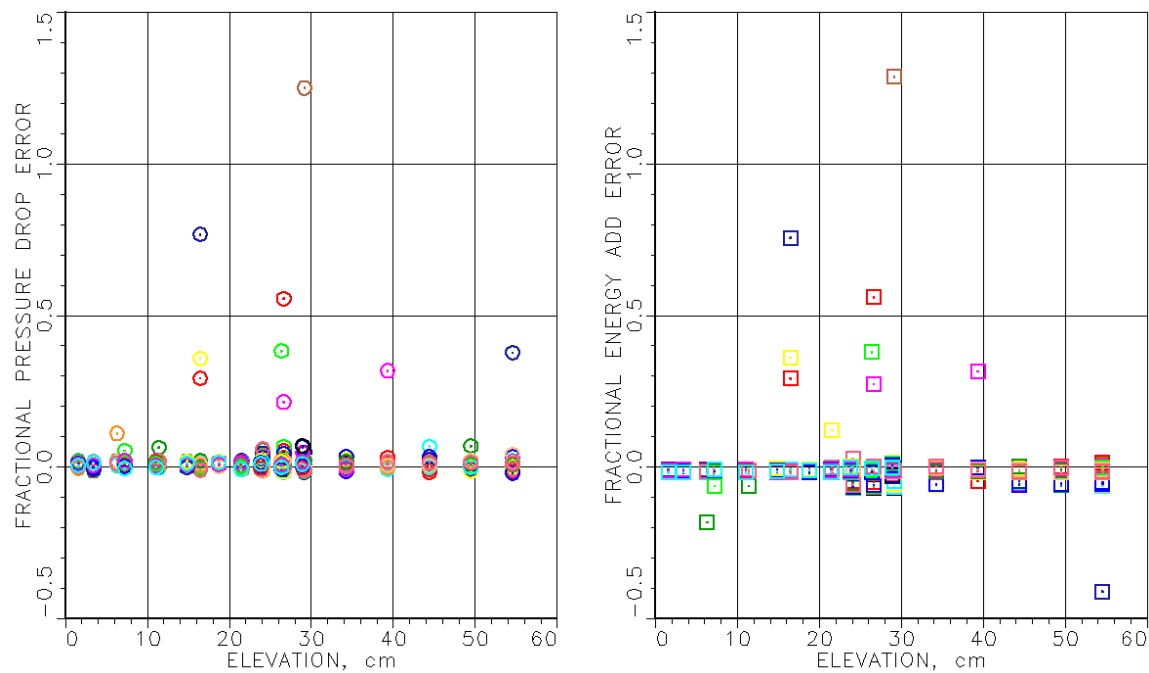


Figure 4-6. Culled data momentum and energy balance results from model. Not all points are modeled to within 2% of data, but results are acceptable.

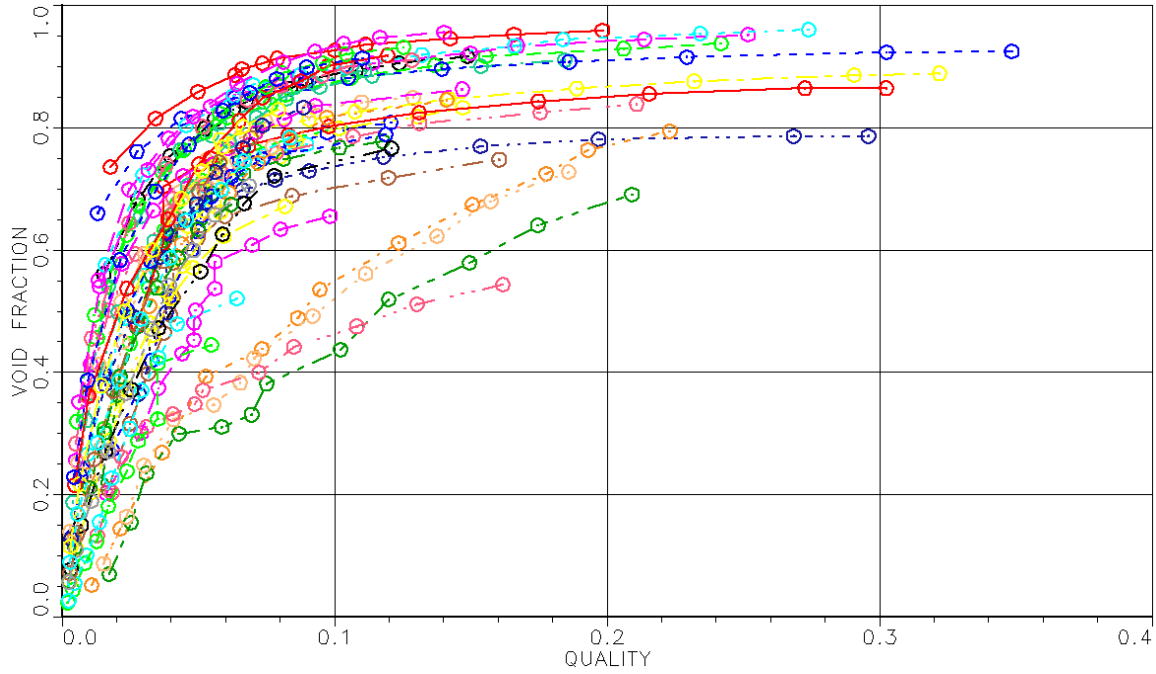


Figure 4-7. Calculated void fraction from model for the culled data set. The four lowest void profiles are runs 23-25, and 27, with the highest mass fluxes.

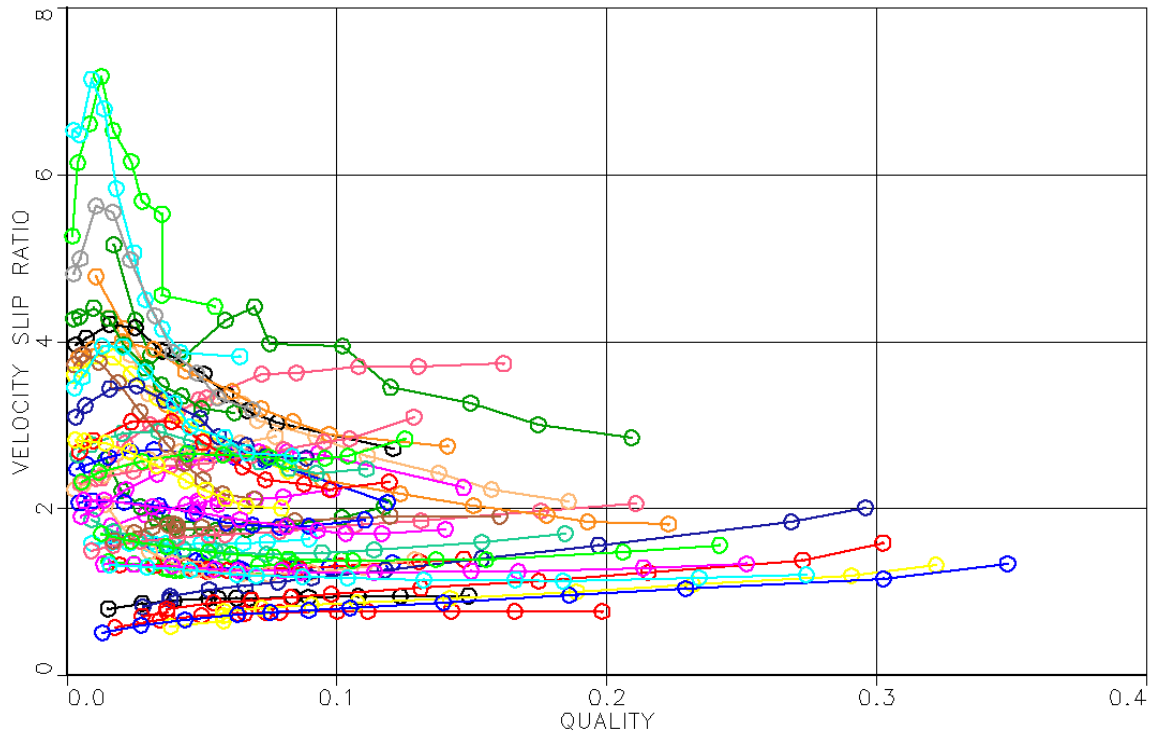


Figure 4-8. Velocity slip ratio vs quality from model for the culled data set. The 3 highest slip ratios correspond to runs 32, 36, and 44 on tube 5.

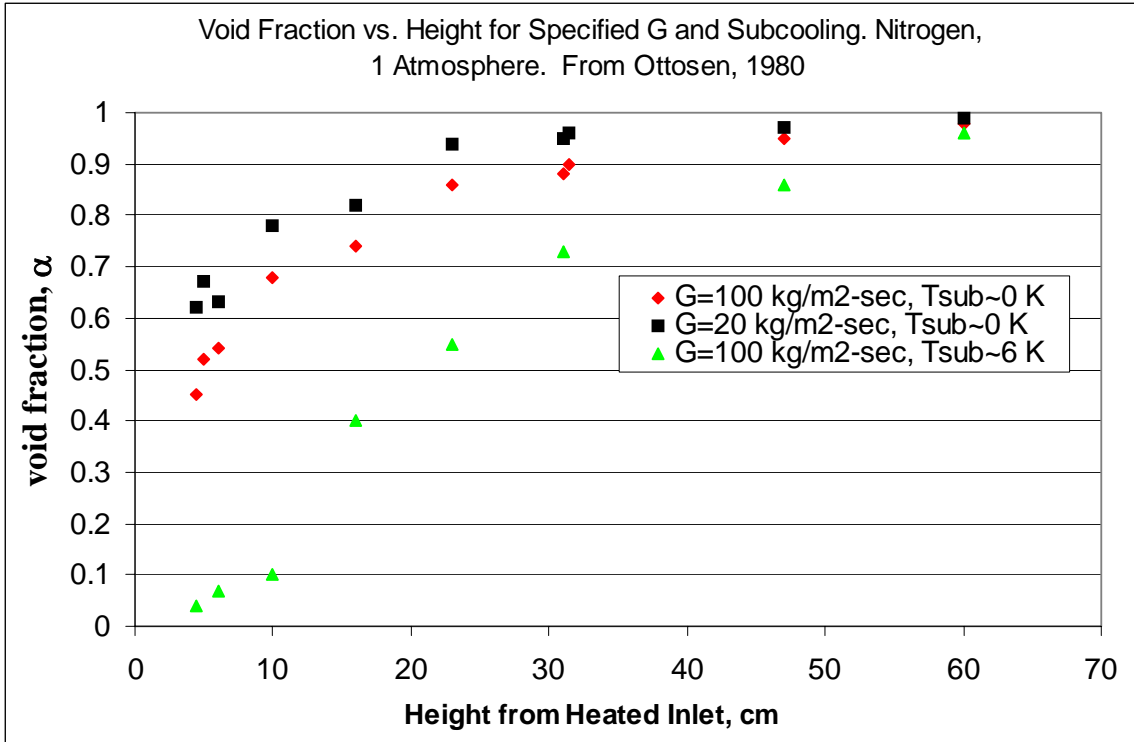


Figure 4-9. Void fraction vs. equilibrium quality for three runs of Ottosen's experiments. Mass flux and inlet subcooling specified.

CHAPTER 5
EVALUATION AND CORRELATION OF DATA AND CORRELATION ASSESSMENT

Data Correlation

Based on the void and slip profiles versus quality in figures 4-7 and 4-8, it is determined that the remaining runs on tube 4 (runs 23-25, and 27) and runs 32, 36, and 44 on tube five lie too far outside the main body of data and will therefore be excluded from the data correlation process. Thus, there remain 36 runs from which a correlation can be obtained. This gives 398 points, and 362 momentum and energy balances for the effort. The mass fluxes range from approximately $300 \text{ kg/m}^2\text{-sec}$ to $1600 \text{ kg/m}^2\text{-sec}$, the pressure range is from 180 kPa to the critical pressure, heat flux ranges from approximately 370 kW/m^2 to 2100 kW/m^2 , with four different tube diameters, and two different tube lengths.

Three different approaches were attempted to correlate the pressure drop data. First was the attempt to correlate the resulting void fraction profiles. As figure 4-7 shows, the 36 runs kept for analyses had a relatively tight grouping of void fractions.

The fact that the void fraction profiles for all 36 runs grouped together rather tightly presents a difficulty in trying to correlate the data. No good parameter for discriminating between two different runs with similar void profiles yet with significantly different operating conditions was found. While some success was achieved with a correlating parameter composed of heat flux, mass flux, and density ratios, the results were much less than desirable. Therefore, the attempt to directly correlate the void fraction data as a function of known parameters was abandoned.

Next, the theory of the drift flux model was applied. In this theory, void fraction is modeled as

$$\alpha = \frac{\beta}{C_0 + u_{gj}/j} \quad (5.1)$$

The volumetric quality, β , and superficial velocity, j , are known functions of mass flux, quality, and liquid and vapor densities. This leaves the distribution parameter, C_0 , and vapor drift velocity, u_{gj} , to be determined for void fraction to be predicted.

Of the correlations reviewed, C_0 is typically between 1.0 and 1.3 for most flow conditions. As Zuber and Findlay (1965) pointed out, C_0 can be below 1.0 when the void fraction is higher near the wall than near the centerline – an uncommon condition in most pre-critical heat flux flow regimes. However, this is the fundamental nature of IFB.

While correlations exist for C_0 and u_{gj} , most of them are based upon a relatively well-mixed flow of liquid and vapor. The vapor is concentrated near the center of the pipe. As such, these correlations typically capture the physics of buoyancy effects. Ishii (1977) presented many correlations related to drift flux theory, none of which pertain to IFB. The literature search did not reveal any formulation or correlation that predicts the drift flux terms for separated, high velocity vertical flow with vapor along the wall. Klausner et al. (1990) recommended a value of 0.98 for C_0 and 1.12 m/sec for u_{gj} in pre-CHF annular vertical upflow. These values were used in the analysis of Fu and Klausner (1997) that resulted in good predictions of pressure drop and heat transfer in this flow regime. These values were also applied to the NASA data. Results show that the predicted slip for all points lay between 0.34 and 1.16, with negative slopes for all runs. While these slip predictions are better for some runs relative to the slip correlation of this dissertation, most slips are better predicted by this dissertation's model.

The standard method of correlating the distribution parameter and the vapor superficial velocity was used. The ratio of vapor superficial velocity to void fraction was plotted against the

mixture superficial velocity. Figure 5-1 presents these curves. A family of relatively linear curves resulted, the slopes and y-intercepts of which give C_0 and u_{gj} . The slopes vary around unity, giving distribution parameter values for most points between 0.6 and 1.2. The vapor drift velocity was observed to vary a significant amount from run to run, and not in an obvious trend. It was concluded that there may be a better way to correlate these data than to develop separate correlations for both the vapor superficial velocity and the distribution parameter.

The third approach to correlating the data attempted to predict the velocity slip ratio, defined as

$$s = \frac{u_v}{u_l} \quad (5.2)$$

Fortunately, this variable varied within an adequate range for the 36 runs, as shown below in figure 5-2. Not only does the level of slip vary to a reasonable degree, but so too did the variation as a function of quality.

A literature search for slip and void fraction correlations has revealed numerous published models. A variety of these were applied to these NASA data. The model by Klausner et al. (1990), was implemented, in which for upflow, C_0 is recommended to be 0.98 and U_{gj} is 1.12 m/s.

Table 5-1 presents the accuracies of these correlations at predicting the slip. It is observed that none of these models predict the slip very well. Unfortunately, no slip correlation specifically developed for IFB was found. The Thom correlation (1964) performed the best, with an 81% prediction accuracy to with 50% of this model's slip. His model is based on work with boiling water.

As a result of the inability of the published correlations to model these data, it was decided to develop a slip correlation. Several different approaches were made to develop a correlating

parameter for slip. First, a mechanistic relation of the vapor and liquid velocities was pursued by applying law-of-the-wall concepts. The goal of this approach was to develop a relation for the velocity ratio that allowed the interfacial conditions to cancel out. Using some rather weak assumptions, a transcendental relation for film thickness and flow conditions was derived. It was found that the interfacial velocity would not cancel out in a velocity ratio since it is an additive term to the interfacial vapor velocity.

As a result of this finding, the search for a correlating parameter shifted to trying various combinations of parameters representing test conditions, and various exponents on these parameters. As previously stated, it was observed that the slip very near a quality of zero and the slope of the slip as a function of quality varied. These observations led to attempting to develop a correlation that predicted the initial slip (near zero quality) and the slope of the slip as a function of quality. Each component was modeled as a linear function of a correlating parameter.

To pursue this approach, the slip profiles for the 36 runs were modeled as linear functions of quality. From this, 36 slip slopes and slip y-intercepts were generated. In turn, the 36 values of each of these two variables were modeled as functions of the correlating parameter, henceforth called the slip factor, f . Ostensibly, a different slip factor could be generated for the 36 y-intercepts and the 36 slopes, each used in a linear model to predict the initial slip and the slip slope.

Due to the no-slip condition at the wall, the inception of vapor generation should correspond to a slip of zero. The zero velocity liquid next to the wall is the first liquid to be vaporized, and this vapor will have zero velocity. This fact is not evident in figure 5-2. It appears that the various slips will extrapolate to finite values at a quality of zero. Probably the

source for this discrepancy lies in the form of the wall friction model used in the pressure drop calculation. Equations 3-15 and 3-29 show that the Blasius equation is used, which is based on law-of-the-wall theory, but is intended for use on a large scale, not for use when the bulk of the vapor would be better modeled by near-wall physics. In addition, the validity of law-of-the-wall theory probably deteriorates when the film thickness is extremely thin. The liquid-vapor interface acts as a second wall to alter the physics from that which is modeled by the Blasius equation.

Regardless, the value of the slip can be extrapolated from the straight line representing each slip curve to a quality of zero, and this family of 36 slips can be correlated. The effect on gross calculations such as pressure drop are minimal, since the void fraction is truly small very near the inlet, whether the slip be modeled is zero at a quality of zero or if it is finite. As void accumulates, the Blasius equation becomes more accurate, so the error in modeling the physics is reduced. The detrimental effect on determining the nature of pressure drop is self-mitigating.

A routine of nested Fortran “do loops” was constructed to optimize the specific dimensionless ratios and their respective exponents that make up the slip factors. A typical trial slip factor might look like the following:

$$f = \left(\frac{\mu_l}{\mu_v} \right)^a \left(\frac{P_{in}}{P_{crit}} \right)^b \left(\frac{G}{G_0} \right)^c \left(\frac{q''}{q_0''} \right)^d \left(\frac{L}{D} \right)^e \quad (5.3)$$

The nested do loops iterated through each exponent, over the range from -2.0 to $+2.0$, in 0.2 increments so that 20 different values of each exponent were tried. Therefore, five nested do loops would generate 20^5 or 3.2 million correlating parameters, each to be statistically compared with the 36 y-intercept values and the 36 slope values.

In the initial application of this method, it was found that the aspect ratio term, L/D , tended towards a very large exponent to optimize the correlation. It was determined that the optimizing

algorithm tended towards this large aspect ratio exponent – easily approaching 5 if allowed – in an attempt to accommodate the variation in slip between the 1961 data and the 1966 data, in which the lengths are 0.305m and 0.61m, respectively. This variation in slip could be a result of experimental differences. In addition, the variation in tube length in the database does not warrant including a tube length effect. Therefore, it was determined to generate separate slip correlations for the 1961 and 1966 data sets.

Low Pressure Slip Correlation

Within this framework, it was observed that the 1961 data could still be well modeled by the original slip y-intercept and slip slope method previously discussed. However, this method did not work well for the 1966 data. The correlation coefficients were too low to support this approach. Instead, it was determined that the 1966 data slip profiles could be better modeled as a constant along the length of the tube for each run, but varying for each run. This approach is similar to the work of Rigot (1973), in which he used an average slip value of 2 for his application.

Taking the 1961 data, for each combination that made up the trial slip factor, a linear least squares analysis was performed on both the y-intercept fit and the slope fit, with the correlation coefficients (R^2) returned for each fit to determine the goodness. Thus, to optimize the fits of the y-intercepts and the slopes, there will be two slip factors, each one with two coefficients used in a linear slip formula. The y-intercepts and slopes will look like the following equations:

$$\text{slip intercept} = m_{int}(f_{int}) + b_{int} \quad (5.4)$$

$$\text{slip slope} = m_{slope}(f_{slope}) + b_{slope} \quad (5.5)$$

Where, for the slip y-intercept, m_{int} and b_{int} are the slope and y-intercept, and for the slip slope, m_{slope} and b_{slope} are the slope and y-intercept. f_{int} and f_{slope} are the slip y-intercept and slip slope factors, hence forth called the intercept slip factor and the slope slip factor.

The following ratios were tried: liquid to vapor viscosity, liquid to vapor density, mass flux to an average mass flux G_0 (1000 kg/m²-sec), heat flux to an average heat flux q_0'' (1000 kW/m²), reduced inlet pressure (to the critical pressure). Note that for the high system pressure correlation analysis, an aspect ratio of tube length to tube diameter was included.

It was found that non-linear effects were involved. That is, the optimum exponent on one ratio is affected by the presence or absence of another ratio, and their associated exponents. Also, it was found that the sensitivity of the goodness of fit varied for different ratios. From this analysis, it was determined that the viscosity and mass flux ratios were not important. Therefore, they were eliminated from subsequent analyses.

It was also found that the intercept slip factor and slope slip factor were optimized using the same grouping of terms with very nearly the same exponents. The best exponent for the heat flux ratio differed slightly for the intercept and slope slip factors. Thus, with only a small degradation in accuracy, a single slip factor, f_1 , can be defined that predicts the slip y-intercept and slope.

The equations for the y-intercept and slope were determined to be

$$\text{slip intercept} = -5.20 + 1.12f_1 \quad (5.6)$$

$$\text{slip slope} = (103 - 14.9f_1)x \quad (5.7)$$

where x is the mass quality, and the slip factor is defined by

$$f_1 = 4.0E3 \left(\frac{P_{in}}{P_{crit}} \right)^{-1.8} \left(\frac{q''}{q_0''} \right)^{1.2} \left(\frac{\rho_l}{\rho_v} \right)^{-1.8} \quad (5.8)$$

The correlation coefficients are 0.82 and 0.71 for the slope and y-intercept, respectively. These equations can easily be combined to produce the correlating equation for slip:

$$s = (103 - 14.9f_1)x - 5.20 + 1.12f_1 \quad (5.9)$$

The test section inlet pressure range over which this correlation applies is up to 500 kPa. Note that the slip factor is not a function of local conditions, and is calculated at the inception of IFB. This is because the slip throughout a run is modeled as a linear function of quality. The slope and y-intercept of the slip are determined at the tube inlet.

Low Pressure Slip Correlation Assessment

The first observation to be made about the low pressure correlating parameter, f_1 , is that it has the opposite effect on the initial slip as it does on the slip slope. Increasing f_1 increases the initial slip, but causes the negative slope of the slip to increase. This must be interpreted in terms of the friction term that is used throughout the flow. The Blasius equation is intended to model $1/7^{\text{th}}$ power law profiles, which implies that it is to be used for flows in which the near-wall friction effects are only a small component of the overall flow. However, at extremely low qualities near the inlet, the velocity profile is dominated or significantly influenced by near-wall and buffer region physics. Vapor velocity increases with distance from the wall at a much lower rate than the $1/7^{\text{th}}$ power law profile. Therefore, slip is overestimated. The slip is artificially high due to the fact that friction is underestimated. As the Blasius model becomes a more accurate representation of the vapor flow physics, the slip will become more accurate. This will happen when the void fraction increases, thus increasing the vapor film thickness. Since slip is initially too high, it will tend to be reduced farther up the tube. The higher that the initial slip is calculated to be, the more will be the decrease at higher elevations. Thus, the magnitude of the negative slope increases as the initial slip value increases.

The low pressure correlating parameter also shows that the initial slip decreases as system pressure increases, increases as applied heat flux increases, and decreases as the liquid to vapor density ratio increases. The pressure and density effects seem to be contradictory. Higher system pressures correspond to a lower liquid to vapor density ratio, which normally corresponds

to lower slip, which is in direct contradiction to the density ratio effect in the slip factor. However, these dependencies must be interpreted in light of the set of parameters included in the optimizing algorithm. Vapor superheat was not explicitly included in the slip factor optimization algorithm. Therefore, if local vapor superheat is truly an influence, then its effect will be accounted for through another parameter that correlates with superheat, such as the density ratio. Therefore, the density ratio is likely a surrogate parameter for the effect of superheat on parameters such as vapor viscosity. Isolating the effect of the density ratio, an increase in this parameter is caused by a decrease in vapor density, which in turn is caused by higher vapor temperatures. This also will lead to higher vapor viscosity, and thus, higher friction and lower vapor velocity. Over a short distance, the liquid velocity does not have time to change, so a reduction in vapor velocity will lead to a reduction in slip. The range of viscosity variation is a factor of roughly 3.5 in these data, which is fairly significant, as a result of the variation in vapor superheat.

The pressure parameter is interpreted to account for the density effect. As described above, higher system pressures decrease the liquid to vapor density ratio. The acceleration each phase experiences is directly a function of their densities and pressure gradient. Since both phases are subject to the same pressure gradient, the variation in density ratio will control the variation in slip. Thus, higher system pressures should decrease slip. This is consistent with the trend in the slip correlation factor.

The initial slip increases with heat flux. The pressure gradient also increases consistently with heat flux. As pressure gradient increases, the effect on slip near the inlet will be to increase it, as described above. The significantly lighter vapor will be accelerated much more than the

denser liquid. Thus, slip will increase. Therefore, the heat flux parameter is interpreted as a surrogate for the pressure gradient.

High Pressure Slip Correlation

The high system pressure correlation is simpler since the slip is being modeled as a constant. The slip is correlated with an R^2 value of 0.72 with the following equation:

$$s = 2.88f_2 - 1.37 \quad (5.10)$$

In this, the correlating parameter f_2 is modeled as

$$f_2 = \left(\frac{\rho_l}{\rho_v}\right)^{0.3} \left(\frac{\mu_l}{\mu_v}\right)^{0.8} \left(\frac{L}{D}\right)^{-0.4} \quad (5.11)$$

The tube inlet pressure range over which this correlation applies is from 500 kPa to the critical pressure (1284 kPa). Note that there is still an aspect ratio effect, but that the exponent is optimized at a much lower value than if the 1961 and 1966 data were combined. This dependence reflects the influence of the three different tube diameters on the data.

High Pressure Slip Correlation Assessment

Equation 5-11 shows that the high pressure slip increases with increasing liquid to vapor density ratio, increasing liquid to vapor viscosity ratio, and decreasing aspect ratio L/D .

The density ratio effect here is interpreted the same way as the pressure ratio effect in the low pressure slip factor. The acceleration each phase experiences is directly a function of their densities and pressure gradient. Since both phases are subject to the same pressure gradient, the variation in density ratio will control the variation in slip. Thus, increasing the liquid to vapor density ratio will increase slip.

The liquid to vapor viscosity ratio probably is at least partially a surrogate for the effects of vapor superheat, just as the density ratio was for the low pressure data. The viscosity ratio shows that, as vapor viscosity decreases, the slip will increase – a physically reasonable effect.

Finally, the effect of the aspect ratio L/D shows that slip increases as this ratio decreases. This can be interpreted in terms of the difference between the absolute film thickness relative to the void fraction as tube diameter varies. Comparing a small and large diameter tube, the film thickness will be larger for the large diameter tube than for the small diameter tube for the same void fraction. Thus, the average velocity of the vapor with the larger film thickness will be higher.

Accuracy of the Slip Correlations

The accuracy of these two correlations at reproducing the model slips are presented in tabular form in table 5-1, and graphically in figure 5-2. Both the table and figure show that excellent agreement is achieved. Figure 5-2 also shows that the high pressure slips from the 1966 experiments (which extend to 55 cm.) are indeed relatively constant, and that the low pressure slips from the 1961 experiments are better modeled by including a slope effect as a function of quality.

The slip correlation can now be used in the model described in chapter 3 to directly solve for the pressure drop. Instead of iteratively solving for the quality and void fraction pairs that best fit the data, the slip as a function of system parameters and local quality can be used to calculate the local slip and subsequently the void fraction. In this application as applied to a particular length segment, properties are a function of the segment inlet pressure and the average vapor temperature across the length segment.

The quality of the slip correlation is assessed by comparing predicted pressure drops with measured pressure drops. For the 1961 data there are 9 pressure drop increments per test that are unaffected by end effects, and 17 tests included for a total of 153 pressure drop increments. For the 1966 data there are 11 acceptable increments per test and 19 tests for a total of 228 increments. Thus, there are 362 pressure drop increments to compare. Accuracy is determined

here in terms of the percentage of incremental pressure drops that are predicted to within a specified percentage of experimental pressure drops. For comparison purposes, the accuracy of incremental pressure drops calculated from a homogeneous equilibrium model (HEM) that incorporates friction, acceleration, and elevation pressure drop components is included in table 5-2.

Figure 5-3 presents the accuracy of predicted versus measured pressure gradients. The dashed lines represent plus and minus 25% from the measured pressure gradient. All data used to generate the slip correlation are included in this plot. The majority of positive error points correspond to the extremely high pressure runs of 15, 16, and 18.

Figures 5-4 through 5-39 present model and prediction results for all 36 runs used in the correlation. These figures will be referred to as quad plots. In the lower left of each figure are the pressure profiles. The black dots are the measured pressure points, the solid red line is the predicted pressure profile using the slip correlations, and the dashed green line is the HEM pressure profile. In the upper left are the slip profiles. The black dots are the slips that result from the momentum and energy balance model, and the solid red line is the predicted slip. Of course, the HEM slip is unity for all runs, so it has been excluded. The top right plot presents the void fractions. Again, the black dots are from the balance model, and the solid red line is the void that results from the slip correlations. Finally, the bottom right presents the three pressure drop components from the balance model. The solid black line is acceleration pressure drop, long dashed red is from friction, and short dashed green is predicted elevation pressure drop.

The HEM pressure profiles frequently have a knee, in which the pressure profile slope is shallow, followed by a significantly steeper region. The knee is the point at which equilibrium quality changes from negative to positive. It can be seen in these runs that the measured pressure

profile does not show any inflection at these points. The predicted pressure profile reflects this characteristic, showing no impact from transitioning from negative to positive equilibrium quality.

Some of the lowest pressure runs show that the HEM predicts a pressure loss that would generate a negative pressure. That is, HEM is incapable of predicting pressure in these cases. These particular points are omitted from the HEM pressure profiles.

Validation of the Slip Correlations

Validation of these slip correlations is supported in several ways. First, the correlations can be applied to runs that were not included in the slip correlation process. The runs that lend themselves to this application are those that had acceptable momentum and energy balances, but that were deemed to have slip or void profiles too removed from the main body of data to keep. These runs are 23, 24, 25, 27, 32, 36, and 44, and their quad plots are presented in figures 5-40 through 5-46. It is evident that the high pressure correlation does not perform well at predicting the pressure drops of the very high mass flux runs 23, 24, 25, and 27. The HEM does significantly better. However, the low pressure correlation performs extremely well on the three runs 32, 36, and 44, which are among the highest mass flux runs of the 1961 data, though still significantly lower than the other four runs. These runs also are at the lower end of the heat flux range on tube five. Therefore, it appears that the high pressure correlation is limited in range of mass flux.

Validation of the high pressure correlation is evident in the failure to reproduce the pressure profile of run eight, given in figure 5-47. This is considered a validating result because of the difficulty run eight gives the HEM at reproducing the measured pressure, and that the predicted pressure and HEM pressure are so similar to each other while departing significantly from the measured pressure profile. Run eight is suspected to have some inconsistency in its

data that causes this difficulty. It is noteworthy that run eight has stood out as drastically different than all other runs during all variations of data modeling.

The ranges of validity of the two correlations should be listed separately. The low pressure correlation is valid from pipe inlet conditions of 180 kPa to 500 kPa, mass fluxes from approximately 580 kg/m²-s to 1650 kg/m²-s, and heat fluxes from approximately 380 kW/m² to 1650 kW/m². The high pressure correlation is valid from pipe inlet conditions of 600 kPa to the critical pressure, mass fluxes from approximately 330 kg/m²-s to 1550 kg/m²-s, and heat fluxes from approximately 700 kW/m² to 2100 kW/m². Note that since the low pressure correlation appeared to perform slightly better than the high pressure correlation, it is recommended to extrapolate the low pressure correlation range from the experimental maximum of 500 kPa up to 600 kPa.

Observations

The high pressure slip correlation can predict the pressure profile with good accuracy even for length segments for which the energy balance was not well satisfied. These are seen in the figures as points in which slip and void change value while the quality remains constant. The high pressure correlation does not appear to work well for all extremely high pressure runs. The highest pressure runs, 15, 16, and 18, are not well reproduced, particularly in the upper half of the tube. However, other high pressure runs, such as 4, 5, and 7, are reasonably well modeled.

The low pressure correlation performs very well, in general. Runs that are less well predicted tend to be those that have a low mass flux to heat flux ratio. However, the three runs that were excluded from the correlation optimization process are quite well reproduced.

The plots of the three different pressure drop components show that acceleration pressure drop is always the main contributor. Friction varies between several percent to up to 50% of the total pressure loss, and elevation pressure drop is insignificant. Since flow velocities are so high,

it might be expected that friction would be a larger contributor to the total pressure loss. Also, the HEM frictional component is consistently significantly higher than this model predicts. This is interpreted to represent the nature of relatively low friction that vapor generates. The combination of low hydrogen vapor viscosity, which in general is about an order of magnitude lower than the liquid viscosity, and the low vapor density combine to cause the vapor friction to be relatively low. In essence, the liquid is riding through the tube on a vapor blanket, thus reducing friction.

The slip correlations and this momentum and energy balance model provide a method in which pressure drop can be accurately predicted regardless of the subcooled nature of the flow. The knees observed in the HEM greatly limit its usefulness in the subcooled region. The assumption of no significant liquid heating (all heated liquid is vaporized), and initializing quality at zero at the inlet appear to be reasonable approximations.

Table 5-1. Accuracies of some common slip correlations.

Slip Model Source	Accuracy to within					Model
	10%	20%	30%	40%	50%	
Pasch	47%	78%	91%	95%	98%	
CISE (Premoli, 1970)	6%	16%	31%	44%	57%	$s = 1 + e1 \sqrt{\frac{y}{1 + ye2}} - ye2$ $e1 = 1.578 \left(\frac{GD}{\mu_l} \right)^{-0.19} \left(\frac{\rho_l}{\rho_v} \right)^{0.22}$ $e2 = 0.0273 \left(\frac{G^2 D}{\sigma \rho_l} \right) \left(\frac{GD}{\mu_l} \right)^{-0.51} \left(\frac{\rho_l}{\rho_v} \right)^{0.08}$ $y = \left(\frac{\rho_l}{\rho_v} \right) \left(\frac{x}{1-x} \right)$
Smith (1969)	12%	25%	34%	43%	51%	$s = e + (1 - e) \sqrt{\frac{\rho_l + e \left(\frac{1-x}{x} \right)}{1 + e \left(\frac{1-x}{x} \right)}}$ $e = 0.4$
Bankoff (1960)	7%	12%	17%	23%	28%	$\alpha = \frac{0.7}{1 + \left(\frac{\rho_v}{\rho_l} \right) \left(\frac{1-x}{x} \right)}$
Chisholm (1983)	12%	23%	34%	43%	52%	$s = \sqrt{1 - x \left(1 - \frac{\rho_l}{\rho_v} \right)}$
Zivi (1964)	1%	3%	6%	8%	12%	$s = \left(\frac{\rho_l}{\rho_v} \right)^{1/3}$
Klausner (1990)	4%	15%	27%	39%	52%	$\alpha = \left[C_0 \left(1 + \left(\frac{1-x}{x} \right) \left(\frac{\rho_v}{\rho_l} \right) \right) + u_{gj} \frac{\rho_v}{Gx} \right]^{-1}$ $C_0 = 0.98$ $u_{gj} = 1.12$
Ahrens (1983)	8%	26%	36%	54%	65%	$s = \left(\frac{\mu_l}{\mu_v} \right)^{0.2}$
Wallis (1969)	1%	2%	2%	4%	4%	$\alpha = \left[1 + \left(\frac{1-x}{x} \right)^{0.72} \left(\frac{\rho_v}{\rho_l} \right)^{0.40} \left(\frac{\mu_l}{\mu_v} \right)^{0.08} \right]^{-1}$
Lockhart & Martinelli (1949)	16%	31%	43%	57%	67%	$\alpha = \left[1 + 0.28 \left(\frac{1-x}{x} \right)^{0.64} \left(\frac{\rho_v}{\rho_l} \right)^{0.36} \left(\frac{\mu_l}{\mu_v} \right)^{0.07} \right]^{-1}$
Zuber & Findlay (1965)	12%	23%	33%	44%	51%	$C_0 = 1.2$ $u_{gj} = 1.53 \left(\frac{g \sigma (\rho_l - \rho_v)}{\rho_l^2} \right)^{0.25}$
Coddington (2002)	16%	26%	36%	51%	64%	$C_0 = 2.57E - 3P + 1.0062$ $u_{gj} = (6.72E - 7P^2 - 8.81E - 5P + 1.05E - 3)G + 5.63E - 3P^2 - 0.123P + 0.8$
Thom (1964)	16%	30%	57%	71%	81%	$\alpha = \left[1 + \left(\frac{1-x}{x} \right)^{1.0} \left(\frac{\rho_v}{\rho_l} \right)^{0.89} \left(\frac{\mu_l}{\mu_v} \right)^{0.18} \right]^{-1}$
Baroczy (1965)	12%	25%	37%	46%	55%	$\alpha = \left[1 + \left(\frac{1-x}{x} \right)^{0.74} \left(\frac{\rho_v}{\rho_l} \right)^{0.65} \left(\frac{\mu_l}{\mu_v} \right)^{0.13} \right]^{-1}$

Table 5-2. Comparison of pressure drop prediction accuracy for the homogeneous equilibrium model and the current slip correlation.

Model	Accuracy to within				
	10%	20%	30%	40%	50%
HEM	12%	27%	37%	46%	56%
slip correlation	42%	66%	81%	85%	89%

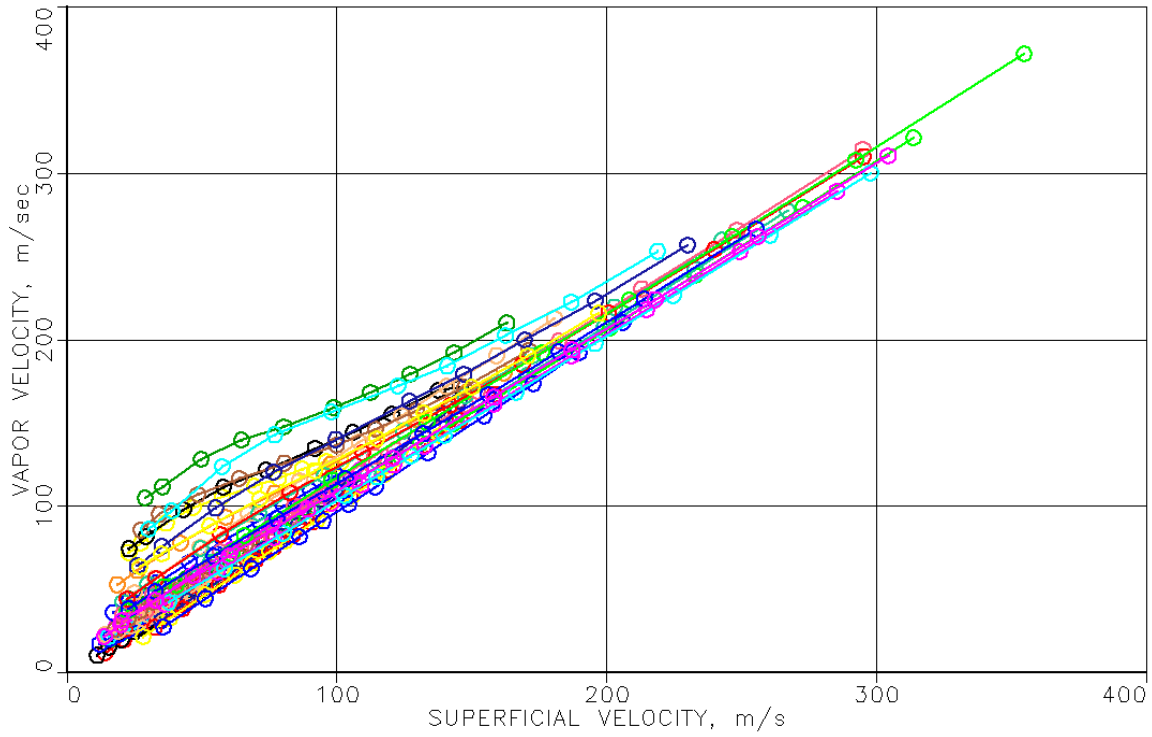


Figure 5-1. Vapor velocity vs. superficial velocity.

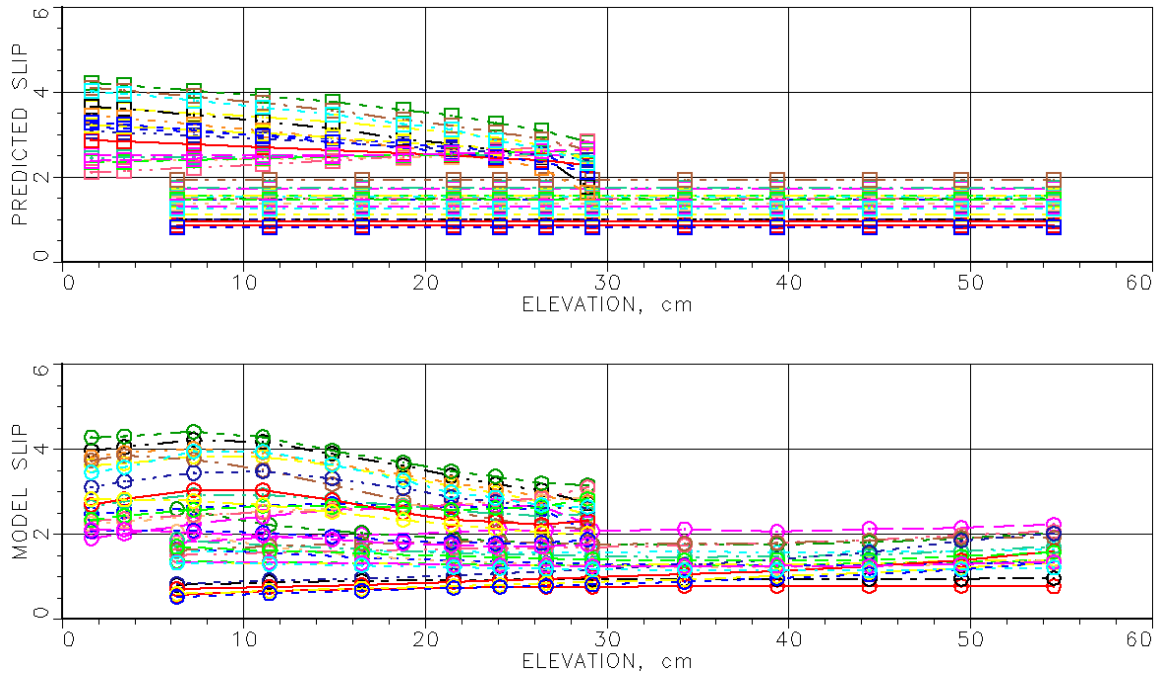


Figure 5-2. Comparison of model slip and slip predicted from correlations.

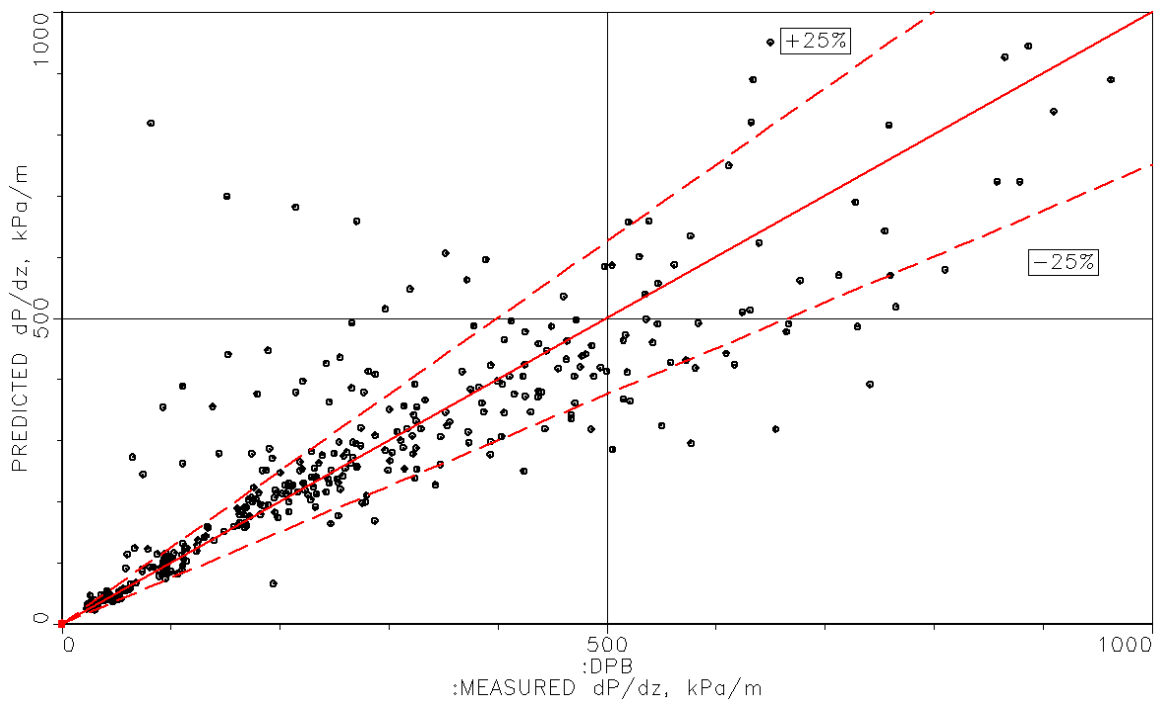


Figure 5-3. Predicted versus measured pressure gradients for all data used in correlating slip.

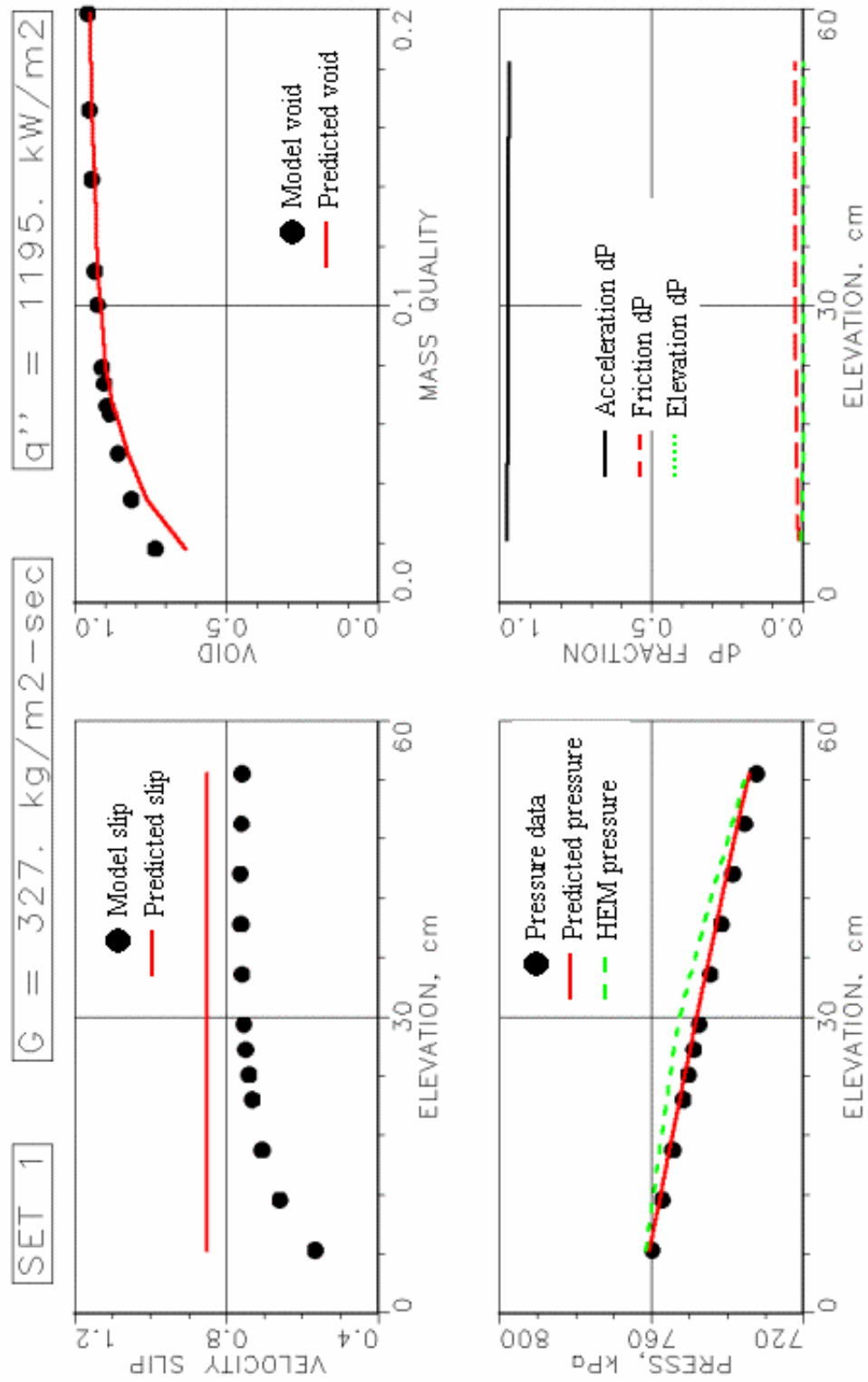


Figure 5-4. Model and prediction results for run 1.

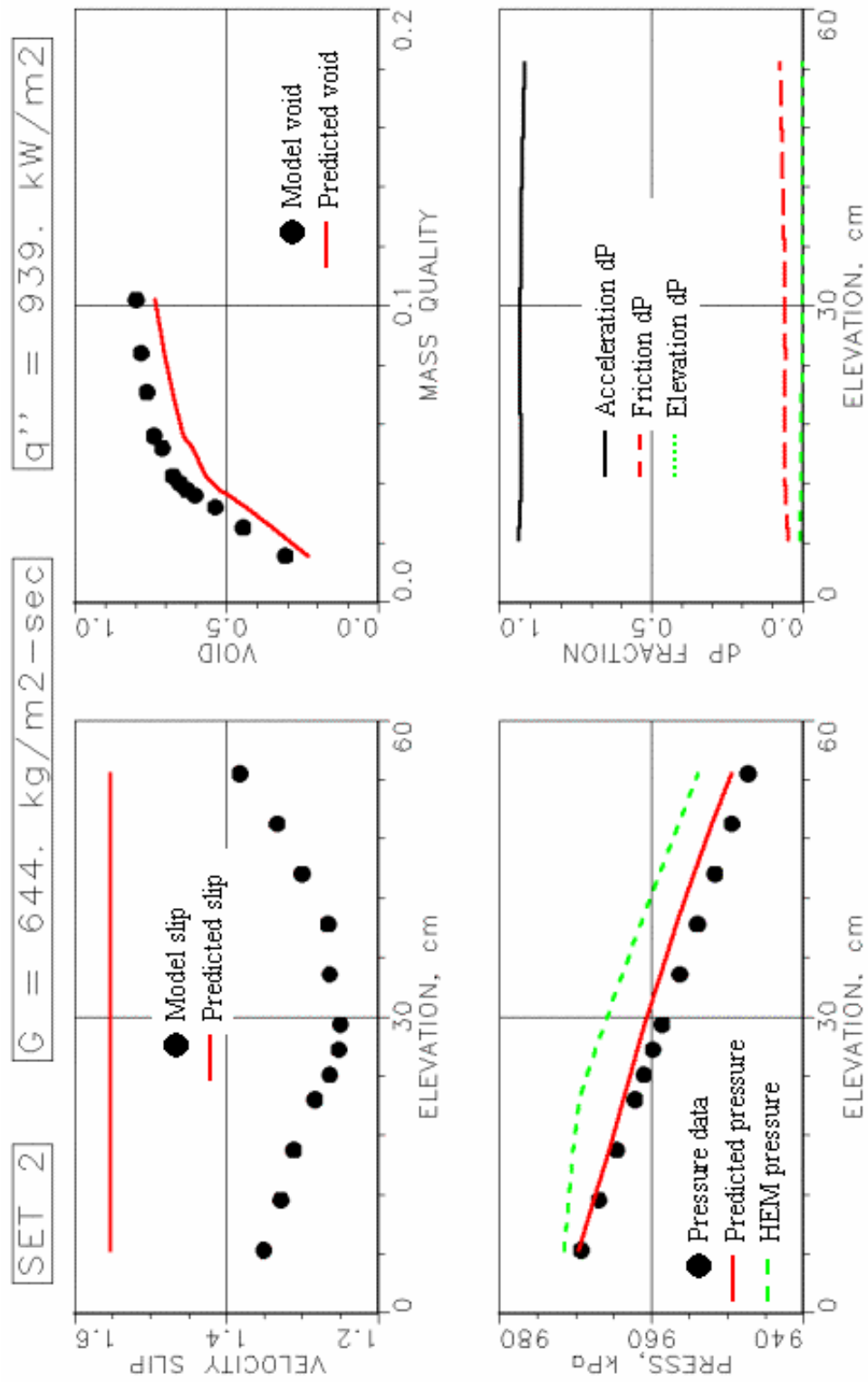


Figure 5-5. Model and prediction results for run 2.

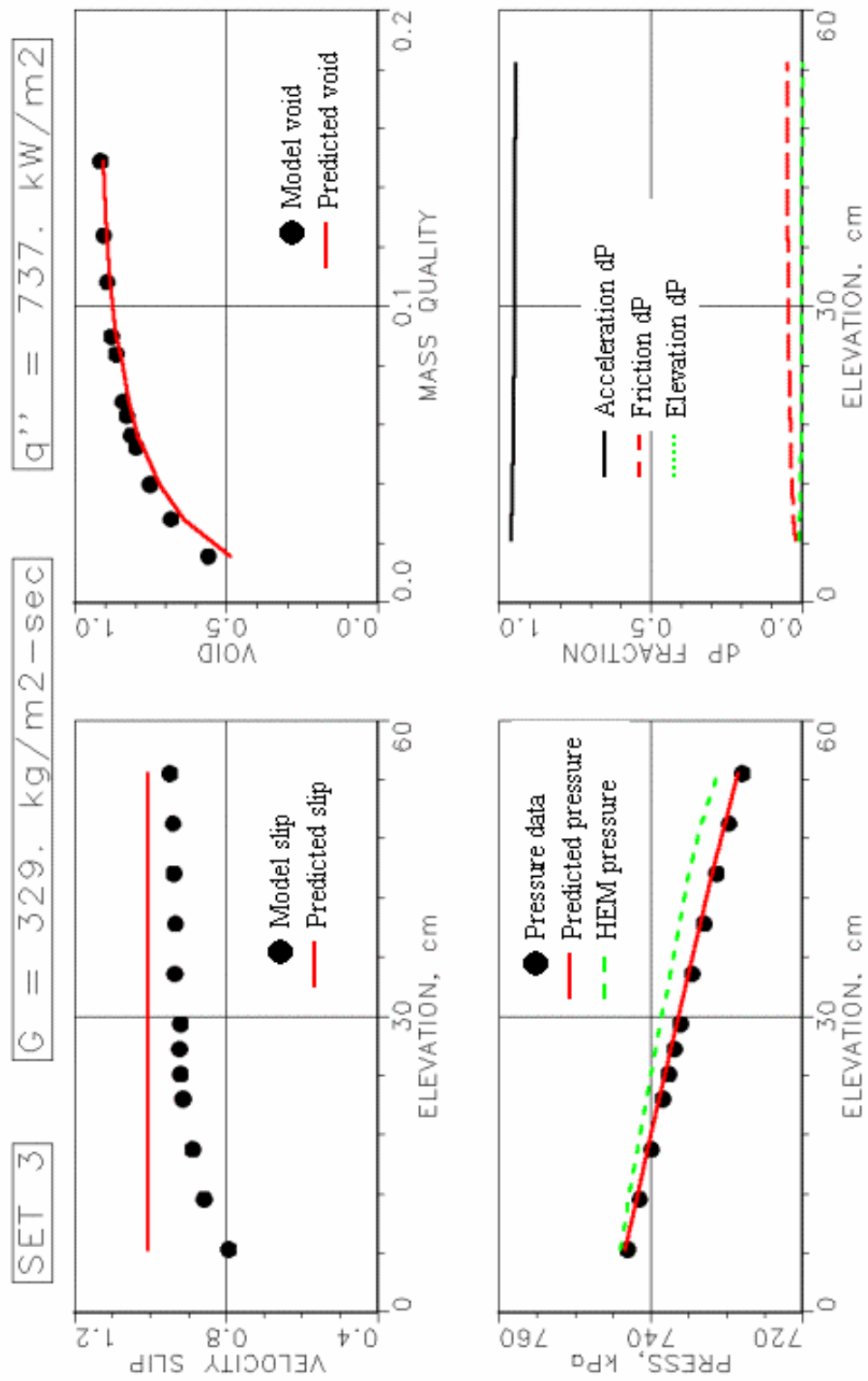


Figure 5-6. Model and prediction results for run 3.

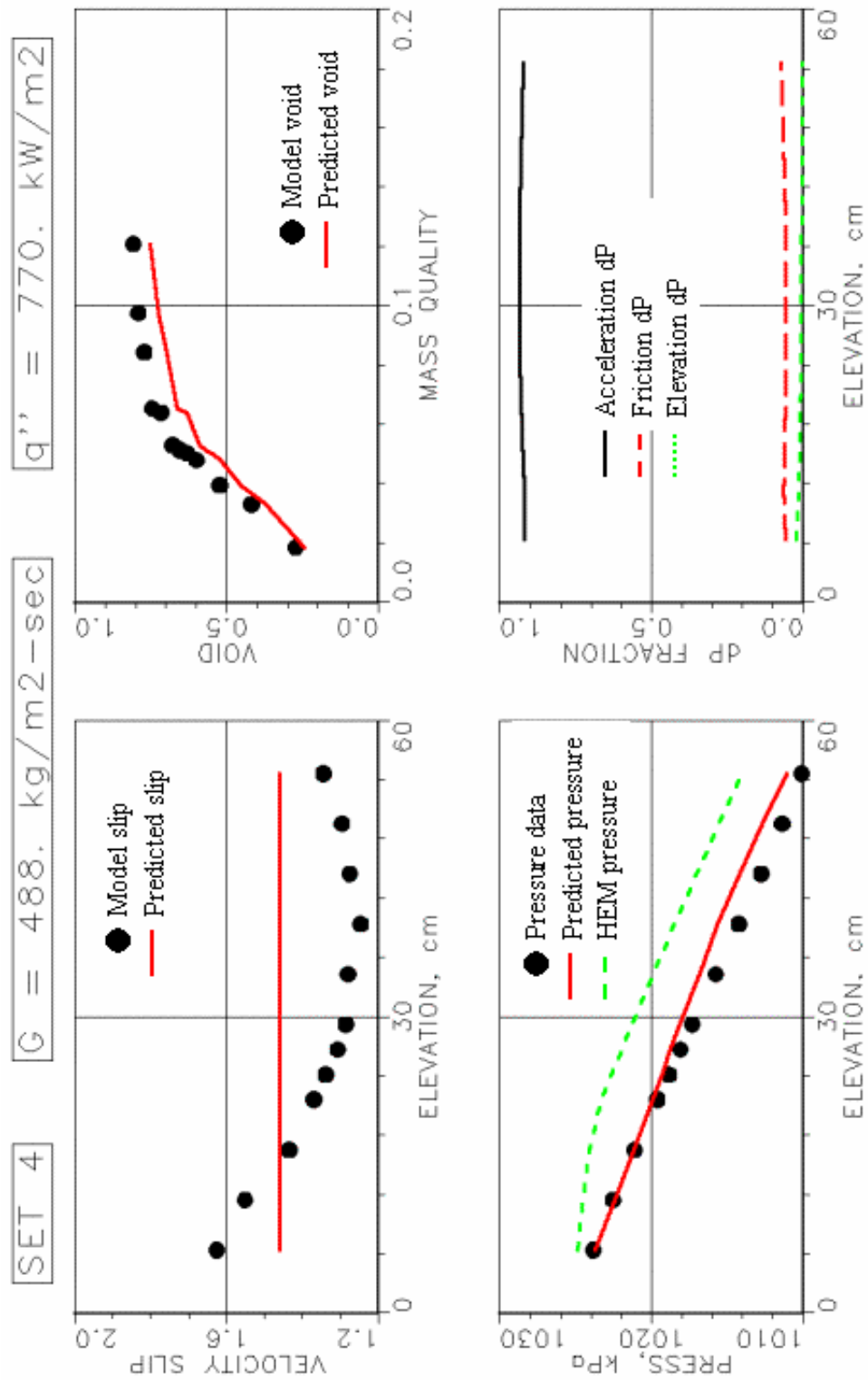


Figure 5-7. Model and prediction results for run 4.

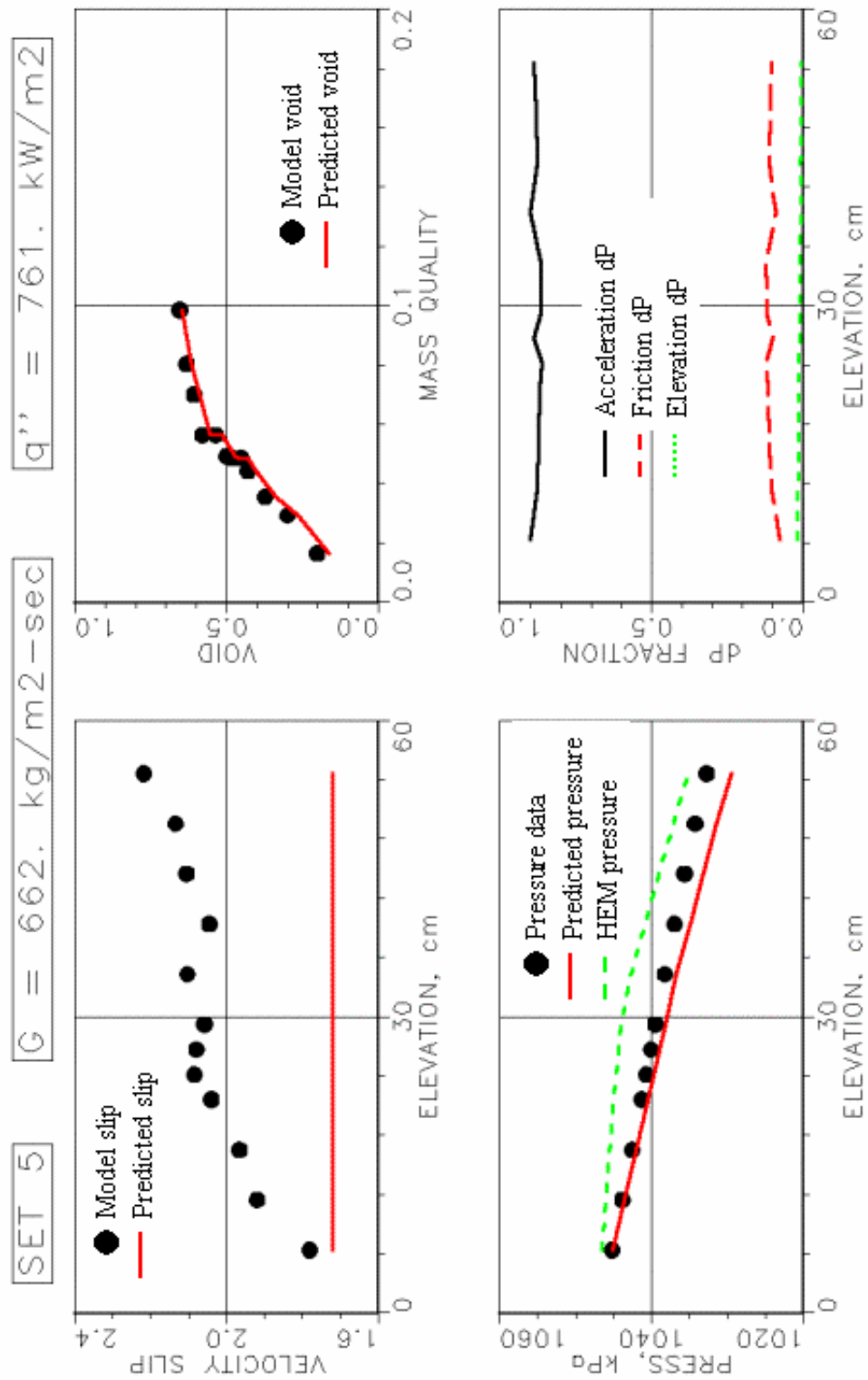


Figure 5-8. Model and prediction results for run 5.

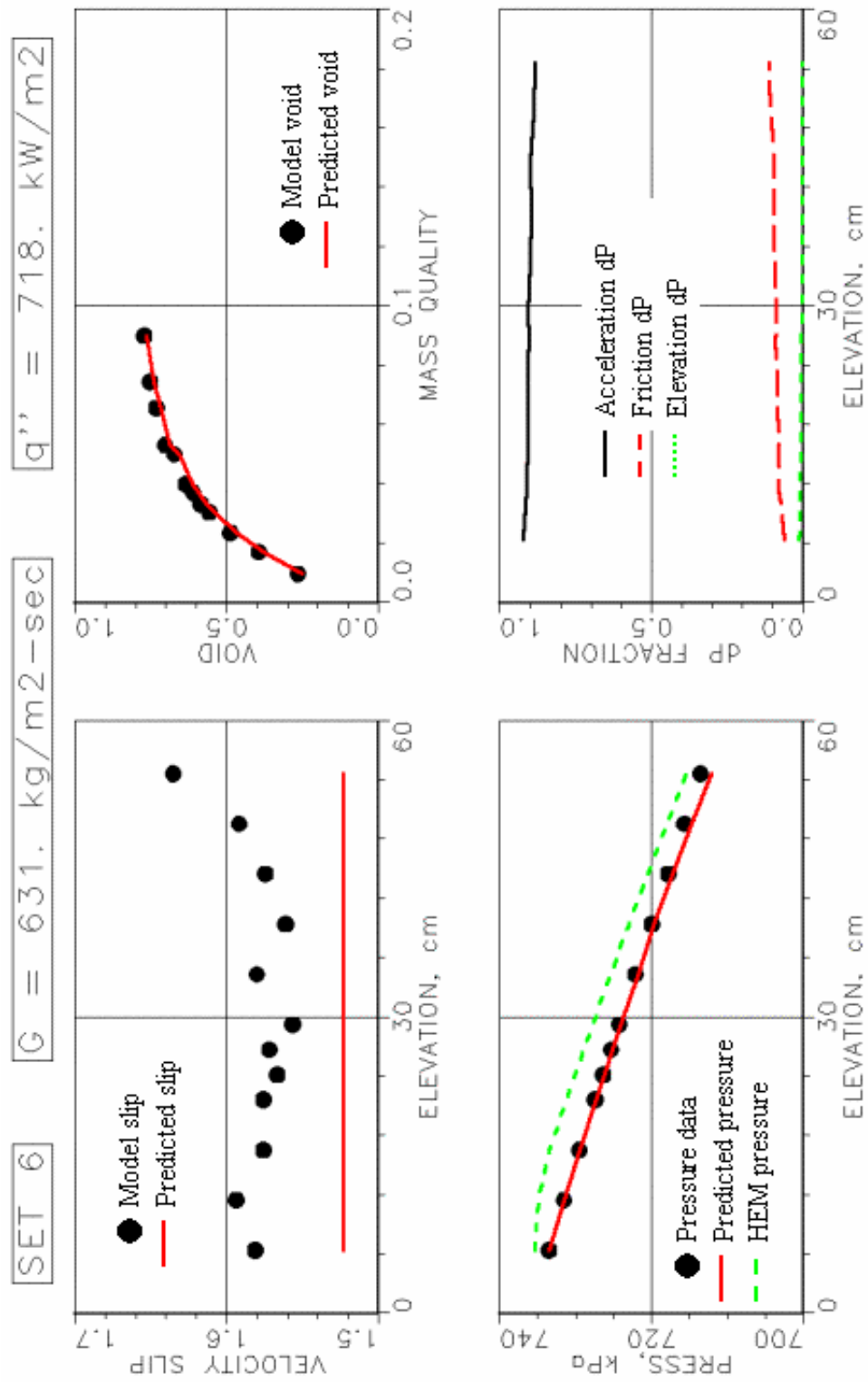


Figure 5-9. Model and prediction results for run 6.

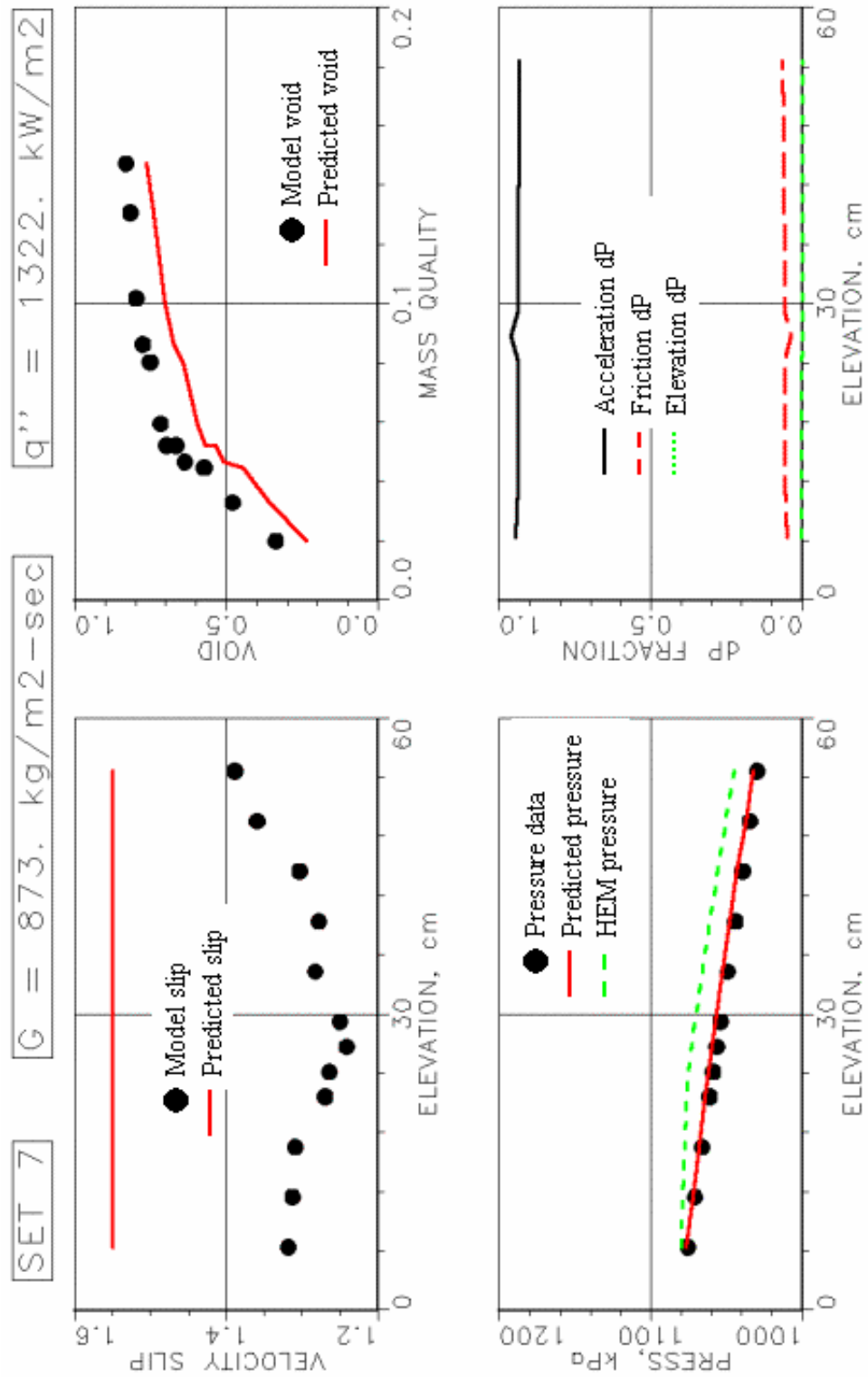


Figure 5-10. Model and prediction results for run 7.

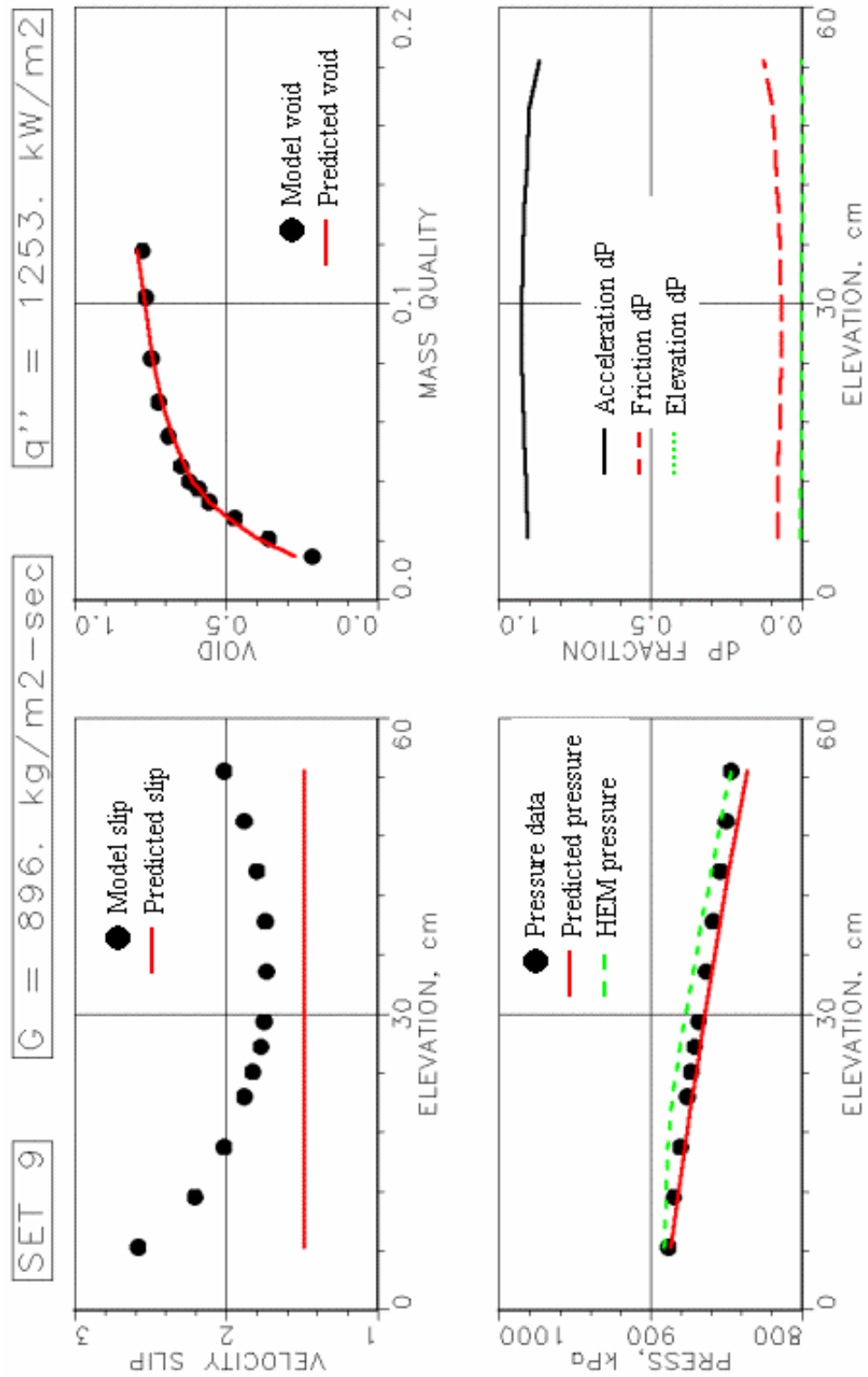


Figure 5-11. Model and prediction results for run 9.

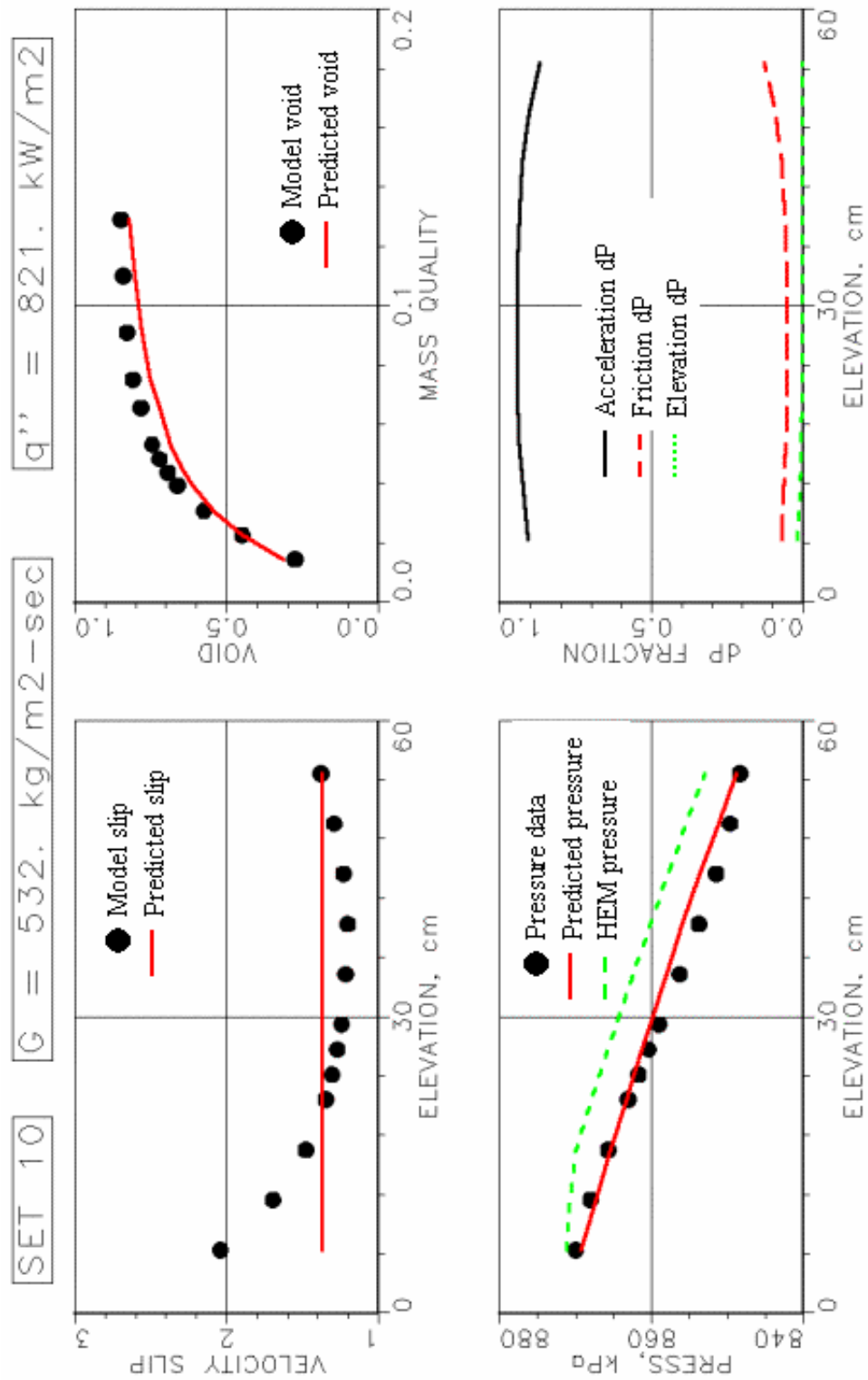


Figure 5-12. Model and prediction results for run 10.

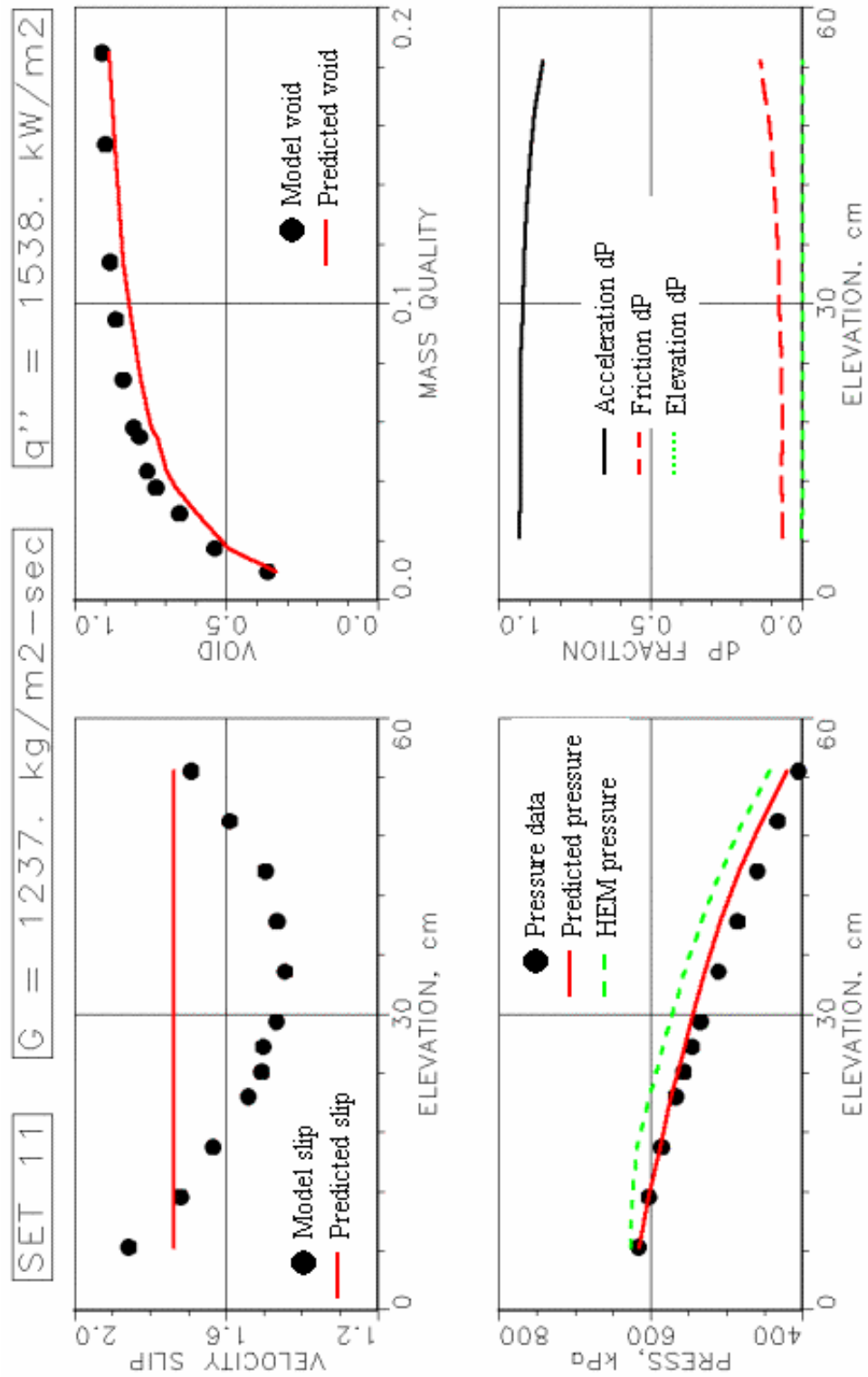


Figure 5-13. Model and prediction results for run 11.

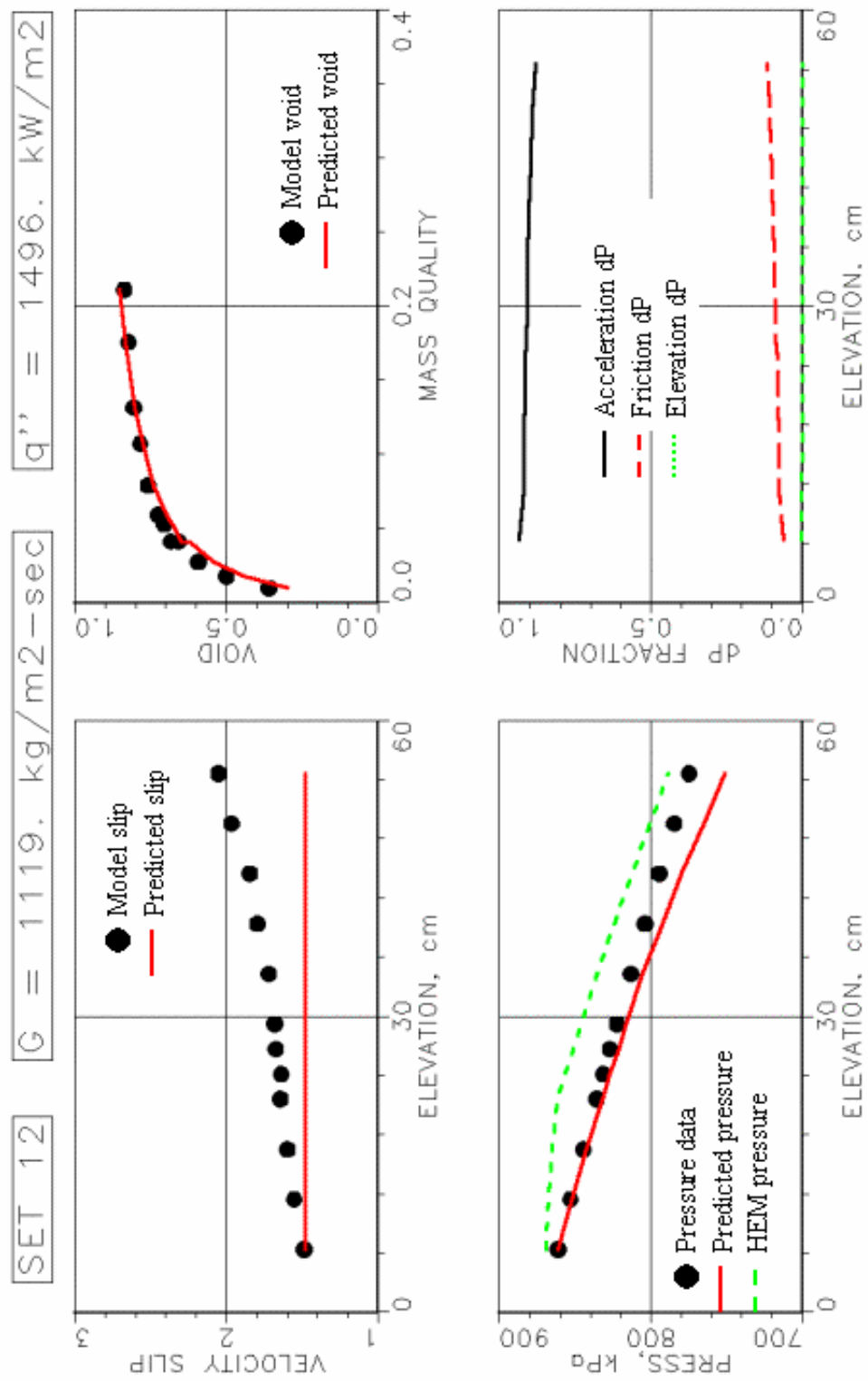


Figure 5-14. Model and prediction results for run 12.

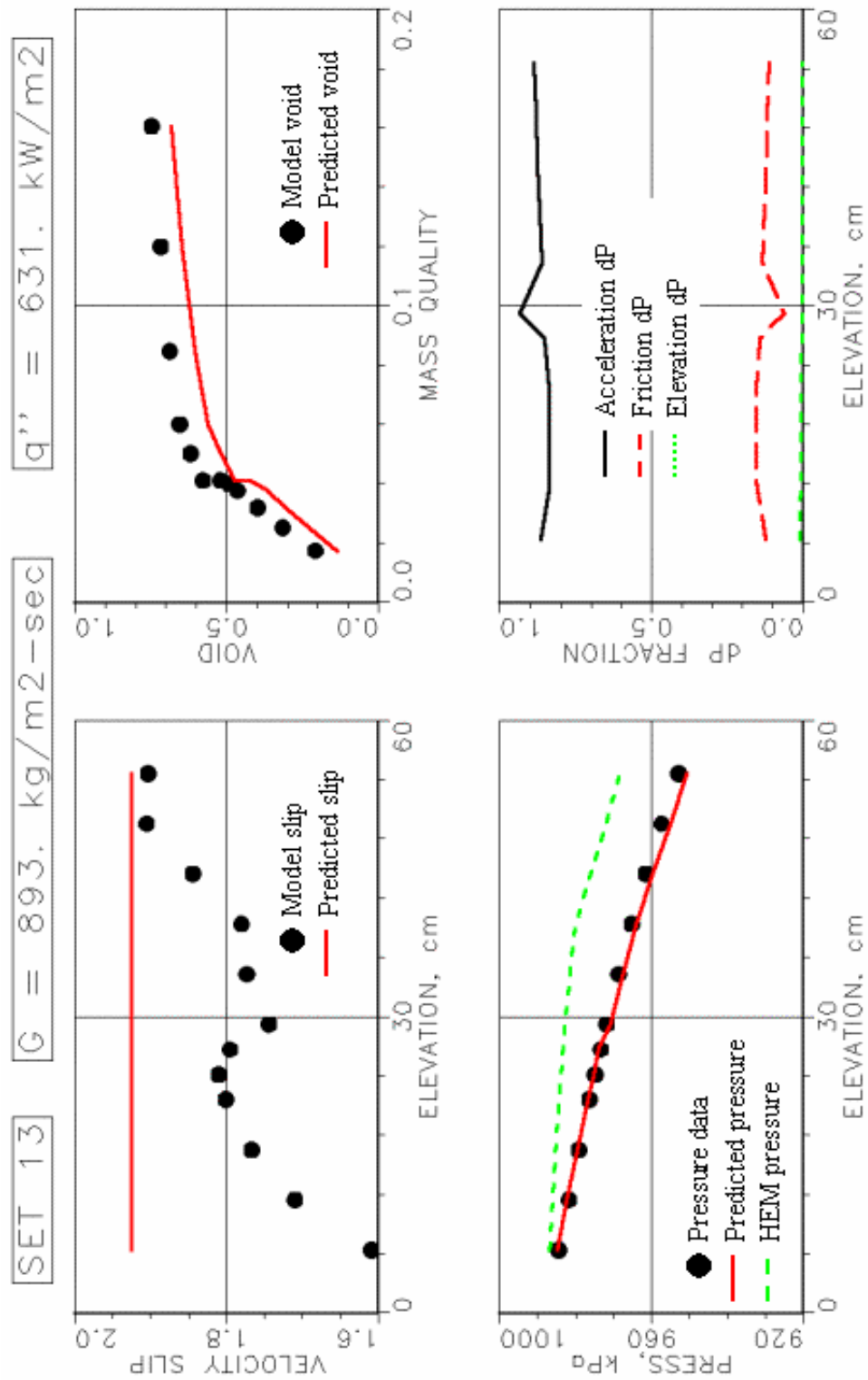


Figure 5-15. Model and prediction results for run 13.

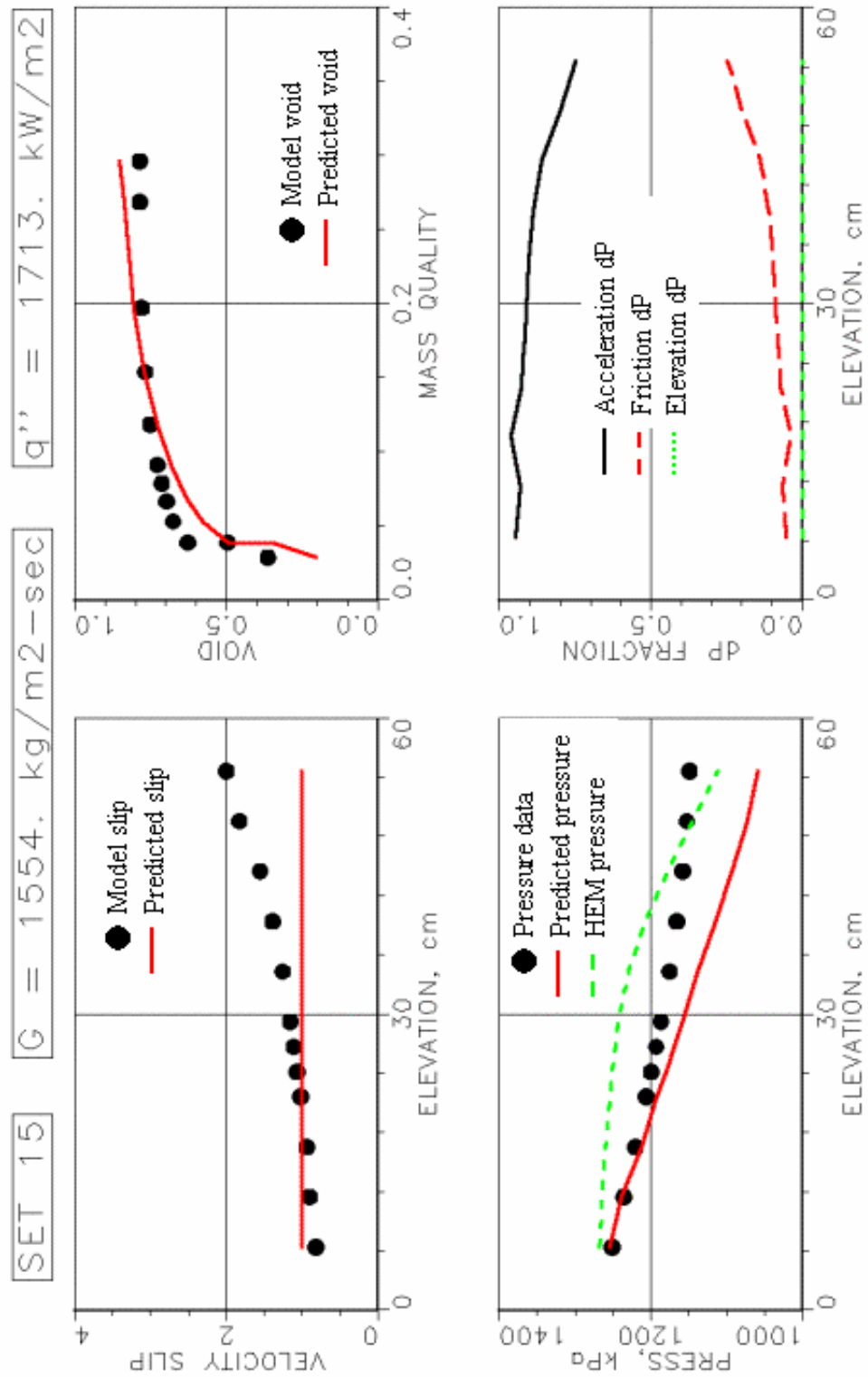


Figure 5-16. Model and prediction results for run 15.

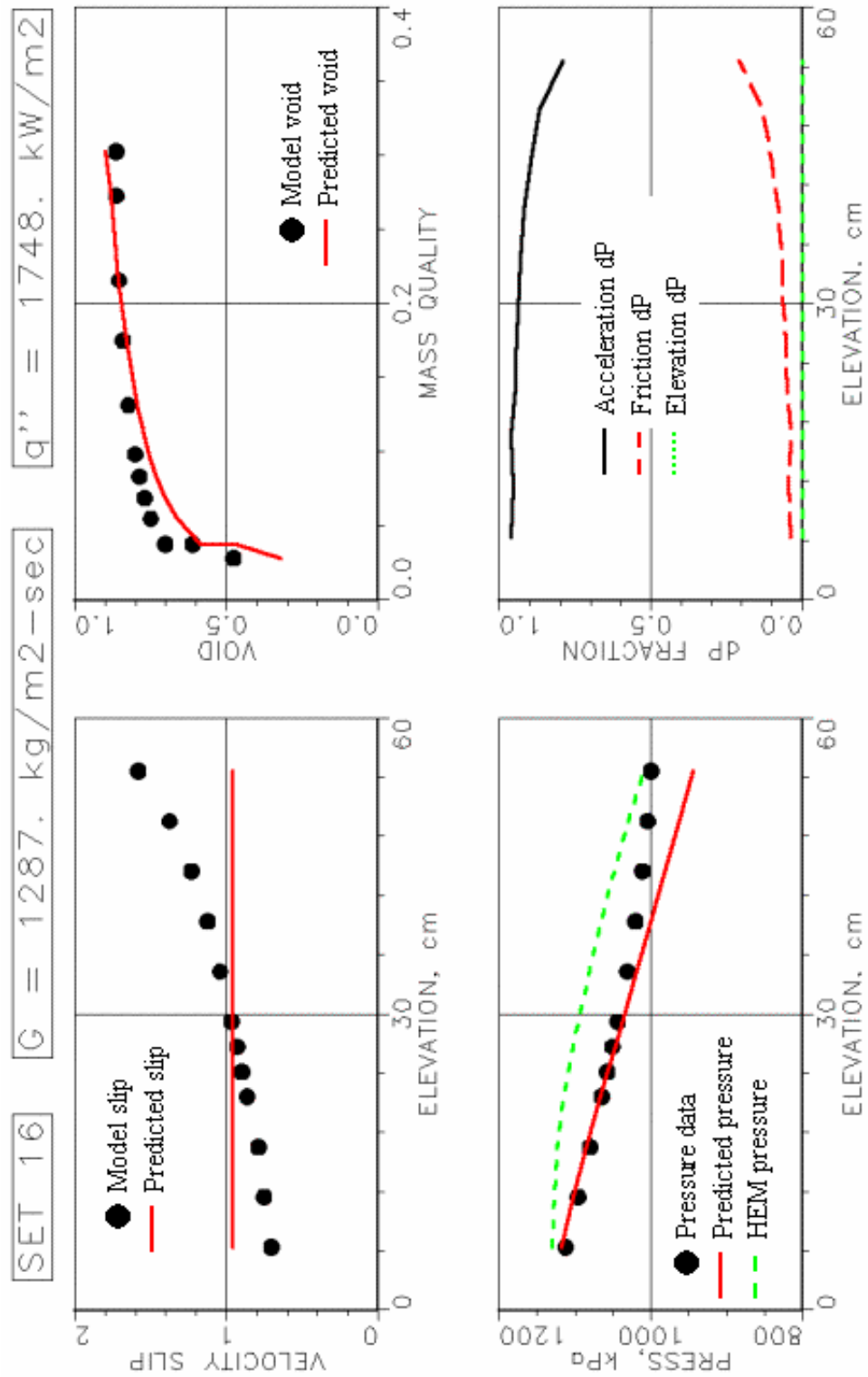


Figure 5-17. Model and prediction results for run 16.

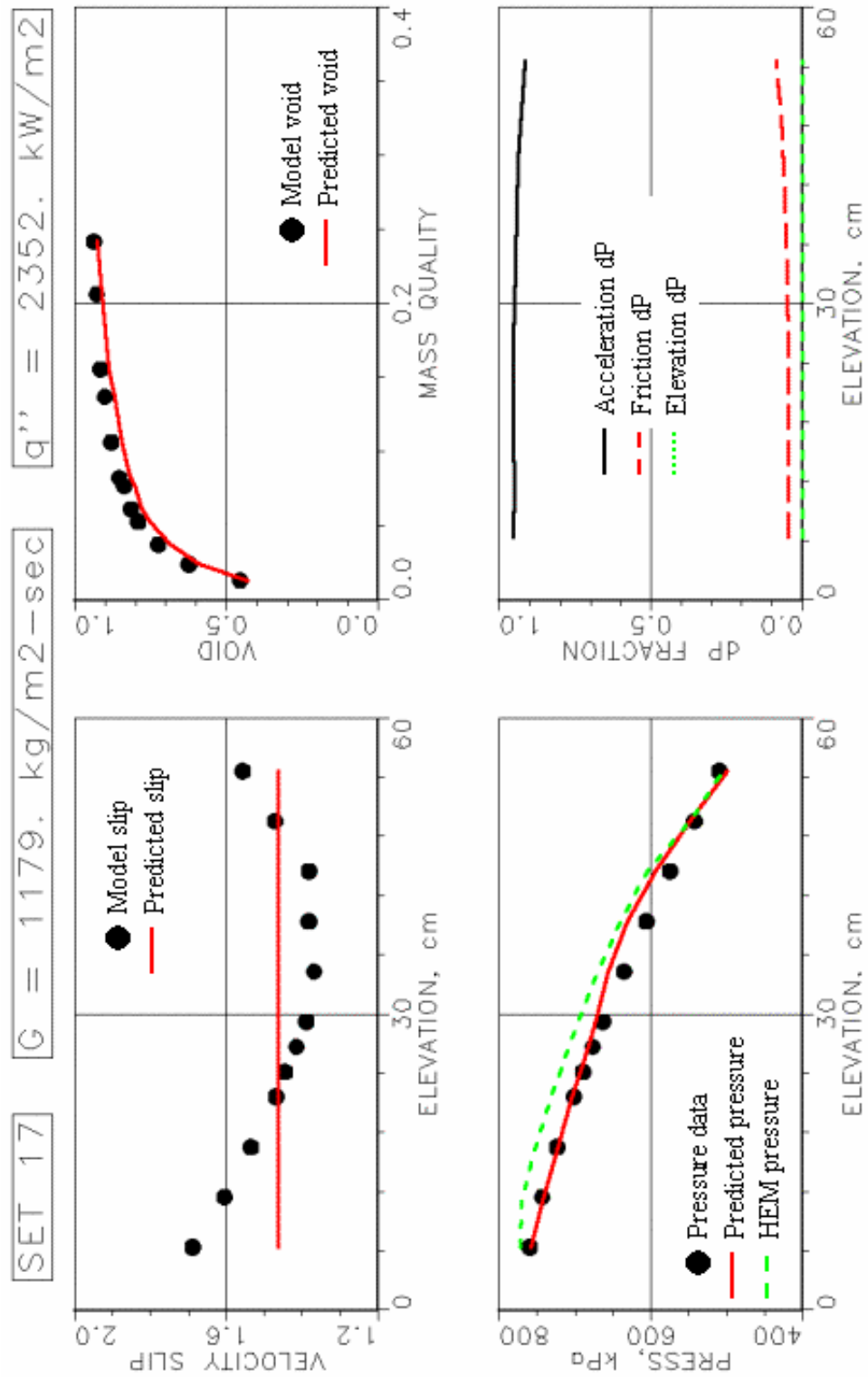


Figure 5-18. Model and prediction results for run 17.

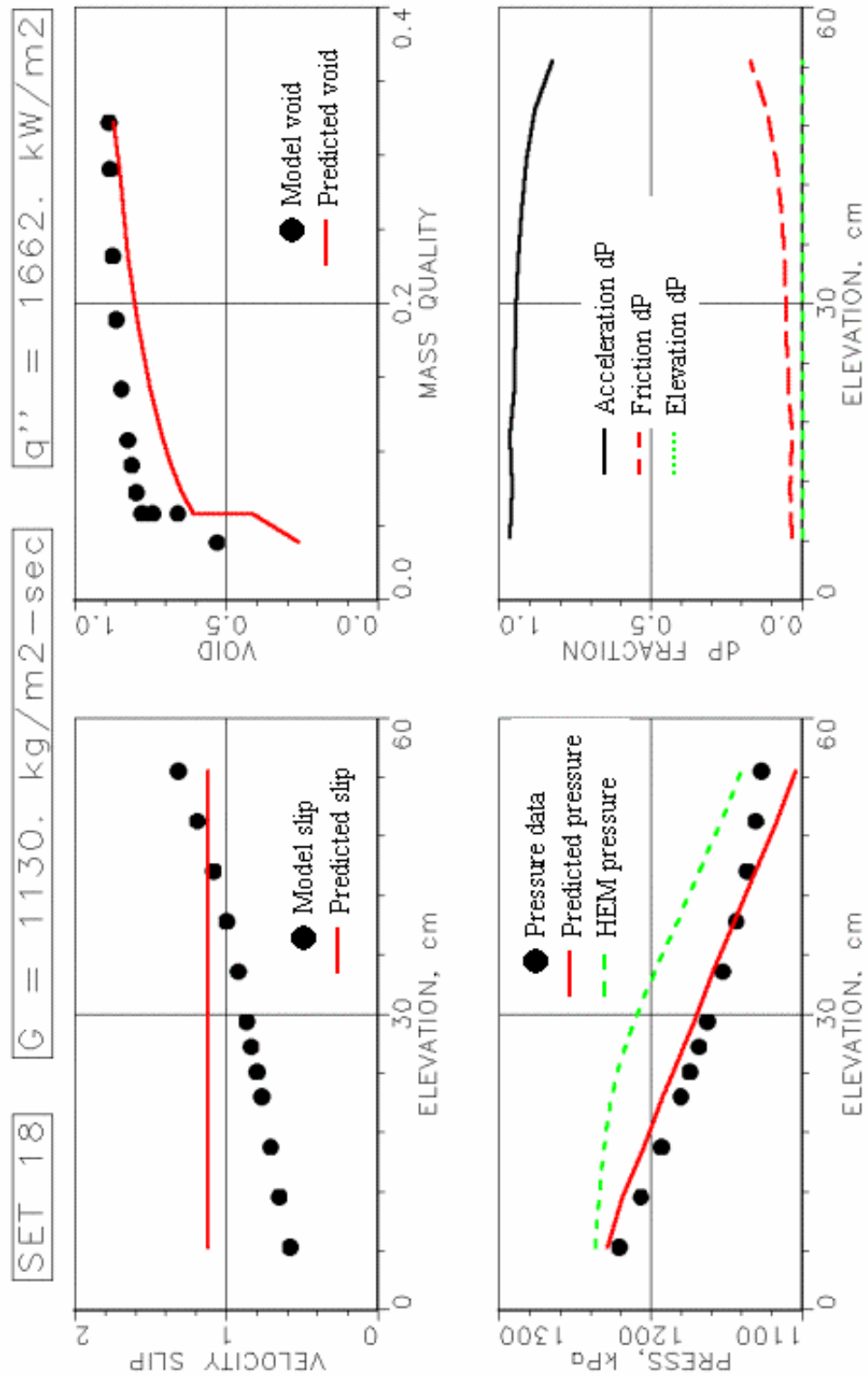


Figure 5-19. Model and prediction results for run 18.

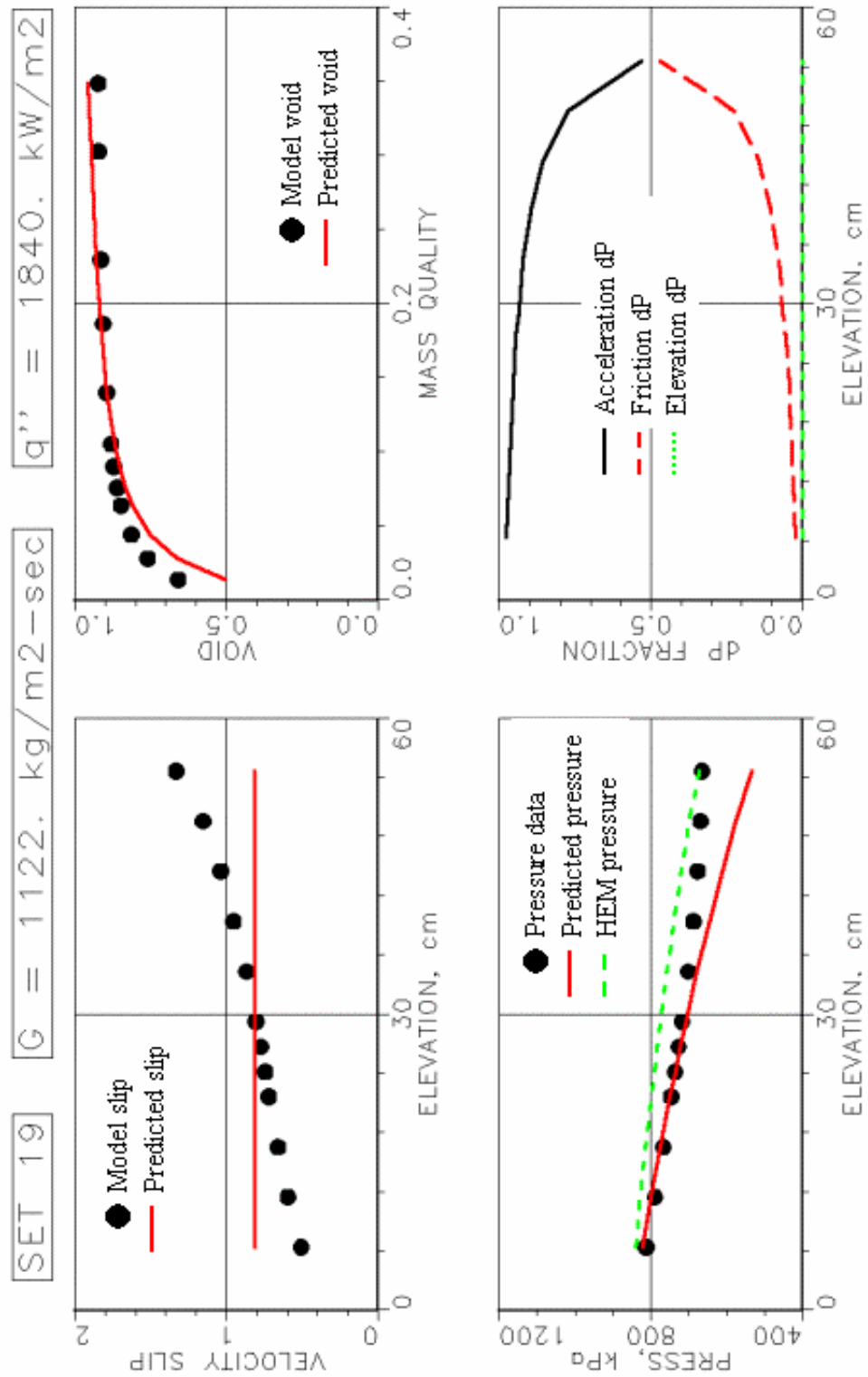


Figure 5-20. Model and prediction results for run 19.

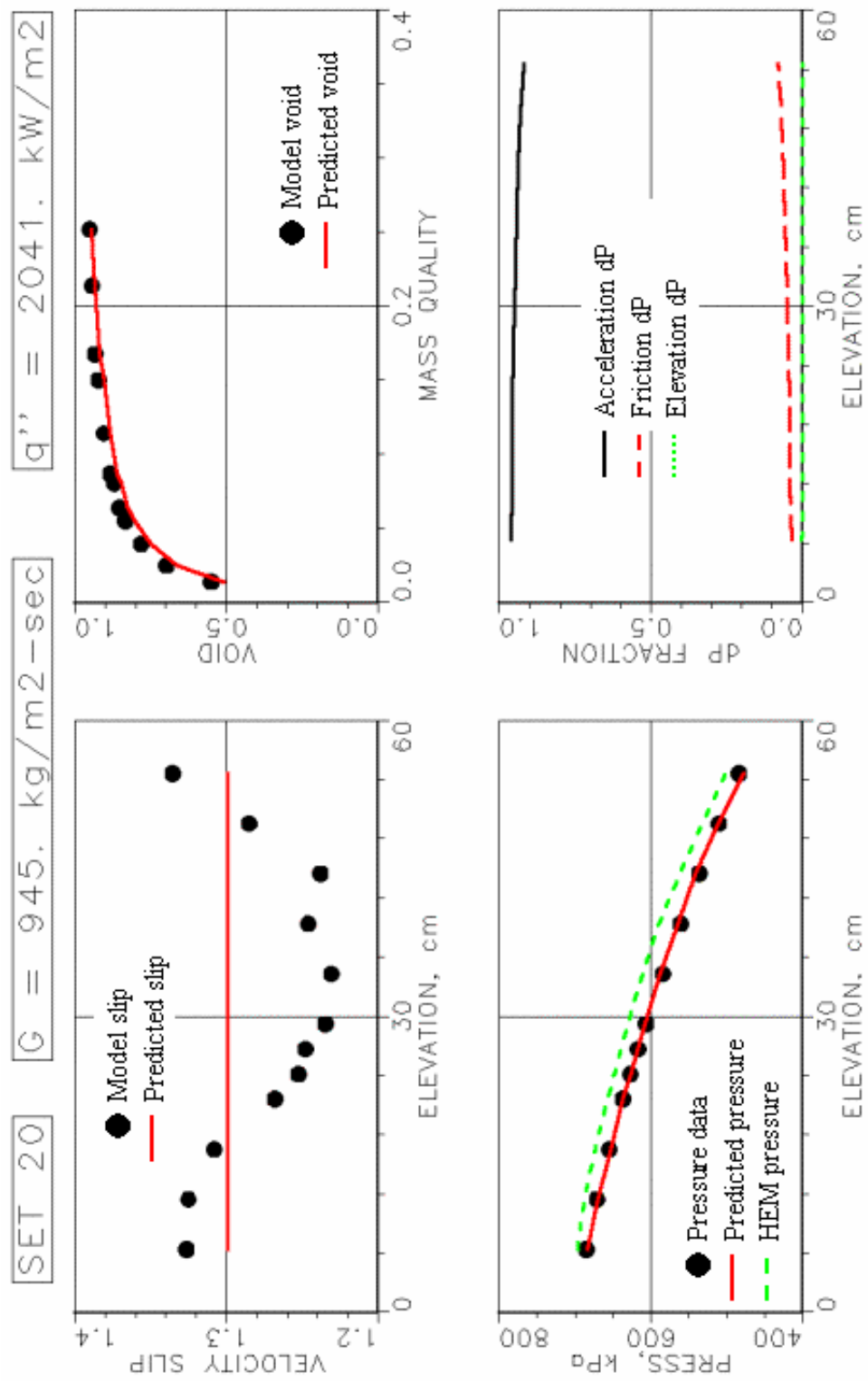


Figure 5-21. Model and prediction results for run 20.

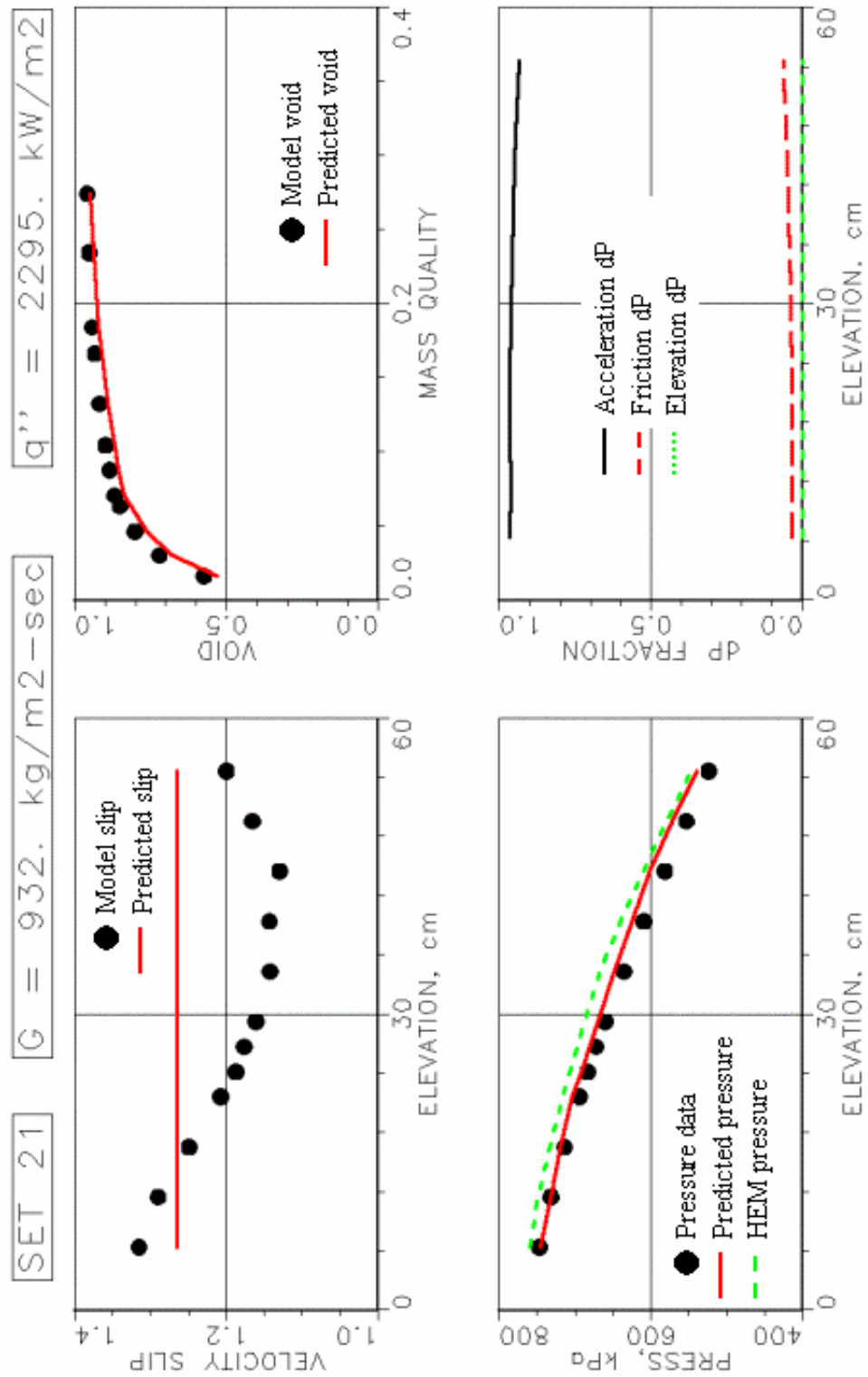


Figure 5-22. Model and prediction results for run 21.

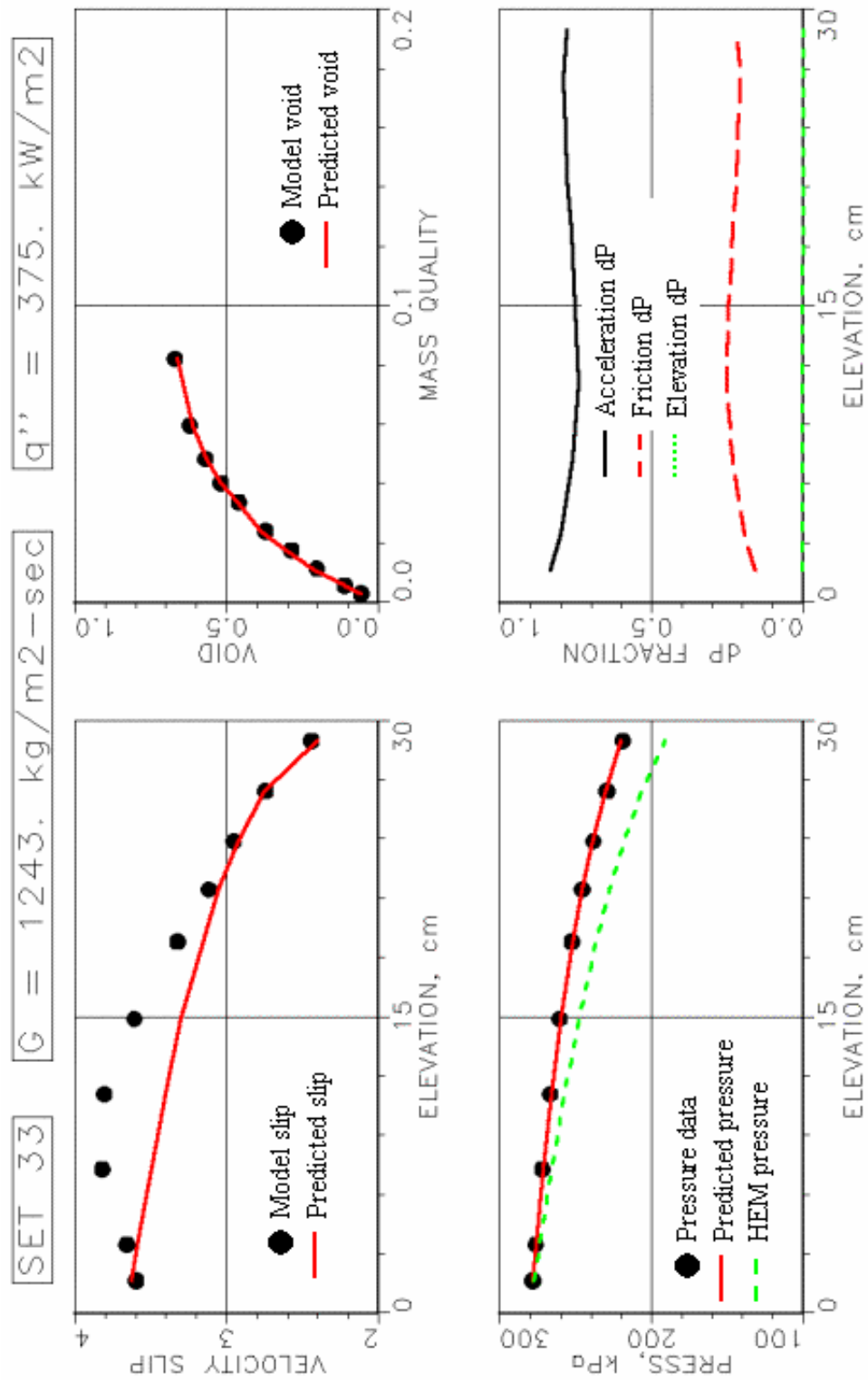


Figure 5-23. Model and prediction results for run 33.

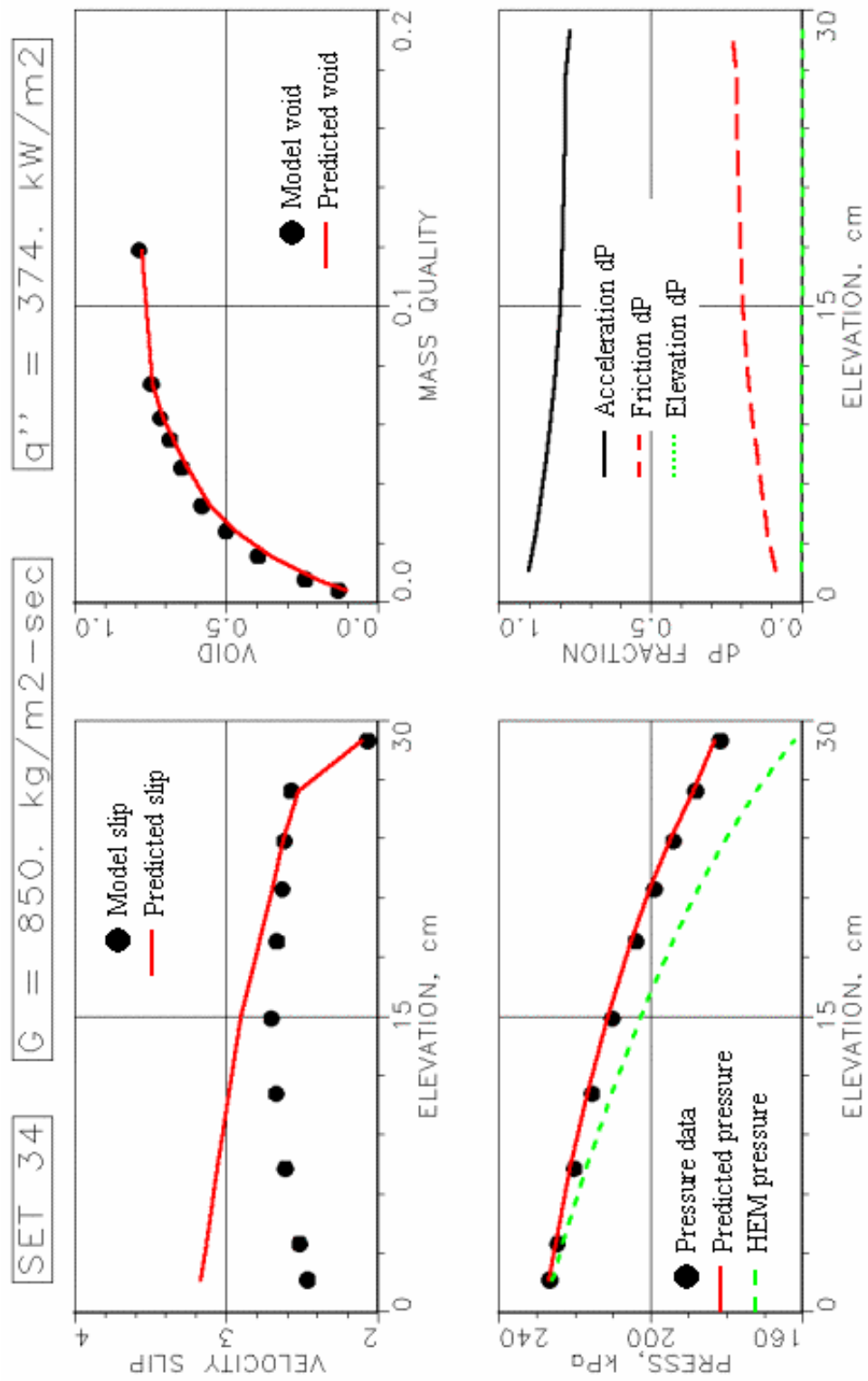


Figure 5-24. Model and prediction results for run 34.

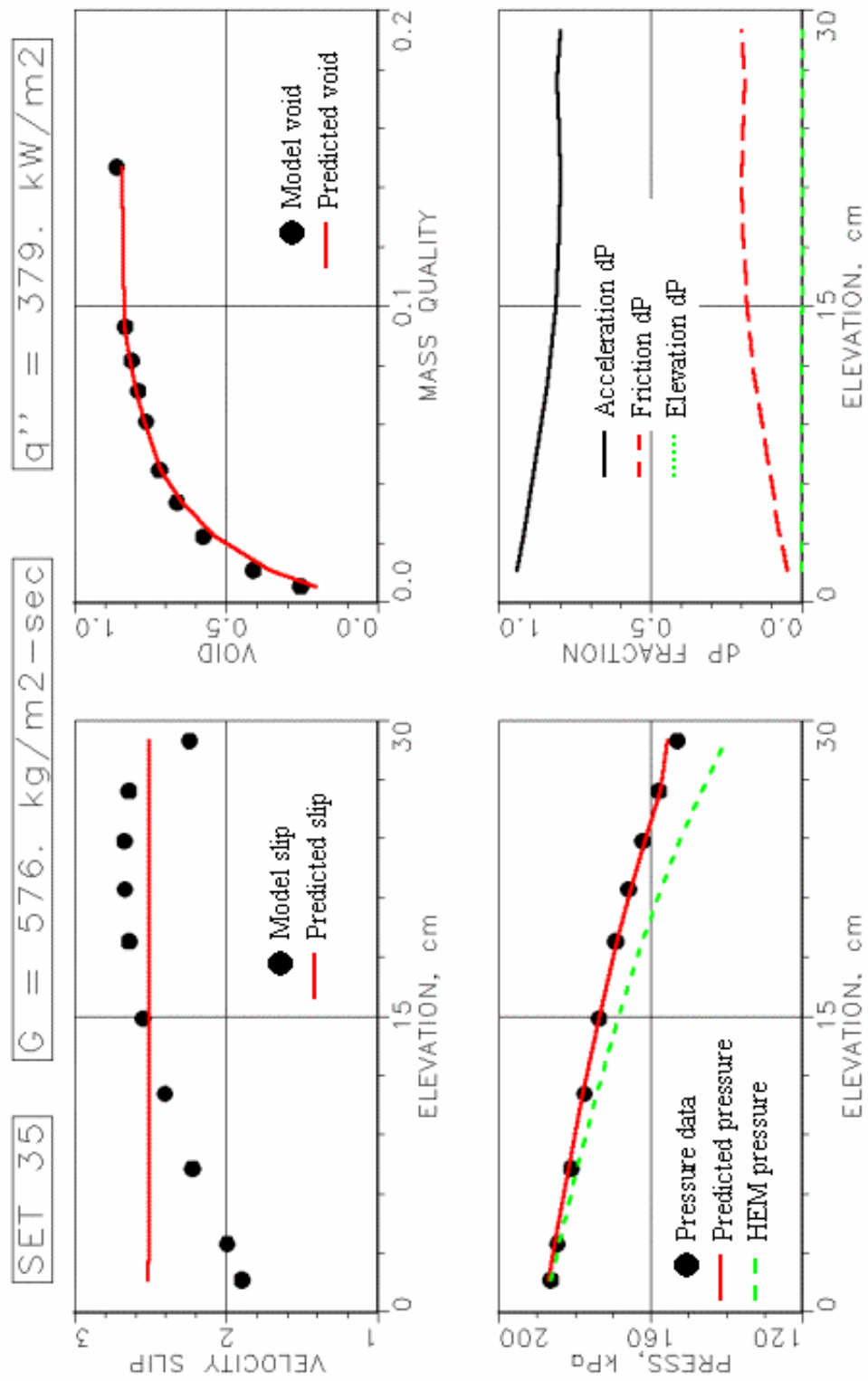


Figure 5-25. Model and prediction results for run 35.

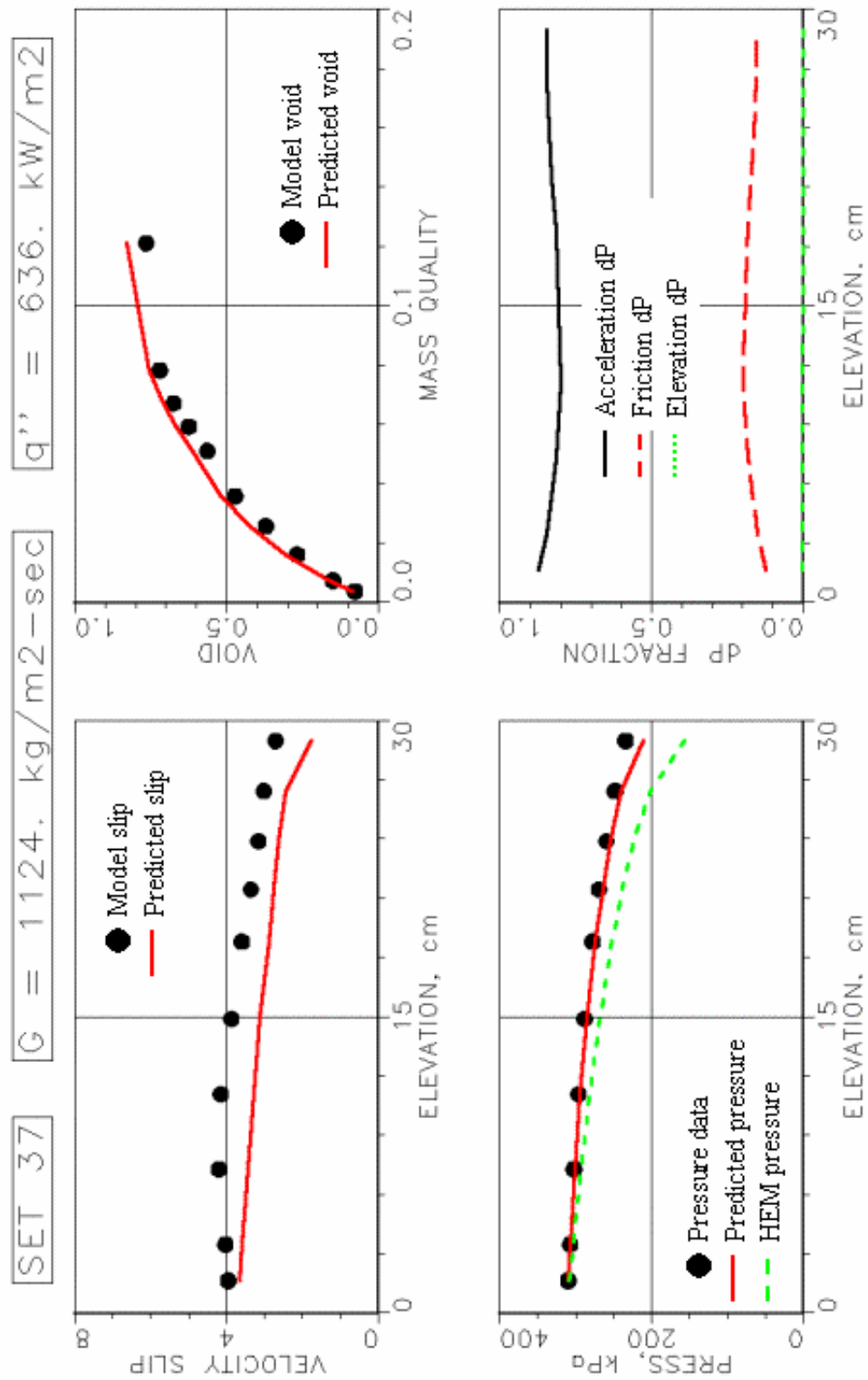


Figure 5-26. Model and prediction results for run 37.

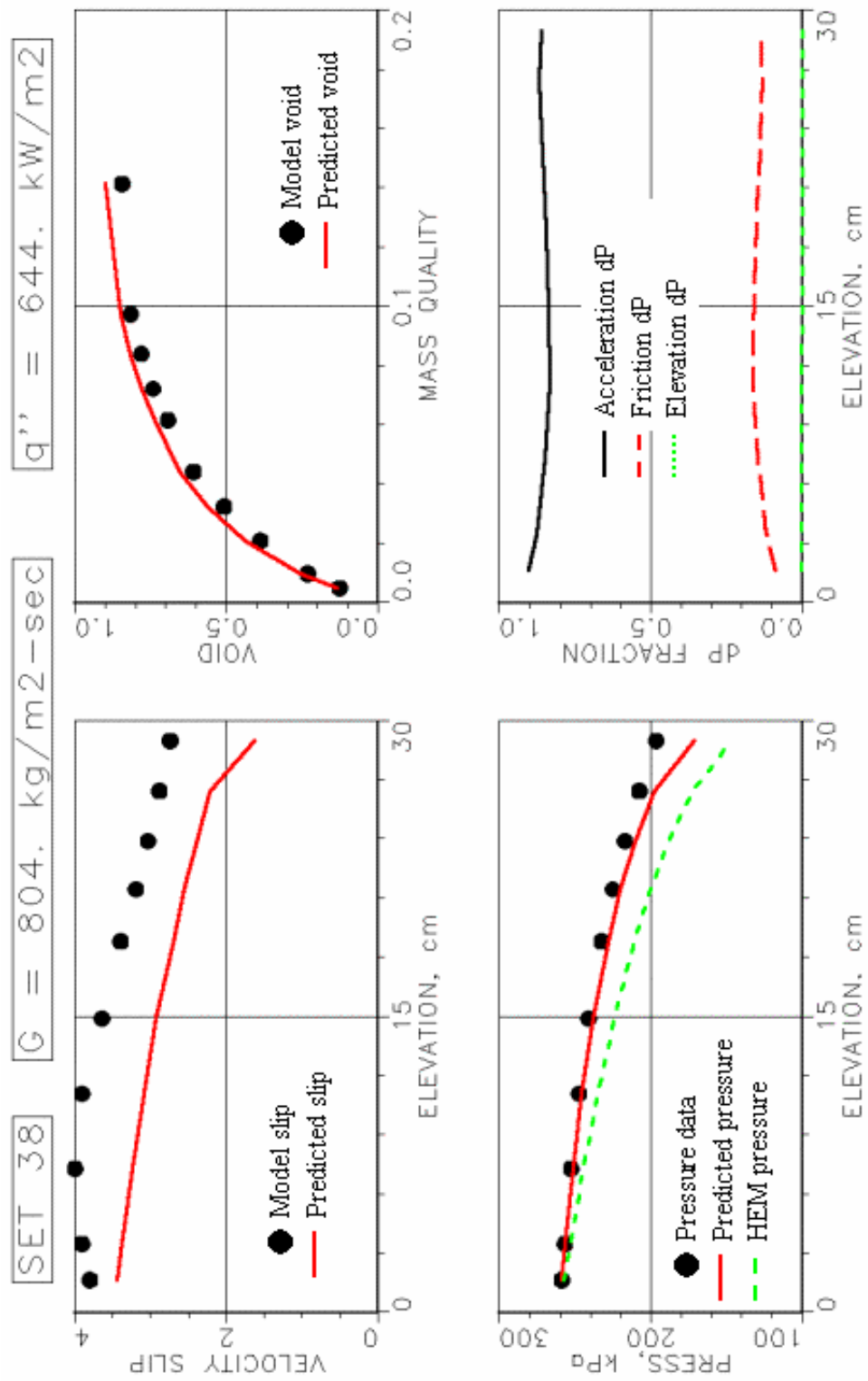


Figure 5-27. Model and prediction results for run 38.

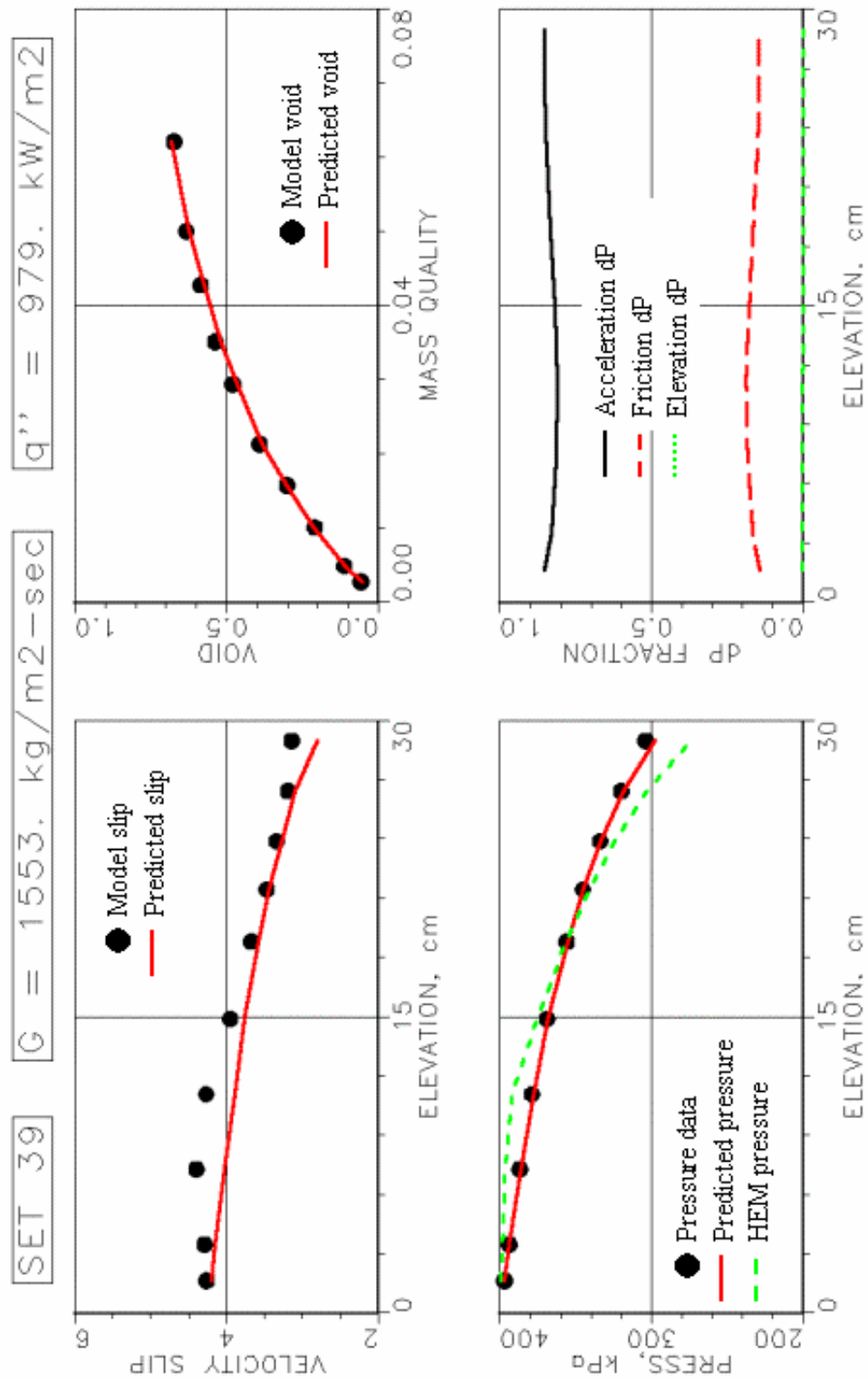


Figure 5-28. Model and prediction results for run 39.

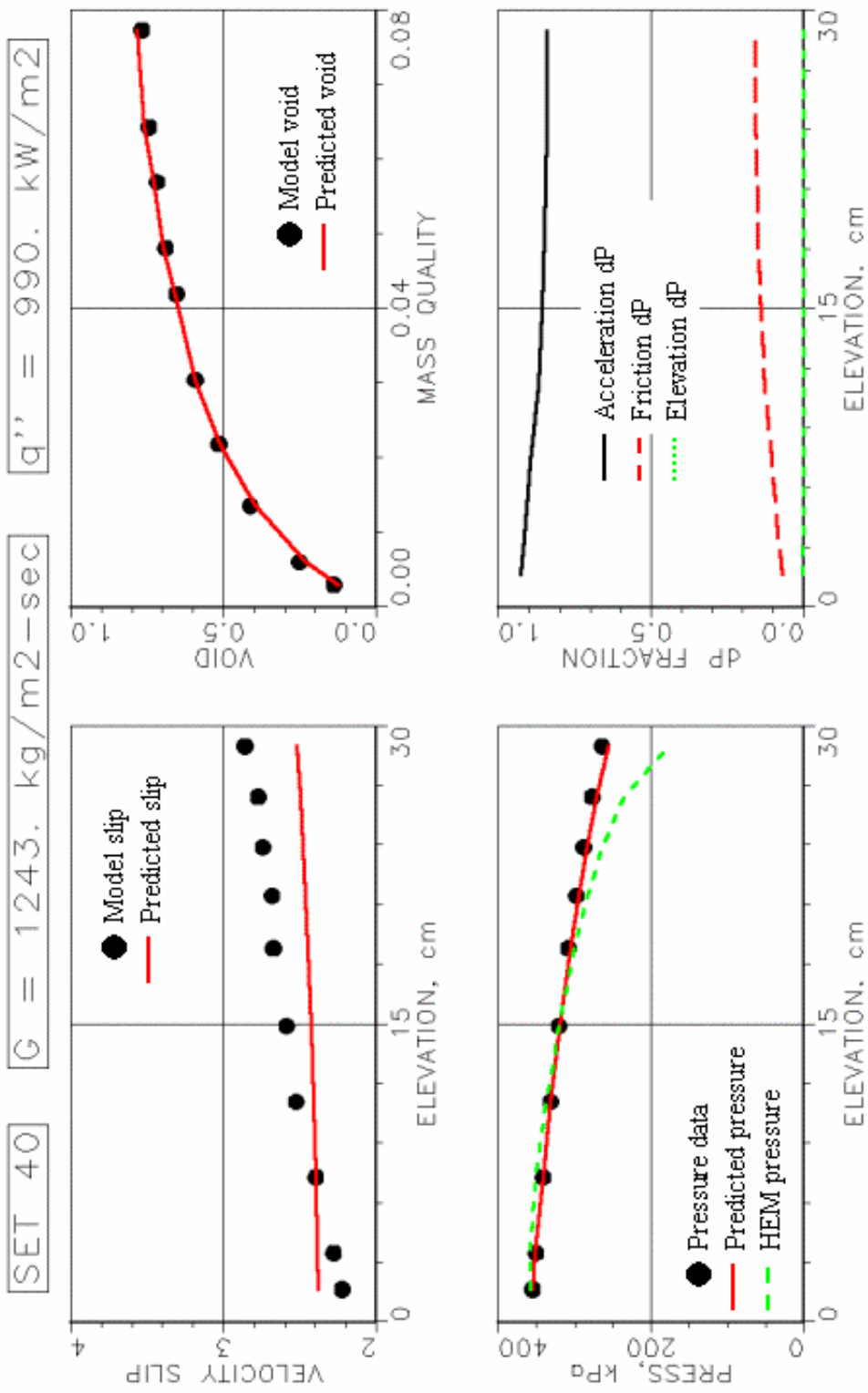


Figure 5-29. Model and prediction results for run 40.

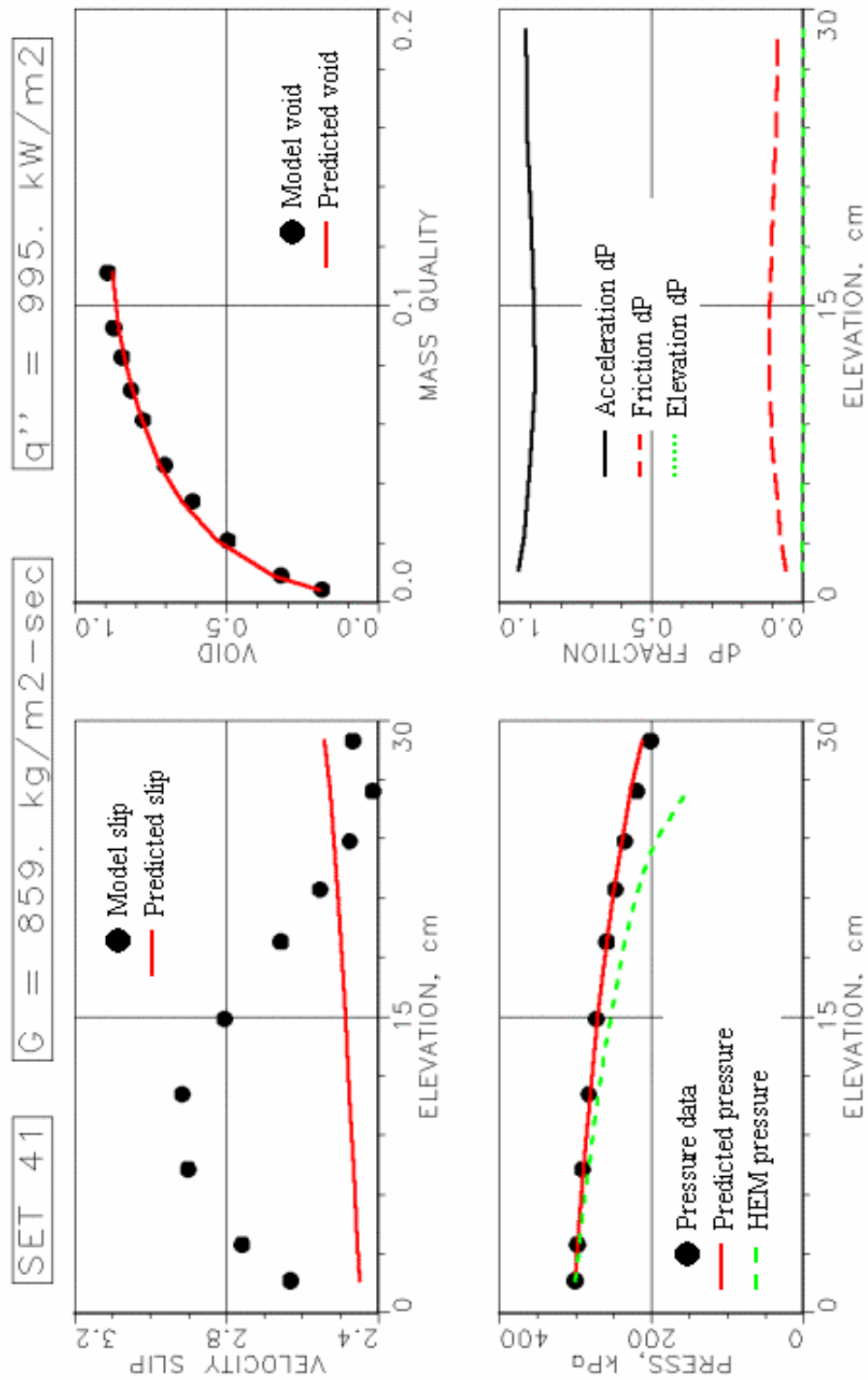


Figure 5-30. Model and prediction results for run 41.

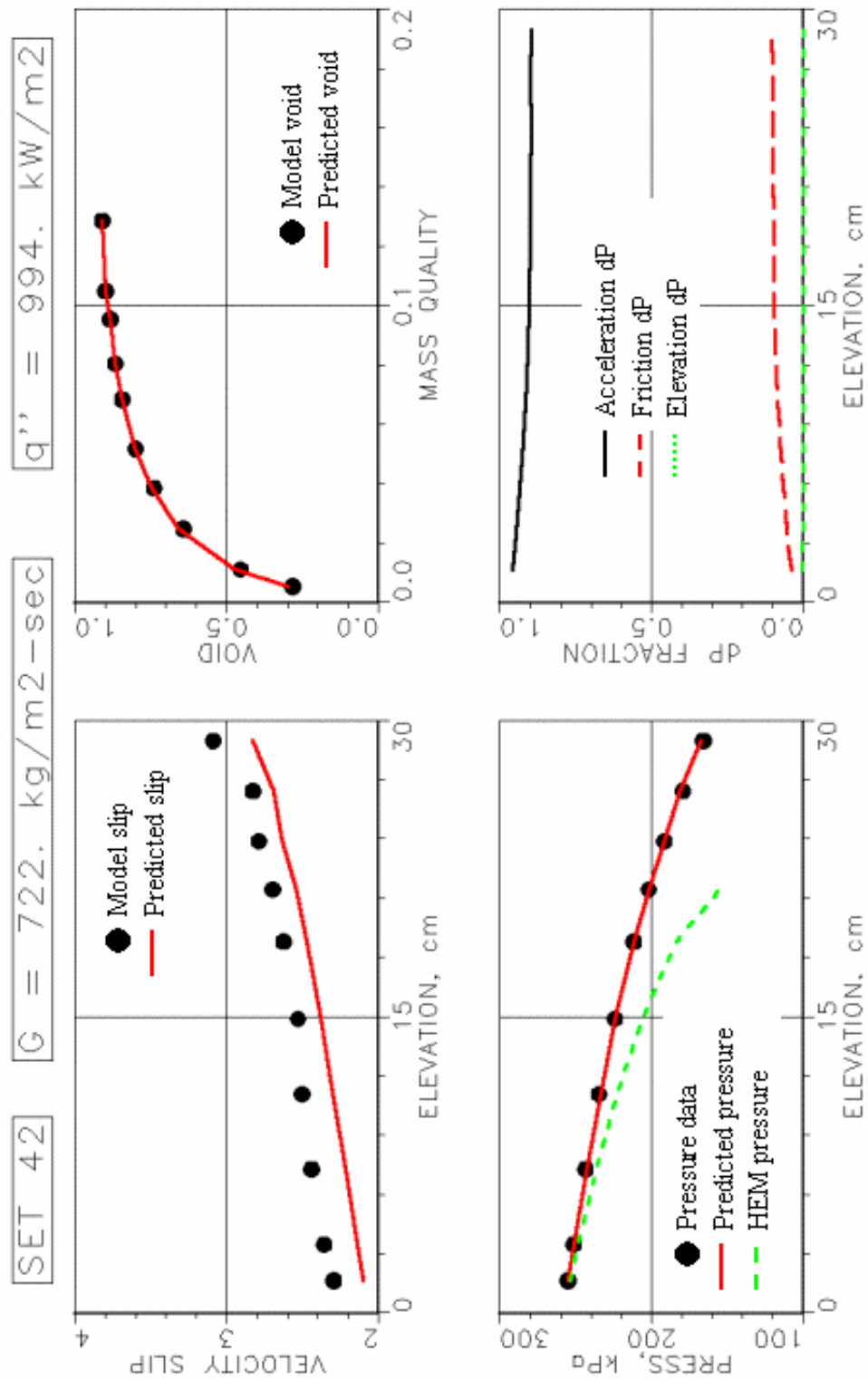


Figure 5-31. Model and prediction results for run 42.

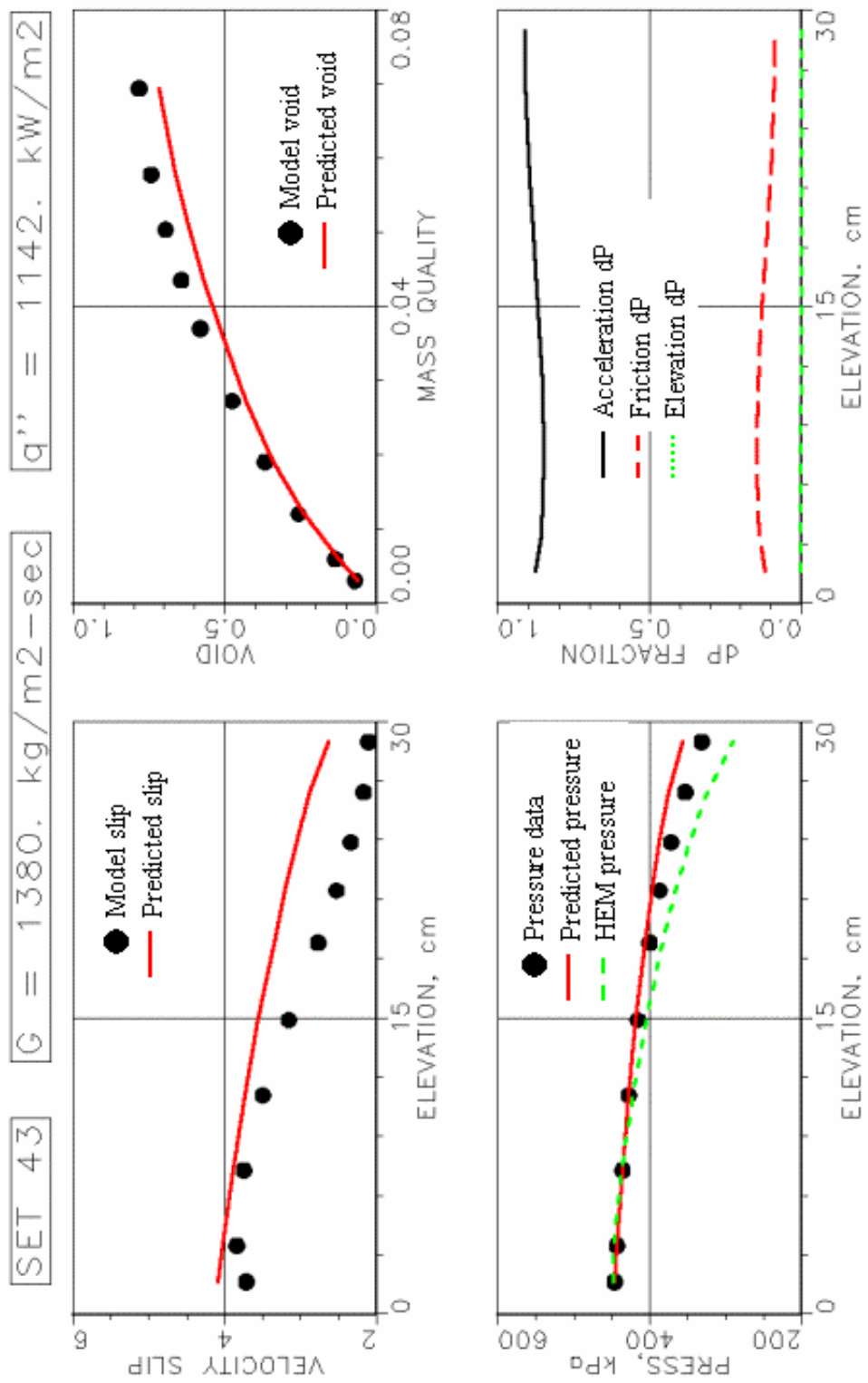


Figure 5-32. Model and prediction results for run 43.

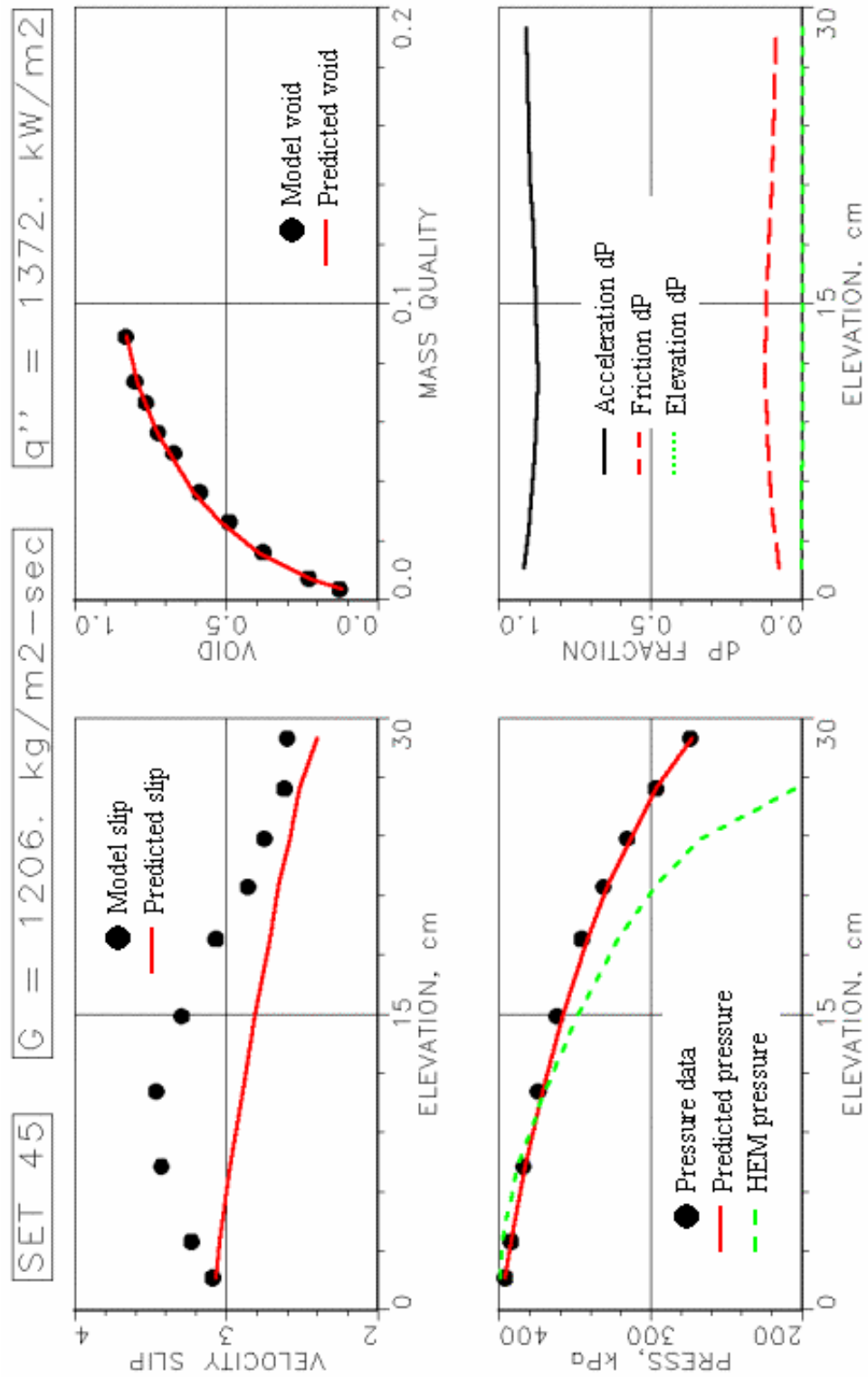


Figure 5-33. Model and prediction results for run 45.

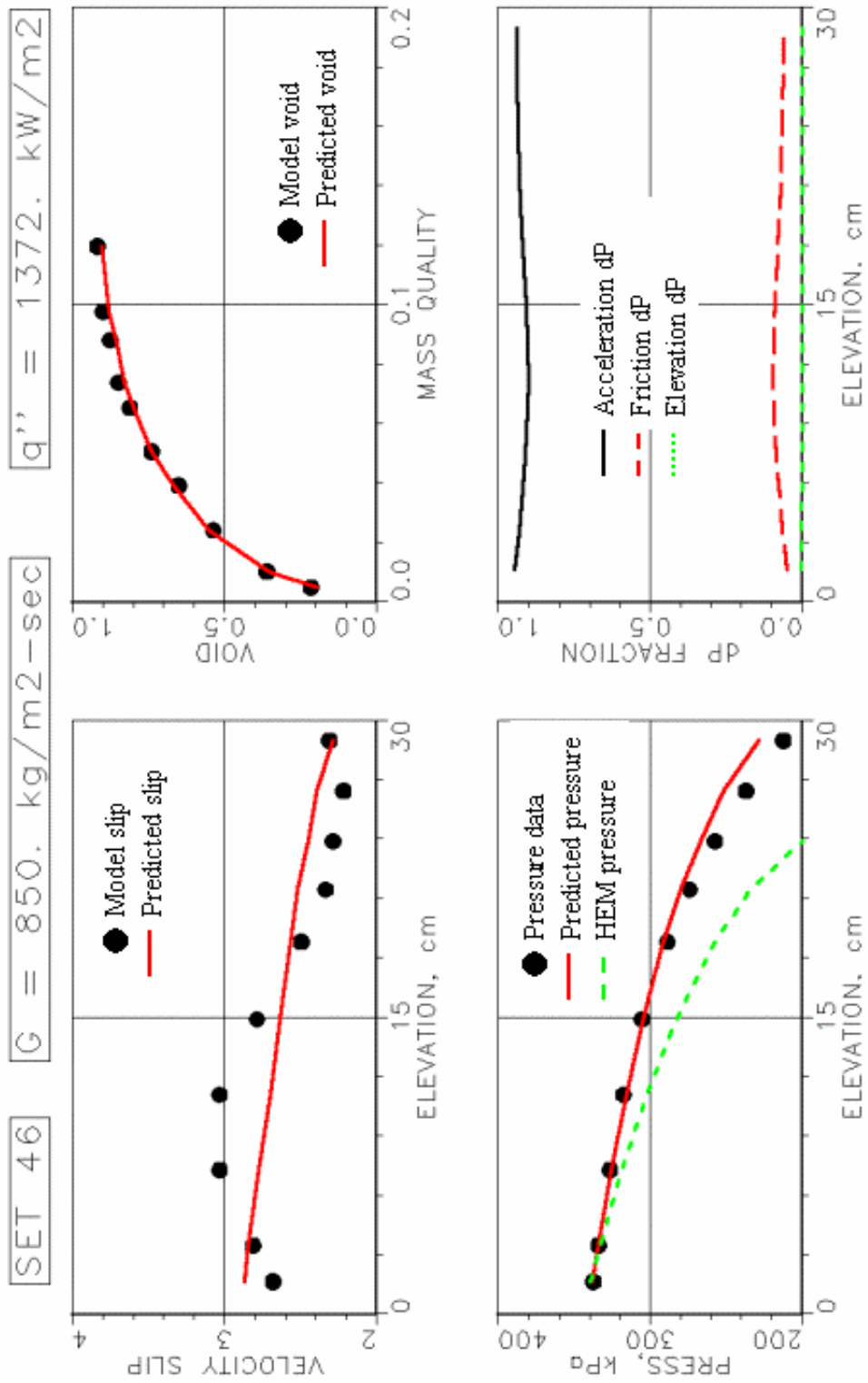


Figure 5-34. Model and prediction results for run 46.

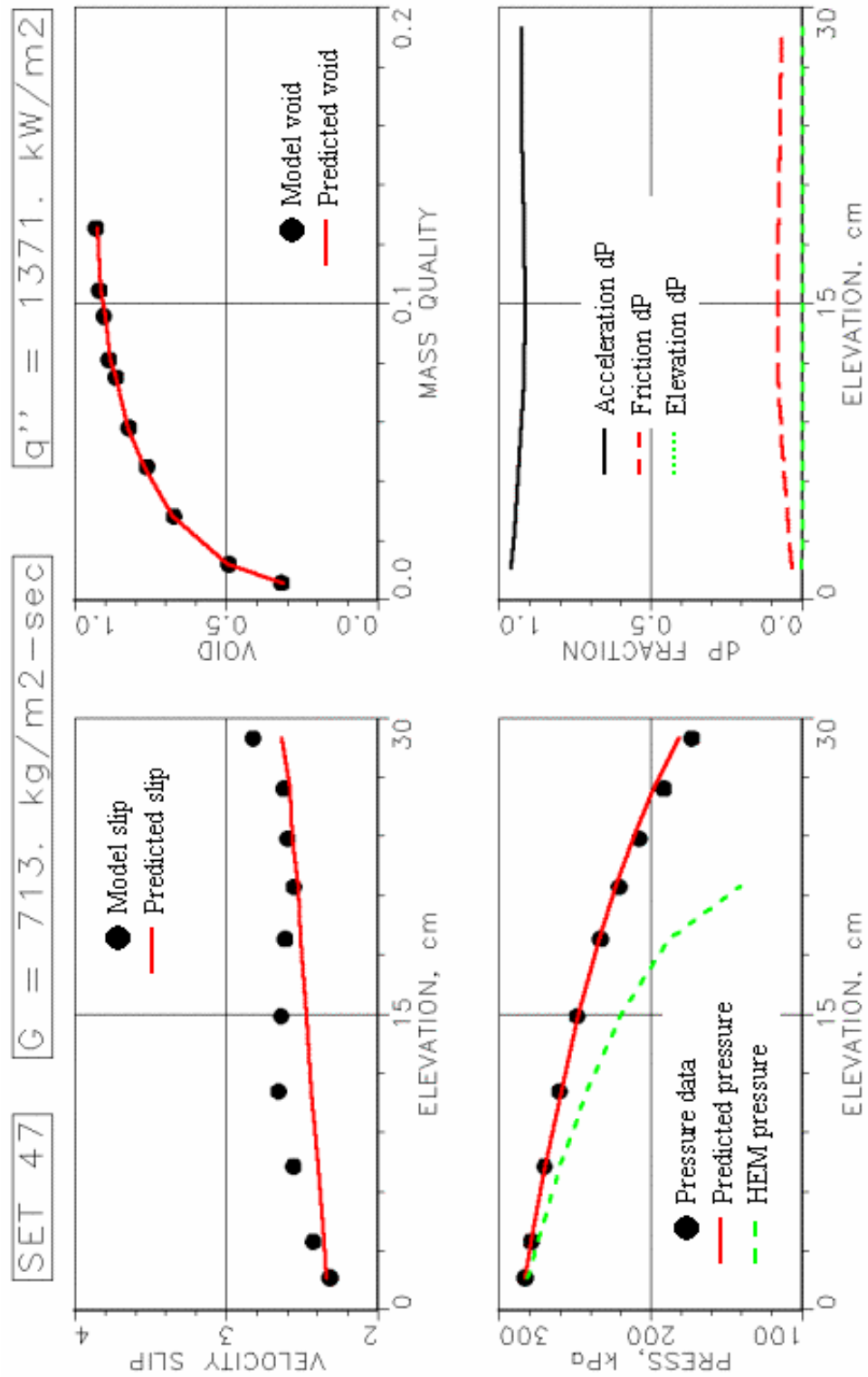


Figure 5-35. Model and prediction results for run 47.

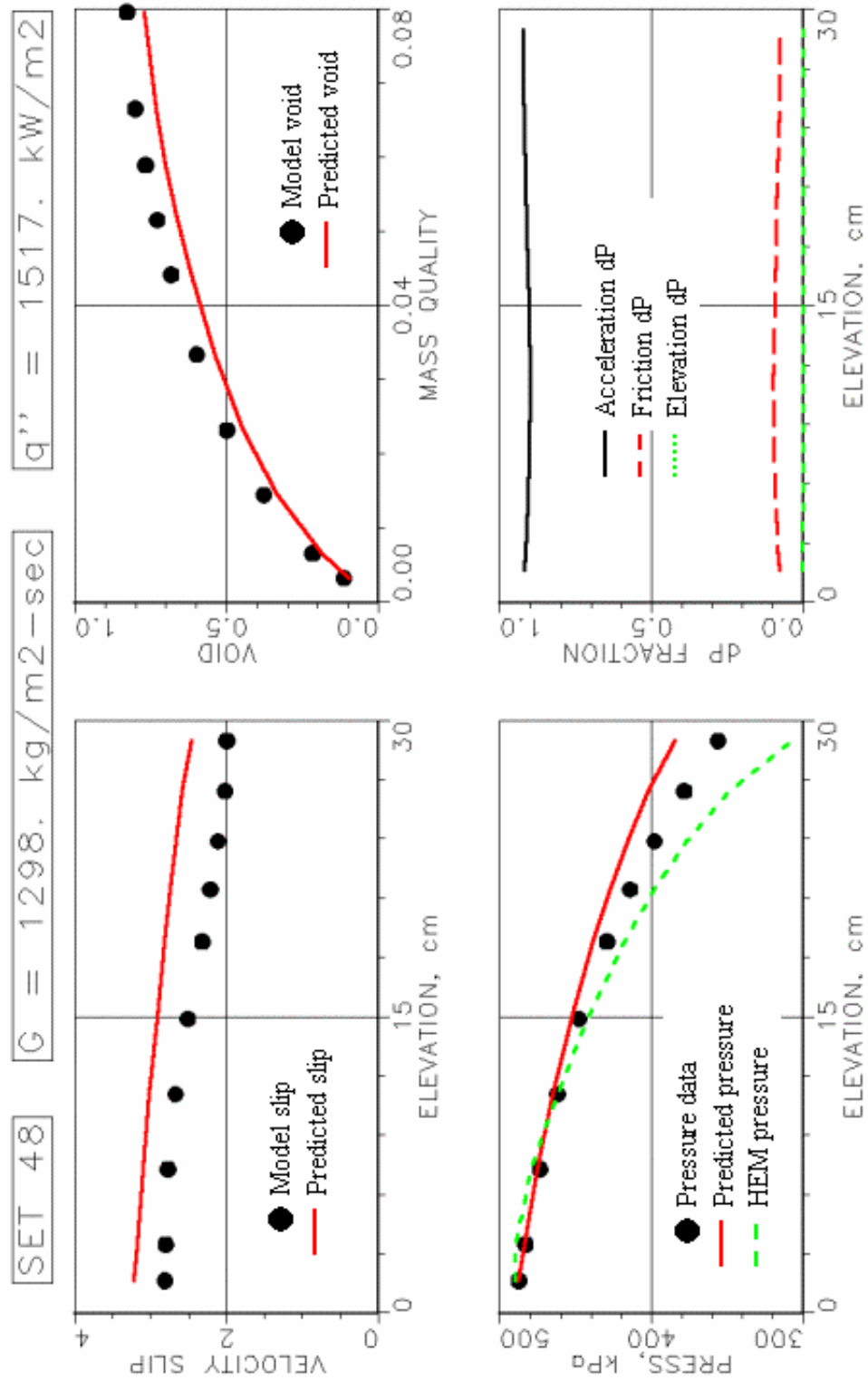


Figure 5-36. Model and prediction results for run 48.

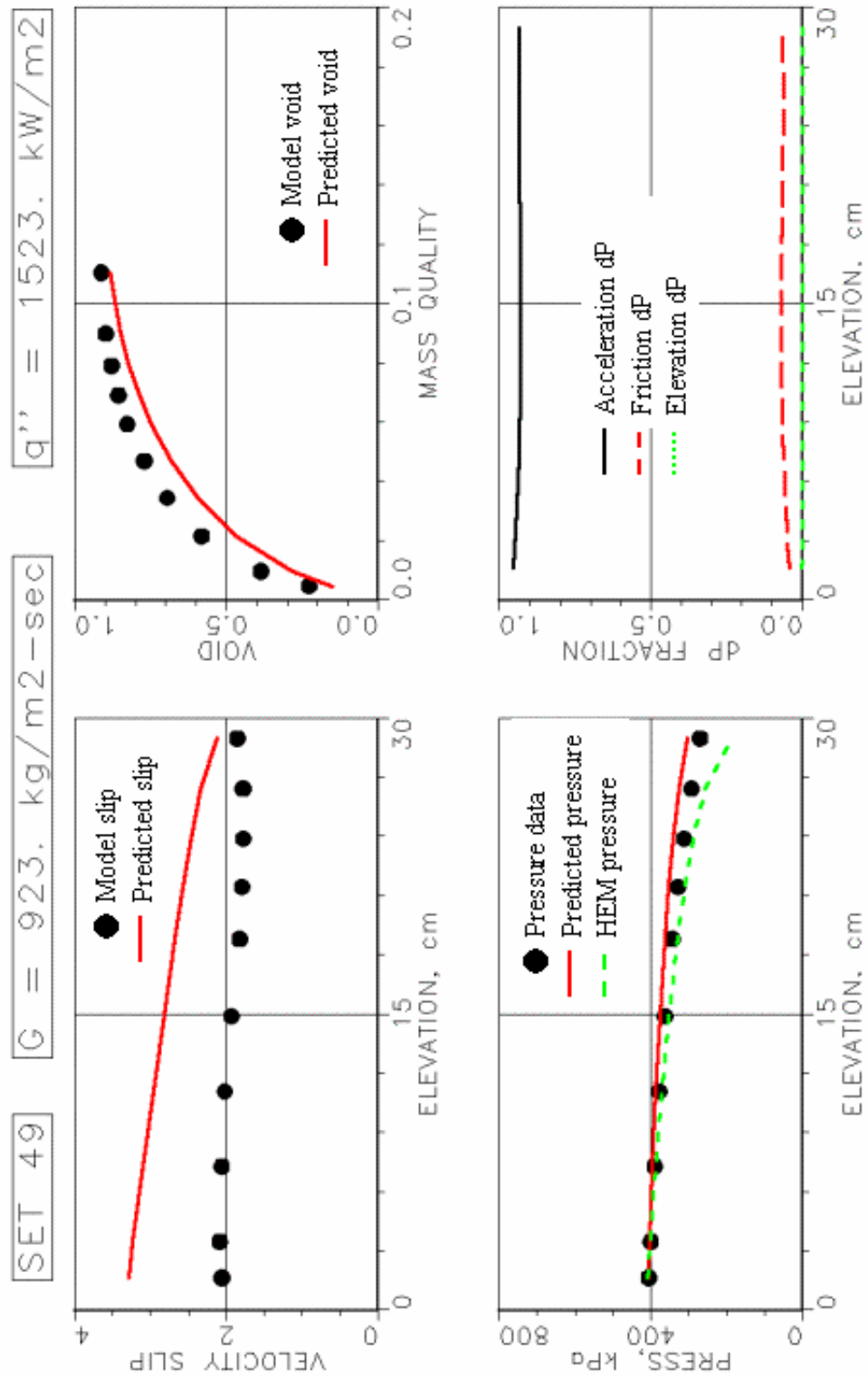


Figure 5-37. Model and prediction results for run 49.

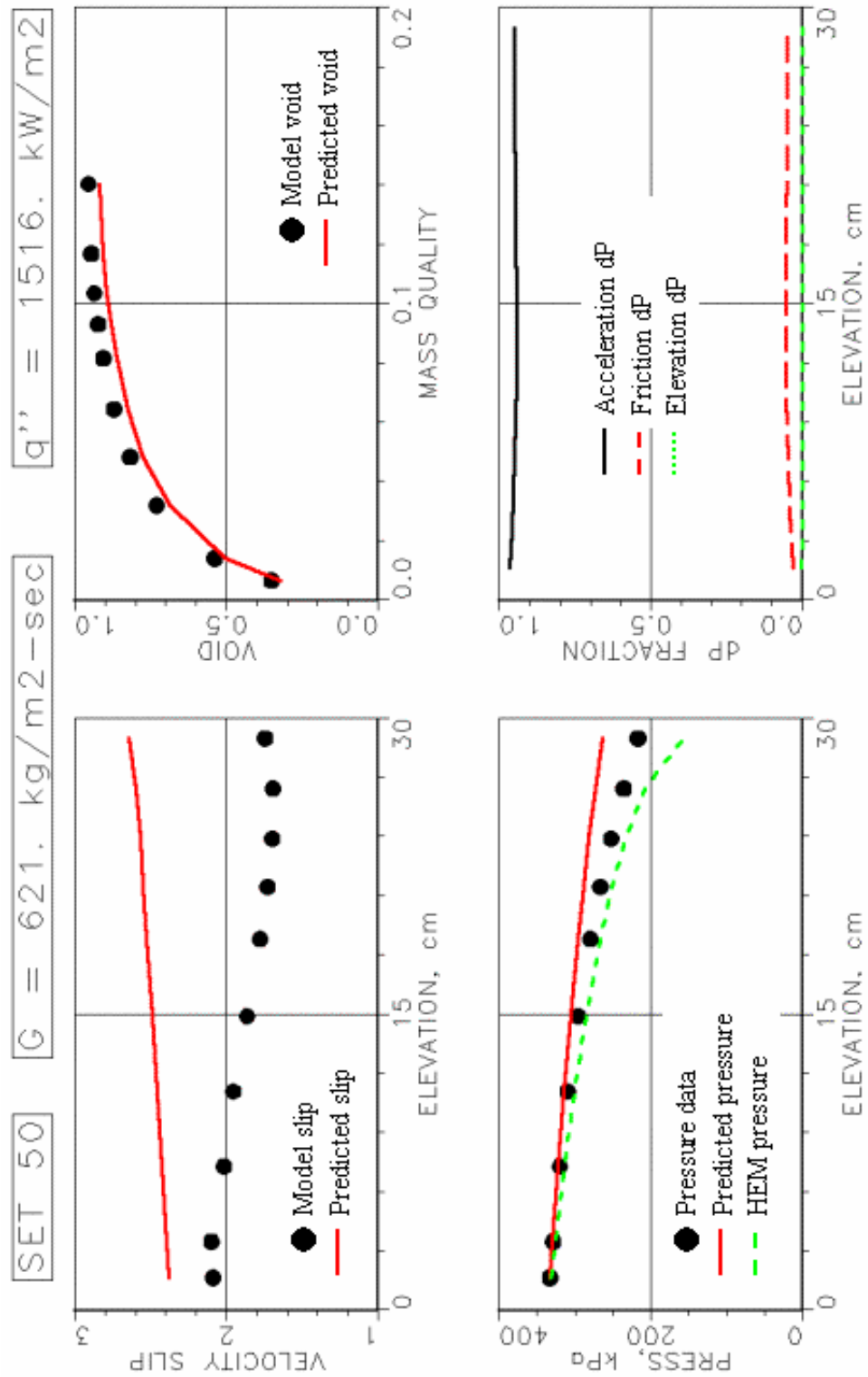


Figure 5-38. Model and prediction results for run 50.

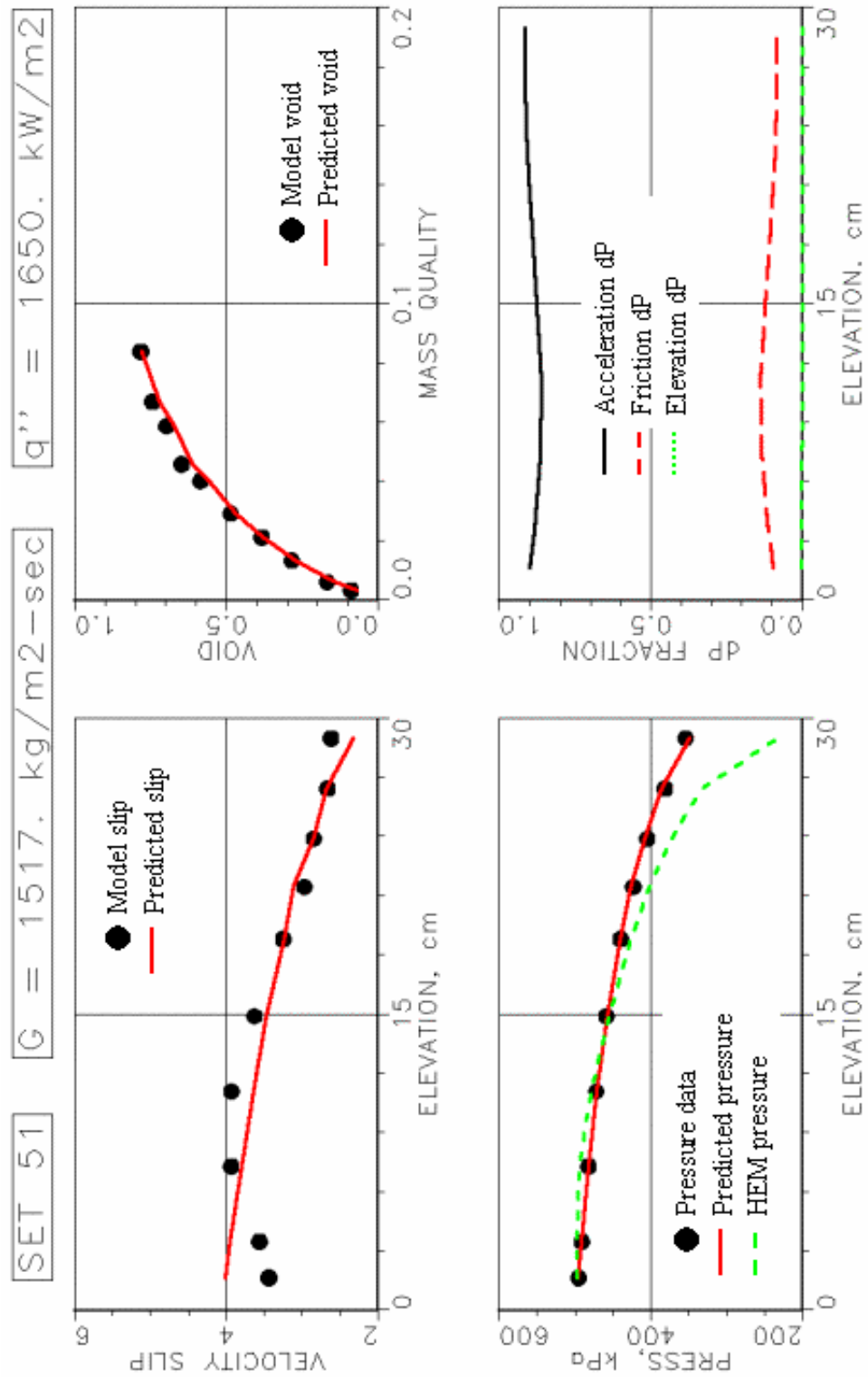


Figure 5-39. Model and prediction results for run 51.

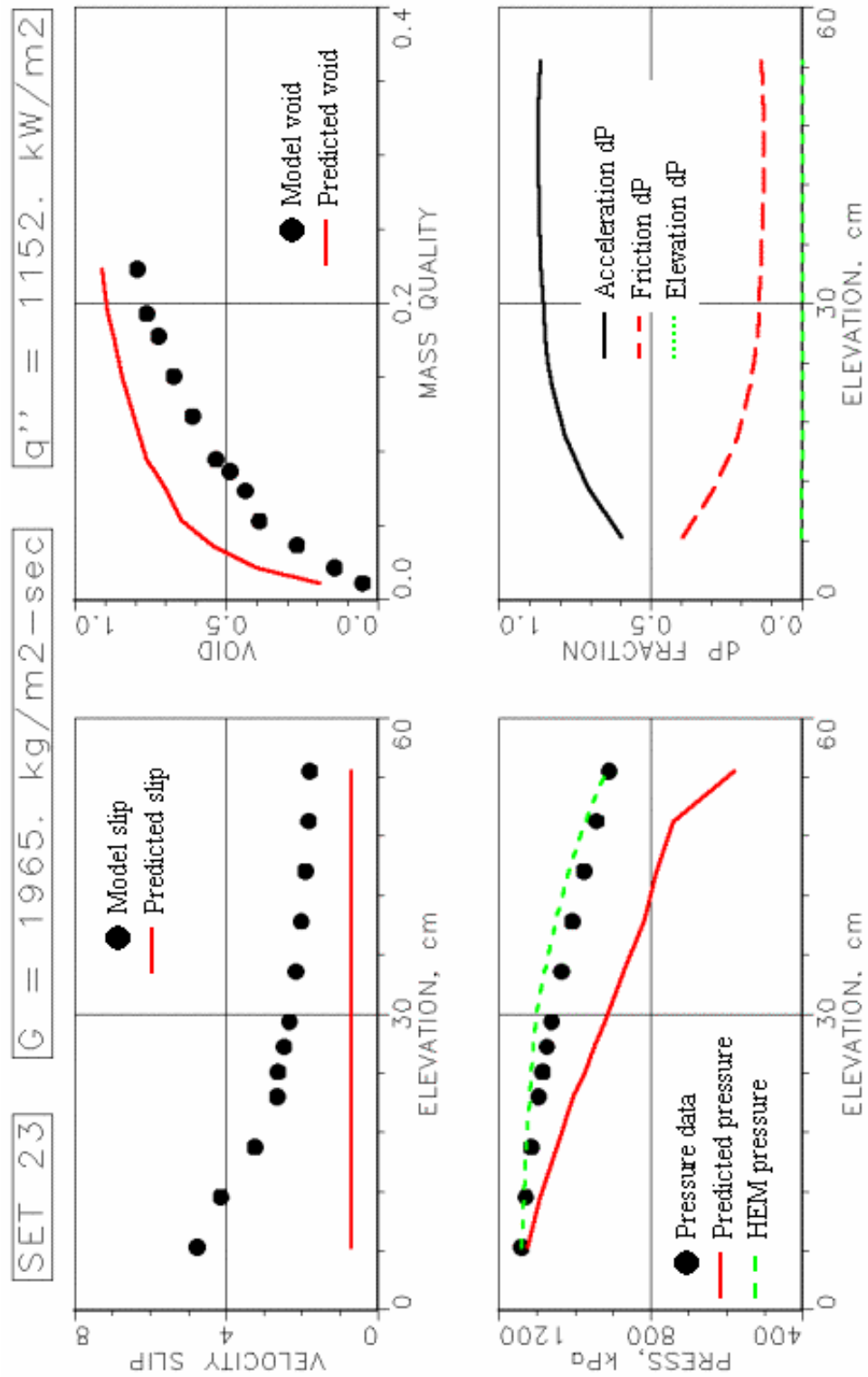


Figure 5-40. Model and prediction results for run 23.

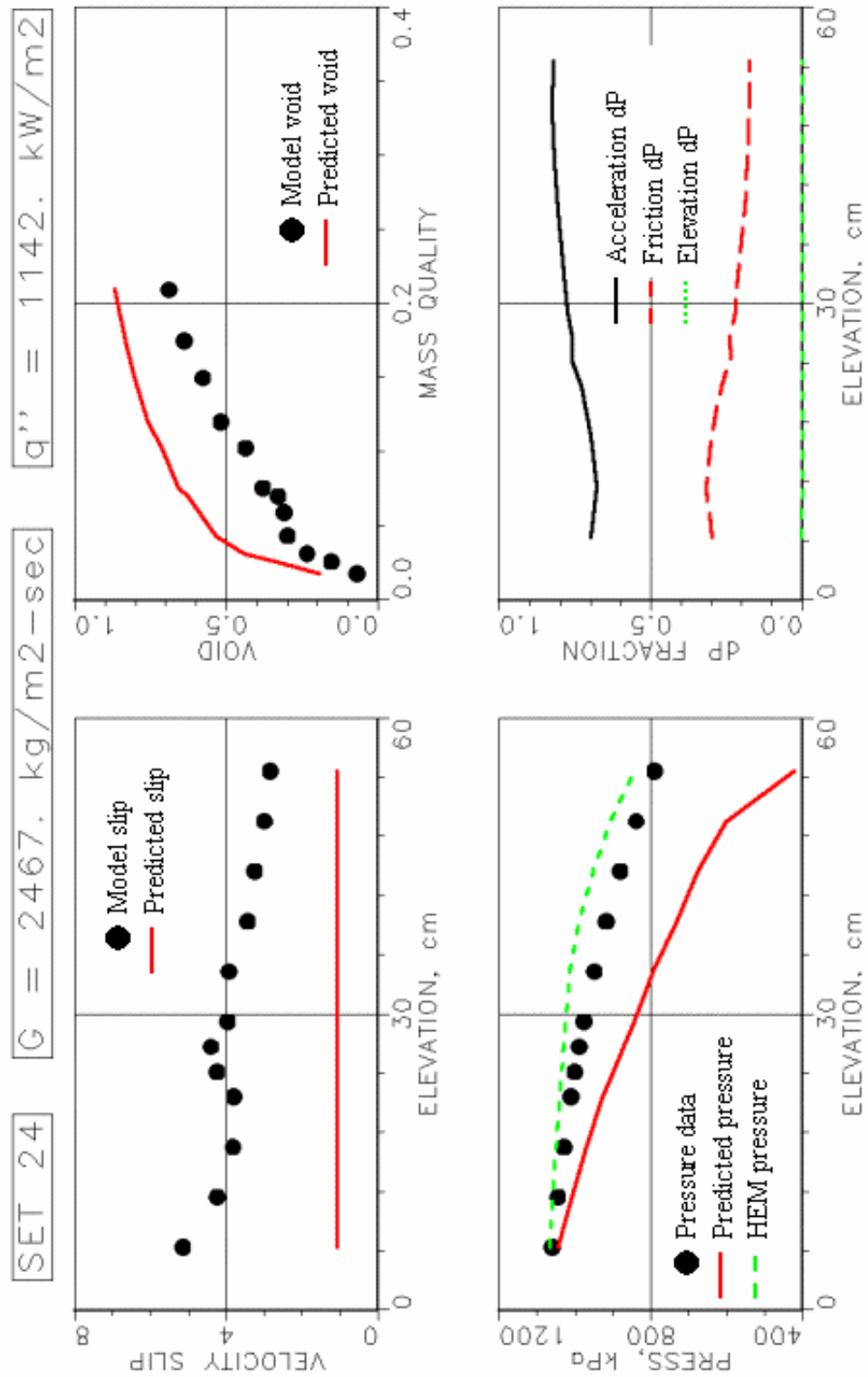


Figure 5-41. Model and prediction results for run 24.

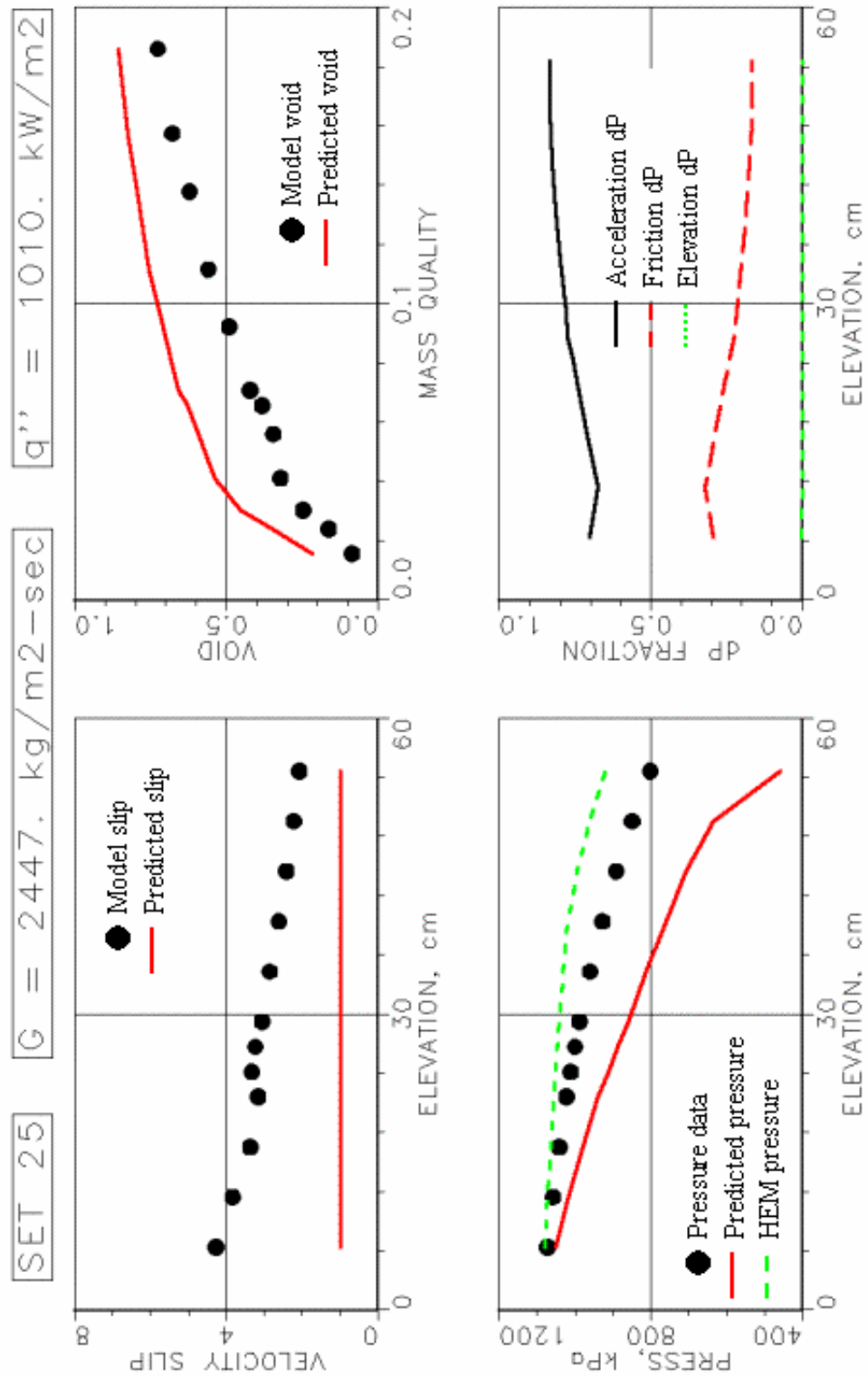


Figure 5-42. Model and prediction results for run 25.

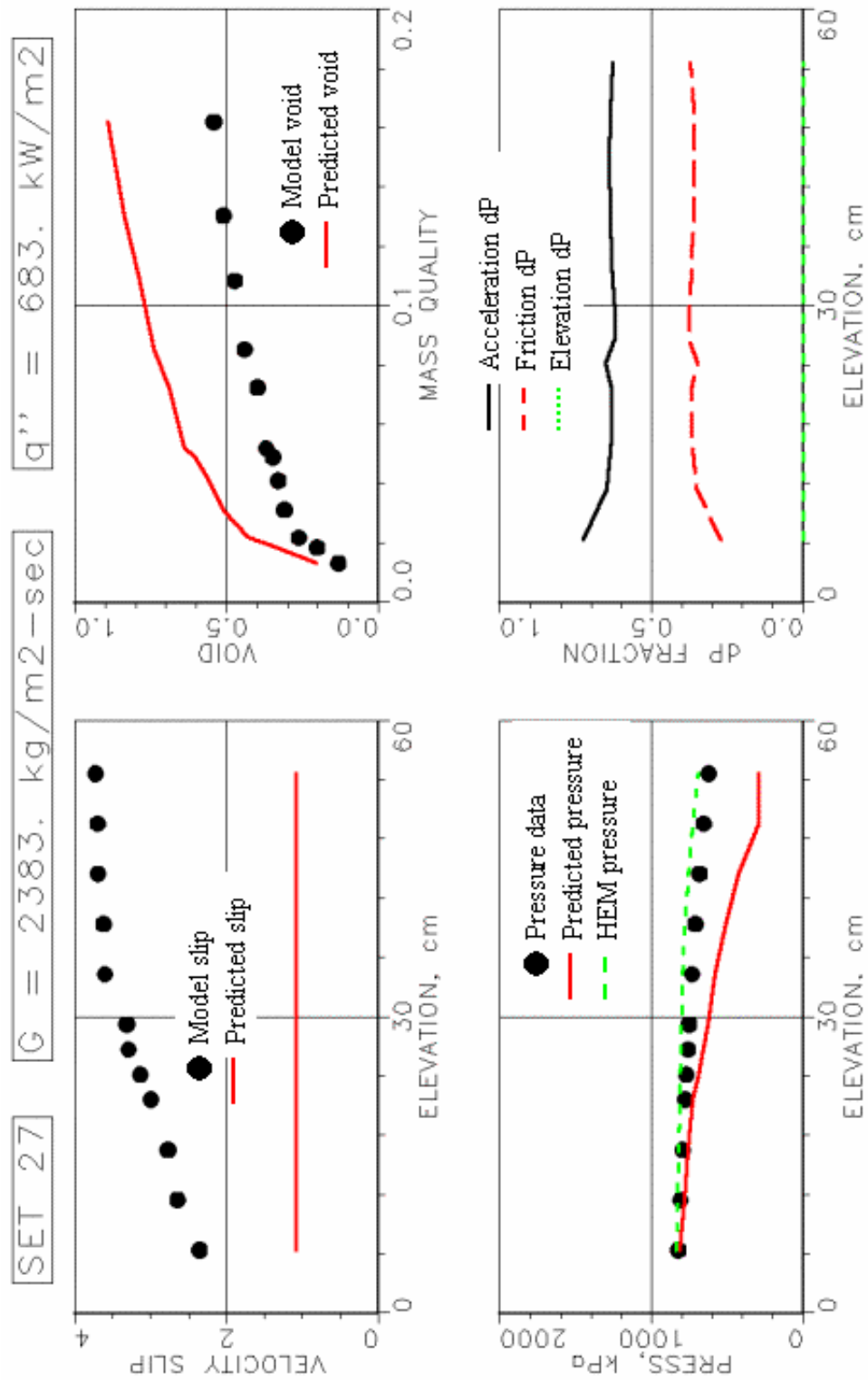


Figure 5-43. Model and prediction results for run 27.

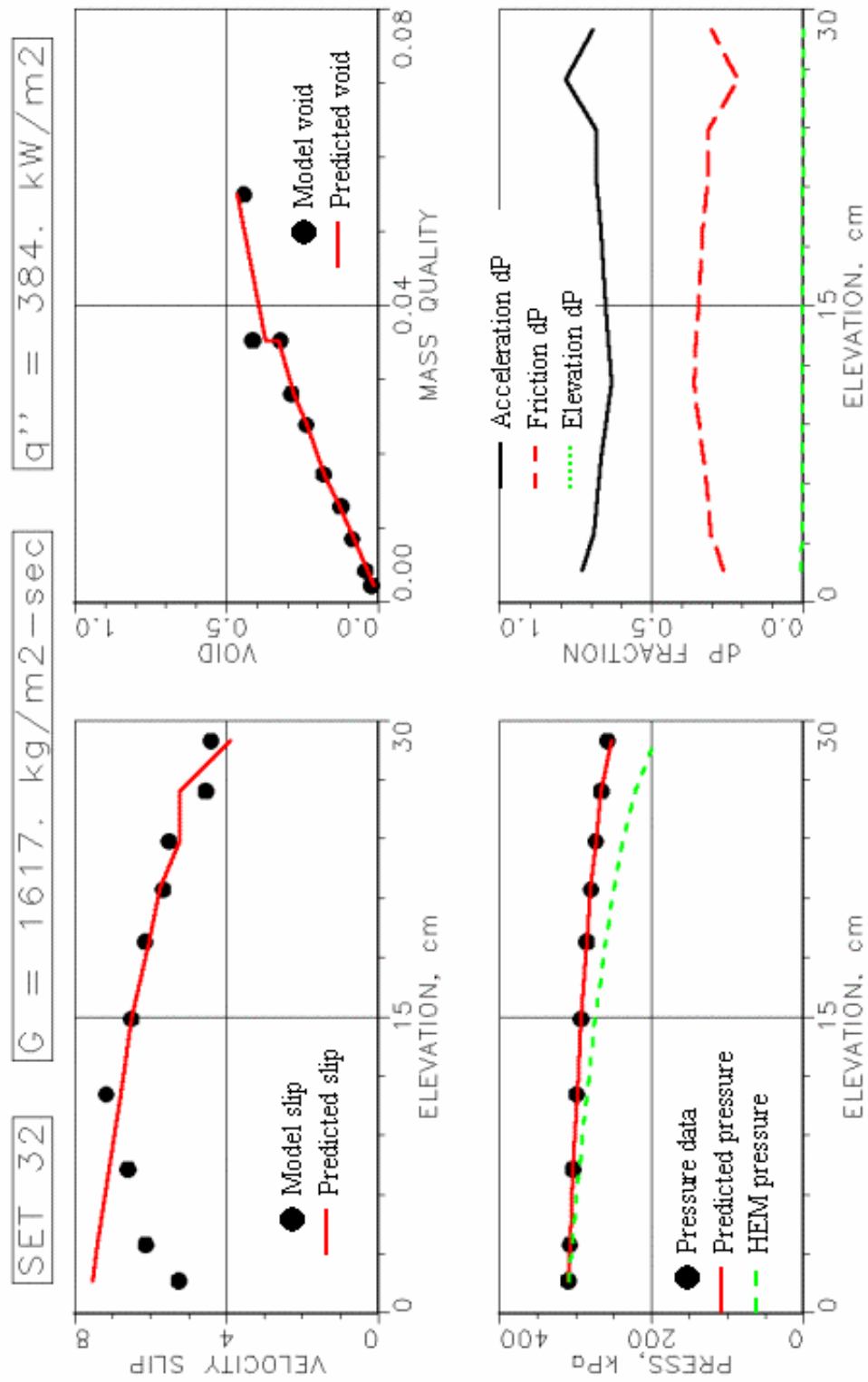


Figure 5-44. Model and prediction results for run 32.

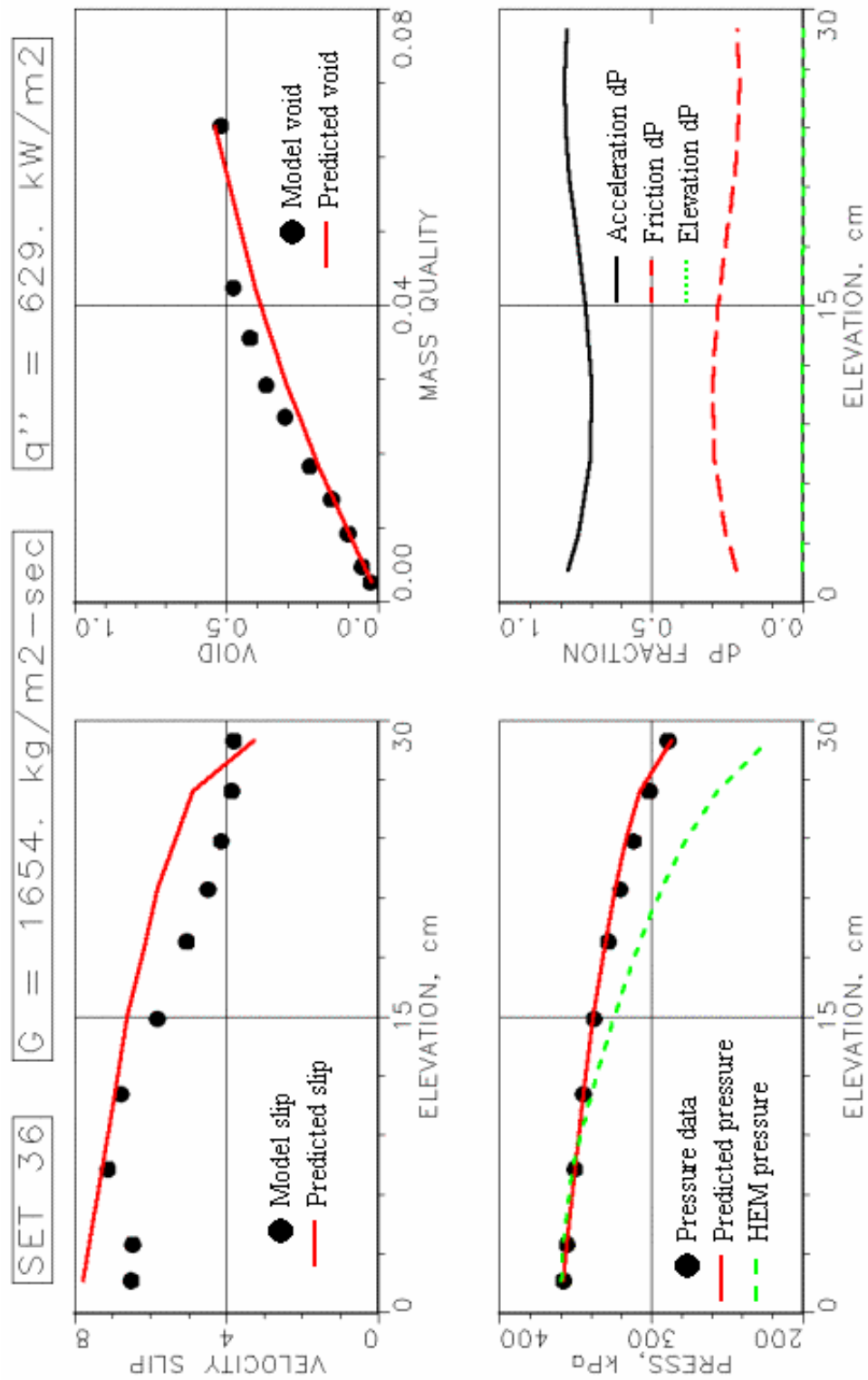


Figure 5-45. Model and prediction results for run 36.

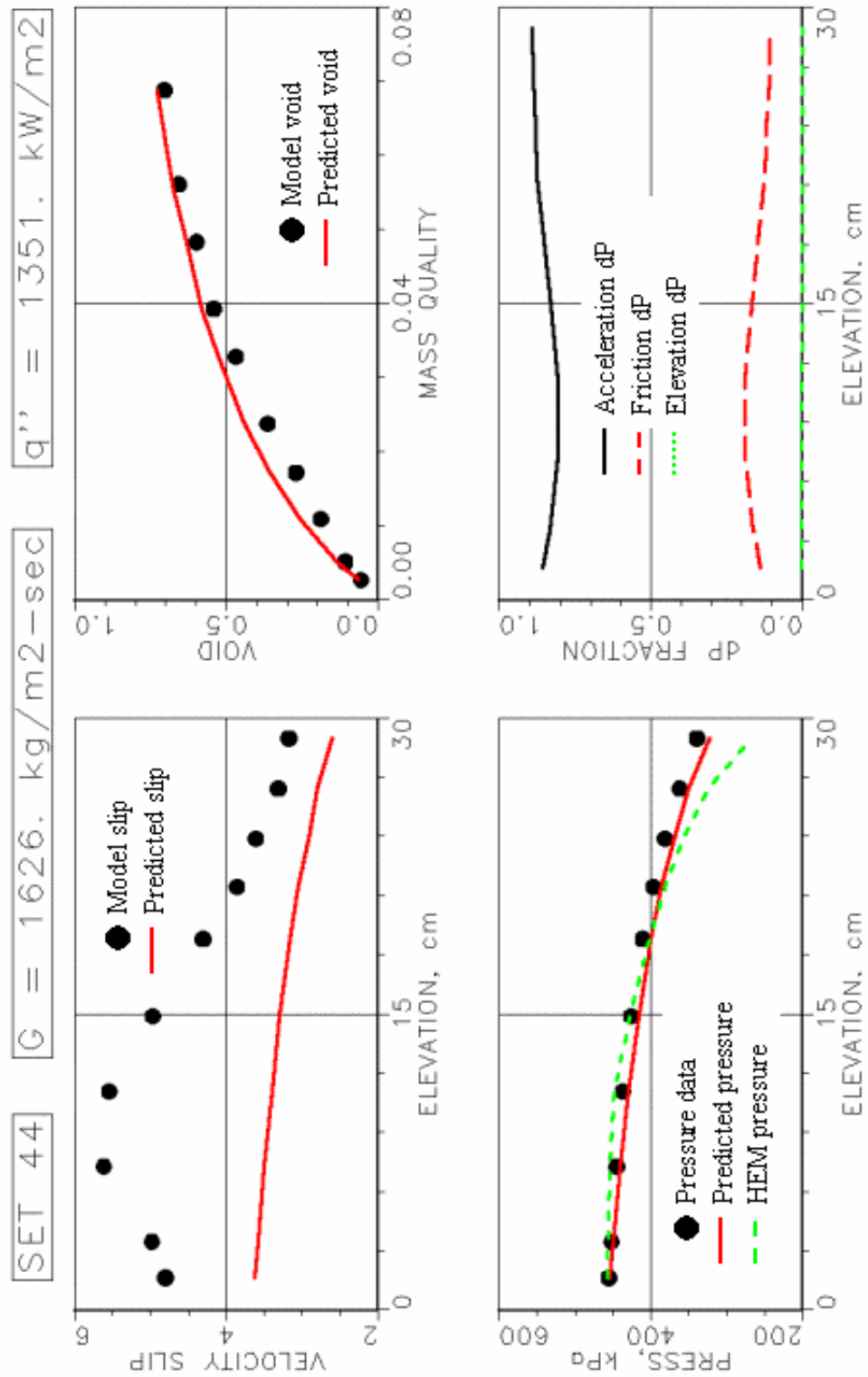


Figure 5-46. Model and prediction results for run 44.

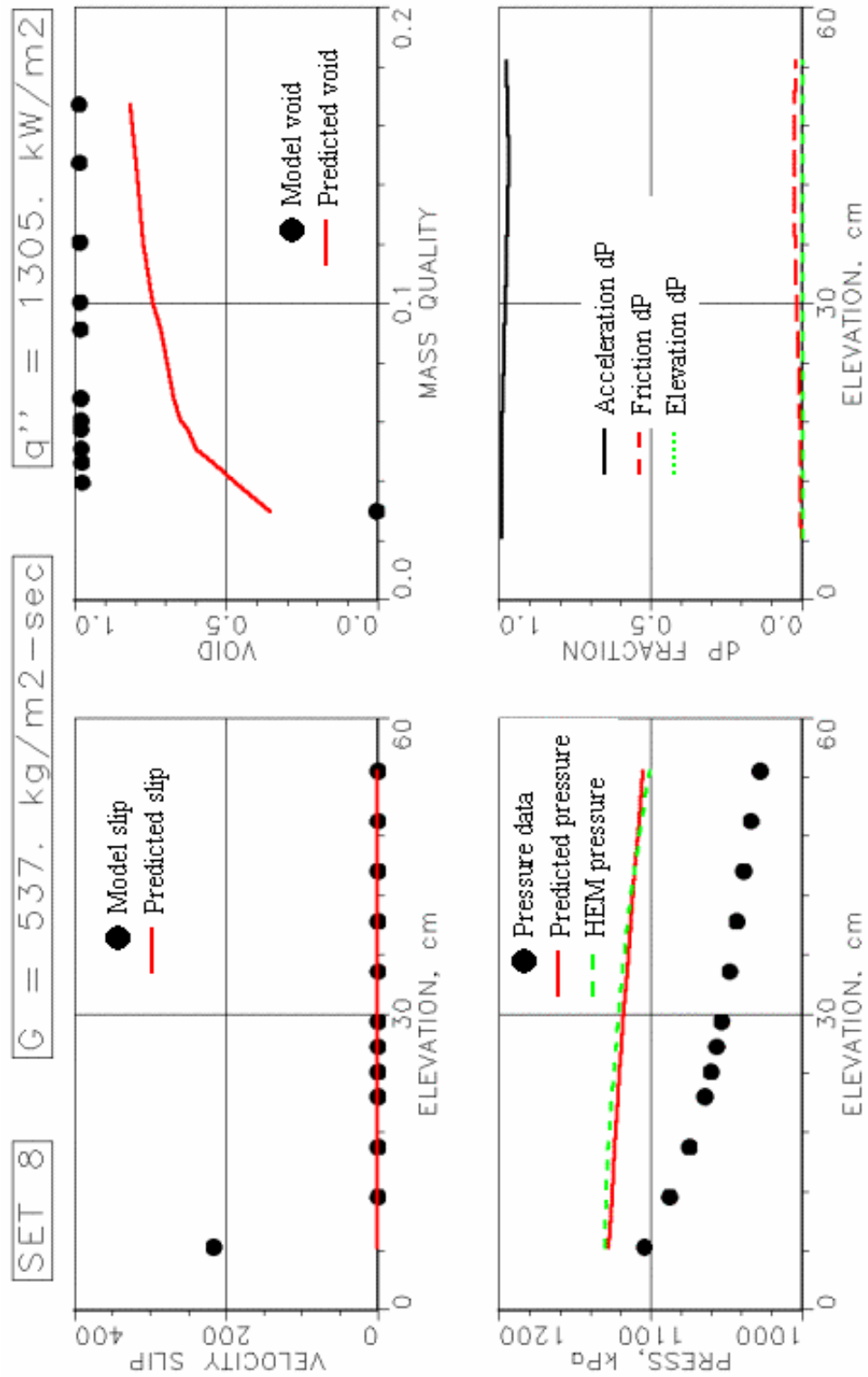


Figure 5-47. Model and prediction results for run 8.

CHAPTER 6 HEAT TRANSFER ANALYSIS

Data Omission

The data that are considered in the heat transfer portion of this analysis include some runs that were excluded in the momentum analysis. Runs eight, 14, 22 – 31, 32, 36, and 44 were all excluded from the velocity slip correlation process for various reasons. However, the nature of the heat transfer analysis is entirely different. Instead of trying to reproduce pressure measurements with an iterative formulation that is a highly sensitive function of the measured pressure gradient and vapor superheat, the heat transfer coefficient (HTC) models are always stable and always converge for any reasonable input.

For this reason, all runs in the data set can be considered in the analysis except those that are not IFB. That is, only runs 22, 26, 29, and 30 must be excluded from the heat transfer analysis. Based on the large difference in predicted pressures from the HEM model and this analysis' predictions compared with the measured pressure as seen in figure 5-47, run eight will also be excluded. The difference between measured and predicted pressures calls into question the validity of the data for run eight. The points influenced by end effects will still be excluded. Therefore, in runs 1-31, the first point will be excluded, while in runs 32-51, points one, two, and 13 will be excluded. This gives 26 runs with 12 points of measurement for the 1966 data, and 20 runs with 10 points of measurement for the 1961 data. In all, there are 512 points for analysis.

The Nature of IFB Heat Transfer

Much of the understanding derived from experiments relevant to IFB has already been presented in chapter one. Comparison of the HTC of these hydrogen data with those trends are discussed below.

The General HTC Profile

Both Takenaka (1989) and Hammouda (1997) experiments generated HTC versus quality profiles as presented in figure 6-1. Both of their experiments involved visual observations of the flow as well as local measurements necessary to determine the HTC. In figure 6-1, it is noted that there is a general decrease in HTC from the initial level when the fluid is subcooled, as the working fluids in both of their experiments were. This is the region of IAFB, in which the vapor film thickness is increasing, thus increasing the resistance to transferring heat from the wall to the low energy liquid, which acts as a heat sink. A minimum is attained near an equilibrium quality of zero. The minimum HTC value is associated with transition from IAFB to AIAFB, or ISFB for very low mass fluxes. The breakup of the liquid core is associated with an inflection point in the HTC. It is after this flow regime transition from AIAFB to DFB that the mass flux influences the gradient of the HTC as a function of quality. Lower mass fluxes decrease this slope.

In general, the HTC variations discussed above have been observed in these hydrogen data. For subcooled flows, there is a reduction in HTC up to an equilibrium quality near zero, at which point the minimum is achieved. Figure 6-2 shows this trend for runs 11 through 14. In this figure, the HTC is plotted versus equilibrium quality. It can be seen that the HTC consistently decreases up to an equilibrium quality near zero, followed by a rise. Note that run 14 never attains a positive equilibrium quality, and its HTC trend is generally downwards throughout the length of the tube. There is variation in the magnitude of the HTC at the minimum, and a relatively small variation in the equilibrium quality at which it occurs. These trends are primarily observed in the 1966 data, in which significant subcooling is prevalent.

The best subset of data that show the variation in HTC as a function of mass flux after the transition from AIAFB to DFB are the 1961 data. In these, there is very little subcooling, so the

reduction in HTC is not evident. It appears that these data have very short segments of IAFB, if any, and proceed to the AIAFB regime very quickly. There appears to be a transition from AIAFB to DFB, though, in which the mass flux impact is evident. Figures 6-3 and 6-4 show this effect for runs 39-42, and 44-47.

An Interpretation of Controlling Effects in IFB Heat Transfer

An approach to understanding the nature of IFB heat transfer is to view the vapor film as a barrier through which heat is transmitted from the wall to the heat sink-like liquid (Giarratano and Smith, 1965). This seems logical since the vapor temperature does not, in general, increase monotonically up the length of the tube as a single-phase fluid would under constant heat flux conditions. In fact, the vapor temperature, assuming the mean film temperature method applies, often decreases along the length of the tube. Therefore, the heat is getting from the wall, through the vapor, and to the liquid, causing vaporization. It is thus reasonable to consider modeling the nature of heat transfer as a single-phase vapor flowing between two boundaries that are at different temperatures.

Takenaka (1989) concluded this as well, though he extended the concept to distinguish between the three main flow regimes – IAFB, AIAFB, and DFB. He observed that his IAFB data Nusselt numbers were well modeled by using only the vapor film Reynolds number. From this, he concluded that the heat transfer in IAFB is governed by the characteristics of the vapor film. He also considered that DFB is similar to the typical post-dryout dispersed flow boiling heat transfer, and can therefore be modeled by established theory. Finally, he believed that the complexity of the geometry of AIAFB would make this regime very difficult to model.

Within this framework and with an understanding of the flow regimes, the effects on the level and trend of the HTC can be considered. There are five factors to consider; vapor properties (a function of pressure and temperature), mass velocity, level of turbulence, film

thickness, and interfacial area for heat transfer from the vapor to the liquid. Liquid properties are essentially constant in all runs. To start with, the flow is in the IAFB regime. The level of turbulence is relatively low, and as void fraction increases, the film thickness increases and the interfacial area for heat transfer decreases. These factors support the conclusion that the HTC should decrease in IAFB as void increases, which the hydrogen data show. Then, as the liquid core becomes agitated, the area for heat transfer to the liquid will increase. While the film thickness will still be increasing, the heat transfer area will increase, leading to a leveling off of the decreasing HTC. Finally, as the liquid core breaks up entering the DFB regime, the heat transfer area increases greatly, leading to a rise in the HTC. In this regime, the mass velocity and level of turbulence are controlling factors for the HTC trend. As both increase, so too does the HTC.

Throughout these variations of flow structure and conditions, the vapor is changing pressure and temperature. Figure 6-5 shows the variation of the vapor properties contained in the Dittus-Boelter HTC model, seen in the following functional relationship for the properties index:

$$h = f \left(\rho_v^{0.8} k_v^{0.6} \left(\frac{C_{p,v}}{\mu_v} \right)^{0.4} \right) \quad (6.1)$$

It is seen in this figure that, for a given run, the variation in pressure has, at most, a small impact on the properties index. For a particular run, the impact of temperature on the properties index is large for high pressure runs, and small for low pressure runs. This explains why the HTC does not vary as much at lower pressures as it does at higher pressures. At low pressure, the vapor temperature can vary significantly with minimal impact on the HTC, while at high pressure, the same temperature variation will have a significant impact. Figure 6-5 also shows that the property index is a strong function of pressure. Higher pressures will lead to higher

properties indices, and therefore higher HTC's. These observations are consistent with the HTC levels and trends observed in these hydrogen data.

Assessment of Various Models

The most accepted pre-CHF boiling HTC models have been applied to these data and found to completely fail. It is necessary to employ a model that is designed for the IFB conditions. Chapter one presents an extensive overview of the work and models associated with heat transfer in IFB. Therefore, this information will not be repeated here.

A few models in the literature predict an experimental HTC based on a standard Dittus-Boelter model with a modifying multiplier or correlating parameter that uses the Lockhart-Martinelli parameter X_{tt} (Hendricks et al. 1961, 1966, Brentari et al., 1965). In these models, the equilibrium quality is used, which makes them inapplicable to a significant portion of these NASA data. In these cases, the mass quality was inserted in place of the equilibrium quality so that they could be applied to the subcooled data. The 1961 and 1966 correlations cannot be modified in this way because they are, in fact, statistically generated correlations based on equilibrium quality – not mass quality. These two correlations were used with mass quality, but the predictive accuracies of the two models suffered significantly. To model these NASA data, either the mass quality must be used, or quality must be excluded from the correlation.

The accuracies of these models are evaluated in terms of their ability to reproduce the experimental HTC, exactly the same way that the pressure drop prediction accuracies were assessed. Table 6-1 presents the results of this statistical analysis. In this table, the percent of the 512 measurements predicted within the specified percent accuracy are listed. Note that the two Hendricks correlations were evaluated against just the positive equilibrium quality data, resulting in only 364 predictions.

The Hendricks correlations perform the best of all the applied models, but only for the positive equilibrium quality data. The 148 subcooled points can be considered as zero correlations, which greatly reduces the overall accuracy of the model. Since it is important to be able to predict the HTC in subcooled conditions, the Hendricks correlations should be compared with other models with this in mind. Figure 6-6 compares the predicted HTC using the TN3095 correlation and the experimental HTC. Note that the subcooled data are zeros on this plot.

Three versions of the Dittus-Boelter model were tried, all using the standard coefficient of 0.023 and exponents on Reynolds number of 0.8 and Prandtl number of 0.4. The first in table 6-1 used bulk conditions evaluated using saturated property values, with a quality-weighted density and specific heat, and the McAdams two-phase viscosity model. The McAdams method of determining two-phase transport properties was also applied to thermal conductivity. In general, the approach applied in this analysis is as follows:

$$\mu_{TP} = \frac{\mu_l}{1 + x \left(\frac{\mu_l}{\mu_v} - 1 \right)} \quad (6.2)$$

The second method listed used properties evaluated at the vapor film conditions. The third version of the Dittus-Boelter model in the table used the method of the first model, but with the vapor-to-wall temperature ratio multiplier of equation 1-44 applied. It is interesting to see that this approach provided the most accurate and consistent model applied to all the 512 points. Figure 6-7 compares the predicted HTC using this modified equilibrium Dittus-Boelter model and the experimental HTC. Note that all 512 points are included in the plot. The points that are predicted extremely high are associated with the highest mass flux runs in the data set. It is apparent after comparing figures 6-6 and 6-7 that the Hendricks 1966 correlation is preferred to any other model in table 6-1 when it can be used. If the flow is subcooled, then the modified

equilibrium Dittus-Boelter model should be used, but with caution, particularly for very high mass flux conditions.

Papadimitriou and Skorek (1991) applied the temperature ratio defined in equation 1-44 to the Dougall and Rohsenow (1963) model. The results of that modification as applied to these hydrogen data can be seen in table 6-1, referenced as ‘Dougall-modified’. It is seen that this modification actually decreases the accuracy of the basic Dougall model.

Lavery and Forslund followed Dougall, working with Rohsenow at MIT. They each studied various aspects of IFB and generated predictive models, as presented in chapter one. Forslund’s model performed the best of the three basic MIT models.

It is interesting to note that the other model that performs reasonably well is the Kays model, which is developed for flow between two parallel plates. This fact supports the approach of modeling the flow as a barrier to heat transfer between two boundaries at different temperatures, as previously discussed.

Models that focus on the effects of buoyancy such as Bromley’s, Bailey’s and Berenson’s, simply do not capture the physics of the mechanisms involved in forced convection heat transfer. The convective nature of these data must be included in an effective model. However, it appears that all the forced convection models applied to these data are incapable of reproducing the HTC in the IAFB region, in which the HTC value is actually decreasing. The physics associated with the downward trend in the HTC observed in runs 11-14 in figure 6-2 is not included in these models. From the AIAFB onwards through the DFB regions, the characteristics of the HTC are reasonably well modeled by most of the forced convection models. The models applied to these data vary in the magnitude of the HTC predicted, but this is not important as it can easily be

remedied by adjusting the coefficient on the model. The important feature to evaluate is whether the model captures the complicated trends of the HTC as a function of quality.

It appears that a good approach to reproducing these trends is to include a wall temperature parameter. As Papadimitriou and Skorek (1991) did, and as is commonly done, a simple, dimensionless way to include this effect is to apply the ratio of wall to vapor temperature to some power. The general argument for including such a term is that it better reflects the physical properties of the vapor film. However, if superheated vapor properties are used in the models, then including a temperature ratio multiplier must be viewed as a correlating parameter and not a mechanistic parameter, since the vapor properties should already capture the physics of the vapor film. If saturated conditions are used for both fluids, then the temperature ratio could be viewed as a mechanistically-based multiplier.

Table 6-1. Comparison of predictive accuracy of various IFB models.

HTC Model Source	# points	Accuracy to within					Model (eqn)
		10%	20%	30%	40%	50%	
TN 765 (1961)	364	31%	61%	81%	92%	97%	1.28
TN 3095 (1966)	364	35%	64%	83%	93%	97%	1.32
DB-equilibrium bulk	512	10%	26%	42%	57%	70%	1.47
DB-film	512	25%	40%	52%	64%	72%	1.47
DB-modified equilibrium bulk	512	32%	53%	67%	77%	84%	1.46 & .47
Bromley (1950)	512	0%	0%	0%	0%	0%	1.33
Bromley forced convection (1953)	512	19%	35%	45%	51%	57%	1.35
Dougall (1961)	512	12%	22%	29%	37%	49%	1.40
Dougall-modified	512	5%	14%	25%	37%	46%	1.40 & .46
Laverty (1967)	512	1%	3%	7%	17%	34%	1.42
Forslund (1968)	512	10%	19%	31%	53%	69%	1.43
Wallis-Collier (1968)	512	0%	0%	0%	2%	10%	1.38
Kays (1980)	512	20%	35%	48%	60%	68%	1.44
Berenson (1961)	512	0%	0%	0%	0%	0%	1.37
Bailey (1972)	512	0%	0%	0%	0%	0%	1.45

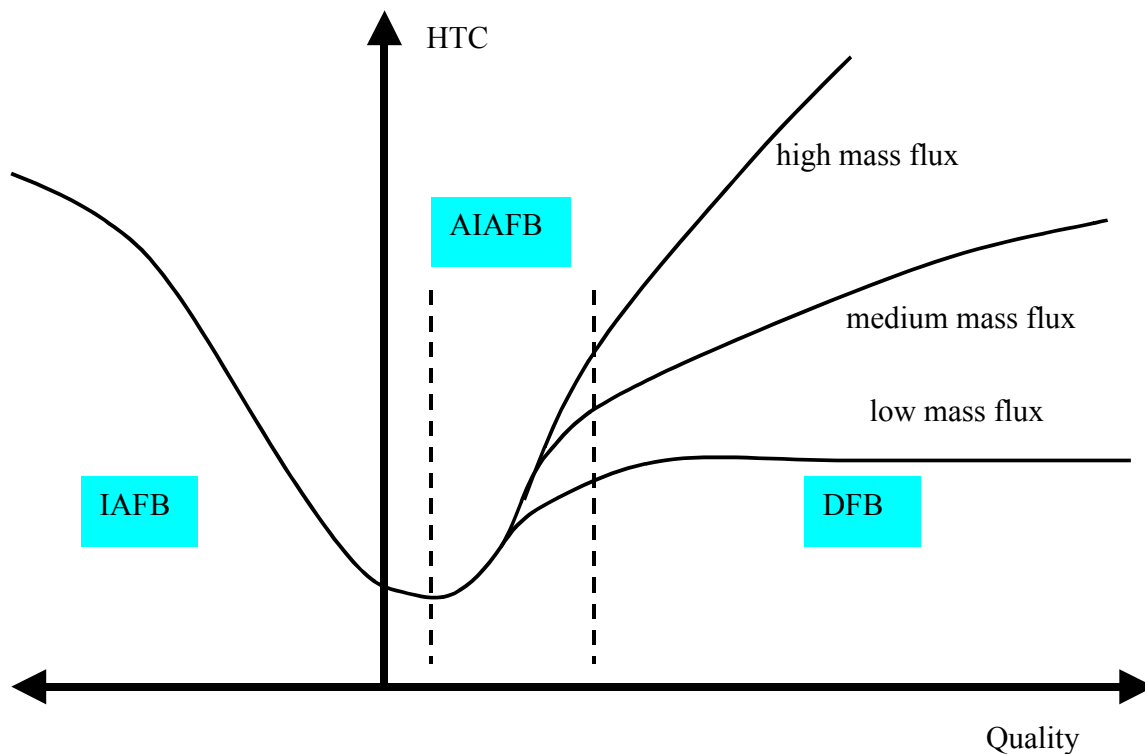


Figure 6-1. Variation of the HTC as a function of quality in IFB flow.

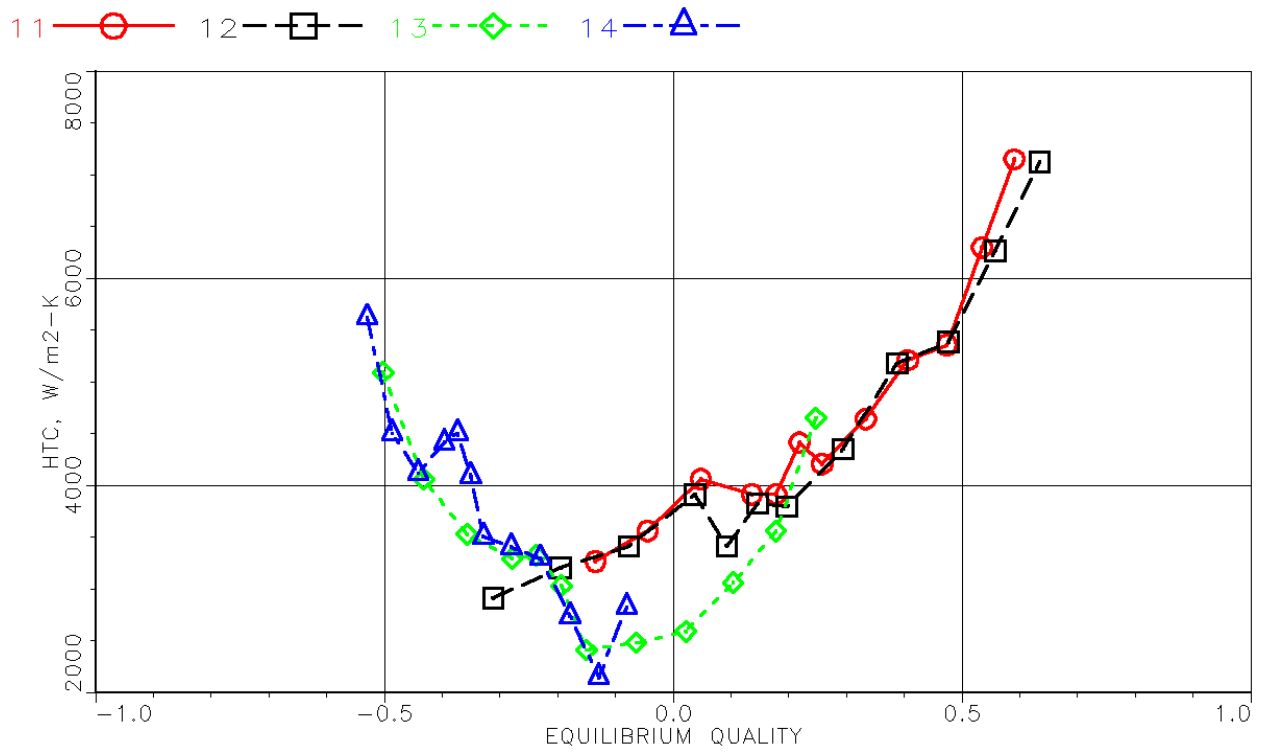


Figure 6-2. Variation of HTC versus equilibrium quality in the IAFB flow regime.

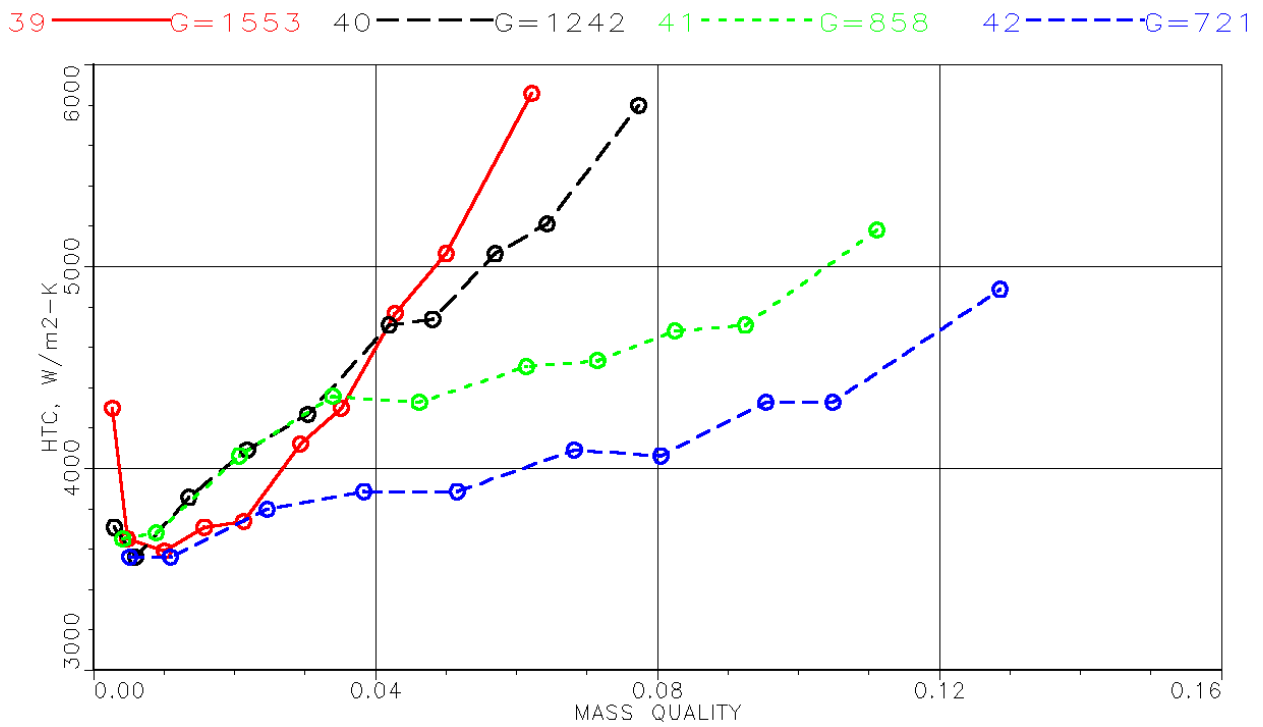


Figure 6-3. Variation of HTC versus mass quality for runs 39-42. Mass flux units are kg/m^2-sec . Trend shows that increasing mass flux increases HTC slope.

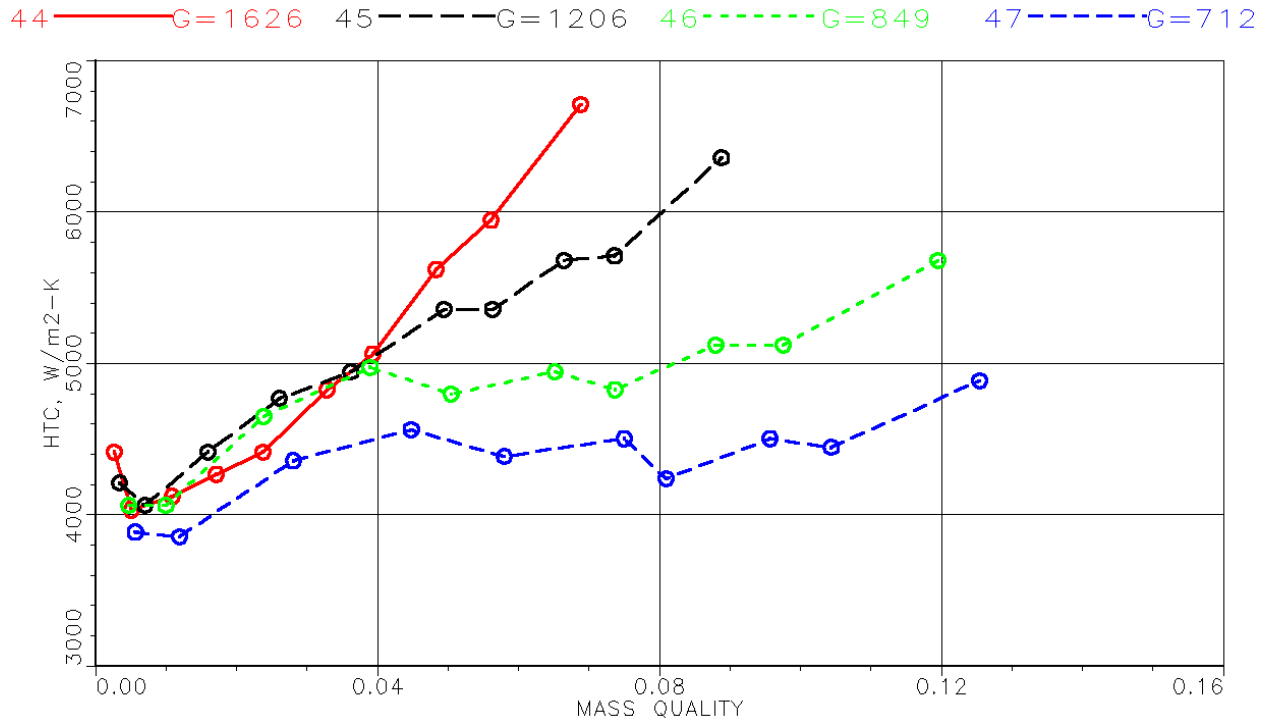


Figure 6-4. Variation of HTC versus mass quality for runs 44-47. Mass flux units are kg/m²-sec. Trend shows that increasing mass flux increases HTC slope.

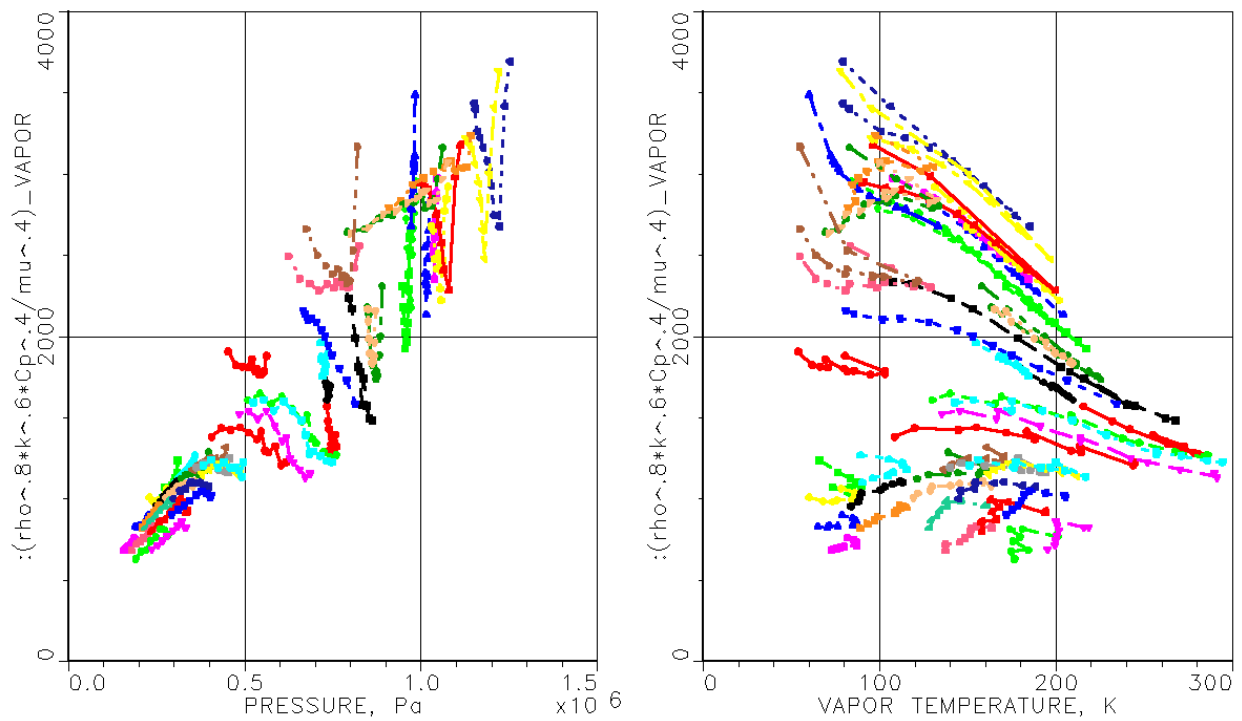


Figure 6-5. Variation of Dittus-Boelter vapor properties with pressure and temperature.

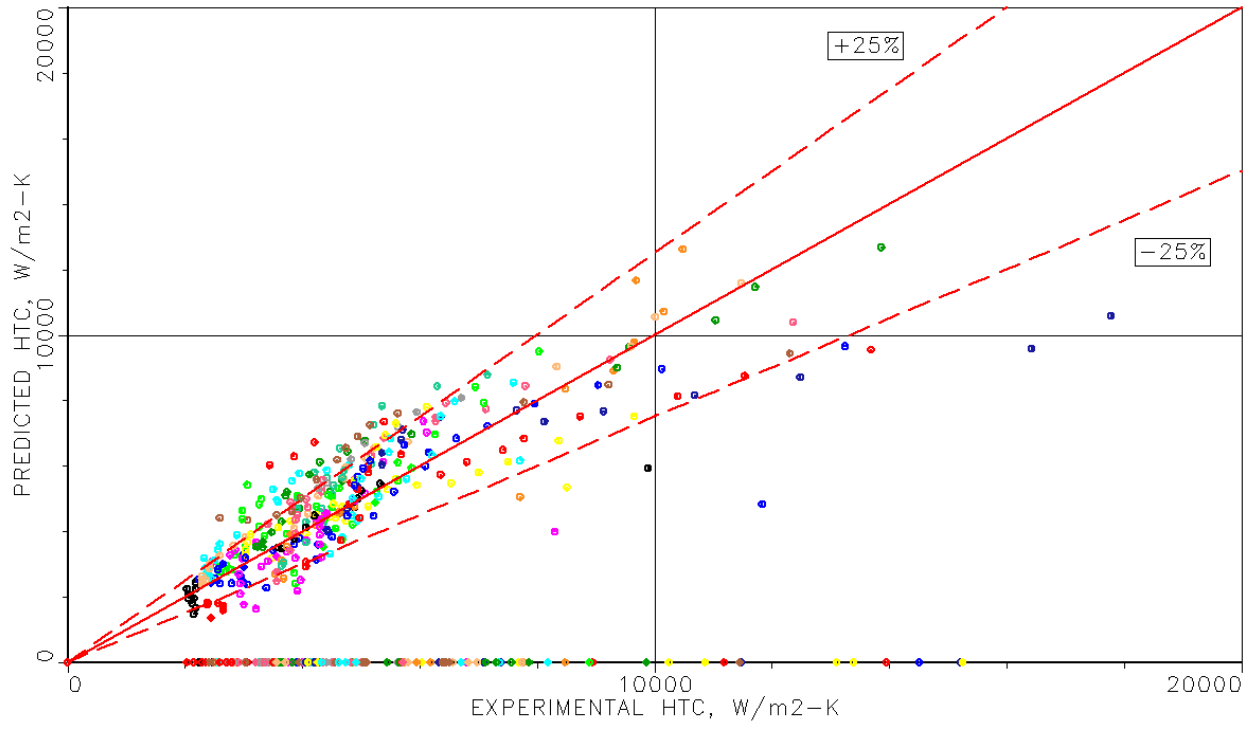


Figure 6-6. Comparison of predicted HTC using the TN 3095 correlation with the experimental HTC. Note subcooled points are set to zero.

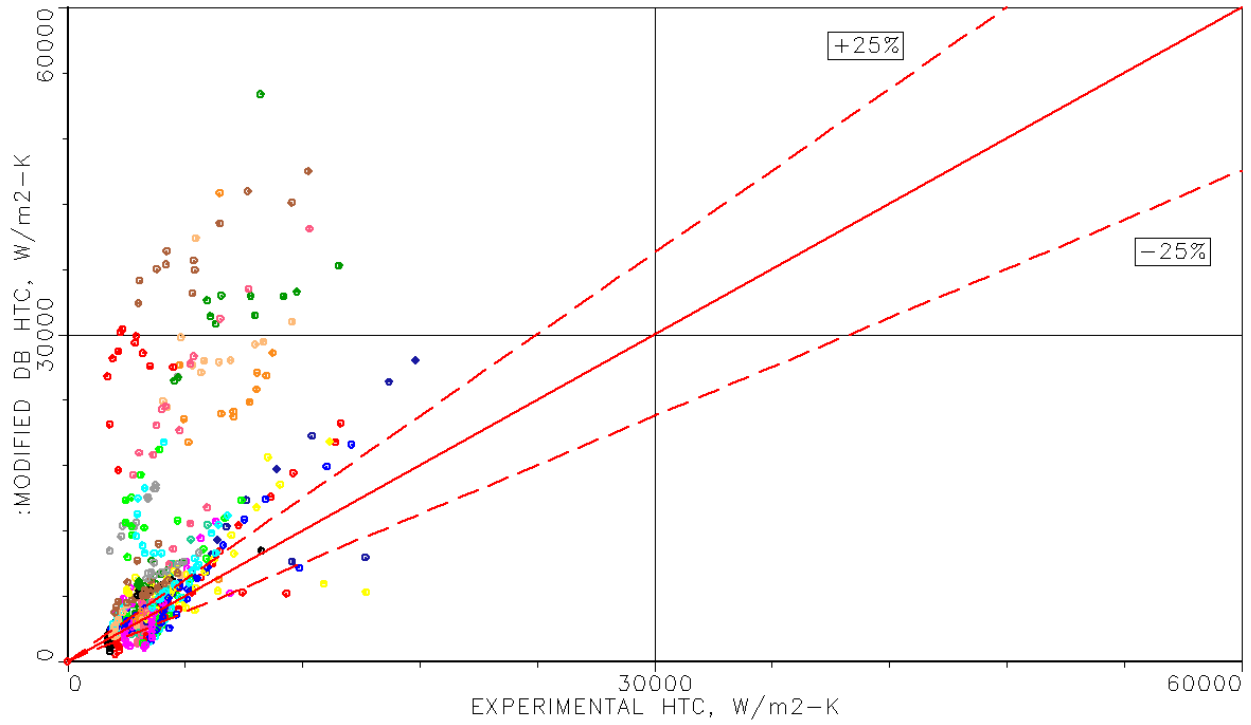


Figure 6-7. Comparison of predicted HTC using the modified equilibrium bulk Dittus-Boelter model with the experimental HTC.

CHAPTER 7 CONCLUSIONS AND RECOMMENDATIONS

General Conclusions

Local pressure and wall temperatures measurements were recorded in steady state, high heat flux conditions with liquid hydrogen entering the bottom of vertical, highly heated metal test sections. Test conditions were such that constant heat flux was established, all heat generated by the applied voltage went into heating the hydrogen, and mass flow rates and inlet conditions were measured. With the heat flux and local wall temperature measurements, the local heat transfer coefficient was determined at 12 locations. Fifty-one tests were conducted, producing 612 points of data. The range of test sections included five different tube diameters ranging from 0.48 cm to 1.29cm, and two different tube lengths of 30.5 cm and 61.0cm. Inlet pressures ranged from 188 kPa to approximately the critical pressure, mass fluxes ranged from 327 kg/m²-s to 3444 kg/m²-s, and heat fluxes from 294 kW/m² to 2093 kW/m².

It was determined that most of the 612 points were in various regimes of inverted film boiling. It was also determined that these hydrogen data behave similarly to other fluids used in previous studies of inverted film boiling. Based on the literature search, it is believed that these data are unique for all hydrogen data in the extent of measurements recorded, heat and mass fluxes, and unique in all inverted film boiling data in the range of system pressures. Therefore, this data set is extremely valuable and should be exploited to the fullest extent possible.

The available data allows for reverse engineering the mass quality, void fraction, and velocity slip by applying a five-equation model and three fundamental assumptions. These assumptions are that the liquid core does not experience sensible heating (which implies a homogeneous, solid liquid core), the vapor temperature is at the mean film temperature, and a

turbulent Blasius-based wall friction correlation with the Rogers friction multiplier is valid throughout the flow.

Pressure Drop Conclusions and Recommendations

From the results of this reverse-engineering method, two velocity slip correlations were developed, one for system inlet pressures above 600 kPa, and the other for system inlet pressures below 600 kPa. Note that since the low pressure correlation appeared to perform slightly better than the high pressure correlation, it is recommended to extrapolate the low pressure correlation range from the experimental maximum of 500 kPa up to 600 kPa. The resulting slip correlations have been shown to reproduce the pressure profiles very well, much better than the homogeneous equilibrium model. Of particular importance is the fact that pressure drops are well modeled even in subcooled conditions – a result that the homogeneous equilibrium model cannot reproduce. Since the pressure profiles were generally smooth with no points of inflection except at the highest system pressures, it is determined that flow regime transitions do not significantly affect the pressure gradient.

It is recommended that the pressure drop of inverted film boiling flows be modeled using the low and high pressure slip correlations presented in equations 5-8 through 5-11 and the conservation and closure conditions presented in chapter 3. The low pressure correlation is valid from pipe inlet conditions of 180 kPa to 600 kPa, mass fluxes from approximately 580 kg/m²-s to 1650 kg/m²-s, and heat fluxes from approximately 380 kW/m² to 1650 kW/m². The high pressure correlation is valid from pipe inlet conditions of 600 kPa to the critical pressure, mass fluxes from approximately 330 kg/m²-s to 1550 kg/m²-s, and heat fluxes from approximately 700 kW/m² to 2100 kW/m².

Heat Transfer Conclusions and Recommendations

The heat transfer coefficient data were found difficult to predict and highly dependent upon the flow regime. Pre – critical heat flux correlations completely fail to predict the heat transfer of inverted film boiling conditions. Pool boiling models for inverted film boiling also are inappropriate. Current forced convection models for inverted film boiling, while far better than the previous two classes of models, still generate large predictive errors. In particular, the physics of inverted annular film boiling, which produce negative slopes with respect to quality, is not captured by any model applied to these data. This indicates that the increasing film thickness, decreasing vapor-liquid heat transfer area, and changing vapor film conditions, are not well modeled. The agitated inverted annular film boiling and dispersed film boiling data are better modeled, which indicates that the turbulence-based physics of heat transfer in these regimes is included in convective heat transfer models.

It is recommended that for the inverted annular film boiling flow regime the modified equilibrium bulk Dittus-Boelter model, presented in equation 1-45 with the multiplier in equation 1-44, be used. For agitated inverted annular film boiling and dispersed film boiling regimes associated with positive equilibrium qualities, the Hendricks model in equation 1-32 should be used.

Recommendations for Future Efforts

It is likely that mechanistic models can be generated for the velocity slip or void fraction. To accomplish this, it is necessary to make measurements for any or all of the conditions for which assumptions were made in this effort. This includes such measurements as wall friction, radial velocity and temperature profiles, void fraction, and sensible heating of the liquid. Additionally, better models for the heat transfer coefficient are likely possible. It is expected that

separate models will be necessary for the inverted annular regimes and the agitated and dispersed regimes.

LIST OF REFERENCES

- Ahrens, F. W., 1983. Heat Pump Modeling, Simulation and Design. Heat Pump Fundamentals, Proceedings of the NATO Advanced Study Institute of Heat, Pump Fundamentals, Espinho, Spain. Ed. J. Berghmans, The Hague, Netherlands.
- Arpaci, Vedat S., 1966, Conduction heat transfer, Addison-Wesley, New York, 283.
- Babelli, I., Revankar, S. T., Ishii, M. 1994, Flow visualization study of post-critical heat flux in inverted flow. Nuclear Engineering and Design 146, 15-24.
- Bailey, J. G. M., 1972. The interaction of droplet and forced convection in post dryout heat transfer at high subcritical pressures, European Two-Phase Flow Group Meeting, Rome, Italy.
- Bankoff, S. G., 1960, A variable density single fluid model for two-phase flow with particular reference to steam-water flow, Journal of Heat Transfer, 82, 265.
- Baroczy, C. J., 1965, Correlation of liquid fraction in two-phase flow with applications to liquid metals, Chemical Engineering Progress Symposium Series, 61 (57), 179-191.
- Berenson, P. J., 1961, Film-boiling heat transfer from a horizontal surface, Journal of Heat Transfer, 83, 351-358.
- Bjorge, Robert W., Hall, Garry R., Rohsenow, Warren M. 1982, Correlation of forced convection boiling heat transfer data. International Journal of Heat and Mass Transfer 25 (6), 753-757.
- Brentari, E. G., Giarratano, P. J., Smith, R. V. Sept., 1965, Boiling heat transfer for oxygen, nitrogen, hydrogen, and helium. Technical Note 317, National Bureau of Standards, Boulder, Colorado.
- Bromley, L. A., LeRoy, N. R., Robbers, J. A. 1953, Heat transfer in forced convection film boiling. Industrial and Engineering Chemistry 45 (12), 2639-2646.
- Bromley, LeRoy A. May, 1950, Heat transfer in stable film boiling. Chemical Engineering Progress 46 (5), 221-227.
- Carey, Van P. 1992, Liquid-vapor phase-change phenomena. Taylor & Francis, New York.
- Celata, G. P. 1998, Modeling of critical heat flux in subcooled flow boiling. Heat Transfer Research 29 (45), 307-319.
- Celata, G. P., Cumo, M., Mariani, A. 1996, The effect of the tube diameter on the critical heat flux in subcooled flow boiling. International Journal of Heat and Mass Transfer 39 (8), 1755-1757.

- Celata, G. P., Cumo, M., Mariani, A., Simoncini, M., Zummo, G. 1994, Rationalization of existing mechanistic models for the prediction of water subcooled flow boiling critical heat flux. *International Journal of Heat and Mass Transfer* 37 (1), 347-360.
- Celata, Gian Piero, Mishima, Kaichiro, Zummo, Giuseppe 2001, Critical heat flux prediction for saturated flow boiling of water in vertical tubes. *International Journal of Heat and Mass Transfer* 44, 4323-4331.
- Chen, John C. Jul., 1966, Correlation for boiling heat transfer to saturated fluids in convective flow. *Industrial & Engineering Chemistry Process Design and Development* 5 (3), 322-329.
- Chisholm, D. 1973, Pressure gradients due to friction during the flow of evaporating two-phase mixtures in smooth tubes and channels. *International Journal of Heat and Mass Transfer* 16, 347-358.
- Chisholm, D., 1983, *Two-phase flow in pipelines and heat exchangers*, George Godwin of Longman Group Limited, New York.
- Chun, Tae Hyun, Baek, Won Pil, Chang, Soon Heung 2000, An integral equation model for critical heat flux at subcooled and low quality flow boiling. *Nuclear Engineering and Design* 199, 13-29.
- Class, C. R., DeHaan, J. R., Piccone, M., Cost, R. B. 1959, Boiling heat transfer to liquid hydrogen from flat surfaces. *Advances in Cryogenic Engineering* 5, 254-261.
- Coddington, Paul, Macian, Rafael 2002, A study of the performance of void fraction correlations used in the context of drift-flux two-phase flow models. *Nuclear Engineering and Design* 215 (3), 199-216.
- Collier, John G. 1981, *Convective boiling and condensation*. 2nd Edition, McGraw-Hill, Berkshire, England.
- Core, T. C., Harkee, J. F., Misra, B., Sato, K. Sept., 1959, Heat transfer studies. WADD TR 60239 Wright Air Development Center Aerojet-General Corporation.
- Dougall, Richard S., Rohsenow, Warren M. Sept., 1963, Film boiling on the inside of vertical tubes with upward flow of the fluid at low qualities. report 9079-26a, Massachusetts Institute of Technology.
- Ehrlich, Melvin P. 1991, Thermodynamically pumped IR laser. *Proceedings of the 26th Intersociety Energy Conversion Engineering* 4, 146-150.
- Forslund, R. P., Rohsenow, W. M. Nov., 1968 Dispersed flow film boiling. *Journal of Heat Transfer* 90, 399-407.

- Fu, Feng, Klausner, James F. 1997, A separated flow model for predicting two-phase pressure drop and evaporative heat transfer for vertical annular flow. *International Journal of Heat and Fluid Flow* 18, 541-549.
- Fujii, T., Takenaka, N., Asano, H., Yasuda, T. 2005, Heat transfer and pressure drop of inverted annular flow. personally sent by author, 171-176.
- Giarratano, P. J., Smith, R. V. Aug., 1965, Comparative study of forced convection boiling heat transfer correlations for cryogenic fluids. *Advances in Cryogenic Engineering* 11, 492-506.
- Gungor, K. E., Winterton, R. H. S. Mar., 1986, A general correlation for flow boiling in tubes and annuli. *International Journal of Heat and Mass Transfer* 29 (3), 351-358.
- Gungor, K. E., Winterton, R. H. S. Mar., 1987, Simplified general correlation for saturated flow boiling and comparisons of correlations with data. *Chemical Engineering Research and Design* 65 (2), 148-156.
- Hammouda, N., Groeneveld, D. C., Cheng, S. C. 1996, An experimental study of subcooled film boiling of refrigerants in vertical up-flow. *International Journal of Heat and Mass Transfer* 39 (18), 3799-3812.
- Hammouda, N., Groeneveld, D. C., Cheng, S. C. 1997, Two-fluid modeling of inverted annular film boiling. *International Journal of Heat and Mass Transfer* 40 (11), 2655-2670.
- Hedayatpour, A., Antar, B. N., Kawaji, M. JulySept., 1993, Cool-down of a vertical line with liquid nitrogen. *Journal of Thermophysics and Heat Transfer* 7 (3), 426-434.
- Hendricks, R. C., Graham, R. W., Hsu, Y. Y., Friedman, R. May, 1961, Experimental heat transfer and pressure drop of liquid hydrogen flowing through a heated tube. NASA TN D-765 NASA.
- Hendricks, R. C., Graham, R. W., Hsu, Y. Y., Friedman, R. Mar., 1966, Experimental heat transfer results for cryogenic hydrogen flowing in tubes at subcritical and supercritical pressures to 800 pounds per square inch. NASA TN D-3095.
- Hsu, Y. Y., Westwater, J. W. 1960, Approximate theory for film boiling on vertical surfaces. *Chemical Engineering Progress Series* 56, 15-24.
- Incropera, F. P. and DeWitt, D. P., 2002, *Fundamentals of heat and mass transfer*, 5th edition, John Wiley & Sons, New York.
- Ishii, M. Oct., 1977, One-dimensional drift-flux model and constitutive equations for relative motion between phases in various two-phase flow regimes. ANL 7747, Argonne National Laboratory.
- Ishii, M., De Jarlais, G. 1987, Flow visualization study of inverted annular flow of post dryout heat transfer region. *Nuclear Engineering and Design* 99, 187-199.

- Ishii, M., De Jarlais, G. 1986, Flow regime transition and interfacial characteristics of inverted annular flow. *Nuclear Engineering and Design* 95, 171-184.
- Ishii, M., Denten, J. P. 1990, Two-phase flow characteristics of inverted bubbly, slug and annular flow in post-critical heat flux region. *Nuclear Engineering and Design* 121, 349-366.
- Iverson, E. B., Carpenter, J. M. May, 2003, Kinetics of irradiated liquid hydrogen. 16th Meeting of the International Collaboration on Advanced Neutron Sources.
- Kandlikar, S. G. Feb., 1990, A general correlation for saturated two-phase flow boiling heat transfer inside horizontal and vertical tubes. *Journal of Heat Transfer* 112, 219-228.
- Kasai, Hideaki, Dino, Wilson Agerico, Muhida, Rifka 2003, Surface science-based reaction design: increasing the ortho-para hydrogen conversion yield via molecular orientation, a case study. *Progress in Surface Science* 72, 53-86.
- Kays, W. M. and Crawford, M. E., 1980, *Convective heat and mass transfer*, 2nd edition, McGraw-Hill, New York.
- Klausner, J. F., Chao, B. T., Soo, S. L., 1990, An improved method for simultaneous determination of frictional pressure drop and vapor volume fraction in vertical flow boiling. *Experimental Thermal Fluid Science*, 3, 404-415.
- Kozlov, S. M., Nozdrin, S. V. 1992, Heat transfer and boundaries of its regimes during hydrogen boiling at different metallic surfaces. *Cryogenics* 32 ICEC supplement, 245-248.
- Laverty, William F., Rohsenow, Warren M. Sept., 1964, Film boiling of saturated liquid flowing upward through a heat tube: high vapor quality range. MIT report 985732 Cambridge, MA.
- Laverty, W. F., Rohsenow, W. M. 1967, Film boiling of saturated nitrogen flowing in a vertical tube. *Journal of Heat Transfer* 89, 90-98.
- Lee, K., Ryley, D. J., 1968, Evaporation of water droplets in superheated steam, *Journal of Heat Transfer*, 90, 445-451.
- Lewis, J. P., Goodykoontz, J. H., Kline, J. F. Sept., 1962, Boiling heat transfer to liquid hydrogen and nitrogen in forced flow. NASA TN D-1314, Lewis Research Center NASA, Cleveland, Ohio.
- Liao, Jun, 2005, Modeling two-phase transport during cryogenic chilldown in a pipeline, Ph.D. dissertation, University of Florida, Dept. of Mechanical and Aerospace Engineering.
- Lockhart, R. W., Martinelli, R. C. Jan, 1949, Proposed correlation of data for isothermal two-phase, two-component flow in pipes. *Chemical Engineering Progress* 45 (1), 39-48.
- Martinelli, R. C., Boelter, L. M. K., Taylor, T. H. M., Thomsen, E. G., Feb., 1944, Isothermal pressure drop for two-phase two-component flow in a horizontal pipe. *ASME Transactions* 66, 139-151.

- Martinelli, R. C., Nelson, D. B. 1948, Prediction of pressure drop during forced-circulation boiling of water. ASME Transactions 70, 695-702.
- Martinelli, R. C., Putnam, J. A., Lockhart, R. W. 1946, Two-phase, two-component flow in the viscous region. Transactions of the American Institute of Chemical Engineers 42, 681-705.
- Milenko, Yu. Ya., Sibileva, R. M. 1997, Natural ortho-para conversion rate in liquid and gaseous hydrogen. Journal of Low Temperature Physics 107 (12), 77-92.
- Natterer, Johannes, Bargon, Joachin 1997, Parahydrogen induced polarization. Progress in Nuclear Magnetic Resonance Spectroscopy 31, 293-315.
- Nijhawan, S., Chen, J. C., Sundaram, R. K., London, E. J. Aug., 1980, Measurement of vapor superheat in post-critical heat flux boiling. Journal of Heat Transfer 102, 465-470.
- Nusselt, W., 1916, Die Oberflächenkondensation des Wasserdampfes. Zeitschr. Ver. deutsch. Ing., 60, 541-569.
- Obot, N. T., Ishii, M. 1988, Two-phase flow regime transition criteria in post-dryout region based on flow visualization experiments. International Journal of Heat and Mass Transfer 31 (12), 2559-2570.
- Ottosen, Per July, 1980, An experimental and theoretical investigation of inverse annular film flow and dispersed droplet flow, important under LOCA conditions. RISOR424 DK 4000, Roskilde, Denmark Riso National Laboratory.
- Papadimitriou, P., Skorek, T. 1992, One-dimensional thermohydraulic code theseus and its application to chilldown process simulation in two-phase hydrogen flows. Cryogenics 32 (4), 362-370.
- Premoli, A. Franceso, D. Di., Prina, A., 1970, An empirical correlation for evaluating two-phase mixture density under adiabatic conditions', paper B9, European Two Phase Flow Group Meeting, Milan, Italy.
- Ptushinskii, Yu. G. Jan., 2004, Low temperature adsorption of gases on metal surfaces (review). Low Temperature Physics 30 (1), 1-26.
- Rigot, G., 1973, Fluid capacity of an evaporator in direct expansion. ORNL-tr-5217, Oak Ridge, TN.
- Rogers, J. D. 1963, Two-phase parahydrogen friction factor. Advances in Cryogenic Engineering 9, 311-315.
- Rogers, J. D. 1967, Oscillations in flowing and heated subcritical hydrogen. Advances in Cryogenic Engineering 13, 223-231.
- Rogers, John D. Nov., 1968, Two phase friction factor for para-hydrogen between one atmosphere and the critical pressure. AIChE Journal 14 (6), 895-902.

- Rohsenow, W. M., Webber, J. H., Ling, A. T., 1956, Transactions of the American Society of Mechanical Engineers, 78, 1637.
- Schrock, V. E., Grossman, L. M. , 1959, Forced convection boiling studies, Univ. of California, Inst. Of Engineering Research, Report No. 73308-UCX-2182, Berkeley, California
- Scott, R. B., Cryogenic Engineering, Met-Chem Research, Boulder, CO, 1959.
- Shah, M. M. May 1984, Prediction of heat transfer during boiling of cryogenic fluids flowing in tubes. Cryogenics 24 (5), 231-236.
- Sherley, J. E. 1962, Nucleate boiling heat transfer data for liquid hydrogen at standard and zero gravity. Advances in Cryogenic Engineering 8, 495-500.
- Smith, S. L., 1969, Void fractions in two-phase flow. a correlation based on an equal velocity head model. Proc. Inst. Mechanical Engineering, 184 (36), 647-664.
- Sparrow, E. M. 1964, The effect of radiation on film boiling heat transfer. International Journal of Heat and Mass Transfer 7 (2), 229-238.
- Takenaka, N., Akagawa, K., Fujii, T., Nishida, K. 1990, Experimental study on flow pattern and heat transfer of inverted annular flow. Nuclear Engineering and Design 120, 293-300.
- Takenaka, N., Fujii, T., Akagawa, K., Nishida, K. 1989, Flow pattern transition and heat transfer of inverted annular flow. International Journal of Multiphase Flow 15 (5), 767-785.
- Thom, J. R. S. 1964, Prediction of pressure drop during forced circulation boiling of water. International Journal of Heat and Mass Transfer 7, 709-724.
- Wallis, Graham B. 1969, One-dimensional two-phase flow, McGraw-Hill, New York.
- Wallis, Graham B. and Collier, John G., 1968, referenced in Collier and Thome, 2001, Convective boiling and condensation, 3rd ed., pg. 284, Oxford Science Publications, Oxford, England.
- Walters, H. H. 1960, Single-tube heat transfer tests with liquid hydrogen, Advances in Cryogenic Engineering 6, 509-516.
- Wright, C. C., Walters, H. H. Aug., 1959, Single tube heat transfer tests, gaseous and liquid hydrogen. WADC TR 59423, Wright Air Development Center.
- Zivi, S. M., May, 1964, Estimation of steady-state steam void-fraction by means of the principle of minimum entropy production. Journal of Heat Transfer, Series C, 86, 247-252.
- Zuber, N., Findlay, J. A. Nov., 1965, Average volumetric concentration in two-phase flow systems. Journal of Heat Transfer 87, 453-468.

BIOGRAPHICAL SKETCH

James Pasch was born in Burlington, Iowa, in 1968, and spent most of the first 25 years of his life there. Three years were spent in Malawi, Africa, in the early 1970's, and 2 years at the U. S. Coast Guard Academy between 1987 and 1989. He earned his Bachelor of Science degree in aerospace engineering from Iowa State University in 1993. His interest in nuclear propulsion drew him to the University of Florida in pursuit of a Master of Engineering degree in nuclear engineering, completed in 1995. He has since had engineering positions at Sverdrup Technology and Pratt & Whitney, and will be returning to Jacobs Sverdrup late 2006. Jim also has master's degrees in engineering management and mechanical engineering, both from the University of Florida.